IFS DOCUMENTATION – Cy36r1
Operational implementation 26 January 2010

PART IV: PHYSICAL PROCESSES

Table of contents

European Centre for Medium-Range Weather Forecasts
Shinfield Park, Reading, RG2 9AX, England

Chapter 1
Overview

Table of contents

1.1 INTRODUCTION

The physical processes associated with radiative transfer, turbulent mixing, subgrid-scale orographic drag, moist convection, clouds and surface/soil processes have a strong impact on the large scale flow of the atmosphere. However, these mechanisms are often active at scales smaller than the horizontal grid size. Parametrization schemes are then necessary in order to properly describe the impact of these subgrid-scale mechanisms on the large scale flow of the atmosphere. In other words the ensemble effect of the subgrid-scale processes has to be formulated in terms of the resolved grid-scale variables. Furthermore, forecast weather parameters, such as two-metre temperature, precipitation and cloud cover, are computed by the physical parametrization part of the model.

This part (Part IV 'Physical processes') of the IFS documentation describes only the physical parametrization package. After all the explicit dynamical computations per time-step are performed, the physics parametrization package is called by the IFS. The physics computations are performed only in the vertical. The input information for the physics consists of the values of the mean prognostic variables (wind components, temperature, specific humidity, liquid/ice water content and cloud fraction), the provisional dynamical tendencies for the same variables and various surface fields, both fixed and variable.

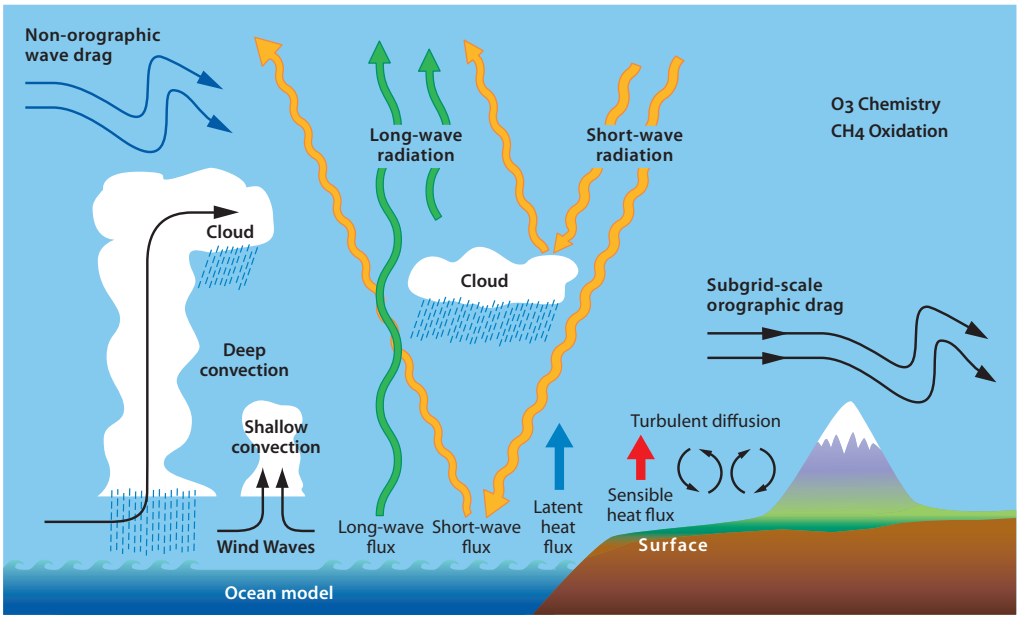

Figure 1.1 *Schematic diagram of the different physical processes represented in the IFS model.*

The time integration of the physics is based on the following.

(i) It has to be compatible with the adiabatic part of the IFS.
(ii) The tendencies from the different physical processes are computed in separate routines.
(iii) As a general approach, the value of a prognostic variable is updated with the tendency from one process and the next process starts from this updated value, in what is usually referred to as the 'method of fractional steps' (details are different for different processes).
(iv) Implicit schemes are used when needed for stability.

The radiation scheme is described in Chapter 2 'Radiation' and is the first process to be called in the physics. To save time in the rather expensive radiation computations, the full radiation part of the scheme is currently called every 1 hour. This is when the computation of the short-wave transmissivities and the long-wave fluxes are performed, using the values of temperature, specific humidity, liquid/ice water content and cloud fraction at time-step $t - \Delta t$, and monthly-mean climatologies for aerosols and the main trace gases (CO_2, O_3, CH_4, N_2O, $CFCl_3$ and CF_2Cl_2). The computation of the fluxes is not necessarily done at every grid-point but is only performed at lower horizontal resolution. The results are then interpolated back to the original grid using the model interpolation routines. The short-wave fluxes are updated every time-step using synchronous values of the zenith angle. The radiation scheme takes into account cloud-radiation interactions in detail by using the values of cloud fraction and liquid/ice water content, at every level, from the prognostic cloud scheme using the Monte Carlo Independent Column Approximation (McICA). The radiation scheme produces tendencies of temperature.

The turbulent diffusion scheme (Chapter 3 'Turbulent diffusion and interactions with the surface') is called after the orographic drag scheme. The surface fluxes are computed using Monin–Obukhov (MO) similarity theory. The computation of the upper-air turbulent fluxes is based on a combined mass-flux/eddy-diffusivity (EDMF) concept. Depending on the atmospheric stability different formulations for determining the K-coefficients and mass-fluxes M are used: for the unstable boundary layer a K-profile closure combined with a mass-flux based on a plume starting near the surface is used. In the stable boundary layer a Louis-type Richardson number Ri dependent K closure is used with $M = 0$. Further from the surface the diffusion coefficients transition to values based on MO similarity. A treatment of unresolved shear enhances the diffusion coefficients. In the lower atmosphere the turbulent orographic form drag parametrization induces drag originating from small scale orography. Because of numerical stability problems the integration of the mass-flux/diffusion equation is performed in an implicit manner. In fact, it uses a so-called 'more than implicit' method, in which the 'implicitness factor' α (which takes the value 0 in a fully explicit scheme and 1 in a fully implicit one) is set to 1.5. During the integration it uses the values of the prognostic variables at $t - \Delta t$ to compute the updraught properties ϕ_u, mass-fluxes M and K-coefficients. But it uses the tendencies updated by the dynamics and radiation on the right hand side of the discretized mass-flux/diffusion equation. The turbulent diffusion scheme also predicts the skin temperature. The turbulent diffusion scheme is written in moist conserved variables liquid static energy s_l and total water q_t and predicts total water variance σ_{qt}. Assuming a total water distribution function this allows for conversion to the cloud variables liquid/ice water content and cloud fraction. This allows for the treatment of stratocumulus. Yet convective clouds are currently excluded from the treatment within the turbulent diffusion scheme. The turbulent diffusion scheme produces tendencies of temperature, specific humidity, liquid/ice water content, cloud fraction and wind components.

The subgrid-scale orographic drag scheme is called before the turbulent diffusion and is described in Chapter 4 'Subgrid-scale orographic drag'. The subgrid-scale orographic drag parametrization represents the low level blocking effects of subgrid-scale orography and the transports due to subgrid-scale gravity waves that are excited when stably stratified flow interacts with the orography. Numerically the scheme requires an implicit treatment for the lowest level. The subgrid-scale orographic drag scheme produces tendencies of the wind components plus implicit coefficient. They are time integrated together with the turbulent diffusion.

The non-orographic gravity parametrization as presented in Chapter 5 accounts for the effects of unresolved non-orographic gravity waves. These waves are generated in nature by processes like deep convection, frontal disturbances, and shear zones. Propagating upward from the troposphere these waves break in the middle atmosphere, comprising the stratosphere and the mesosphere, where they exert a

strong drag on the flow. The parametrization uses a globally uniform wave spectrum, and propagates it vertically through changing horizontal winds and air density, thereby representing the wave breaking effects due to critical level filtering and non-linear dissipation.

The moist convection scheme is described in Chapter 6 'Convection' . The scheme is based on the mass-flux approach and is divided in deep, mid-level and shallow convection. For deep convection the convective mass-flux is determined by assuming Convective Available Potential Energy (CAPE) is adjusted towards zero over a specified timescale. For mid-level convection the cloud base mass-flux is directly related to the large scale vertical velocity. The intensity of shallow convection is estimated by assuming an equilibrium of moist static energy in the sub cloud layer. The cloud scheme (see below) is called once before convection to obtain first guess entry profiles for convection. The convection scheme provides tendencies of temperature, specific humidity and wind components.

In Chapter 7 'Clouds and large-scale precipitation' the prognostic cloud scheme is described. It solves two prognostic equations for liquid/ice water content and cloud fraction. The cloud scheme represents the cloud formation by cumulus convection, the formation of boundary layer and stratiform clouds. The scheme also takes into account several important cloud processes like cloud-top entrainment, precipitation of water and ice and evaporation of precipitation. Supersaturation with respect to ice is allowed. In the numerical integration of the equations the terms depending linearly on the values of liquid/ice water and cloud fraction are integrated analytically. The cloud scheme produces tendencies of all the prognostic variables.

The soil/surface scheme is described in Chapter 8 'Surface parametrization'. The scheme includes prognostic equations for temperature and moisture in four soil layers and snow mass. The soil equations use an implicit time integration scheme. An interception layer collects water from precipitation and dew fall. The evaporative fluxes consider separately the fractional contributions from snow cover, wet and dry vegetation and bare soil.

Chapter 9 'Methane oxidation' describes a simple parametrization of the upper-stratospheric moisture source due to methane oxidation. A parametrization representing photolysis of vapour in the mesosphere is also included.

Chapter 10 'Ozone chemistry parametrization' gives a brief description of the ozone parametrization and Chapter 11 'Climatological data' describes the distributions of climatological fields.

1.2 OVERVIEW OF THE CODE

CALLPAR is the routine that controls the physical parametrization package with the exception of the main radiation routine RADINTG. RADINTG controls the computation of the short-wave transmissivities and the long-wave fluxes. RADINTG is called outside CALLPAR because of the need to make the radiation space interpolation compatible with the distributed memory version of the IFS. GP_MODEL is a high level routine that controls all computations in grid-point space. It calls both CALLPAR via interface routines EC_PHYS_DRV, EC_PHYSG, EC_PHYS and RADINTG via driver RADDRV.

In CALLPAR the physics routines are called in the following order:

SURFRAD	Computes radiative properties of the surface.
CLDPP	Computes cloud parameters required for the post processing (e.g. total cloud cover).
RADHEATN	Computes the temperature tendencies and the downward radiation fluxes at the surface with updated (every time-step) values for the zenith angle.
GWDRAG	Computes the tendencies for u, v and T due to the parametrization of subgrid-scale orographic drag. It also computes subgrid orographic coefficients for use in VDFMAIN.
VDFOUTER	Calls VDFMAIN in two sub time steps for numerical stability. VDFMAIN computes the vertical exchange of u, v, T, q, a, l and i by turbulence.
CLOUDSC	First guess call of cloud scheme to determine preliminary entry profiles for convection.
GWDRAG_WMSS	Computes the tendencies for u, v and T due to the parametrization of non-orographic gravity waves.
CUCALLN	Interface to call CUMASTRN that controls the computation of the tendencies for u, v, T and q and the cloud detrainment term due to the parametrization of moist convective processes.
CLOUDSC	Computes tendencies for u, v, T, q, a, l and i due to the parametrization of the cloud processes.
METHOX	Computes tendencies for q due to methane oxidation and water vapour photolysis.
SURFTSTP	Controls the soil/surface scheme.
STOCHADIATEN	Optionally add stochastic perturbations to physics tendencies.
O3CHEM	Computes tendencies for O_3 due to ozone chemistry.
SLTEND	Optionally average tendencies from radiation, convection and cloud in time and space along the semi-Lagrangian trajectory.

Chapter 2
Radiation

Table of contents

2.1 RADIATIVE HEATING

Table 2.1 gives the timeline of the major changes affecting the representation of the radiation transfer (RT) in the ECMWF model over the last twenty years.

Since 5 June 2007, with Cy32r2 of the ECMWF IFS operational libraries, a new approach to the inclusion of the cloud effects on radiation fields (the Monte-Carlo Independent Column Approximation, McICA) has been introduced in the ECMWF radiation schemes (McRad, Morcrette *et al.*, 2008a), which are based on the Rapid Radiation Transfer Model (RRTM), originally developed at AER, Inc. (Mlawer *et al.*, 1997; Iacono *et al.*, 2008). The McICA approach is described in Section 2.4 together with a description of the long-wave (Section 2.5) and short-wave (Section 2.6) parts of the radiation scheme.

The previous radiation schemes based on Morcrette (1991) operational in the high-resolution 10-day forecasts from May 1989 to June 2000 are still described in this documentation as they form the basis for

Table 2.1 *Major changes in the representation of radiation transfer in the ECMWF forecasting system.*

Cycle	Implementation date	Description
SPM 32	02/05/1989	RT schemes from Univ.Lille
SPM 46	01/02/1993	Optical properties for ice and mixed phase clouds
IFS 14R3	13/02/1996	Revised LW and SW absorption coefficients from HITRAN'92
IFS 16R2	15/05/1997	Voigt profile in long-wave RT scheme
IFS 16R4	27/08/1997	Revised ocean albedo from ERBE
IFS 18R3	16/12/1997	Revised LW and SW absorption coefficients from HITRAN'96
IFS 18R5	01/04/1998	Seasonal land albedo from ERBE
IFS 22R3	27/06/2000	RRTM_{LW} as long-wave RT scheme short-wave RT scheme with 4 spectral intervals
IFS 23R4	12/06/2001	Hourly, instead of 3-hourly, calls to RT code during data assimilation cycle
IFS 25R1	09/04/2002	Short-wave RT scheme with 6 spectral intervals
IFS 26R3	07/10/2003	New aerosol climatology adapted from Tegen et al. (1997), new radiation grid
IFS 28R3	28/09/2004	Radiation called hourly in high resolution forecasts
IFS 32R2	05/06/2007	McICA approach to RT with RRTM_{LW} and RRTM_{SW} revised cloud optical properties, MODIS-derived land albedo

the linearized schemes for short-wave (Section 2.2) and long-wave (Section 2.3) radiation transfer used in the assimilation.

The solution of the radiative transfer equation to obtain the fluxes is unfortunately very expensive, so depending on the model configuration (high resolution 10-day forecast, medium-resolution EPS, low resolution "climate" simulation or seasonal forecast), savings in computer time spent in the radiation calculations are obtained by using a reduced (coarser) radiation grid (Morcrette *et al.*, 2008b) and/or by calling the full radiation with a reduced time frequency. These reduced radiation configurations are described in Section 2.7 together with the interpolation scheme used for obtaining the radiative fluxes at every grid point and every time step for the relevant instantaneous temperature profile and solar zenith angle.

The radiative heating rate is computed as the divergence of net radiation fluxes $\mathcal{F}$ so that

$$\left(\frac{\partial T}{\partial t}\right)_{\text{rad}} = -\frac{g}{c_p}\frac{\partial \mathcal{F}}{\partial p} \tag{2.1}$$

where c_p is the specific heat at constant pressure of moist air

$$c_p = c_{p_{\text{dry}}}\{1 + (c_{p_{\text{vap}}} - c_{p_{\text{dry}}})q/c_{p_{\text{dry}}}\}$$

and $c_{p_{\text{dry}}}$ and $c_{p_{\text{vap}}}$ are the specific heats at constant pressure of dry air and water vapour, respectively.

A description of the inputs, in particular the climatologically defined quantities of radiative importance is given in Section 2.8. Finally, an alphabetical list of the subroutines of the radiation scheme is given in Section 2.9.

2.2 THE PRE-CY32R2 SHORT-WAVE RADIATION SCHEME

The rate of atmospheric heating by absorption and scattering of short-wave radiation is

$$\frac{\partial T}{\partial t} = \frac{g}{c_p}\frac{\partial \mathcal{F}_{\text{SW}}}{\partial p} \tag{2.2}$$

where $\mathcal{F}_{\text{SW}}$ is the net total short-wave flux (the subscript SW will be omitted in the remainder of this section).

$$\mathcal{F}(\delta) = \int_0^\infty \mathrm{d}\nu \left[\int_0^{2\pi} \mathrm{d}\phi \left\{\int_{-1}^{+1} \mu \mathcal{L}_\nu(\delta, \mu, \phi)\, \mathrm{d}\mu\right\}\right] \tag{2.3}$$

is the diffuse radiance at wavenumber ν, in a direction given by the azimuth angle, ϕ, and the zenith angle, θ, with $\mu = \cos\theta$. In (2.3), we assume a plane parallel atmosphere, and the vertical coordinate is the optical depth δ, a convenient variable when the energy source is outside the medium

$$\delta(p) = \int_p^0 \beta_v^{\text{ext}}(p')\,\mathrm{d}p' \tag{2.4}$$

$\beta_\nu^{\text{ext}}(p)$ is the extinction coefficient, equal to the sum of the scattering coefficient β_ν^{sca} of the aerosol (or cloud particle absorption coefficient β_ν^{abs}) and the purely molecular absorption coefficient k_ν. The diffuse radiance $\mathcal{L}_\nu$ is governed by the radiation transfer equation

$$\begin{aligned}\mu\frac{\mathrm{d}\mathcal{L}_\nu(\delta,\mu,\phi)}{\mathrm{d}\delta} &= \mathcal{L}_\nu(\delta,\mu,\phi) - \frac{\varpi_\nu(\delta)}{4}P_\nu(\delta,\mu,\phi,\mu_0,\phi_0)\mathcal{E}_\nu^0\exp(-\delta/\mu_r)\\ &\quad - \frac{\varpi_\nu(\delta)}{4}\int_0^{2\pi}\mathrm{d}\phi'\left\{\int_{-1}^{+1}\Phi_\nu(\delta,\mu,\phi,\mu',\phi')\mathcal{L}_\nu(\delta,\mu',\phi')\,\mathrm{d}\mu'\right\}\end{aligned} \tag{2.5}$$

$\mathcal{E}_\nu^0$ is the incident solar irradiance in the direction $\mu_0 = \cos\theta_0$, ϖ_ν, is the single scattering albedo $(= \beta_\nu^{\text{sca}}/k_v)$ and $\Phi(\delta,\mu,\phi,\mu',\phi')$ is the scattering phase function which defines the probability that radiation coming from direction (μ',ϕ') is scattered in direction (μ,ϕ). The short-wave part of the scheme, originally developed by Fouquart and Bonnel (1980) solves the radiation transfer equation and integrates the fluxes over the whole short-wave spectrum between 0.2 and 4 µm. Upward and downward fluxes are obtained from the reflectances and transmittances of the layers, and the photon-path-distribution method allows to separate the parametrization of the scattering processes from that of the molecular absorption.

2.2.1 Spectral integration

Solar radiation is attenuated by absorbing gases, mainly water vapour, uniformly mixed gases (oxygen, carbon dioxide, methane, nitrous oxide) and ozone, and scattered by molecules (Rayleigh scattering), aerosols and cloud particles. Since scattering and molecular absorption occur simultaneously, the exact amount of absorber along the photon path length is unknown, and band models of the transmission function cannot be used directly as in long-wave radiation transfer (see Section 2.2). The approach of the photon path distribution method is to calculate the probability $\Pi(\mathcal{U})\,\mathrm{d}\mathcal{U}$ that a photon contributing to the flux $\mathcal{F}_{\text{cons}}$ in the conservative case (i.e., no absorption, $\omega_\nu = 1, k_\nu = 0$) has encountered an absorber amount between $\mathcal{U}$ and $\mathcal{U} + \mathrm{d}\mathcal{U}$. With this distribution, the radiative flux at wavenumber v is related to $\mathcal{F}_{\text{cons}}$ by

$$\mathcal{F}_v = \mathcal{F}_{\text{cons}}\int_0^\infty \Pi(\mathcal{U})\exp(-k_\nu\mathcal{U})\,\mathrm{d}\mathcal{U} \tag{2.6}$$

and the flux averaged over the spectral interval $\Delta\nu$ can then be calculated with the help of any band model of the transmission function $t_{\Delta\nu}$

$$\mathcal{F} = \frac{1}{\Delta\nu}\int_{\Delta\nu}\mathcal{F}_\nu\,\mathrm{d}\nu = \mathcal{F}_{\text{cons}}\int_0^\infty \Pi(\mathcal{U})t_{\Delta\nu}(\mathcal{U})\,\mathrm{d}\nu \tag{2.7}$$

To find the distribution function $\Pi(\mathcal{U})$, the scattering problem is solved first, by any method, for a set of arbitrarily fixed absorption coefficients k_1, thus giving a set of simulated fluxes $\mathcal{F}_{k_1}$. An inverse Laplace transform is then performed on (2.6) (Fouquart, 1974). The main advantage of the method is that the actual distribution $\Pi(\mathcal{U})$ is smooth enough that (2.6) gives accurate results even if $\Pi(\mathcal{U})$ itself is not known accurately. In fact, $\Pi(\mathcal{U})$ needs not be calculated explicitly as the spectrally integrated fluxes are

$$\begin{aligned}\mathcal{F} &= \mathcal{F}_{\text{cons}}t_{\Delta v}(\langle\mathcal{U}\rangle) \quad &&\text{in the limiting case of weak absorption}\\ \mathcal{F} &= \mathcal{F}_{\text{cons}}t_{\Delta v}(\langle\mathcal{U}^{1/2}\rangle) \quad &&\text{in the limiting case of strong absorption}\end{aligned}$$

where $\langle\mathcal{U}\rangle = \int_0^\infty \Pi(\mathcal{U})\mathcal{U}\,\mathrm{d}\mathcal{U}$ and $\langle\mathcal{U}^{1/2}\rangle = \int_0^\infty \Pi(\mathcal{U})\mathcal{U}^{1/2}\,\mathrm{d}\mathcal{U}$.

The atmospheric absorption in the water vapour bands is generally strong, and the scheme determines an effective absorber amount $\mathcal{U}_{\text{e}}$ between $\langle\mathcal{U}\rangle$ and $\langle\mathcal{U}^{1/2}\rangle$ derived from

$$\mathcal{U}_{\text{e}} = \ln(\mathcal{F}_{k_{\text{e}}}/\mathcal{F}_{\text{cons}})/k_{\text{e}} \tag{2.8}$$

where k_e is an absorption coefficient chosen to approximate the spectrally averaged transmission of the clear sky atmosphere

$$k_e = \frac{1}{\mathcal{U}_{tot}/\mu_0} \ln(t_{\Delta v}(\mathcal{U}_{tot}/\mu_0)) \tag{2.9}$$

where U_{tot} is the total amount of absorber in a vertical column and $\mu_0 = \cos\theta_0$. Once the effective absorber amounts of H_2O and uniformly mixed gases are found, the transmission functions are computed using Pade approximants

$$t_{\Delta\nu}(\mathcal{U}) = \frac{\sum_{i=0}^{N} a_i \mathcal{U}^{i-1}}{\sum_{j=0}^{N} b_j \mathcal{U}^{j-1}} \tag{2.10}$$

Absorption by ozone is also taken into account, but since ozone is located at low pressure levels for which molecular scattering is small and Mie scattering is negligible, interactions between scattering processes and ozone absorption are neglected. Transmission through ozone is computed using (2.7) where $\mathcal{U}_{O_3}$ the amount of ozone is

$$\mathcal{U}^{d}_{O_3} = M \int_{p}^{0} d\mathcal{U}_{O_3} \qquad \text{for the downward transmission of the direct solar beam}$$

$$\mathcal{U}^{u}_{O_3} = r \int_{p_s}^{0} d\mathcal{U}_{O_3} + \mathcal{U}^{d}_{O_3}(p_{surf}) \qquad \text{for the upward transmission of the diffuse radiation}$$

$r = 1.66$ is the diffusivity factor (see Section 2.2), and M is the magnification factor (Rodgers, 1967) used instead of r to account for the sphericity of the atmosphere at very small solar elevations

$$M = 35/\sqrt{\mu_0^2 + 1} \tag{2.11}$$

To perform the spectral integration, it is convenient to discretize the solar spectrum into subintervals in which the surface reflectance, molecular absorption characteristics, and cloud optical properties can be considered as constants. One of the main causes for such a spectral variation is the sharp increase in the reflectivity of the vegetation in the near-infrared. Also, water vapour does not absorb below 0.69 μm nor do liquid water clouds. Till June 2000, the ECMWF short-wave scheme considered only two spectral intervals, one for the visible (0.2–0.69 µm), one for the near-infrared (0.69–4.00 µm) parts of the solar spectrum. From June 2000 to April 2002, the near-infrared interval was sub-divided into three intervals (0.69–1.19–2.38–4.00 µm) to account better for the spectral variations of the cloud optical properties. Till April 2002, all the molecular absorption coefficients (for O_3, H_2O, uniformly mixed gases) were derived from statistical models of the transmission function using spectroscopic parameters derived from various versions of the HITRAN database (Rothman *et al.*, 1986, 1992). In April 2002, following the recomputation of all the molecular absorption coefficients from an updated version of the short-wave line-by-line model of Dubuisson *et al.* (1996) using spectroscopic data from HAWKS (2000), the ultraviolet and visible part of the spectrum are now considered in three spectral intervals (0.20–0.25–0.69 µm) making the scheme having a total of six spectral intervals over which the aerosol and cloud optical properties are also defined. The cut-off at 0.69 µm allows the scheme to be more computational efficient, in as much as the interactions between gaseous absorption (by water vapour and uniformly mixed gases) and scattering processes are accounted for only in the near-infrared interval(s).

2.2.2 Vertical integration

Considering an atmosphere where a fraction C^{tot}_{cld} (as seen from the surface or the top of the atmosphere) is covered by clouds (the fraction C^{tot}_{cld} depends on which cloud-overlap assumption is assumed for the calculations), the final fluxes are given as a weighted average of the fluxes in the clear sky and in the cloudy fractions of the column

$$\mathcal{F}^{-}(j) = C^{tot}_{cld}\mathcal{F}^{-}_{cld}(j) + (1 - C^{tot}_{cld})\mathcal{F}^{-}_{clr}$$

where the subscripts 'clr' and 'cld' refer to the clear-sky and cloudy fractions of the layer, respectively. In contrast to the scheme of Geleyn and Hollingsworth (1979), the fluxes are not obtained through the solution of a system of linear equations in a matrix form. Rather, assuming an atmosphere divided into

homogeneous layers, the upward and downward fluxes at a given layer interface j are given by

$$\begin{aligned}\mathcal{F}^-(j) &= \mathcal{F}_0 \prod_{k=j}^{N} \mathcal{T}_{\rm bot}(k) \\ \mathcal{F}^+(j) &= \mathcal{F}^-(j)\mathcal{R}_{\rm top}(j-1)\end{aligned} \tag{2.12}$$

where $\mathcal{R}_{\rm top}(j)$ and $\mathcal{T}_{\rm bot}(j)$ are the reflectance at the top and the transmittance at the bottom of the jth layer. Computation of the values of $\mathcal{R}_{\rm top}$ starts at the surface and works upwards, whereas determining values of $\mathcal{T}_{\rm bot}$ starts at the top of the atmosphere and works downward. $\mathcal{R}_{\rm top}$ and $\mathcal{T}_{\rm bot}$ account for the presence of cloud in the layer by using

$$\begin{aligned}\mathcal{R}_{\rm top} &= C_{\rm cld}\mathcal{R}_{\rm cld} + (1 - C_{\rm cld})\mathcal{R}_{\rm clr} \\ \mathcal{T}_{\rm bot} &= C_{\rm cld}\mathcal{T}_{\rm cld} + (1 - C_{\rm cld})\mathcal{T}_{\rm clr}\end{aligned} \tag{2.13}$$

where $C_{\rm cld}$ is the cloud fractional coverage of the layer within the cloudy fraction $C_{\rm cld}^{\rm tot}$ of the column.

(a) Cloudy fraction layer

$\mathcal{R}_{t_{\rm cdy}}$ and $\mathcal{R}_{b_{\rm cdy}}$ are the reflectance at the top and transmittance at the bottom of the cloudy fraction of the layer calculated with the Delta-Eddington approximation. Given $\delta_{\rm c}$, $\delta_{\rm a}$, and $\delta_{\rm g}$, the optical thicknesses for the cloud, the aerosol and the molecular absorption of the gases ($= k_{\rm e}U$), respectively, and $g_{\rm c}$ and $g_{\rm a}$ the cloud and aerosol asymmetry factors, $\mathcal{R}_{t_{\rm cdy}}$ and $\mathcal{R}_{b_{\rm cdy}}$ are calculated as functions of the total optical thickness of the layer

$$\delta = \delta_{\rm c} + \delta_{\rm a} + \delta_{\rm g} \tag{2.14}$$

of the total single scattering albedo

$$\varpi^* = \frac{\delta_{\rm c} + \delta_{\rm a}}{\delta_{\rm c} + \delta_{\rm a} + \delta_{\rm g}} \tag{2.15}$$

of the total asymmetry factor

$$g^* = \frac{\delta_{\rm c}}{\delta_{\rm c} + \delta_{\rm a}} g_{\rm c} + \frac{\delta_{\rm a}}{\delta_{\rm c} + \delta_{\rm a}} g_{\rm a} \tag{2.16}$$

of the reflectance $\mathcal{R}_-$ of the underlying medium (surface or layers below the jth interface), and of the cosine of an effective solar zenith angle $\mu_{\rm eff}(j)$ which accounts for the decrease of the direct solar beam and the corresponding increase of the diffuse part of the downward radiation by the upper scattering layers

$$\mu_{\rm eff}(j) = [(1 - C_{\rm cld}^{\rm eff}(j))/\mu + rC_{\rm cld}^{\rm eff}(j)]^{-1} \tag{2.17}$$

with $C_{\rm cld}^{\rm eff}(j)$ the effective total cloudiness over level j

$$C_{\rm cld}^{\rm eff}(j) = 1 - \prod_{i=j+1}^{N} (1 - C_{\rm cld}(i)E(i)) \tag{2.18}$$

and

$$E(i) = 1 - \exp\left[-\frac{(1 - \varpi_{\rm c}(i)g_{\rm c}(i)^2)\delta_{\rm c}(i)}{\mu}\right] \tag{2.19}$$

$\delta_{\rm c}(i)$, $\varpi_{\rm c}(i)$ and $g_{\rm c}(i)$ are the optical thickness, single scattering albedo and asymmetry factor of the cloud in the ith layer, and r is the diffusivity factor. The scheme follows the Eddington approximation first proposed by Shettle and Weinman (1970), then modified by Joseph *et al.* (1976) to account more accurately for the large fraction of radiation directly transmitted in the forward scattering peak in case of highly asymmetric phase functions. Eddington's approximation assumes that, in a scattering medium of optical thickness δ^*, of single scattering albedo ω, and of asymmetry factor g, the radiance $\mathcal{L}$ entering (2.58) can be written as

$$\mathcal{L}(\delta, \mu) = \mathcal{L}_0(\delta) + \mu\mathcal{L}_1(\delta) \tag{2.20}$$

In that case, when the phase function is expanded as a series of associated Legendre functions, all terms of order greater than one vanish when (2.3) is integrated over μ and ϕ. The phase function is therefore

given by

$$P(\Theta) = 1 + \beta_1(\Theta)\mu$$

where Θ is the angle between incident and scattered radiances. The integral in (2.3) thus becomes

$$\int_0^{2\pi} d\phi' \left\{ \int_{-1}^{+1} p(\mu, \phi, \mu', \phi')\mathcal{L}(\mu', \phi')\, \mathrm{d}\mu' \right\} = 4\pi(L_0 + \pi\mathcal{L}_1) \tag{2.21}$$

where

$$g = \frac{\beta_1}{3} = \frac{1}{2}\int_{-1}^{+1} P(\Theta)\mu\, \mathrm{d}\mu$$

is the asymmetry factor.

Using (2.21) in (2.3) after integrating over μ and dividing by 2π, we get

$$\mu\frac{\mathrm{d}}{\mathrm{d}\delta}(\mathcal{L}_0 + \mu\mathcal{L}_1) = -(\mathcal{L}_0 + \mu\mathcal{L}_1) + \varpi(\mathcal{L}_0 + g\mu\mathcal{L}_1) + 1/4\varpi\mathcal{F}_0 \exp(-\delta/\mu_0)(1 + 3g\mu_0\mu) \tag{2.22}$$

We obtain a pair of equations for $\mathcal{L}_0$ and $\mathcal{L}_1$ by integrating (2.22) over μ

$$\begin{aligned} \frac{\mathrm{d}\mathcal{L}_0}{\mathrm{d}\delta} &= -3(1-\varpi)\mathcal{L}_0 + \frac{3}{4}\varpi\mathcal{F}_0 \exp(-\delta/\mu_0) \\ \frac{\mathrm{d}\mathcal{L}_1}{\mathrm{d}\delta} &= -(1-\varpi g)\mathcal{L}_1 + \frac{3}{4}\varpi g\mu_0\mathcal{F}_0 \exp(-\delta/\mu_0) \end{aligned} \tag{2.23}$$

For the cloudy layer assumed non-conservative ($\varpi < 1$), the solutions to (2.22) and (2.23), for $0 \le \delta \le \delta^*$, are

$$\begin{aligned} \mathcal{L}_0(\delta) &= C_1 \exp(-K\delta) + C_2 \exp(+K\delta) - \alpha \exp(-\delta/\mu_0) \\ \mathcal{L}_1(\delta) &= P\{C_1 \exp(-K\delta) - C_2 \exp(+K\delta) - \beta \exp(-\delta/\mu_0)\} \end{aligned} \tag{2.24}$$

where

$$\begin{aligned} K &= \{3(1-\varpi)(1-\varpi g)\}^{1/2} \\ P &= \{3(1-\varpi)/(1-\varpi g)\}^{1/2} \\ \alpha &= 3\varpi F_0\mu_0\{1 + 3g(1-\varpi)\}/\{4(1-K^2\mu_0^2)\} \\ \beta &= 3\varpi F_0\mu_0\{1 + 3g(1-\varpi)\mu_0^2\}/(4(1-K^2\mu_0^2)) \end{aligned}$$

The two boundary conditions allow to solve the system for C_1 and C_2; the downward directed diffuse flux at the top of the atmosphere is zero, that is

$$\mathcal{F}^-(0) = \left[\mathcal{L}_0(0) + \frac{2}{3}\mathcal{L}_1(0)\right] = 0$$

which translates into

$$(1 + 2P/3)C_1 + (1 - 2P/3)C_2 = \alpha + 2\beta/3 \tag{2.25}$$

The upward directed flux at the bottom of the layer is equal to the product of the downward directed diffuse and direct fluxes and the corresponding diffuse and direct reflectance ($\mathcal{R}_\mathrm{d}$ and $\mathcal{R}_-$, respectively) of the underlying medium

$$\begin{aligned} \mathcal{F}^+(\delta^*) &= \left\{\mathcal{L}_0(\delta^*) - \frac{2}{3}\mathcal{L}_1(\delta^*)\right\} \\ &= \mathcal{R}_-\left\{\mathcal{L}_0(\delta^*) + \frac{2}{3}\mathcal{L}_1(\delta^*)\right\} + \mathcal{R}_\mathrm{d}\mu_0\mathcal{F}_0 \exp(-\delta^*/\mu_0) \end{aligned}$$

which translates into

$$\begin{aligned} &\{1 - \mathcal{R}_- - 2(1+\mathcal{R}_-)P/3\}C_1 \exp(-K\delta^*) + \{1 - \mathcal{R}_- + 2(1+\mathcal{R}_-)P/3\}C_2(+K\delta^*) \\ &\quad = \{(1-\mathcal{R}_-)\alpha - 2(1+\mathcal{R}_-)\beta/3 + \mathcal{R}_\mathrm{d}\mu_0\mathcal{F}_0\} \exp(-\delta^*/\mu_0) \end{aligned} \tag{2.26}$$

In the Delta-Eddington approximation, the phase function is approximated by a Dirac delta function forward-scatter peak and a two-term expansion of the phase function

$$P(\theta) = 2f(1-\mu) + (1-f)(1+3g'\mu)$$

where f is the fractional scattering into the forward peak and g' the asymmetry factor of the truncated phase function. As shown by Joseph *et al.* (1976), these parameters are

$$\begin{aligned} f &= g^2 \\ g' &= g/(g+1) \end{aligned} \tag{2.27}$$

The solution of the Eddington's equations remains the same provided that the total optical thickness, single scattering albedo and asymmetry factor entering (2.22) and (2.26) take their transformed values

$$\begin{aligned} \delta'^* &= (1+\varpi f)\delta^* \\ \omega' &= \frac{(1-f)\varpi}{1-\varpi f} \end{aligned} \tag{2.28}$$

Practically, the optical thickness, single scattering albedo, asymmetry factor and solar zenith angle entering (2.22)–(2.26) are δ^*, ϖ^*, g^* and μ_{eff} defined in (2.16) and (2.17).

(*b*) *Clear-sky fraction of the layers*

In the clear-sky part of the atmosphere, the short-wave scheme accounts for scattering and absorption by molecules and aerosols. The following calculations are practically done twice, once for the clear-sky fraction $(1-C_{\text{cld}}^{\text{tot}})$ of the atmospheric column μ with equal to μ_0, simply modified for the effect of Rayleigh and aerosol scattering, the second time for the clear-sky fraction of each individual layer within the fraction $C_{\text{cld}}^{\text{tot}}$ of the atmospheric column containing clouds, with μ equal to μ_{e}.

As the optical thickness for both Rayleigh and aerosol scattering is small, $\mathcal{R}_{\text{clr}}(j-1)$ and $\mathcal{T}_{\text{clr}}(j)$, the reflectance at the top and transmittance at the bottom of the jth layer can be calculated using respectively a first- and a second-order expansion of the analytical solutions of the two-stream equations similar to that of Coakley Jr. and Chylek (1975). For Rayleigh scattering, the optical thickness, single scattering albedo and asymmetry factor are respectively δ_{R}, $\varpi_{\text{R}}=1$ and $g_{\text{R}}=0$, so that

$$\begin{aligned} \mathcal{R}_{\text{R}} &= \frac{\delta_{\text{R}}}{2\mu+\delta_{\text{R}}} \\ \mathcal{T}_{\text{R}} &= \frac{2\mu}{(2\mu+\delta_{\text{R}})} \end{aligned} \tag{2.29}$$

The optical thickness δ_{R} of an atmospheric layer is simply

$$\delta_{\text{R}} = \delta^*\{p(j)-p(j-1)\}/p_{\text{surf}} \tag{2.30}$$

where δ_{R}^* is the Rayleigh optical thickness of the whole atmosphere parametrized as a function of the solar zenith angle (Deschamps *et al.*, 1983)

For aerosol scattering and absorption, the optical thickness, single scattering albedo and asymmetry factor are respectively δ_{a}, ϖ_{a}, with $1-\varpi_{\text{a}} \ll 1$ and g_{a}, so that

$$\begin{aligned} \text{den} = 1 &+ \{1-\varpi_{\text{a}}+\text{back}(\mu_{\text{e}})\varpi_{\text{a}}\}(\delta_{\text{a}}/\mu_{\text{e}}) \\ &+ (1-\varpi_{\text{a}})\{1-\varpi_{\text{a}}+2\,\text{back}(\mu_{\text{e}})\varpi_{\text{a}}\}(\delta_{\text{a}}^2/\mu_{\text{e}}^2) \end{aligned} \tag{2.31}$$

$$\begin{aligned} \mathcal{R}(\mu_{\text{e}}) &= \frac{(\text{back}(\mu_{\text{e}})\varpi_{\text{a}}\delta_{\text{a}})/\mu_{\text{a}}}{\text{den}} \\ \mathcal{T}(\mu_{\text{e}}) &= 1/\text{den} \end{aligned} \tag{2.32}$$

where $\text{back}(\mu_{\text{e}}) = (2-3\mu_{\text{e}}g_{\text{a}})/4$ is the backscattering factor.

Practically, $\mathcal{R}_{\rm clr}$ and $\mathcal{T}_{\rm clr}$ are computed using (2.32) and the combined effect of aerosol and Rayleigh scattering comes from using modified parameters corresponding to the addition of the two scatterers with provision for the highly asymmetric aerosol phase function through Delta-approximation of the forward scattering peak (as in (2.23) and (2.24)).

$$\begin{aligned}\delta^+ &= \delta_{\rm R} + \delta_{\rm a}(1-\varpi_a g_a^2)\\ g^+ &= \frac{g_{\rm a}}{1+g_{\rm a}}\frac{\delta_{\rm a}}{(\delta_{\rm R}+\delta_{\rm a})}\\ \varpi^+ &= \frac{\delta_{\rm R}}{\delta_{\rm a}+\delta_{\rm a}}\varpi_{\rm R} + \frac{\delta_{\rm a}}{\delta_{\rm R}+\delta_{\rm a}}\frac{\varpi_{\rm a}(1-g_{\rm a}^2)}{1-\varpi_{\rm a}g_{\rm a}^2}\end{aligned} \tag{2.33}$$

As for their cloudy counterparts, $\mathcal{R}_{\rm clr}$ and $\mathcal{T}_{\dot{\rm c}lr}$ must account for the multiple reflections due to the layers underneath

$$\mathcal{R}_{\rm clr} = \mathcal{R}(\mu_{\rm e}) + \mathcal{R}_{-}\mathcal{T}(\mu_{\rm e})(1-\mathcal{R}^*\mathcal{R}_{-}) \tag{2.34}$$

and $\mathcal{R}_{-}$ is the reflectance of the underlying medium $\mathcal{R}_{-} = \mathcal{R}_t(j-1)$ and r is the diffusivity factor.

Since interactions between molecular absorption and Rayleigh and aerosol scattering are negligible, the radiative fluxes in a clear-sky atmosphere are simply those calculated from (2.10) and (2.28) attenuated by the gaseous transmissions (2.8).

2.2.3 Multiple reflections between layers

To deal properly with the multiple reflections between the surface and the cloud layers, it should be necessary to separate the contribution of each individual reflecting surface to the layer reflectance and transmittances in as much as each such surface gives rise to a particular distribution of absorber amount. In the case of an atmosphere including N cloud layers, the reflected light above the highest cloud consists of photons directly reflected by the highest cloud without interaction with the underlying atmosphere, and of photons that have passed through this cloud layer and undergone at least one reflection on the underlying atmosphere. In fact, (2.5) should be written

$$\mathcal{F} = \sum_{i=0}^{N}\mathcal{F}_{\rm cl}\int_0^{\infty}\mathcal{P}_1(\mathcal{U})t_{\Delta v}(\mathcal{U})\mathrm{d}v \tag{2.35}$$

where $\mathcal{F}_{\rm cl}$ and $\mathcal{P}_1(\mathcal{U})$ are the conservative fluxes and the distributions of absorber amount corresponding to the different reflecting surfaces.

Fouquart and Bonnel (1980) have shown that a very good approximation to this problem is obtained by evaluating the reflectance and transmittance of each layer (using (2.22) and (2.28)) assuming successively a non-reflecting underlying medium ($\mathcal{R}_{-}=0$), then a reflecting underlying medium ($\mathcal{R}_{-}\neq 0$). First calculations provide the contribution to reflectance and transmittance of those photons interacting only with the layer into consideration, whereas the second ones give the contribution of the photons with interactions also outside the layer itself.

From those two sets of layer reflectance and transmittances ($\mathcal{T}_{\rm t0}$, $\mathcal{T}_{\rm b0}$) and ($\mathcal{R}_{\rm t\neq}$, $\mathcal{T}_{\rm b\neq}$) respectively, effective absorber amounts to be applied to computing the transmission functions for upward and downward fluxes are then derived using (2.6) and starting from the surface and working the formulas upward

$$\begin{aligned}\mathcal{U}_{\rm e0}^{-} &= \ln\left(\mathcal{T}_{\rm b0}/\mathcal{T}_{\rm bc}\right)/k_{\rm e}\\ \mathcal{U}_{\rm e\neq}^{-} &= \ln\left(\mathcal{T}_{\rm b\neq}/\mathcal{T}_{\rm bc}\right)/k_{\rm e}\\ \mathcal{U}_{\rm e0}^{+} &= \ln\left(\mathcal{R}_{\rm t0}/\mathcal{R}_{\rm tc}\right)/k_{\rm e}\\ \mathcal{U}_{\rm e\neq}^{+} &= \ln\left(\mathcal{R}_{\rm t\neq}/\mathcal{R}_{\rm tc}\right)/k_{\rm e}\end{aligned} \tag{2.36}$$

where $\mathcal{R}_{\rm tc}$ and $\mathcal{T}_{\rm bc}$ are the layer reflectance and transmittance corresponding to a conservative scattering medium.

Finally the upward and downward fluxes are obtained as

$$\mathcal{F}^{+}(j) = \mathcal{F}_0\{\mathcal{R}_{t0}t_{\Delta\nu}(\mathcal{U}^{+}_{e0}) + (\mathcal{R}_{t\neq} - \mathcal{R}_{t0})t_{\Delta\nu}(\mathcal{U}^{+}_{e\neq})\} \tag{2.37}$$

$$\mathcal{F}^{-}(j) = \mathcal{F}_0\{\mathcal{T}_{b0}t_{\Delta\nu}(\mathcal{U}^{+}_{e0}) + (\mathcal{T}_{b\neq} - \mathcal{T}_{b0})t_{\Delta\nu}(\mathcal{U}^{-}_{e\neq})\} \tag{2.38}$$

2.2.4 Cloud short-wave optical properties

As seen in Subsection 2.2.2(a), the cloud radiative properties depend on three different parameters: the optical thickness δ_c, the asymmetry factor g_c, and the single scattering albedo ϖ_c.

Presently the cloud optical properties are derived from Fouquart (1987) for the water clouds, and Ebert and Curry (1992) for the ice clouds.

The optical thickness δ_c is related to the cloud liquid water amount U_{LWP} by

$$\delta_c = \frac{3\mathcal{U}_{LWP}}{2r_e}$$

where r_e is the mean effective radius of the size distribution of the cloud water droplets. Presently r_e is parametrized as a linear function of height from 10 μm at the surface to 45 μm at the top of the atmosphere, in an empirical attempt at dealing with the variation of water cloud type with height. Smaller water droplets are observed in low-level stratiform clouds whereas larger droplets are found in mid-level cumuliform water clouds.

In the two-, four-, and six-spectral interval versions of the short-wave radiation scheme, the optical properties of liquid water clouds are defined from Fouquart (1987) and those for ice clouds from Ebert and Curry (1992). Alternative optical properties are also available for liquid water clouds (Slingo, 1989) and ice clouds (Fu, 1996).

The effective radius of the liquid water cloud particles is computed from the cloud liquid water content using the diagnostic formulation of Martin *et al.* (1994) and specified concentrations of cloud concentration nuclei over land and ocean. For ice clouds, the effective dimension of the cloud particles is diagnosed from temperature using a revision of the formulation by Ou and Liou (1995).

2.3 THE PRE-CY22R3 LONG-WAVE RADIATION SCHEME

As already noted, since cycle Cy22r3, two long-wave radiation schemes have been available in the ECMWF model, the pre-cycle Cy22r3 by Morcrette (1991), and the current long-wave radiation transfer scheme, the Rapid Radiation Transfer Model (RRTM) (see Section 2.5).

The rate of atmospheric cooling by emission-absorption of long-wave radiation is

$$\frac{\partial T}{\partial t} = \frac{g}{c_p}\frac{\partial \mathcal{F}_{LW}}{\partial p} \tag{2.39}$$

where $\mathcal{F}_{LW}$ is the net long-wave radiation flux (the subscript 'LW' is omitted in the remainder of this section).

Assuming a non-scattering atmosphere in local thermodynamic equilibrium, $\mathcal{F}$ is given by

$$\mathcal{F} = \int_{-1}^{1} \mu\, d\mu \left[\int_0^{\infty} d\upsilon \left\{\mathcal{L}_\upsilon(p_{surf}, \mu)t_\upsilon(p_{surf}, p, \mu) + \int_{p'=p_{surf}}^{0} \mathcal{L}_\upsilon(p', \mu)\, dt_\upsilon\right\}\right] \tag{2.40}$$

where $\mathcal{L}_\upsilon(p, \mu)$ is the monochromatic radiance at wavenumber υ at level p, propagating in a direction θ (the angle that this direction makes with the vertical), where $\mu = \cos\theta$ and $t_\upsilon(p, p'; r)$ is the monochromatic transmission through a layer whose limits are at p and p' seen under the same angle θ, with $r = \sec\theta$. The subscript 'surf' refers to the earth's surface.

2.3.1 The pre-cycle Cy22r3 scheme

After separating the upward and downward components (indicated by superscripts + and −, respectively), and integrating by parts, we obtain the radiation transfer equation as it is actually estimated in the long-wave part of the radiation code

$$\begin{aligned}\mathcal{F}_v^+(p) &= [B_v(T_{\text{surf}}) - B_v(T_{0+})]t_v(p_{\text{surf}}, p; r) + B_v(T(p)) + \int_{p'=p_{\text{surf}}}^{p} t_v(p, p'; r)\, \mathrm{d}B_v \\ \mathcal{F}_v^-(p) &= [B_v(T_\infty) - B_v(T_{\text{top}})]t_v(p, 0; r) + B_v(T(p)) + \int_{p'=p}^{0} t_v(p', p; r)\, \mathrm{d}B_v\end{aligned} \tag{2.41}$$

where, taking benefit of the isotropic nature of the long-wave radiation, the radiance L_v of (2.40) has been replaced by the Planck function $B_v(T)$ in units of flux, Wm^{-2} (here, and elsewhere, B_v is assumed to always includes the π factor). T_{surf} is the surface temperature, T_{0+} that of the air just above the surface, $T(p)$ is the temperature at pressure-level p, T_{top} that at the top of the atmospheric model. The transmission t_v is evaluated as the radiance transmission in a direction θ to the vertical such that $r = \sec\theta$ is the diffusivity factor (Elsasser, 1942). Such an approximation for the integration over the angle is usual in radiative transfer calculations, and tests on the validity of this approximation have been presented by Rodgers and Walshaw (1966) and Liu and Schmetz (1988) among others. The use of the diffusivity factor gives cooling rates within 2% of those obtained with a 4-point Gaussian quadrature.

2.3.2 Vertical integration

The integrals in (2.41) are evaluated numerically, after discretization over the vertical grid, considering the atmosphere as a pile of homogeneous layers. As the cooling rate is strongly dependent on local conditions of temperature and pressure, and energy is mainly exchanged with the layers adjacent to the level where fluxes are calculated, the contribution of the distant layers is simply computed using a trapezoidal rule integration, but the contribution of the adjacent layers is evaluated with a 2-point Gaussian quadrature, thus at the ith level

$$\int_{p'=p_{\text{surf}}}^{p_i} t_v(p, p'; r)\, \mathrm{d}B_v = \sum_{l=1}^{2} \mathrm{d}B_v(l) w_l t_v(p_i, p_l; r) + \frac{1}{2}\sum_{j=1}^{i-2} \mathrm{d}B_v(j)[t_v(p_i, p_j; r) + t_v(p_i, p_{j-1}; r)] \tag{2.42}$$

where p_l is the pressure corresponding to the Gaussian root and w_l is the Gaussian weight. $\mathrm{d}B_v(j)$ and $\mathrm{d}B_v(l)$ are the Planck function gradients calculated between two interfaces, and between mid-layer and interface, respectively.

2.3.3 Spectral integration

The integration over wavenumber v is performed using a band emissivity method, as first discussed by Rodgers (1967). The long-wave spectrum is divided into six spectral regions.

(i) 0–350 cm^{-1} and 1450–1880 cm^{-1}
(ii) 500–800 cm^{-1}
(iii) 800–970 cm^{-1} and 1110–1250 cm^{-1}
(iv) 970–1110 cm^{-1}
(v) 350–500 cm^{-1}
(vi) 1250–1450 cm^{-1} and 1880–2820 cm^{-1}

corresponding to the centres of the rotation and vibration-rotation bands of H_2O, the 15 μm band of CO_2, the atmospheric window, the 9.6 μm band of O_3, the 25 μm "window" region, and the wings of the vibration-rotation band of H_2O, respectively. Over these spectral regions, band fluxes are evaluated with the help of band transmissivities precalculated from the narrow-band model of Morcrette and Fouquart (1985) – See Appendix of Morcrette *et al.* (1986) for details.

Integration of (2.41) over wavenumber ν within the kth spectral region gives the upward and downward fluxes as

$$\begin{aligned}\mathcal{F}_k^+(p) &= \{B_k(T_{\rm surf}) - B_k(T_{0+})\}t_{B_k}\{r\mathcal{U}(p_{\rm surf},p), T_{\mathcal{U}}(p_{\rm surf},p)\} + B_k(T_p) \\ &\quad + \int_{p'=p_{\rm surf}}^{p} t_{{\rm d}B_k}\{r\mathcal{U}(p,p'), T_{\mathcal{U}}(p,p')\}\,{\rm d}B_k \end{aligned} \tag{2.43}$$

$$\begin{aligned}\mathcal{F}_k^-(p) &= \{B_k(T_0) - B_k(T_\infty)\}t_{B_k}\{r\mathcal{U}(p,0), T_{\mathcal{U}}(p,0)\} - B_k(T_p) \\ &\quad - \int_{p'=p}^{0} t_{{\rm d}B_k}\{r\mathcal{U}(p',p), T_{\mathcal{U}}(p',p)\}\,{\rm d}B_k \end{aligned} \tag{2.44}$$

The formulation accounts for the different temperature dependencies involved in atmospheric flux calculations, namely that on T_p, the temperature at the level where fluxes are calculated, and that on $T_{\mathcal{U}}$, the temperature that governs the transmission through the temperature dependence of the intensity and half-widths of the lines absorbing in the concerned spectral region. The band transmissivities are non-isothermal accounting for the temperature dependence that arises from the wavenumber integration of the product of the monochromatic absorption and the Planck function. Two normalized band transmissivities are used for each absorber in a given spectral region: the first one for calculating the first right-hand-side term in (2.41), involving the boundaries; it corresponds to the weighted average of the transmission function by the Planck function

$$t_B(\overline{\mathcal{U}p}, T_p, T_{\mathcal{U}}) = \frac{\int_{v_1}^{v_2} B_v(T_p)t_v(\overline{\mathcal{U}p}, T_{\mathcal{U}})\,{\rm d}v}{\int_{v_1}^{v_2} B_v(T_p)\,{\rm d}v} \tag{2.45}$$

the second one for calculating the integral term in (2.41) is the weighted average of the transmission function by the derivative of the Planck function

$$t_{{\rm d}B}(\overline{\mathcal{U}p}, T_p, T_{\mathcal{U}}) = \frac{\int_{v_1}^{v_2}\{{\rm d}B(T_p)/{\rm d}T\}t_v(\overline{\mathcal{U}p}, T_{\mathcal{U}})\,{\rm d}v}{\int_{v_1}^{v_2}\{{\rm d}B(T_p)/{\rm d}T\}\,{\rm d}v} \tag{2.46}$$

where $\overline{\mathcal{U}p}$ is the pressure weighted amount of absorber.

The effect on absorption of the Doppler broadening of the lines (important only for pressure lower than 10 hPa) is included simply using the pressure correction method of Fels (1979). A finite line width (assumed to represent the Doppler half-width of the line) is retained under low pressure conditions where the pure Lorentz line width (proportional to pressure) would normally become negligible (Giorgetta and Morcrette, 1995).

In the scheme, the actual dependence on T_p is carried out explicitly in the Planck functions integrated over the spectral regions. Although normalized relative to $B(T_p)$ or ${\rm d}B(T_p)/{\rm d}T$, the transmissivities still depend on $T_{\mathcal{U}}$, both through Wien's displacement of the maximum of the Planck function with temperature and through the temperature dependence of the absorption coefficients. For computational efficiency, the transmissivities have been developed into Pade approximants

$$t(\overline{\mathcal{U}p}, T_u) = \frac{\sum_{i=0}^{2} c_i \mathcal{U}_{\rm eff}^{i/2}}{\sum_{j=0}^{2} d_j \mathcal{U}_{\rm eff}^{i/2}} \tag{2.47}$$

where $\mathcal{U}_{\rm eff} = r(\overline{\mathcal{U}p})\Psi(T_{\mathcal{U}}, \overline{\mathcal{U}p})$ is an effective amount of absorber which incorporates the diffusivity factor r, the weighting of the absorber amount by pressure $\overline{\mathcal{U}p}$, and the temperature dependence of the absorption coefficients. The function $\Psi(T_{\mathcal{U}}, \overline{\mathcal{U}p})$ takes the form

$$\Psi(T_{\mathcal{U}}, \overline{\mathcal{U}p}) = \exp[a(\overline{\mathcal{U}p})(T_{\mathcal{U}} - 250) + b(\overline{\mathcal{U}p})(T_{\mathcal{U}} - 250)^2] \tag{2.48}$$

The temperature dependence due to Wien's law is incorporated although there is no explicit variation of the coefficients c_i and d_j with temperature. These coefficients have been computed for temperatures between 187.5 and 312.5 K with a 12.5 K step, and transmissivities corresponding to the reference temperature the closest to the pressure weighted temperature $T_{\mathcal{U}}$ are actually used in the scheme.

2.3.4 The incorporation of the effects of clouds

The incorporation of the effects of clouds on the long-wave fluxes follows the treatment discussed by Washington and Williamson (1977). Whatever the state of the cloudiness of the atmosphere, the scheme starts by calculating the fluxes corresponding to a clear-sky atmosphere and stores the terms of the energy exchange between the different levels (the integrals in (2.41)) Let $\mathcal{F}_0^+(i)$ and $\mathcal{F}_0^-(i)$ be the upward and downward clear-sky fluxes. For any cloud layer actually present in the atmosphere, the scheme then evaluates the fluxes assuming a unique overcast cloud of emissivity unity. Let $\mathcal{F}_n^+(i)$ and $\mathcal{F}_n^+(i)$ the upward and downward fluxes when such a cloud is present in the nth layer of the atmosphere. Downward fluxes above the cloud, and upward fluxes below the cloud, are assumed to be given by the clear-sky values

$$\begin{aligned} \mathcal{F}_n^+(i) &= \mathcal{F}_0^+(i) \quad \text{for } i \le n \\ \mathcal{F}_n^-(i) &= \mathcal{F}_0^-(i) \quad \text{for } i > n \end{aligned} \tag{2.49}$$

Upward fluxes above the cloud ($\mathcal{F}_n^+(k)$ for $k \le n+1$) and downward fluxes below it ($\mathcal{F}_n^-(k)$ for $k > n$) can be expressed with expressions similar to (2.42) provided the boundary terms are now replaced by terms corresponding to possible temperature discontinuities between the cloud and the surrounding air

$$\begin{aligned} \mathcal{F}_n^+(k) &= \{\mathcal{F}_{\rm cld}^+ - B(n+1)\}t(p_k, p_{n+1}; r) + B(k) + \int_{p'=p_{n-1}}^{p_k} t(p_k, p'; r)\, {\rm d}B \\ \mathcal{F}_n^-(k) &= \{\mathcal{F}_{\rm cld}^- - B(n)\}t(p_k, p_n; r) + B(k) + \int_{p'=p_k}^{p_n} t(p_k, p'; r)\, {\rm d}B \end{aligned} \tag{2.50}$$

where $B(i)$ is now the total Planck function (integrated over the whole long-wave spectrum) at level i, and $\mathcal{F}_{\rm cld}^+$ and $\mathcal{F}_{\rm cld}^-$ are the long-wave fluxes at the upper and lower boundaries of the cloud. Terms under the integrals correspond to exchange of energy between layers in clear-sky atmosphere and have already been computed in the first step of the calculations. This step is repeated for all cloudy layers. The fluxes for the actual atmosphere (with semi-transparent, fractional and/or multi-layered clouds) are derived from a linear combination of the fluxes calculated in previous steps with some cloud overlap assumption in the case of clouds present in several layers. Let N be the index of the layer containing the highest cloud, $C_{\rm cld}(i)$) the fractional cloud cover in layer i, with $C_{\rm cld}(0) = 1$ for the upward flux at the surface, and with $C_{\rm cld}(N+1) = 1$ and $\mathcal{F}_{N+1}^- = \mathcal{F}_0^-$ to have the right boundary condition for downward fluxes above the highest cloud.

Whereas the maximum and random overlap assumptions are also available in the code (Morcrette and Fouquart, 1986), the maximum-random overlap assumption is operationally used in the ECMWF model, and the cloudy upward $\mathcal{F}^+$ and downward $\mathcal{F}^-$ fluxes are obtained as

$$\begin{aligned} \mathcal{F}^+(i) &= \mathcal{F}_0^+(i) && \text{for } i = 1 \\ \mathcal{F}^-(i) &= C_{\rm cld}(i-1)\mathcal{F}_{i-1}^+(i-) + \sum_{n=0}^{i-2} C_{\rm cld}(n)\mathcal{F}_n^+(i) \prod_{l=n+1}^{i-1}\{1 - C_{\rm cld}(l)\} && \text{for } 2 \le i \le N+1 \\ \mathcal{F}^+(i) &= C_{\rm cld}(N)\mathcal{F}_N^+(i) + \sum_{n=0}^{N-1} C_{\rm cld}(n)\mathcal{F}_n^+(i) \prod_{l=n+1}^{N}\{1 - C_{\rm cld}(l)\} && \text{for } i \ge N+2 \end{aligned} \tag{2.51}$$

In the case of semi-transparent clouds, the fractional cloudiness entering the calculations is an effective cloud cover equal to the product of the emissivity due to the condensed water and the gases in the layer by the horizontal coverage of the cloud layer, with the emissivity, $\varepsilon_{\rm cld}$, related to the condensed water amount by

$$\varepsilon_{\rm cld} = 1 - \exp(-k_{\rm abs}\mathcal{U}_{\rm LWP}) \tag{2.52}$$

where $k_{\rm abs}$ is the condensed water mass absorption coefficient (in $\rm m^2 kg^{-1}$) following Smith and Shi (1992).

2.4 THE MONTE-CARLO INDEPENDENT COLUMN APPROXIMATION, McICA

The McICA approach is an approximation to the full Independent Column Approximation (ICA). As discussed by Barker *et al.* (2003) and Pincus *et al.* (2003), for the , the average monochromatic radiative

flux, over a domain sub-divided in N columns, in which each layer can only have a cloud fraction of 0 or 1, is

$$\langle F \rangle = \frac{1}{N} \sum_{n=1}^{N} F_n \tag{2.53}$$

In sub-column n, using a radiation parametrisation (plane-parallel, and considering a homogeneous cloud water distribution in all overcast layers) with a correlated k-distribution (CKD) approach to deal with absorption, the total flux F_n is

$$F_n = \sum_{k=1}^{K} c_k F_{n,k} \tag{2.54}$$

Combining (2.53) and (2.54) gives

$$\langle F \rangle = \frac{1}{N} \sum_{n=1}^{N} \sum_{k=1}^{K} c_k F_{n,k} \tag{2.55}$$

A radiation code explicitly integrating the double sum in (2.55) would be far too expensive for GCM applications. The McICA solution to this problem is to approximate (3) as

$$\langle F \rangle_M = \sum_{k=1}^{K} F_{n_k,k} \tag{2.56}$$

where $F_{n_k,k}$ is the monochromatic radiative flux for a single randomly selected sub-column n_k.

From this definition, the McICA solution (2.56) equals the ICA solution only when all N sub-columns are identical or $N = 1$. As discussed in Räisänen and Barker (2004), McICA's incomplete pairing of sub-columns and spectral intervals ensures that its solution will contain random, but unbiased, errors.

McICA can in principle be used within any radiation transfer scheme provided a cloud generator is used to define how the cloud information is distributed over each spectral element in the radiation spectrum. However, to take full benefit of the McICA approach, radiation schemes with a sufficiently large number of transmission calculations are required. With the version of the ECMWF model used for this study, the long-wave radiation fluxes are computed using the Rapid Radiation Transfer Model ($\mathrm{RRTM_{LW}}$), already in use at ECMWF since June 2000. For consistency in terms of radiative transfer solution and database of spectroscopic parameters, the short-wave radiation fluxes are now computed with $\mathrm{RRTM_{SW}}$. The application of the McICA approach involves using a cloud generator together with slightly modified but otherwise standard radiation schemes.

Table 2.2 summarizes the main features of the McRad radiation package. The ECMWF version of $\mathrm{RRTM_{LW}}$ (Mlawer *et al.*, 1997, Morcrette *et al.*, 2001) describes the long-wave spectrum with 16 spectral intervals, corresponding to a total of $K = 140$ g-points, with a g-point being a point in the space of the line intensities within a given spectral interval (Lacis and Oinas, 1991). $\mathrm{RRTM_{SW}}$ (Mlawer and Clough, 1997) describes the short-wave spectrum with 14 spectral intervals, corresponding to a total of $K = 112$ g-points. Each of the long-wave or short-wave spectral intervals have a different number of g-points, depending how much the absorption coefficient varies within the spectral interval, but also how much the spectral interval contributes overall to the total flux, and this over the whole depth of the atmosphere represented by the atmospheric model. For each of these g-points, an essentially monochromatic type radiation transfer is carried out using a two-stream method using an approximate provision for the long-wave scattering and using a Delta two-stream method with scattering in the short-wave.

The McICA versions of $\mathrm{RRTM_{LW}}$ and $\mathrm{RRTM_{SW}}$ differ from the original versions in two respects:

Table 2.2 *Characteristics of the long-wave and short-wave radiation schemes in McRad. (*) refer to the configuration operational with McRad. Note: CFC11 is $CFCl_3$ and CFC12 is CF_2Cl_2.*

	$RRTM_{LW}$	$RRTM_{SW}$
Solution of RT Equation	two-stream method	two-stream method
Number of spectral intervals	16 (140 g-points)	14 (112 g-points)
Absorbers	H_2O, CO_2, O_3, CH_4, N_2O, $CFC11$, $CFC12$, aerosols	H_2O, CO_2, O_3, CH_4, N_2O, $CFC11$, $CFC12$, aerosols
Spectroscopic database	HITRAN, 1996	HITRAN, 1996
Absorption coefficients	from LBLRTM line-by-line model	from LBLRTM line-by-line model
Cloud handling	true cloud fraction	true cloud fraction
Cloud optical properties		
method	16-band spectral emissivity	14-band τ, g, ω
Data: ice clouds water clouds	Ebert & Curry, 1992 Fu et al., 1998 (*) Smith & Shi, 1992 Lindner & Li, 2000 (*)	Ebert & Curry, 1992 Fu, 1996 (*) Fouquart, 1987 Slingo, 1989 (*)
Cloud overlap assumption set up in cloud generator	maximum-random or generalized (*)	maximum-random or generalized (*)
Reference	Mlawer et al., 1997 Morcrette et al., 2001	Mlawer and Clough, 1997

(i) Avoiding any explicit reference to cloud fraction greatly simplifies the part of the algorithms devoted to the vertical integration, which now deals simply with optical thicknesses. For a given g-point, a cloud when present fully occupies a model layer. Therefore any cloudy calculation only involves modifying the optical parameters.

(ii) This enables the removal of the 0.7 correction factor multiplying the cloud optical thickness, which had been introduced in December 1997 (Cahalan *et al.*, 1994; Tiedtke, 1996) in the ECMWF IFS to account approximately for the effect of cloud inhomogeneities at the sub-grid level.

As stated in the Introduction, the McICA representation of cloud-radiation interactions requires the cloud information to be distributed by a cloud generator over the vertical with the constraint that the total cloudiness and cloud water loading for a grid-point is conserved.

The purpose of the cloud generator is, starting from a cloud profile (cloud fraction and cloud water content) provided by a traditional cloud scheme (Tiedtke, 1993 for the ECMWF model), to distribute randomly the cloud information (in terms of presence (1) or absence (0)) into each of the layers covered by the original cloud profile. This distribution is done N times (McICA with N going to infinity would be equal to ICA) with the constraint that a summation over the N profiles would recreate the original vertical distribution of partial cloudiness. In the ECMWF model, for each radiation time-step (every one hour of model time for the T_L799L91 and T_L399L62 forecasts, every three hours for seasonal simulations at T_L159L91 and each radiation grid-point, the cloud generator is used twice, to produce two cloud distributions relevant, respectively, to the 140 g-points of the LW- and 112 g-points of SW radiation schemes. We use the cloud generator of Räisänen *et al.*, 2004, which can distribute vertically either the cloud cover according to a maximum-random overlap assumption or both the cloud cover and cloud water assuming a generalized overlap (Hogan and Illingworth, 2000, 2003). The results presented hereafter corresponds to the operational McRad configuration with a generalized overlap with decorrelation lengths of 2 km for cloud cover and 1 km for cloud water, and a normalized standard deviation of the cloud condensate of 1.

Clouds when present occupy the full horizontal extent of the layer, and the vertical distribution of such clouds (of 0 or 1 cloud cover) is defined independently for each of the 140 (112) g-points of the long-wave (short-wave) scheme by the cloud generator, with the constraint that the total cloudiness and cloud water loading for a grid-point is conserved when N tends to infinity.

Table 2.3 *Spectral distribution of the absorption by atmospheric gases in* $\mathrm{RRTM_{LW}}$.
Note: CCl_4 and CFC22 ($CHClF_2$) are presently not accounted for in the ECMWF model.

		Gases included	
Spectral intervals cm^{-1}	**Number of g-points**	**Troposphere**	**Stratosphere**
10–250	8	H_2O	H_2O
250–500	14	H_2O	H_2O
500–630	16	H_2O, CO_2	H_2O, CO_2
630–700	14	H_2O, CO_2	O_3, CO_2
700–820	16	H_2O, CO_2, CCl_4	O_3, CO_2, CCl_4
820–980	8	H_2O, CFC11, CFC12	CFC11, CFC12
980–1080	12	H_2O, O_3	O_3
1080–1180	8	H_2O, CFC12, CFC22	O_3, CFC12, CFC22
1180–1390	12	H_2O, CH_4	CH_4
1390–1480	6	H_2O	H_2O
1480–1800	8	H_2O	H_2O
1800–2080	8	H_2O	
2080–2250	4	H_2O, N_2O	
2250–2380	2	CO_2	CO_2
2380–2600	2	N_2O, CO_2	
2600–3000	2	H_2O, CH_4	

2.5 THE RAPID RADIATION TRANSFER MODEL: LONG-WAVE ($\mathrm{RRTM_{LW}}$)

Since cycle Cy22r3, two long-wave radiation schemes are available in the ECMWF model, the pre-cycle Cy22r3 by Morcrette (1991) discussed in Section 2.3, and the current long-wave radiation transfer scheme, the Rapid Radiation Transfer Model, which has been used in a standard way from June 2000 to May 2007, and within the McICA framework since 5 June 2007.

As stated in Mlawer *et al.* (1997), the objective in the development of RRTM has been to obtain an accuracy in the calculation of fluxes and heating rates consistent with the best line-by-line models. It utilizes the correlated-k method and shows its filiation to the Atmospheric and Environmental Research, Inc. (AER) line-by-line model (LBLRTM, Clough *et al.*, 1989, 1992, Clough and Iacono, 1995) through its use of absorption coefficients for the relevant k-distributions derived from LBLRTM. Therefore the k-coefficients in RRTM include the effect of the CKD2.2 water vapour continuum (Clough *et al.*, 1989). Table 2.3 presents the spectral intervals of the $\mathrm{RRTM_{LW}}$ scheme and the absorbers taken into account in the spectral computations.

The main point in the correlated-k method (Lacis and Oinas, 1991; Fu and Liou, 1992) is the mapping of the absorption coefficient $k(\nu)$ from the spectral space (where it varies irregularly with wavenumber ν) to the g-space (where $g(k)$ is the probability distribution function, i.e. the fraction of the absorption coefficients in the set smaller than k). The effect of this reordering is a rearrangement of the sequence of terms in the integral over wavenumber in the radiative transfer equation (RTE), which makes it equivalent to what would be done for monochromatic radiation.

In the ECMWF model, no provision is presently taken for scattering in the long-wave. Therefore, in order to get the downward radiance, the integration over the vertical dimension is simply done starting from the top of the atmosphere, going downward layer by layer. At the surface, the boundary condition (in terms of spectral emissivity, and potential reflection of downward radiance) is computed, then, in order to get the upward radiance, the integration over the vertical dimension is repeated, this time from the surface upward.

The spectrally averaged radiance (between ν_1 and ν_2) emerging from an atmospheric layer is

$$\bar{R} = \frac{1}{(\nu_1 - \nu_2)} \int_{\nu_2}^{\nu_1} \mathrm{d}\nu \left\{ R_0(\nu) + \int_{t_v}^{1} [B(\nu, T(t'_\nu)) - R_0(\nu)] \, \mathrm{d}t' \right\} \tag{2.57}$$

where R_0 is the incoming radiance to the layer, $B(\nu, T)$ is the Planck function at wavenumber ν and temperature T, t_ν is the transmittance for the layer optical path, and t'_ν is the transmittance at a point along the optical path in the layer. Under the mapping $\nu \rightarrow g$, this becomes

$$\bar{R} = \int_0^1 \mathrm{d}g \left\{ B_{\mathrm{eff}}(g, T_g) + [R_0(g) - B_{\mathrm{eff}}(g, T_g)] \exp\left[-k(g, P, T) \frac{\rho \Delta z}{\cos \phi} \right] \right\} \tag{2.58}$$

where $B_{\mathrm{eff}}(g, T)$ is an effective Planck function for the layer that varies with the layer's transmittance such as to ensure continuity of flux across layer boundaries for opaque conditions. The dependence of the transmittance is now written in terms of the absorption coefficient $k(g, P, T)$ at layer pressure P and temperature T, the absorber density ρ, the vertical thickness of the layer Δz, and the angle ϕ of the optical path.

For a given spectral interval, the domain of the variable g is partitioned into subintervals (see Table 2.3, number of g-points), each corresponding to a limited range of $k(g)$ values and for which a characteristic value κ_j of the absorption coefficient is chosen. These κ_j are then used to compute the outgoing radiance

$$\bar{R} = \sum_j W_j \left[B_{\mathrm{eff}_j} + (R_{0j} - B_{\mathrm{eff}_j}) \exp\left(-\kappa_j \frac{\rho \Delta z}{\cos \phi} \right) \right] \tag{2.59}$$

where W_j is the size of the sub-intervals ($\sum W_j = 1$).

The accuracy of these absorption coefficients has been established by numerous and continuing high-resolution validations of LBLRTM with spectroscopic measurements, in particular those from the Atmospheric Radiation Measurement program (ARM). Compared to the original RRTM (Mlawer *et al.*, 1997), the version used at ECMWF has been slightly modified to account for cloud optical properties and surface emissivity defined for each of the 16 bands over which spectral fluxes are computed. For efficiency reason, the original number of g-points ($256 = 16 \times 16$) has been reduced to 140 (see Table 2.3). Other changes are the use of a diffusivity approximation (instead of the three-angle integration over the zenith angle used in the original scheme) to derive upward and downward fluxes from the radiances, and the modification of the original cloud random overlapping assumption to include (to the same degree of approximation as used in the operational SW scheme) a maximum-random overlapping of cloud layers. Given the monochromatic form of the RTE, the vertical integration is simply carried out one layer at a time from the top-of-the-atmosphere to the surface to get the downward fluxes. The downward fluxes at the surface are then used with the spectral surface emissivities and the surface temperature to get the upward long-wave fluxes in each of the 140 subintervals. Then the upward fluxes are obtained in a similar fashion from the surface to the ToA.

For the relevant spectral intervals of the RRTM schemes, ice cloud optical properties are derived from Ebert and Curry (1992), and water cloud optical properties from Fouquart (1987). Whereas in the previous operational scheme the cloud emissivity used to compute the effective cloud cover is defined over the whole LW spectrum from spectrally averaged mass absorption coefficients and the relevant cloud water and/or ice paths (following Smith and Shi, 1992), in RRTM, the cloud optical thickness is defined as a function of spectrally varying mass absorption coefficients and relevant cloud water and ice paths, and is used within the true cloudy fraction of the layer. Alternate sets of cloud optical properties are also available for RRTM, based on Savijarvi and Räisänen (1997) for liquid water clouds, and Fu *et al.* (1998) for ice clouds.

2.6 THE RAPID RADIATION TRANSFER MODEL: SHORT-WAVE ($\mathrm{RRTM_{SW}}$)

As its long-wave counterpart $\mathrm{RRTM_{LW}}$, $\mathrm{RRTM_{SW}}$ uses absorption coefficient data for the g-points obtained directly from the line-by-line radiative transfer model LBLRTM (Clough *et al.*, 2005), which has been extensively validated against observations, principally at the ARM-South Great Plains site. Fluxes and heating rates are calculated over 14 contiguous bands (see Table 2.4) in the short-wave. Modelled sources of extinction are water vapour, carbon dioxide, ozone, methane, oxygen, nitrogen, aerosols and Rayleigh scattering. A two-stream algorithm (similar to the the one described in Section 2.2) is used to perform scattering calculations (see also Oreopoulos and Barker, 1999). Table 2.4 presents the spectral intervals of the $\mathrm{RRTM_{SW}}$ scheme and the absorbers taken into account in the spectral computations.

Table 2.4 *Spectral distribution of the absorption by atmospheric gases in* $\mathrm{RRTM_{SW}}$.

		Gases included	
Spectral intervals $\mathbf{cm^{-1}}$	**Number of g-points**	**Troposphere**	**Stratosphere**
800–2600	12	H_2O	CO_2
2600–3250	6	H_2O, CH_4	
3250–4000	12	H_2O, CO_2	H_2O, CO_2
4000–4650	8	H_2O, CH_4	CH_4
4650–5150	8	H_2O, CO_2	CO_2
5150–6150	10	H_2O, CH_4	H_2O, CH_4
6150–7700	10	H_2O, CO_2	H_2O, CO_2
7700–8050	2	H_2O, O_2	O_2
8050–12850	10	H_2O	
12850–16000	8	H_2O, O_2	O_2
16000–22650	6	H_2O	
22650–29000	6		
29000–38000	8	O_3	O_3
38000–50000	2	O_3, O_2	O_3, O_2

2.7 HORIZONTAL AND TEMPORAL INTERPOLATIONS

As stated in the introduction, the cost of the radiation scheme described in the previous sections is prohibitive if it were used to compute the radiative fluxes at every time step and every grid point of the model.

A new interface for radiation computations was developed and implemented in October 2003 with Cy26r3. Full radiation computations are now performed using the so-called halo configuration that can be defined according to needs for the various spatial resolutions.

The previous spatial sampling (operational till Cy26r1), was done only in the longitudinal direction. It was going from one out of four points prevalent in sub-tropical and tropical latitudes and reduced gradually to every point in polar areas. On output, Lagrangian cubic interpolation was used. The scheme worked efficiently on vector systems with less than 100 processors and scalar systems with about 1000 processors. The only real problem was the complexity of the message passing, a direct result of the use of a non-standard grid for radiation calculations.

The new interface for radiation computations was developed to address this complexity, and uses a standard IFS model grid, but with a coarser resolution than the current model grid. Further, interpolation between model and radiation grids are performed using the interfaces already existing within the IFS for the semi-Lagrangian interpolation, and as a result should reduce future code maintenance. By using such a standard grid for radiation computations, there is no longer a load balance issue, as each processor is given an equal number of grid points for model and radiation grids.

A new coarser resolution grid is computed, independent of that for the rest of the physics. Interpolation between model and radiation grids are performed using interfaces existing within the IFS libraries and as a result helps reduce code maintenance. Then radiation computations are done, and output fluxes are interpolated back to the reduced grid, at times of full radiation computations. This halo-related grid can be chosen differently with the forecast application (seasonal runs, EPS, high-resolution 10-day forecasts). This radiation grid had been used between October 2003 and June 2007, with a coarsening factor of two in both latitude and longitude w.r.t. the rest of the model (see Table 2.3 for Cy31r2).

The implementation of the more computer-intensive McRad, through its use of $\mathrm{RRTM_{SW}}$ with an increased number of spectral intervals, has led to the search for an optimal radiation grid for the different weather forecasting applications run at ECMWF. Depending on the model resolution, associated time-step, and the frequency for calling the full radiation schemes, the cost of the model integration drastically increased. However, comparisons of results with the different radiation grids (from R399 to R95 for the $\mathrm{T_L}$799L91 high-resolution model, from R255 to R31 for the $\mathrm{T_L}$399L62 model run in the

Table 2.5 *Impact of the McRad radiation package on the timing of the ECMWF model forecasts for different configurations and different horizontal resolutions. Dyn is the resolution for the dynamics, Rad that for the radiation. Freq is the frequency (hour) for calling the full radiation scheme, %Rad is the fraction of computer time taken by the radiative transfer calculations. Ratio is the factor by which McRad increases the computer cost relative to the previous operational configuration (ref31R2).*

Configuration	Dyn	Rad	Freq	%Rad	Ratio
T_L799L91					
ref31R2	799	399	1	7.3	1.000
McRad	799	511	1	36.4	1.456
	799	399	1	26.5	1.262
	799	**319**	1	19.2	1.147
	799	255	1	13.8	1.076
	799	159	1	6.7	0.994
	799	95	1	3.4	0.960
T_L399L62					
ref31R2	399	159	3	4.1	1.000
McRad	399	255	3	31.6	1.403
	399	159	3	16.4	1.148
	399	**95**	3	7.7	1.039
	399	63	3	3.8	0.998
	399	47	3	3.0	0.989
	399	31	3	2.1	0.980
T_L159L91					
ref31R2	159	63	3	8.0	1.000
McRad	159	159	3	67.5	2.831
	159	95	3	45.1	1.675
	159	**63**	3	27.7	1.273
	159	47	3	19.5	1.143
	159	31	3	11.0	1.034

Ensemble Prediction System, from R159 to R31 for the T_L159L91 model used for seasonal forecasts, were systematically carried out. For the radiation grid, a best compromise was chosen (R319 for T_L799, R95 for T_L399, R63 for T_L159), which allows the maximum benefit of McRad within the time constraints for delivering the various operational products.

As seen in Table 2.5, the full radiation scheme is called with a frequency that depends on the applications. Before Cy23r4, the full radiation computations were only performed every three hours. With Cy23r4, the frequency was changed to one-hour during the first 12 hours used for data assimilation. Since Cy28r3, the frequency was increased to every one-hour during the 10 days of the high-resolution forecast (presently T_L799L91). Other applications (Ensemble Prediction System, EPS, and seasonal forecasts) use a three-hour frequency for calling the full radiation computations. A temporal interpolation then provides the relevant interaction of the short-wave radiative fluxes with the solar zenith angle at every time step and every grid point.

To do so, a short-wave transmissivity is defined at each model level such that

$$\mathcal{F}_s = \tau_e \mathcal{S}_0 \tag{2.60}$$

where $\mathcal{F}_s$ is the net solar (short-wave) flux and $\mathcal{S}_0$ is the solar flux at the top of the atmosphere. $\mathcal{F}_s$ is defined only for a full radiation time step. At every time step, the net solar fluxes are computed therefore from the transmissivity derived for the last full radiation time step, using (2.60) with the correct solar angle for every grid point. The net long-wave fluxes at kept at the values given by the full radiation calculation.

2.8 INPUT TO THE RADIATION SCHEME

2.8.1 Model variables

Temperature values are needed at the boundaries of the layers, where the fluxes are computed. They are derived from the full level temperatures with a pressure weighted interpolation

$$T_{k+1/2} = T_k \frac{p_k(p_{k+1} - p_{k+1/2})}{p_{k+1/2}(p_{k+1} - p_k)} + T_{k+1} \frac{p_{k+1/2}(p_{k+1/2} - p_k)}{p_{k+1/2}(p_{k+1} - p_k)} \tag{2.61}$$

At the bottom of the atmosphere, either the surface temperature or the temperature at 2 m is used, while at the top of the atmosphere the temperature is extrapolated from the first full level and second half level temperatures.

2.8.2 Clouds

Cloud fraction, and liquid/ice water content is provided in all layers by the cloud scheme.

2.8.3 Aerosols

The aerosol climatology used in the operational model up to Cy26r1 was given as annual mean geographical distributions defined from T5 spectral coefficients, for different aerosol types, respectively, maritime, continental, urban and desert, plus a uniformly distributed stratospheric background aerosols, with fixed vertical distributions, following Tanre *et al.* (1984). In the last fifteen years, chemical and/or transport models have addressed the life cycles of various aerosol types and attempted an inventory of their spatio-temporal distributions. Out of these studies, a new climatology for the annual cycle of the aerosol distribution of various aerosol types has been compiled by Tegen *et al.* (1997), which has been implemented in the ECMWF forecast system from Cy26r3 onwards. Table 2.6 describes the characteristics of the aerosol components for each tropospheric aerosol type and Table 2.7 compares the maximum optical thicknesses in the old and new climatologies.

2.8.4 Carbon dioxide, ozone and trace gases

Carbon dioxide, methane, nitrous oxide, CFC-11 and CFC-12 have constant volume concentrations of 353 ppm, 1.72 ppm, 0.31 ppm, 280 ppt, and 484 ppt, respectively (IPCC/SACC, 1990), except in ERA-40 for the variation in concentrations is derived from (IPCC/SACC, 1995).

Two climatologies are available for the ozone distribution. In the first one (NOZOCL = 0), the ozone mixing ratio q_{O_3} depends on height, latitude, longitude and season. Its vertical distribution is assumed to be such that its integral from 0 to the pressure p is

$$\int_0^p q_{O_3} \mathrm{d}p = \frac{a}{1 + (b/p)^{3/2}} \tag{2.62}$$

The constants a and b are related to the total amount of ozone and the height of its maximum mixing ratio. They are imposed in terms of a limited series of spherical harmonics (T10) for the geographical distribution and a Fourier series for the seasonal variation. The total amount of ozone was taken from London *et al.* (1976) and the altitude of the maximum concentration was derived from Wilcox and Belmont (1977). Plots of these values can be found in the Appendix. In the second climatology (NOZOCL = 1), the ozone mixing ratio q_{O_3} depends on height, latitude and month, and is taken from Fortuin and Langematz (1994).

2.8.5 Ground albedo and emissivity

The background land albedo, α_{sb}, is interpolated to the model grid from the monthly mean values of a snow-free albedo produced for the combined 1982–1990 years. The albedo for that dataset was computed using the method of Sellers *et al.* (1996), but with new maps of soil reflectance, new values of vegetation reflectance and the biophysical parameters described in Los *et al.* (2000). More information on the original data and plots of the monthly mean albedo are shown in Chapter 11.

Spectral albedos for parallel and diffuse radiation are needed by the radiative code. In addition, the surface energy balance equation (see Chapter 3 on vertical diffusion) needs a spectrally integrated

Table 2.6 *Characteristics of the aerosol components for each tropospheric aerosol type in the new climatology for cycle Cy26r3 of the ECMWF model (adapted from Hess et al. (1998)).*

Type	RH(%)	Component	Number (cm^{-1})	Volume ($\mu m^3/m^3$)	Mass ($\mu g^3/m^3$)	Density (g/cm^3)
"Continental" organic	80					
		Insoluble	4.00E-01	4.75E+06	9.49E+00	2.00
		Water soluble	7.00E+03	1.57E+07	1.99E+01	1.27
		soot	8.30E+03	4.96E+05	4.96E-01	1.00
"Maritime" sulphate	95					
		Water soluble	1.50E+03	7.45E+06	8.35E+00	1.12
		sea salt (accum.)	2.00E+01	1.64E+08	1.72E+02	1.05
		sea salt (coarse)	3.20E-03	9.85E+05	1.04E+00	1.05
"Desert" dust-like	50					
		Water soluble	2.00E+03	2.81E+06	4.00E+00	1.42
		Mineral (nuclei)	2.70E+02	2.88E+06	7.49E+00	2.60
		Mineral (accum.)	3.05E+01	6.47E+07	1.69E+02	2.60
		Mineral (coarse)	1.42E-01	1.77E+07	4.60E+01	2.60
"Urban" black carbon	80					
		Insoluble	1.50E+00	1.78E+07	3.56E+01	2.00
		Water soluble	2.80E+04	6.28E+07	7.97E+01	1.27
		Soot	1.30E+05	7.78E+06	7.78E+01	1.00

Type: First definition (e.g. continental) is the aerosol component as known within both the ECMWF model and the OPAC software; second definition (e.g. organic) is the 3D distribution to which it is linked in the climatology of Tegen *et al.* (1997). RH is the relative assumed for the computations of the relevant optical properties. The *nuclei, accumulation*, and *coarse* modes refer to various size ranges for the component particles.

Table 2.7 *Maximum optical thickness in the two aerosol climatologies.*

OLD	Annual	January	July	NEW
Continental	0.2	0.235	0.231	Organic
Maritime	0.05	0.099	0.232	Sulphate
Desert	1.9	0.184	1.01	Dust-like
Urban	0.1	0.039	0.039	Black carbon
Background trop.	0.03			
Background stratos	0.045	0.045	0.045	Background stratos.

Aerosol types of the new and old climatologies are paired according to the dominant components in each mix.

Table 2.8 *Diffuse and parallel albedo and window emissivity for each tile.*

Tile	1	2	3	4	5	6	7	8
Description	**Open sea**	**Sea ice**	**Interception layer**	**Low vegetation**	**Exposed snow**	**High vegetation**	**Shaded snow**	**Bare ground**
Diffuse albedo	0.06	Ebert and Curry (1993)	α_{sb}	α_{sb}	α_{sn}	α_{sb}	0.15	α_{sb}
Parallel albedo	Taylor *et al.* (1996)	Ebert and Curry (1993)	α_{sb}	α_{sb}	α_{sn}	α_{sb}	0.15	α_{sb}
Window emissivity	0.99	0.98	0.96	0.93–0.96	0.98	0.93–0.96	0.93–0.96	0.93–0.96

parallel+diffused albedo, specified for each independent surface functional unit, tile. The procedure is summarized in Table 2.8. Over open water, the surface albedo for direct parallel radiation is a fit to low-flying aircraft measurements over the ocean given by Taylor *et al.* (1996)

$$\alpha_{sp} = \frac{0.037}{1.1\mu_0^{1.4} + 0.15} \tag{2.63}$$

For sea ice, monthly values based on Ebert and Curry (1993) albedos for the Arctic Ocean are interpolated to the forecast time. The bare sea ice albedo value in Ebert and Curry is taken as a representative value for summer, and the dry snow albedo value is used for the winter months. Values for the Antarctic are shifted by six months. Separate values for visible and near-infrared spectral bands are used. The time-varying snow albedo (α_{sn}, see Chapter 8), is used for the exposed snow tile only. Finally, the average of the diffuse and parallel albedos are spectrally integrated for each tile.

The thermal emissivity of the surface outside the 800–1250 cm^{-1} spectral region is assumed to be 0.99 everywhere. In the window region, the spectral emissivity is constant for open water, sea ice, the interception layer and exposed snow tiles. For low and high vegetation and for shaded snow the emissivity depends on the water content in the top soil layer. Emissivity decreases linearly from 0.96 for soils at or above field capacity to 0.93 for soils at or below permanent wilting point. The same formulation is used for bare ground, except for desert areas ($\alpha_{sb} > 0.3$), where a value of 0.93 is used independently of the soil water content. Finally, a broadband emissivity is obtained by convolution of the spectral emissivity and the Planck function at the skin temperature.

2.8.6 Solar zenith angle

Equations to compute the annual variation of the solar constant I, the solar declination δ_s and the difference between solar time and official time can be found in Paltridge and Platt (1976). These equations are used to give the cosine of the solar angle at the ground. Because of the curvature of the earth, the zenith angle is not quite constant along the path of a sun ray. Hence the correction applied to $\mu^a 0$ to give an average μ_0 for the atmosphere is

$$\mu_0 = \frac{\frac{H}{a}}{(\mu_0^a)^2 + \frac{H}{a}\left(2 + \frac{H}{a}\right) - (\mu_0^a)^2} \tag{2.64}$$

where a is the earth radius and H is the atmospheric equivalent height. H/a is fixed at 0.001277.

2.9 THE RADIATION CODE

Routine RADHEAT or RADHEATN (depending whether the diagnostic or prognostic cloud scheme is used) is called at every time step to compute the radiative fluxes and heating using the solar zenith angle computed in CPGLAG and emissivities and transmissivities (PEMTU, PTRSOL) computed at full radiation time steps in RADINT. or RADINTG (see Subsection 2.9.2). The other routines are called either once at the beginning of the run (SUECRAD and below) or once per full radiation step at the first row (ECRADFR and below), or at every full radiation time step for all rows. In this section, we briefly describe the function of each routine.

2.9.1 Set-up routines

- SUECRAD provides the interface with the user, via the namelist NAERAD. It defines the constants of Table 2.5 and sets the configuration for the radiative computations (from SUPHEC).
- ECRADFR modifies the frequency of full radiative computations (from CNT4).
- SUAERLandSUAERSNset up the long-wave and short-wave radiative characteristics of the aerosols (from SUECRAD).
- SUECRAD defines the geographical distribution of aerosols, in terms of spectral coefficients (from UPDTIER).
- SUAERV defines the globally averaged vertical distribution of the aerosols (from SUECRAD).
- SUCLOP sets up the long-wave and short-wave radiative properties of the ice and water clouds (from SUECRAD).
- SUECOZO computes the Legendre coefficients for the ozone distribution according to the time of the year, using the Fourier coefficients defined in DATA statements (from UPDTIER).
- SULWN sets up the coefficients for the pre-Cy22r3 long-wave radiative computations (from SUECRAD).
- SURDI sets up the concentrations of radiatively active gases and security parameters for the radiative computations (from SUECRAD).
- SUSWN sets up the coefficients for the pre-Cy32r2 short-wave radiative computations (from SUECRAD).
- UPDTIER updates the time for full radiative computations (from ECRADFR).
- The routines SUAERH, SUECOZO are called only once per full radiation step, at the first row.
- SURRTAB precomputes the array linking gaseous optical thickness and the transmission function (RRTM). (called from SUECRAD).
- SURRTFTR includes all coefficients related to the g-point configuration (RRTM). (called from SUECRAD).
- SURRTPK defines the limits of the spectral intervals, and the coefficients of the spectrally defined and spectrally integrated Planck functions (RRTM). (called from SUECRAD).
- SURRTRF defines the pressure and temperature reference profiles used for the tabulation of the absorption coefficients (RRTM). (called from SUECRAD).
- SUSRTAER defines the optical properties of aerosols for the RRTM_{SW} scheme.
- SUSRTALB defines the coefficients used for dealing with the surface albedo in the RRTM_{SW} scheme.
- SUSRTCOP defines the short-wave radiative properties of the ice and water clouds for use in the RRTM_{SW} scheme.
- SUSRTM includes all coefficients related to the g-point configuration in the RRTM_{SW} scheme.
- RRTM_CMBGBn, for each of the 16 spectral intervals of RRTM_{LW}, remaps the absorption coefficients from 16 to the final number of g-points (called from RRTM_INIT_140GP).
- RRTM_INIT_140GP performs the g -point reduction from 16 per band to a band-dependent number (column 2 in Table 2.3). It also computes the relative weighting for the new g-point combinations (called from SUECRAD).
- RRTM_KGBn contain the various absorption coefficients for all gases relevant to the different spectral bands of RRTM_{LW}.
- SRTM_CMBGBn, for each of the 14 spectral intervals of RRTM_{SW}, remaps the absorption coefficients from 14 to the final number of g-points (called from SRTM_INIT).
- SRTM_KGBn contain the various absorption coefficients for all gases relevant to the different spectral bands of RRTM_{SW}.

2.9.2 Main routines

- RADINT or RADINTG is called by RADDRV to launch the full radiation computations, depending on whether the pre-Cy26r1 sampling configuration or the Cy26r1 halo configuration is used for spatial interpolation (see Section 2.7). Zonal mean diagnostic of the temperature, clouds and albedo are computed. Temperature is vertically interpolated. Depending on the value of the variable NRINT an interpolation of all input variables to a coarser grid may be carried out. It may be necessary to subdivide the latitude belt in a few parts for the actual calculation of radiative fluxes because of storage space limitations. For this reason a loop over these parts follows. Inside this loop a call

to routine RADLSW provides solar and thermal fluxes for a subset of points of that latitude row. These fluxes are converted into transmissivities and emissivities and after completion of the whole latitude circle they are transferred to the full grid when the calculations are carried out with the coarse resolution (NRINT > 1).

- RADLSW is the driver routine of the solar and thermal fluxes by calling specialized routines SW for short-wave radiation and either RRTM_RRTM_140GP or LW for long-wave radiation.

2.9.3 Specialized routines

- RADSRF is called from RADPAR/CALLPAR to compute surface albedo and emissivity. It computes the gridpoint diffuse and parallel spectral albedos and a spectrally integrated albedo (for postprocessing). It also computes the emissivity inside and outside the window region, and the spectrally integrated emissivity. Finally, it computes spectrally integrated tile albedos to be used by the surface energy balance routine (see Chapter 3 on vertical diffusion).
- LW organizes the long-wave computation by calling in turn LWU, LWBV, LWC.
- LWU computes the effective absorber amounts including the pressure and temperature dependencies in the spectral intervals of the long-wave radiation scheme.
- LWBV calls LWB and LWV.
- LWB computes the Planck function with relation to temperature for all levels and spectral intervals.
- LWV organizes the vertical integration by calling LWVN which deals with the contribution to the flux of the layers adjacent to the level of computation of flux, LWVD which deals with the contribution from the more distant layers, and LWVB which computes the contribution of the boundary terms.
- LWTT and LWTTM compute the relevant transmission functions needed in LWVN, LWVD, and LWVB.
- LWC introduces the effect of clouds on the long-wave fluxes.
- SW organizes the short-wave computation by calling in turn SWU, SW1S, and SW2S.
- SWU computes the effective absorber amounts including the pressure and temperature dependencies of the absorption.
- SW1S and SW2S deal with the short-wave radiation transfer in the two spectral intervals used to describe the solar spectrum. They both call SWCLR, which deals with the conservative scattering processes (Rayleigh) and the scattering/absorption by aerosols in the totally clear sky part of the atmospheric column, then SWR which deals with the same processes for the clear sky layers in an otherwise cloudy column, and SWDE which computes the reflectivity and transmissivity of a layer including non-conservative scatterers (cloud particles) with the Delta-Eddington approximation.
- SWTT andSWTT1, computes the relevant transmission functions.
- RRTM_RRTM_140GP organizes the long-wave computation by calling in turn, within a loop on the individual vertical columns, RRTM_ECRT_140GP, RRTM_SETCOEF_140GP, RRTM_GASABS1A_140GP and RRTM_RTRN1A_140GP.
- RRTM_ECRT_140GP defines the surface spectral emissivity, and the spectral aerosol thickness, and the layer absorber amounts and cloud quantities as used in RRTM.
- RRTM_SETCOEF_140GP computes the indices and fractions related to the pressure and temperature interpolations. It also calculates the values of the integrated Planck function for each spectral band at the level and layer temperatures.
- RRTM_GASABS1A_140GP launches the calculation of the spectrally defined optical thickness for gaseous absorption. It calls RRTM_TAUMOLn.
- RRTM_RTRN1A_140GP computes the downward then upward fluxes, using a diffusivity-type approximation for the angle integration. Cloud overlap is treated with a generalized maximum/random overlap method. Adjacent layers are treated with maximum overlap, non-adjacent cloud groups are treated with random overlap. For adjacent cloud layers, cloud information is carried from the previous two layers.
- RRTM_RRTM_140GP_MCICA, RRTM_ECRT_140GP_MCICA, RRTM_RTRN1A_140GP_MCICA are the McICA equivalent of the routines defined above.
- SU_MCICA includes coefficients required to run the Räisänen and Barker (2004) cloud generator.
- McICA_CLD_GEN prepares in and out of the cloud generator for use in the McICA version of the radiation scheme.

- McICA_CLD_GENERATOR is the stochastic generation of sub-grid scale cloudy columns for use in the McICA version of the radiation scheme.
- SRTM_SRTM_224GP organizes the short-wave computation by calling in turn, within a loop on the individual vertical columns, SRTM_SETCOEF and SRTM_SPCVRT, SRTM_VRTQDR and SRTM_REFTRA.
- SRTM_SETCOEF computes the indices and fractions related to the pressure and temperature interpolations.
- SRTM_SPCVRT computes the short-wave radiation fluxes using a two-stream method, calling first the routines setting up the spectral coefficients (SRTM_TAUMOLn), then the vertical quadrature (SRTM_VRTQDR).
- SRTM_REFTRA computes the reflectivity and transmissivity of a layer of given optical thickness using a two-stream approximation.
- SRTM_SRTM_224GP_MCICA and SRTM_SPCVRT_MCICA are the McICA equivalent of the routines defined above.

2.9.4 Heating rate computation

- RADHEAT or RADHEATN, depending whether the diagnostic or the prognostic cloud scheme is used, recomputes at each time step the net radiative fluxes from the layers' effective emissivity and transmissivity, using the actual temperature and solar zenith angle. It also computes the downward long-wave and short-wave radiation at the surface.

APPENDIX A. LIST OF SYMBOLS

B_ν	Planck function integrated over the half sphere with the factor involving π absorbed: in units of flux (Wm^{-2})
C_{cld}	fractional cloud cover
c_p	specific heat at constant pressure of moist air
$c_{p_{\mathrm{dry}}}$	specific heat at constant pressure of dry air
$c_{p_{\mathrm{vap}}}$	specific heat at constant pressure of water vapour
$\mathcal{E}_\nu^0$	incident solar radiance in the direction θ_0
$\mathcal{F}$	radiative flux
f	fractional scattering into the forward peak
g	acceleration of gravity
g	asymmetry factor for aerosol scattering
k	absorption coefficient
$\mathcal{L}_\nu$	monchromatic radiance at wavenumber ν
M	magnification factor ($= 35/\sqrt{(\mu_0^2+1)}$)
m_{O_3}	ozone mixing ratio
P	scattering phase function
p	pressure
$\Pi(\mathcal{U})\,\mathrm{d}\mathcal{U}$	probability of a photon encountering an absorber amount between $\mathcal{U}$ and $\mathcal{U}+\mathrm{d}\mathcal{U}$
q	specific humidity
r	diffusivity factor ($=\sec\theta$)
r_e	mean effective radius of cloud water droplets
$\mathcal{R}$	reflectance
S_0	solar flux at the top of the atmosphere
$\mathcal{T}$	transmittance
T	temperature
t_ν	monochromatic transmission at wavenumber ν
$\mathcal{U}$	absorber amount
α	surface albedo
β_ν^{abs}	cloud particle absorbtion coefficient
β_ν^{ext}	extinction coefficient
β_ν^{sca}	scattering coefficient

δ_{g}	molecular absorption of gases
δ	optical depth
$\varepsilon_{\mathrm{cld}}$	cloud emissivity
μ	$= \cos\theta$
ν	wavenumber
ϖ_ν	single scattering albedo ($= \beta_\nu^{\mathrm{sca}}/k_\nu$)
Φ	scattering phase function
φ	azimuth angle
θ	zenith angle
θ_0	direction of incident solar beam
Θ	angle between incident and scattered radiances

Chapter 3

Turbulent transport and interactions with the surface

Table of contents

3.1 INTRODUCTION

The parametrization scheme described in this chapter represents the turbulent transfer of heat, momentum and moisture between the surface and the lowest model level and the turbulent transport of the same quantities plus liquid and ice water between model levels. The scheme computes the physical tendencies of the six prognostic variables (u, v, T, q, q_l and q_i) due to the vertical exchange by turbulent processes. These tendencies are obtained as the difference between the results of an implicit time-step from t to $t+1$. All the diagnostic computations (such as the calculation of the exchange coefficients, etc.) are done at time t. The surface boundary condition is formulated separately for eight different tiles: water, ice, wet skin, low vegetation, exposed snow, high vegetation, snow under vegetation, and bare soil.

The different tiles have their own surface energy balance and their own skin temperature. In this version of the IFS, the mixture of land and ocean tiles is still not used, i.e. a grid box is either 100% ocean (water + ice) or 100% land (tile 3 to 8). Details about tiles are given in Chapter 8.

The equation for the vertical turbulent transport of any conservative quantity ϕ is described using an Eddy-Diffusivity Mass-Flux (EDMF) framework

$$\frac{\partial \phi}{\partial t} = \frac{1}{\rho}\frac{\partial}{\partial z}\left(\rho K_\phi \frac{\partial \phi}{\partial z} - M(\phi_u - \bar{\phi})\right) = \frac{1}{\rho}\frac{\partial J_\phi}{\partial z} \tag{3.1}$$

The vertical turbulent flux J_ϕ (positive downwards) is written using a first-order turbulence closure, where K_ϕ is the exchange coefficient plus a mass-flux component to describe the strongest eddies active in the mixed layer. Because the mass-flux is zero at the surface and the top boundary conditions are satisfied by vertical diffusion

$$\begin{aligned} K_\phi \frac{\partial \phi}{\partial z} &= 0 \quad \text{at} \quad p = p_{\text{top}} \\ K_\phi \frac{\partial \phi}{\partial z} &\rightarrow \sum_{i=1}^{N_{\text{T}}} F_i C_{\phi i} |U(z)| (\phi(z) - \phi_{\text{surf}i}) \text{ as } z \rightarrow 0 \end{aligned} \tag{3.2}$$

where p_{top} is the pressure at the top of the atmosphere. For heat and moisture the surface boundary condition is provided tile by tile and fluxes are averaged over the N_{T} tiles, weighted by their fraction F_i. The transfer coefficient $C_{\phi i}$ at the lowest model level depends upon the static stability. The variable ϕ_{surf} represents the value of ϕ at the surface. For heat and moisture, eight tiles are used (see Chapter 10). For wind, a single tile is used with a no slip condition at the surface.

The vertical turbulent transport processes are applied to the two horizontal wind components, u and v, the specific total water q_t and the generalized liquid water static energy s_l,

$$q_{\text{t}} = q + q_l + q_{\text{i}} \tag{3.3}$$

$$s_l = gz + c_p T - L_{\text{c}} q_l - L_{\text{d}} q_{\text{i}} \tag{3.4}$$

where q, q_l, q_{i} are the specific humidity, specific liquid water and specific ice water, c_p is the specific heat at constant pressure of dry air, g is the constant of gravity, and L_{c} and L_{d} are the latent heats of condensation and deposition respectively. Note that the influence of water vapor on c_p is neglected throughout the formulation of vertical turbulent fluxes (as is also done in the other physics components).

The problem is simplified by assuming that z remains constant with respect to time during the turbulent transport process (even if in reality T variations would modify $z(p)$). Exchange coefficients (with the dimension of a pressure thickness) are then computed for momentum and for heat (sensible plus latent) (the subscripts 'M, 'H' and 'Q' are used to identify the exchange coefficient for momentum, heat and total water), with different formulations for the stable and the unstable case (depending on the sign of a stability parameter, either the Obukhov length or the bulk Richardson number in the surface layer). The mass-flux term is calculated based on an entraining plume model closed at the surface. The implicit linear equations for the fluxes of momentum, firstly for u and v and secondly for s_l and q_{t}, are solved by a Gaussian-elimination/back-substitution method.

The surface boundary condition is applied between the downward scanning elimination and the upward scanning back substitution. It involves a no-slip condition for u and v and the tile-by-tile solution of the surface energy balance for the boundary condition of q and dry static energy

$$s = gz + c_p T \tag{3.5}$$

The water tile is an exception as it ignores the surface energy balance and uses the specified SST and the saturation specific humidity as boundary conditions.

Finally, the tendency of temperature is computed, modified by the effects of local dissipation (it is assumed that there is no storage of turbulence kinetic energy). The tiled surface fluxes of heat and moisture are also computed for later use by the surface scheme.

3.2 THE SURFACE LAYER

The surface layer approximation is applied between the lowest model level (about 10 m above the surface in the 60 and 91 level models) and the surface and for each tile separately. It is assume that the turbulent fluxes are constant with height and equal to the surface values. They can be expressed, using Monin–Obukhov similarity theory, in terms of the gradients of wind, dry static energy and specific humidity, which are assumed to be proportional to universal gradient functions of a stability parameter:

$$\begin{aligned}\frac{\kappa z}{u_*}\frac{\partial u}{\partial z} &= \Phi_{\mathrm{M}}\left(\frac{z}{\mathcal{L}}\right)\\ \frac{\kappa z}{s_*}\frac{\partial s}{\partial z} &= \Phi_{\mathrm{H}}\left(\frac{z}{\mathcal{L}}\right)\\ \frac{\kappa z}{q_*}\frac{\partial q}{\partial z} &= \Phi_{\mathrm{Q}}\left(\frac{z}{\mathcal{L}}\right)\end{aligned} \tag{3.6}$$

The scaling parameters u_*, s_* and q_* are expressed in terms of surface fluxes J_ϕ by

$$\begin{aligned}\rho u_*^2 &= J_{\mathrm{M}}\\ \rho u_* s_* &= J_{\mathrm{s}}\\ \rho u_* q_* &= J_{\mathrm{q}}\end{aligned} \tag{3.7}$$

The stability parameter $\mathcal{L}$ is the Obukhov length defined as

$$\mathcal{L} = -u_*^3 \Big/ \left(\frac{\kappa g}{T_n} Q_{0\mathrm{v}}\right) \quad \text{with} \quad Q_{0\mathrm{v}} = \frac{u_* s_* - (c_{p_{\mathrm{vap}}} - c_{p_{\mathrm{dry}}}) T_n u_* q_*}{c_p} + \varepsilon T_n u_* q_* \tag{3.8}$$

$Q_{0\mathrm{v}}$ is the virtual temperature flux in the surface layer, κ is the Von Kármán constant ($=0.4$), T_n is a reference temperature taken as a near-surface temperature (the temperature of the lowest atmospheric level n) and $\varepsilon = (R_{\mathrm{vap}}/R_{\mathrm{dry}}) - 1$, where R_{vap} and R_{dry} are the gas constants for water vapour and dry air, respectively.

In the surface layer, the gradient functions (3.6) can be integrated to profiles

$$u = \frac{\tau_x}{\kappa\rho u_*}\left\{\log\left(\frac{z_n + z_{0\mathrm{M}}}{z_{0\mathrm{M}}}\right) - \Psi_{\mathrm{M}}\left(\frac{z_n + z_{0\mathrm{M}}}{\mathcal{L}}\right) + \Psi_{\mathrm{M}}\left(\frac{z_{0\mathrm{M}}}{\mathcal{L}}\right)\right\} \tag{3.9}$$

$$v = \frac{\tau_y}{\kappa\rho u_*}\left\{\log\left(\frac{z_n + z_{0\mathrm{M}}}{z_{0\mathrm{M}}}\right) - \Psi_{\mathrm{M}}\left(\frac{z_n + z_{0\mathrm{M}}}{\mathcal{L}}\right) + \Psi_{\mathrm{M}}\left(\frac{z_{0\mathrm{M}}}{\mathcal{L}}\right)\right\} \tag{3.10}$$

$$s - s_{\mathrm{surf}} = \frac{J_s}{\kappa\rho u_*}\left\{\log\left(\frac{z_n + z_{0\mathrm{M}}}{z_{0\mathrm{H}}}\right) - \Psi_{\mathrm{H}}\left(\frac{z_n + z_{0\mathrm{M}}}{\mathcal{L}}\right) + \Psi_{\mathrm{H}}\left(\frac{z_{0\mathrm{H}}}{\mathcal{L}}\right)\right\} \tag{3.11}$$

$$q - q_{\mathrm{surf}} = \frac{J_q}{\kappa\rho u_*}\left\{\log\left(\frac{z_n + z_{0\mathrm{M}}}{z_{0\mathrm{Q}}}\right) - \Psi_{\mathrm{H}}\left(\frac{z_n + z_{0\mathrm{M}}}{\mathcal{L}}\right) + \Psi_{\mathrm{H}}\left(\frac{z_{0\mathrm{Q}}}{\mathcal{L}}\right)\right\} \tag{3.12}$$

$z_{0\mathrm{M}}$, $z_{0\mathrm{H}}$ and $z_{0\mathrm{Q}}$ are the roughness lengths for momentum, heat and moisture. The stability profile functions Ψ are derived from the gradient functions (3.6) with the help of the relationship $\Phi = 1 - \zeta(\partial\Psi/\partial\zeta)$. These profiles are used for the surface atmosphere interaction as explained in the following sections and also for the interpolation between the lowest model level and the surface (post-processing of 10 m wind and 2 m temperature and moisture).

In extremely stable situations, i.e. for very small positive $\mathcal{L}$, the ratio $z/\mathcal{L}$ is large, resulting in unrealistic profile shapes with standard stability functions. Therefore the ratio $z/\mathcal{L}$ is limited to 5 by defining a height h such that $h/\mathcal{L} = 5$. If $z < h$, then the profile functions described above, are used up to $z = h$ and the profiles are assumed to be uniform above that. This modification of the profiles for exceptionally stable situations (no wind) is applied to the surface transfer formulation as well as to the interpolation for post-processing.

3.2.1 Surface fluxes

Surface fluxes for heat and moisture are computed separately for the different tiles, so most of the surface layer computations loop over the tile index. Here a general description is given of the aerodynamic aspects

of the transfer between the surface and the lowest model level. The description of the individual tiles can be found in Chapter 8.

Assuming that the first model level above the surface is located in the surface boundary layer at a specified height z_n, the gradient functions (3.6) can be integrated to profiles for wind, dry static energy and specific humidity. The surface fluxes are expressed in terms of differences between parameters at level z_n and surface quantities (identified by the subscript 'surf'; the tile index has been omitted in this general description) so

$$\begin{aligned} J_{\mathrm{M}} &= \rho C_{\mathrm{M}} |U_n|^2 \\ J_{\mathrm{s}} &= \rho C_{\mathrm{H}} |U_n| (s_n - s_{\mathrm{surf}}) \\ J_{\mathrm{q}} &= \rho C_{\mathrm{Q}} |U_n| (\alpha_n q_n - \alpha_{\mathrm{surf}} q_{\mathrm{surf}}) \end{aligned} \tag{3.13}$$

where $q_{\mathrm{surf}} = q_{\mathrm{sat}}(T_{\mathrm{surf}})$, α_n and α_{surf} are provided by the land scheme, and $s_{\mathrm{surf}} = c_p T_{\mathrm{surf}}$, (the humidity equation simplifies over water where $\alpha_n = 1$ and $\alpha_{\mathrm{surf}} = 1$).

The transfer coefficients can be expressed as

$$C_{\mathrm{M}} = \frac{\kappa^2}{\left[\log\left(\frac{z_n+z_{0\mathrm{M}}}{z_{0\mathrm{M}}}\right) - \Psi_{\mathrm{M}}\left(\frac{z_n+z_{0\mathrm{M}}}{\mathcal{L}}\right) + \Psi_{\mathrm{M}}\left(\frac{z_{0\mathrm{M}}}{\mathcal{L}}\right)\right]^2} \tag{3.14}$$

$$C_{\mathrm{H}} = \frac{\kappa^2}{\left[\log\left(\frac{z_n+z_{0\mathrm{M}}}{z_{0\mathrm{M}}}\right) - \Psi_{\mathrm{M}}\left(\frac{z_n+z_{0\mathrm{M}}}{\mathcal{L}}\right) + \Psi_{\mathrm{M}}\left(\frac{z_{0\mathrm{M}}}{\mathcal{L}}\right)\right]\left[\log\left(\frac{z_n+z_{0\mathrm{M}}}{z_{0\mathrm{H}}}\right) - \Psi_{\mathrm{H}}\left(\frac{z_n+z_{0\mathrm{M}}}{\mathcal{L}}\right) + \Psi_{\mathrm{H}}\left(\frac{z_{0\mathrm{H}}}{\mathcal{L}}\right)\right]} \tag{3.15}$$

$$C_{\mathrm{Q}} = \frac{\kappa^2}{\left[\log\left(\frac{z_n+z_{0\mathrm{M}}}{z_{0\mathrm{M}}}\right) - \Psi_{\mathrm{M}}\left(\frac{z_n+z_{0\mathrm{M}}}{\mathcal{L}}\right) + \Psi_{\mathrm{M}}\left(\frac{z_{0\mathrm{M}}}{\mathcal{L}}\right)\right]\left[\log\left(\frac{z_n+z_{0\mathrm{M}}}{z_{0\mathrm{Q}}}\right) - \Psi_{\mathrm{Q}}\left(\frac{z_n+z_{0\mathrm{M}}}{\mathcal{L}}\right) + \Psi_{\mathrm{Q}}\left(\frac{z_{0\mathrm{Q}}}{\mathcal{L}}\right)\right]} \tag{3.16}$$

The wind speed $|U_n|$ is expressed as

$$|U_n|^2 = u_n^2 + v_n^2 + w_*^2 \tag{3.17}$$

with w_* the free convection velocity scale defined by

$$w_* = \left(z_{\mathrm{i}} \frac{g}{T_n} Q_{\mathrm{ov}}\right)^{1/3} \tag{3.18}$$

The parameter z_{i} is a scale height of the boundary layer depth and is set to constant value of 1000 m, since only the order of magnitude matters. The additional term in equation (3.17) represents the near surface wind induced by large eddies in the free-convection regime. When the surface is heated, this term guarantees a finite surface wind-forcing in the transfer law even for vanishing u_n and v_n, and prevents $|U_n|$ and $\mathcal{L}$ from becoming zero. Beljaars (1994) showed that this empirical term, when added into the standard Monin–Obukhov scaling, is in agreement with scaling laws for free convection. When used with the roughness lengths defined below, it provides a good fit to observational data, both over land and over sea.

3.2.2 Stability functions

The empirical forms of the dimensionless gradient functions Φ (given by (3.6)) have been deduced from field experiments over homogeneous terrain.

(i) *Unstable conditions* ($\zeta = z/\mathcal{L} < 0$). The gradient functions proposed by Dyer and Hicks are used (Dyer, 1974; Hogström, 1988). Therefore

$$\begin{aligned} \Phi_{\mathrm{M}}(\zeta) &= (1 - 16\zeta)^{-1/4} \\ \Phi_{\mathrm{H}}(\zeta) &= \Phi_{\mathrm{Q}}(\zeta) = (1 - 16\zeta)^{-1/2} \end{aligned} \tag{3.19}$$

These functions can be integrated to the universal profile stability functions, Ψ, (Paulson, 1970) so that

$$\Psi_{\rm M}(\zeta) = \frac{\pi}{2} - 2\,\mathrm{atan}(x) + \log\frac{(1+x)^2\cdot(1+x^2)}{8}$$
$$\Psi_{\rm H}(\zeta) = \Psi_{\rm Q}(\zeta) = 2\log\left\{\frac{1+x^2}{2}\right\} \tag{3.20}$$

with $x = (1-16\zeta)^{1/4}$. The Ψ-functions are used in the surface layer and the Φ-functions for unstable stratification are used above the surface layer for local closure.

(ii) *Stable conditions* ($\zeta = z/\mathcal{L} > 0$). The code contains gradient function $\Phi_{\rm M}$ as documented by Hogström (1988), and $\Phi_{\rm H}$ as derived from the Ellison and Turner relation for the ratio $\Phi_{\rm M}/\Phi_{\rm H}$ giving

$$\Phi_{\rm M}(\zeta) = 1 + 5\zeta$$
$$\Phi_{\rm H}(\zeta) = \Phi_{\rm Q}(\zeta) = (1+4\zeta)^2 \tag{3.21}$$

These functions were meant to be used for local closure above the surface layer, but are not used at all in the current model version, because Richardson number dependent functions are used instead (see section on exchange coefficients above the surface layer).
The stable profile functions as used in the surface layer, are assumed to have the empirical forms proposed by Holtslag and Bruin (1988), with a modification to allow for the effects of a critical flux Richardson number for large ζ: The profiles are given by

$$\Psi_{\rm M}(\zeta) = -b\left(\zeta - \frac{c}{d}\right)\exp(-d\zeta) - a\zeta - \frac{bc}{d}$$
$$\Psi_{\rm H}(\zeta) = \Psi_{\rm Q}(\zeta) = -b\left(\zeta - \frac{c}{d}\right)\exp(-d\zeta) - \left(1+\frac{2}{3}a\zeta\right)^{1.5} - \frac{bc}{d} + 1 \tag{3.22}$$

where $a = 1$, $b = 2/3$, $c = 5$, and $d = 0.35$.

3.2.3 Computation of the Obukhov length

The transfer coefficients needed for the surface fluxes require the estimation of stability parameter ζ, itself a function of the surface fluxes. Therefore, an implicit equation, relating ζ to bulk Richardson number $Ri_{\rm bulk}$, is solved using

$$Ri_{\rm bulk} = \zeta\cdot\frac{\left[\log\left(\frac{z_n+z_{0\rm M}}{z_{0\rm H}}\right) - \Psi_{\rm H}\left(\frac{z_n+z_{0\rm M}}{\mathcal{L}}\right) + \Psi_{\rm H}\left(\frac{z_{0\rm H}}{\mathcal{L}}\right)\right]}{\left[\log\left(\frac{z_n+z_{0\rm M}}{z_{0\rm M}}\right) - \Psi_{\rm M}\left(\frac{z_n+z_{0\rm M}}{\mathcal{L}}\right) + \Psi_{\rm M}\left(\frac{z_{0\rm M}}{\mathcal{L}}\right)\right]^2} \tag{3.23}$$

with

$$Ri_{\rm bulk} = \left(\frac{g}{\theta_v}\right)\frac{z_n(\theta_{\rm vn} - \theta_{\rm vsurf})}{|U_n|^2} \tag{3.24}$$

where $\theta_{\rm vn}$ and $\theta_{\rm vsurf}$ are the virtual potential temperatures at level z_n and at the surface, and $\theta_{\rm v}$ is a virtual potential temperature within the surface layer. Equation (3.24) can be expressed in terms of dry static energy:

$$Ri_{\rm bulk} = \frac{gz_n}{|U_n|^2}\left[\frac{2(s_n - s_{\rm surf})}{(s_n + s_{\rm surf} - gz_n)} + \varepsilon(q_n - q_{\rm surf})\right] \tag{3.25}$$

Knowing $Ri_{\rm bulk}$ at time t, a first guess of the Obukhov length is made from fluxes computed at the previous time step. Equation (3.23) is solved numerically using the Newton iteration method to retrieve ζ.

In contrast to the previous formulation used in the model (Louis *et al.*, 1982), the present scheme allows a consistent treatment of different roughness lengths for momentum, heat and moisture. The revised stability functions also reduce diffusion in stable situations resulting in more shallow stable boundary layers.

3.2.4 Roughness lengths

The integration constants z_{0M}, z_{0H} and z_{0Q}, in the equations for the transfer coefficients C_M, C_H and C_Q ((3.14) to (3.16)) are called roughness lengths because they are related to the small scale inhomogeneities of the surface that determine the air–surface transfer.

(i) *Over land.* The roughness lengths over land are assumed to be fixed and related to the land surface cover. Every time step the dominant tile is determined and the roughness lengths are set according to a table that relates the roughness length to vegetation type or to land cover (bare soil and exposed snow). The roughness length for momentum is different from the one for heat, but the ones for heat and moisture are assumed to be the same (See Chapter 8 for the tables).

(ii) *Over sea.* The specification of surface roughness lengths is particularly important over the sea. Because of the fixed boundary conditions for temperature and moisture the sea is, in principle, an infinite source of energy to the model. Following Beljaars (1994) the surface roughness lengths are expressed by

$$\begin{aligned} z_{0M} &= \alpha_M \frac{\nu}{u_*} + \alpha_{Ch} \frac{u_*^2}{g} \\ z_{0H} &= \alpha_H \frac{\nu}{u_*} \\ z_{0Q} &= \alpha_Q \frac{\nu}{u_*} \end{aligned} \tag{3.26}$$

These expressions account for both low and high wind regimes.

- At low wind speed the sea surface becomes aerodynamically smooth and the sea surface roughness length scales with the kinematic viscosity ν ($= 1.5 \times 10^{-5} \mathrm{m^2 s^{-1}}$).
- At high wind speed the Charnock relation is used. The chosen constants are $\alpha_M = 0.11$, $\alpha_H = 0.40$, and $\alpha_Q = 0.62$ (Brutsaert, 1982). The Charnock coefficient, α_{Ch}, is set equal to 0.018 for the uncoupled model, and is provided by the wave model in coupled mode.

The smooth-surface parametrization is retained in high wind speed regimes for heat and moisture because observations indicate that the transfer coefficients for heat and moisture have very little wind-speed dependence above 4 $\mathrm{ms^{-1}}$ (Miller *et al.*, 1992; Godfrey and Beljaars, 1991). In (3.26) friction velocity u_*, is calculated from

$$u_* = C_M^{1/2} (u_n^2 + v_n^2 + w_*^2)^{1/2} \tag{3.27}$$

with w_* from (3.18) using fluxes from the previous time step.

3.2.5 Concept

The concept behind the EDMF approach is to describe the strong large-scale organized updraughts with mass fluxes and the remaining small-scale turbulent part with diffusion. The up/down-draughts described by the mass flux term allow for non-local mixing, while the local mixing described by the diffusion term is limited to down gradient transports. Siebesma and Cuijpers (1995) arbitrarily define a strong updraught as a fixed small fractional area a_u containing the strongest upward vertical motions. The horizontal distribution of a field ϕ can then be described with perturbation terms in both updraught and environment areas separately

$$\phi_u = \phi'_u + \overline{\phi}^u \qquad \text{and} \qquad \phi_e = \phi'_e + \overline{\phi}^e \tag{3.28}$$

where u and e refer to the updraught and environment areas both for the field and the averaging operator. The domain average then becomes

$$\overline{\phi} = a_u \overline{\phi}^u + (1 - a_u) \overline{\phi}^e \tag{3.29}$$

After some manipulation the vertical turbulent flux breaks into three terms

$$\overline{w'\phi'} = a_u \overline{w'\phi'_u}^u + (1 - a_u) \overline{w'\phi'_e}^e + \frac{M}{\rho} (\phi_u - \phi_e) \tag{3.30}$$

where $M = \rho a_u w_u$ is the mass flux of the strongest updraughts. It is assumed $a_u \ll 1$ while $\overline{w'\phi'_u}^u$ and $\overline{w'\phi'_e}^e$ are of same order of magnitude. This permit the first term on the RHS to be neglected and $\phi_e \simeq \overline{\phi}$. The second term on the RHS can be approximated by diffusion with a coefficient of K_ϕ. Then

$$\rho\overline{w'\phi'} = -\rho K_\phi \frac{\partial\overline{\phi}}{\partial z} + M(\phi_u - \overline{\phi}) \tag{3.31}$$

Equation (3.31) is the basic equation for vertical turbulent transport of ϕ and will be considered for the moist conserved variables of generalized liquid water static energy s_l and total water mass mixing ratio q_t.

The application of the EDMF approach to stratocumulus and dry boundary layers as used in the ECMWF model was developed by Köhler (2005) with details in (Tompkins *et al.*, 2004, chapter 5).

3.2.6 Mass flux component and plume model

The mass flux employs a single bulk plume model and is closed near the surface as a fraction of the tail of the vertical velocity distribution.

An air parcel is traced through its updraught to find cloud base, cloud/PBL top and the updraught properties. This is done with an entraining/detraining bulk plume model for the variables $\phi = \{s_l, q_t\}$ (e.g. Betts, 1973) and updraught kinetic energy $\frac{1}{2}w_u^2$ (Simpson and Wiggert, 1969)

$$\frac{\partial\phi_u}{\partial z} = -\epsilon(\phi_u - \overline{\phi}) \tag{3.32}$$

$$\frac{1}{2}\frac{\partial w_u^2}{\partial z} = -\epsilon(w_u^2 - \overline{w}^2) + g\frac{\theta_{v,u} - \overline{\theta_v}}{\overline{\theta_v}} \tag{3.33}$$

where ϵ is the fractional entrainment rate. The last term represents the buoyancy acceleration. The environmental kinetic energy $\frac{1}{2}\overline{w}^2$ can be neglected. The top of the boundary layer z_i (inversion height) is found when the vertical velocity drops to zero. z_i is interpolated between model levels. If condensation occurs, a cloud base height z_{cb} is defined, which is also interpolated between model layers.

The parcel is initialised by taking mean fields at the lowest model level z_n and adding an excess that scales with the surface fluxes (Troen and Mahrt, 1986), i.e. for variables $\phi = \{s_l, q_t\}$

$$\phi_u(z_n) = \overline{\phi(z_n)} + b\frac{\overline{w'\phi'}^{surf}}{\sigma_w(z_n)} \tag{3.34}$$

where surf refers to the surface mean and b is a parameter estimated as 1.0 based on LES experiments (Siebesma and Teixeira, 2000). For the standard deviation of vertical velocity σ_w an empirical expression based on atmospheric data, tank measurements and LES data is used (Holtslag and Moeng, 1991)

$$\sigma_w \simeq 1.2\left(u_*^3 + 1.5\kappa w_*^3\frac{z}{z_i}\right)^{1/3}\left(1 - \frac{z}{z_i}\right)^{1/2} = 1.2\left(u_*^3 + 1.5\kappa\frac{g}{\overline{\theta_v}^{surf}}\overline{w'\theta'_v}^{surf} z\right)^{1/3}\left(1 - \frac{z}{z_i}\right)^{1/2} \tag{3.35}$$

where $\kappa = 0.4$ is the Von Kármán's constant, $u_* \equiv (\overline{u'w'}^{surf2} + \overline{u'w'}^{surf2})^{1/4}$ is the friction velocity, and $w_* \equiv (z_i\frac{g}{\overline{\theta_v}^{surf}}\overline{w'\theta'_v}^{surf})^{1/3}$ is the free convective velocity scale. Because z_i is not known yet when the updraught properties are computed and since σ_w at the lowest model level is not very sensitive to z_i, the last term $(1 - \frac{z}{z_i})^{1/2}$ in equation (3.35) is neglected.

The parcel entrainment ϵ is written as

$$\epsilon = \frac{1}{w\tau_\epsilon} + c_\epsilon\frac{1}{z} \tag{3.36}$$

For the first term a mixing time scale τ_ϵ of 500 s has been selected (Siebesma, 1998; Cheinet, 2003, 2004). The second term represents the limiting of the length scale by the proximity of the surface and is inspired by the LES simulations by Siebesma and Teixeira (2000). They found that in the convective boundary

layer ϵ scales with $1/z$ near the surface with a factor c_ϵ equal to 0.55. Sensitivity experiments have shown that the second term is rather crucial as it has a big impact on the resulting boundary layer depths.

With the different height scales defined and the updraught properties known, it is still necessary to define the profiles of mass flux and diffusion coefficients. The mass flux M is directly calculated from the entrainment ϵ and the detrainment δ

$$\frac{\partial M}{\partial z} = (\epsilon - \delta) M. \tag{3.37}$$

M is initialised at the lowest level as $\rho a_\mathrm{u} \overline{w_\mathrm{u}}$, where a_u represents the updraught fraction in the surface layer. This is a free parameter in the parametrization that can be set to any fraction of the vertical velocity spectrum that one intends to parametrise with the mass flux. Here $a_\mathrm{u} = 0.05$. Assuming a Gaussian distribution of vertical velocities, the mean of the upper 5% tail of the distribution corresponds to a

$$\overline{w_\mathrm{u}}(a_\mathrm{u}, \sigma_\mathrm{w}) = b\sigma_\mathrm{w} \tag{3.38}$$

with $b = 2.05$. This $\overline{w_\mathrm{u}}(a_\mathrm{u}, \sigma_\mathrm{w})$ is also used to initialize the parcel. For simplicity, the temperature and moisture perturbations are assumed to be correlated with the vertical velocity perturbations. Therefore, the parameter b is also used in (3.34). Detrainment is set to $3 \cdot 10^{-4} m^{-1}$ above cloud base and zero below. This corresponds to a bulk plume model.

The updraught equation is integrated from the surface to the top using backward finite differences. All finite difference equations are written in conservative form.

3.2.7 Diffusion component

A first-order closure specifies the turbulent flux of a given quantity ϕ at a given model level proportional to the vertical gradient of that quantity. Therefore the diffusion component in the EDMF framework can be written as

$$J_\phi^K = \rho K_\phi \frac{\partial \phi}{\partial z}. \tag{3.39}$$

The exchange coefficients K_ϕ are estimated at half model levels. The computation of the exchange coefficients depends on the stability regimes (locally and at the surface) and on the vertical location above the surface. Fig. 3.1 summarizes the various areas where each scheme (EDMF with non-local K-profiles in the mixed layer, local diffusion dependent on the Richardson number following Louis et al, local diffusion with Monin–Obukhov functions) is applied.

In unstable surface conditions ($Q_{0\mathrm{v}} < 0$), the exchange coefficients are expressed as integral profiles for the entire convective mixed layer. This K-profile closure is based on the form proposed by Troen and Mahrt (1986). This approach is more suitable than the local diffusion one when the length scale of the largest transporting turbulent eddies have a similar size as the boundary layer height itself (unstable and convective conditions). It also allows for an explicit entrainment parametrization in the capping inversion (Beljaars and Viterbo, 1999). Eddy-diffusion coefficients are the sum of a surface and cloud top driven K-profile, which are overwritten with an explicit BL top entrainment. For the surface driven diffusion a simple K-profile is specified, similar to the previous dry scheme (Troen and Mahrt, 1986; Holtslag, 1998)

$$\begin{aligned} K_\mathrm{H}^\mathrm{sfc} &= \kappa u_* \Phi_\mathrm{H0}^{-1} \left(1 - \frac{z}{z_\mathrm{i}}\right)^2 \\ K_\mathrm{M}^\mathrm{sfc} &= \kappa u_* \Phi_\mathrm{M0}^{-1} \left(1 - \frac{z}{z_\mathrm{i}}\right)^2 \end{aligned} \tag{3.40}$$

where Φ_{H0} and Φ_{M0} are stability functions given by

$$\begin{aligned} \Phi_\mathrm{H0} &= \left(1 - 39\frac{z}{\mathcal{L}}\right)^{-1/3} \\ \Phi_\mathrm{M0} &= \left(1 - 15\frac{z}{\mathcal{L}}\right)^{-1/3} \end{aligned} \tag{3.41}$$

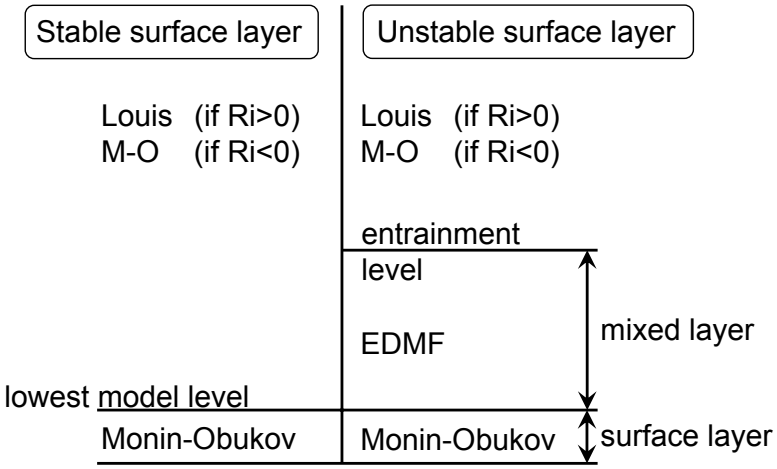

Figure 3.1 *Schematic diagram of the different boundary layer regimes.*

and $\mathcal{L} = -u_*^3(\kappa \overline{w'\theta'_{\rm v}} g/\theta_{\rm v})^{-1}$ is the Obukhov length. Cloud top driven diffusion is described after Lock *et al.* (2000) as

$$K_{\rm H}^{\rm top} = 0.85\kappa v_{\rm cld} \frac{z - z_{\rm mb}}{z_{\rm i} - z_{\rm mb}} \left(1 - \frac{z - z_{\rm mb}}{z_{\rm i} - z_{\rm mb}}\right)^{1/2} \tag{3.42}$$

where $z_{\rm i}$ is the inversion height or cloud top and $z_{\rm mb}$ is the level below cloud base to which the top driven mixing extends. A value of $z_{\rm mb} = 0$ is assumed, implying a strong coupling between the cloud layer and the sub-cloud layer. Parameter $v_{\rm cld}$ represents a top entrainment velocity scale encompassing a radiative cooling and a buoyancy reversal term

$$v_{\rm cld}^3 = v_{\rm rad}^3 + v_{\rm br}^3 \tag{3.43}$$

The buoyancy reversal term is neglected and the radiation term is written as

$$v_{\rm rad}^3 = \frac{g}{\theta_0} z_{\rm i} \Delta R/(\rho c_p) \tag{3.44}$$

after Lock (1998), where ΔR is the radiative flux jump at cloud top.

Boundary layer top entrainment at $z = z_{\rm i}$ is explicitely specified from surface and cloud top driven components

$$\begin{aligned} \overline{w'\theta'_{\rm v}}^{\rm entr} &= -0.2\overline{w'\theta'_{\rm v}}^{\rm s} - 0.2\triangle R/(\rho c_p) = -K_{\rm H}^{\rm e}\frac{\partial \theta_{\rm v}}{\partial z} \approx -K_{\rm H}^{\rm e}\frac{\Delta\theta_{\rm v}}{\Delta z} \equiv w_{\rm e}\Delta\theta_{\rm v}, \text{ with} \\ (\Delta\theta_{\rm v})_{k+1/2} &= \frac{1}{c_{p_{\rm dry}}}\{s_k - s_{k+1} - 0.5(\delta - \varepsilon)(q_k - q_{k+1})(s_k + s_{k+1})\} \end{aligned} \tag{3.45}$$

and $w_{\rm e}$ representing the top entrainment velocity.

For both top driven and entrainment diffusion coefficients the turbulent Prantl number is $Pr = K_{\rm M}/K_{\rm H} = 0.75$:

$$\begin{aligned} K_{\rm M}^{\rm top} &= 0.75 K_{\rm H}^{\rm top} \\ K_{\rm M}^{\rm e} &= 0.75 K_{\rm H}^{\rm e} \end{aligned} \tag{3.46}$$

Within the PBL the total diffusion coefficient for s_l and $q_{\rm t}$ is specified as

$$K_{\rm H} = K_{\rm H}^{\rm sfc} + K_{\rm H}^{\rm top} \tag{3.47}$$

while at the top of the PBL

$$K_{\rm H} = max(K_{\rm H}^{\rm sfc} + K_{\rm H}^{\rm top}, K_{\rm H}^{\rm e}) \tag{3.48}$$

is used.

3.2.8 Cloud

In order to provide coupling of the boundary layer scheme to the cloud scheme, the variance of total water is computed from the following equation (Deardorff, 1974)

$$\frac{\partial \sigma_{\rm qt}^2}{\partial t} = -2\overline{w'q_{\rm t}'}\frac{\partial q_{\rm t}}{\partial z} - \frac{\partial\left(\overline{w'\sigma_{\rm qt}^{2'}}\right)}{\partial z} - \frac{\sigma_{\rm qt}^2}{\tau_{\sigma{\rm qt}}} \tag{3.49}$$

The first term is the generation term in the presence of a vertical $q_{\rm t}$ gradient, the second term represents transport which is neglected and the third term is the decay term. The associated decay time scale is written as

$$\tau_{\sigma{\rm qt}} = \frac{z_{\rm i}}{\overline{w_{\rm u}}^{\rm PBL}} \tag{3.50}$$

where the updraught velocity $\overline{w_{\rm u}}^{\rm PBL}$ is averaged over the height of the boundary layer $z_{\rm i}$.

The change in total water and total water variance needs to be transformed into the Tiedtke (1993) cloud scheme's prognostic variables of cloud water and cloud cover. At the beginning of the boundary layer parametrization time step, the model variables, $q_{\rm v}$, q_l, $q_{\rm i}$, T, and $f_{\rm c}$ (cloud cover), are converted to $q_{\rm t}$, q_l, and $\sigma_{\rm qt}(q_{\rm v}, q_l + q_{\rm i}, q_{\rm sat}(T))$, assuming a Beta distribution as used by Tompkins (2002). The variance of the total water $\sigma_{\rm qt}$ is diagnosed that gives the specified liquid water and cloud cover. Then, (3.49) is integrated for one time step and the total water distribution function is used to diagnose the equivalent change in cloud cover and cloud water/ice. The differences between cloud variables before and after the time step are then used as a tendency (from boundary layer processes) for the cloud scheme.

3.2.9 Boundary layer types and their distinction

Distinguishing between cumulus and well-mixed stratocumulus is a crucial component of the system. For the stratocumulus regime, shallow convection is turned off, while for the cumulus regime the BL top is set to the cloud base and the BL mass-flux is turned off. Klein and Hartmann (1993) showed empirically that the stratus cloud cover increases with the static stability of the atmosphere defined as $\theta_{700{\rm hPa}} - \theta_{\rm sfc}$. This criterion is adopted for distinguishing between stratocumulus and shallow convection. It provides a very robust diagnostic of the observed stratocumulus regions. A threshold of 20 K is used, which corresponds to a seasonally averaged stratocumulus cloud cover of 60% according to their data.

3.3 THE EXCHANGE COEFFICIENTS ABOVE THE SURFACE AND MIXED LAYER

3.3.1 General

Above the surface and mixed layers the turbulent transports are determined based on local stability (see Fig. 3.1). First, the local Richardson number is computed in each vertical layer using

$$\begin{aligned} |\Delta U|^2_{k+1/2} &= (u_k - u_{k+1})^2 + (v_k - v_{k+1})^2 \\ \left(\frac{\Delta s_{\rm v}}{c_p T}\right)_{k+1/2} &= \frac{2(s_k - s_{k+1})}{(s_k - gz_k + s_{k+1} - gz_{k+1})} + \varepsilon(q_k - q_{k+1}) \\ Ri_{k+1/2} &= (gz_k - gz_{k+1})\frac{\{(\Delta s_{\rm v})/(c_p T)\}_{k+1/2}}{|\Delta U|^2_{k+1/2}} \end{aligned} \tag{3.51}$$

Given the value of Ri, in stable local conditions the stability parameter $\zeta = z/\mathcal{L}$ is deduced from precomputed tables giving $\zeta = \zeta(Ri)$. A cubic spline interpolation is performed (Press *et al.*, 1992, pp 107–111). In unstable local conditions, we simply set $\zeta = Ri$.

3.3.2 The exchange coefficients

(*a*) *Turbulence length scale*

The mixing lengths $l = \kappa z$ used in the surface layer is bounded in the outer layer by introducing an asymptotic length scale λ (Blackadar, 1962) given by

$$\frac{1}{l} = \frac{1}{\kappa z} + \frac{1}{\lambda}. \tag{3.52}$$

The underlying idea is that vertical extent of the boundary layer limits the turbulence length scale. Since the results in the boundary layer are not very sensitive to the exact value of the asymptotic length scales, this parameter is chosen to be a constant. The value used is $\lambda = 150$ m.

(*b*) *M–O similarity with* $Ri < 0$

In this regime, the exchange coefficients K_ϕ are based on local similarity (Nieuwstadt, 1984) stating that the expressions of the surface layer similarity can be used in the outer layer (strictly speaking only valid for stable conditions):

$$\begin{aligned} K_{\mathrm{M}} &= \frac{l_{\mathrm{M}}^2}{\Phi_{\mathrm{M}}^2} \cdot \left|\frac{\partial U}{\partial z}\right| \\ K_{\mathrm{H}} &= \frac{l_{\mathrm{H}}^2}{\Phi_{\mathrm{M}}\Phi_{\mathrm{H}}} \left|\frac{\partial U}{\partial z}\right| \end{aligned} \tag{3.53}$$

with Φ_{M} and Φ_{H} specified in (3.19). Here it is used for the unstable regime above the boundary layer, basically to provide strong vertical mixing in statically unstable situations.

(*c*) *Revised Louis scheme for* $Ri > 0$

The use of (3.53) to define the exchange coefficients in the stable regime close to the surface was found to be detrimental to the scores of the model (Beljaars, 1995) because of insufficient turbulent exchange in the lower troposphere. Therefore enhanced diffusion coefficients according to the Louis, Tiedtke, Geleyn scheme (Louis *et al.*, 1982), revised by (Beljaars, 1995; Beljaars and Viterbo, 1999; Viterbo *et al.*, 1999) are used close to the surface and M-O similarity as in (3.53) above. To achieve this interpolation the term lf^2, a combination of length scale l and Ri functionality $f(Ri)$, is treated in the equation of the diffusion coefficient

$$K = \left|\frac{\partial U}{\partial z}\right| l^2 f(Ri) \tag{3.54}$$

as follows:

$$\frac{1}{l\sqrt{f(Ri)}} = \frac{1}{\kappa z\sqrt{f_{LTG}(Ri)}} + \frac{1}{\lambda\sqrt{f_{MO}(Ri)}} \tag{3.55}$$

This combined formulation allows a continuous transition between the LTG coefficients $f_{LTG}(Ri)$ near the surface to about $z = \lambda/\kappa = 375m$ (for $f_{LTG}(Ri) = f_{MO}(Ri)$) and MO coefficients $f_{MO}(Ri)$ above. The LTG functional dependencies with Ri for momentum $f_{\mathrm{LTG,M}}$ and heat/moisture $f_{\mathrm{LTG,H}}$ are

$$\begin{aligned} f_{\mathrm{LTG,M}}(Ri) &= \frac{1}{1 + 2bRi(1 + dRi)^{-1/2}} \\ f_{\mathrm{LTG,H}}(Ri) &= \frac{1}{1 + 2bRi(1 + dRi)^{1/2}} \end{aligned} \tag{3.56}$$

with $b = 5$ and $d = 1$ (these functions are revised versions of the Louis *et al.*, 1982 functions and were introduced in September 1995 in order to enhance turbulent transport in stable layers, see Viterbo *et al.*, 1999).

3.4 TREATMENT OF UNRESOLVED SHEAR IN THE DIFFUSION EQUATION

A vertical shear power spectrum analysis of Cabauw tower observations (temporal) and IFS experiments at resolutions from T159 to T2047 (spatial) indicates up to 20% of the shear power missing due to unresolved scales as well as damping at scales close to truncation. From the IFS resolution study it can be concluded that the peak missing shear is at around 1 km height, a typical value of boundary layer height. The impact of this missing shear is empirically parametrized as an added shear in the diffusion equation including the Richardson number (see Section 3.3)

$$\left.\frac{\partial U}{\partial z}\right|_K = \left.\frac{\partial U}{\partial z}\right|_{resolved} + a(p)\, b. \tag{3.57}$$

with the peak amplitude b set to a value of 0.5 m/s per 100 m depth. The normalized profile is written as

$$a = 27.2\, x\, e^{-10x}, \tag{3.58}$$

with $x = \left(1 - \frac{p}{p_s}\right)$ to vanish at the surface and top of atmosphere and peak at about 900 hPa with a value of 1.0.

3.5 TURBULENT OROGRAPHIC FORM DRAG (TOFD)

With the introduction of CY31R1, the orographic contribution to the aerodynamic roughness length has been replaced by an explicit specification of stress on model levels due to turbulent orographic form drag (TOFD). The TOFD scheme is based on the work of Wood and Mason (1993) in which the orographic surface drag is parametrized for sinusoidal hills and on the suggestion by Wood *et al.* (2001) to distribute this drag explicitly in the vertical. It is further inspired by the notion that fine scale data sets with sufficient horizontal resolution to compute slope or silhouette parameters on a global scale, are not available. The TOFD scheme, as described in detail by Beljaars *et al.* (2004b), has three key aspects.

First,the orographic spectrum is parametrized and the effect of all the scales is obtained by integrating over the spectrum (5 km down to 10 m). The standard deviation of filtered orography σ_{flt} is used as input for the scheme. It is defined in such a way that it can be measured from the available data at 1 km resolution (see appendix describing the climatological fields).

Secondly, the total drag is represented as a spectral integral over all wave numbers contributing to the variance of the slope. Drag, due to small horizontal orography scales is distributed over a shallow layer, whereas large scales affect deep layers. Convergence problems associated with the variance of the slope when computed as the integral over the spectrum, have been alleviated by including the wind forcing level in the spectral integral. Physically, it means that smaller horizontal scales have a wind forcing at a lower level than the large horizontal scales.

Thirdly, simplifications are applied to avoid explicit evaluation of the integral over the orographic spectrum. For numerical stability it is also necessary to have an implicit formulation that can be solved as part of the vertical diffusion tridiagonal solver.

The parametrization results in the following additional tendency (stress divergence) in the equations for the horizontal wind vector $\vec{U}$

$$\frac{\partial}{\partial z}\vec{\tau}_o/\rho = -2\alpha_{\rm tofd}\,\beta_{\rm tofd}\,C_{\rm md}C_{\rm corr}\,|\vec{U}(z)|\vec{U}(z)\int_{k_o}^{k_\infty}\frac{k^2}{l_{\rm w}}F_o(k)\,e^{-z/l_{\rm w}}dk \tag{3.59}$$

with

$$
\begin{aligned}
l_{\rm w} &= \min(2/k, 2/k_1), \\
F_o(k) &= a_1 k^{n_1}\ , \text{ for } k_o < k < k_1, \\
F_o(k) &= a_2 k^{n_2}\ , \text{ for } k_1 < k < k_\infty, \\
n_1 &= -1.9\ , & n_2 &= -2.8, \\
a_1 &= \sigma_{\rm flt}^2 (I_H k_{\rm flt}^{n_1})^{-1}\ , & a_2 &= a_1 k_1^{n1-n2}, \\
k_o &= 0.000628\ {\rm m}^{-1}\ , & k_1 &= 0.003\ {\rm m}^{-1}, \\
k_{\rm flt} &= 0.00035\ {\rm m}^{-1}\ , & k_\infty &= 2\pi c_{\rm m}/z_o, \\
I_{\rm H} &= 0.00102\ {\rm m}^{-1}\ , & c_{\rm m} &= 0.1, \\
\alpha_{\rm tofd} &= 27\ , & \beta_{\rm tofd} &= 1, \\
C_{\rm md} &= 0.005\ , & C_{\rm corr} &= 0.6.
\end{aligned}
\tag{3.60}
$$

The parameter $\alpha_{\rm tofd}$ was determined from LES data as 12. But during extensive testing an optimal value of $12(1.5)^2 = 27$ was determined that reflects a 50% increase in the standard deviation of filtered orography $\sigma_{\rm flt}$. Spectrum $F_o(k)$ of the sub-grid orography is represented with empirical power laws (power n_1 and n_2) in two different scale ranges. The integral of the right hand side of (3.59) can be pre-computed for different heights, without giving a computational burden. However, with hybrid vertical coordinates (as in the ECMWF model), model level heights vary with surface pressure, and therefore it is more convenient to have an analytical expression. A good approximation of (3.59) is

$$
\frac{\partial \vec{U}}{\partial t} = \frac{\partial}{\partial z}\vec{\tau}_{\rm xo}/\rho = -\alpha_{\rm tofd}\ \beta_{\rm tofd}\ C_{\rm md} C_{\rm corr}\ |\vec{U}(z)|\vec{U}(z)\ 2.109\ e^{-(z/1500)^{1.5}} a_2 z^{-1.2}
\tag{3.61}
$$

The use of (3.61) rather than (3.59) gives virtually identical results in single column simulations.

The two components of the stress divergence are included in the momentum equations and solved together with the turbulent transport equations. An implicit formulation is needed for stability. The standard way of time stepping a non-linear problem with implicit equations is by evaluating the non-linear part at the old time level and keeping the linear part for the new time level. In this case it means that the absolute wind speed $|U|$ is taken from the old time level and that the $U(z)$ and $V(z)$ components are evaluated implicitly.

With (3.61), and the constants in (3.60), the entire parametrization depends on a single geographical parameter namely the standard deviation of the filtered orography $\sigma_{\rm flt}$. Equation (3.61) is written as

$$
\begin{aligned}
\frac{\partial \vec{U}}{\partial t} &= -C_{\rm tofd}|\vec{U}(z)|\vec{U}(z)\ , \\
C_{\rm tofd} &= -\alpha_{\rm tofd}\ \beta_{\rm tofd}\ C_{\rm md} C_{\rm corr}\ 2.109\ e^{-(z/1500)^{1.5}} a_2 z^{-1.2}
\end{aligned}
\tag{3.62}
$$

The expression in (3.62) is computed in subroutine VDFTOFDC. Output $C^*_{\rm tofd} = C_{\rm tofd}\alpha\Delta t|\vec{U}(z)|$ is passed to the implicit solver in VDFDIFM.

3.6 SOLUTION OF THE EDMF EQUATIONS

The equations for turbulent transfer are solved simultaneously for diffusion, mass fluxes, TOFD, the implicit and explicit terms from the sub-grid orography scheme ($\beta_{\rm so}\phi$ and $\alpha_{\rm so}$), and the tendencies from the adiabatic (subscript 'dyn') and radiative processes (subscript 'rad') as source terms in the right-hand side:

$$
\frac{\partial \phi}{\partial t} = -g\frac{\partial J_\phi}{\partial p} - C_{\rm tofd}|\vec{U}|\phi - \beta_{\rm so}\phi + \alpha_{\rm so} + \left.\frac{\partial \phi}{\partial t}\right|_{\rm dyn} + \left.\frac{\partial \phi}{\partial t}\right|_{\rm rad}
\tag{3.63}
$$

Flux J_ϕ (defined down-ward) has a diffusive part and a massflux term:

$$
J_\phi = \rho K \frac{\partial \phi}{\partial z} - M(\phi_{\rm u} - \phi)
\tag{3.64}
$$

Since the thickness of the model layers Δz is small near the ground and the time step is long, the time-stepping procedure must be implicit in order to avoid numerical instability ($K\Delta t/(\Delta z)^2 > 1$). The advantage of doing the implicit computation with as many processes as possible in a single equation (3.63) is to maintain balance between processes which avoids time step dependence for long time steps. (Beljaars, 1991, Janssen *et al.*, 1992, Beljaars *et al.*, 2004a). Several time discretizations including explicit and implicit solutions can be written by defining a general time level $\hat{\phi}$ and the implicitness factor α.

$$\hat{\phi} \equiv \alpha\phi^{t+1} + (1-\alpha)\phi^{t} \tag{3.65}$$

For $\alpha = 0$ the scheme is explicit, for $\alpha = 0.5$ we have a Crank–Nicholson and for $\alpha = 1$ we have an implicit backward scheme. In the model, $\alpha = 1.5$, to avoid non-linear instability from the K-coefficients. The diffusion coefficients, mass fluxes and other coefficients are computed from the mean variables at $t-1$ making them explicit. The time tendency can then be written as

$$\frac{\partial\phi}{\partial t} = \frac{\phi^{t+1}-\phi^{t}}{\triangle t} = \frac{\hat{\phi}-\phi^{t}}{\alpha\triangle t} = f(\hat{\phi}) + g(\phi^{t}) \tag{3.66}$$

with implicit terms $f(\hat{\phi})$ and explicit terms $g(\phi^t)$. Equation (3.63) is written in discrete form for $1 < k < n$ using upwind differencing in the mass-flux term:

$$\begin{aligned}\frac{\hat{\phi}-\phi^{t}}{\alpha\triangle t} = \frac{\Delta\phi_{\rm dyn}}{\triangle t} + \frac{\Delta\phi_{\rm rad}}{\triangle t} \; &- C_{\rm tofd}|\vec{U}|\hat{\phi}_k - \beta_{\rm so}\hat{\phi}_k + \alpha_{\rm so} \\ &+\frac{g}{\triangle p_k}\Big(\rho_{k-\frac{1}{2}}K_{k-\frac{1}{2}}\frac{\hat{\phi}_{k-1}-\hat{\phi}_k}{\triangle z_{k-\frac{1}{2}}} + M_{k-1}\big(\phi_{u,k-1}-\hat{\phi}_{k-1}\big) \\ &-\rho_{k+\frac{1}{2}}K_{k+\frac{1}{2}}\frac{\hat{\phi}_k-\hat{\phi}_{k+1}}{\triangle z_{k+\frac{1}{2}}} - M_k\big(\phi_{u,k}-\hat{\phi}_k\big)\Big)\end{aligned} \tag{3.67}$$

with $\triangle z_{k+\frac{1}{2}} = z_k - z_{k+1}$ and $\triangle p_k = p_{k+\frac{1}{2}} - p_{k-\frac{1}{2}}$. This can be rewritten as

$$\frac{\hat{\phi}_{k-1}}{\alpha}A + \frac{\hat{\phi}_k}{\alpha}B + \frac{\hat{\phi}_{k+1}}{\alpha}C = RHS \tag{3.68}$$

$$\begin{aligned}A &= \frac{1}{\triangle p_k}\Big(-K^*_{k-\frac{1}{2}} + M^*_{k-1}\Big) \\ B &= \frac{1}{\triangle p_k}\Big(+K^*_{k-\frac{1}{2}} + K^*_{k+\frac{1}{2}} - M^*_k\Big) + 1 + C_{\rm tofd}|\vec{U}|\alpha\Delta t + \beta_{\rm so}\alpha\Delta t \\ C &= \frac{1}{\triangle p_k}\Big(-K^*_{k+\frac{1}{2}}\Big) \\ RHS &= \frac{\phi^t_k}{\alpha} + \frac{1}{\triangle p_k}M^*_{k-1}\frac{\phi_{u,k-1}}{\alpha} - \frac{1}{\triangle p_k}M^*_k\frac{\phi_{u,k}}{\alpha} + \Delta\phi_{\rm dyn} + \Delta\phi_{\rm rad} + \alpha_{\rm so}\Delta t\end{aligned}$$

leading to the inversion of a tridiagonal matrix to solve for $\hat{\phi}/\alpha$. The coefficients K and M area rescaled for convenience as $K^*_{k+1/2} = K_{k+1/2}\alpha\rho_{k+1/2}\big(\frac{g\Delta t}{\Delta z_{k+1/2}}\big)$ and $M^* = Mg\alpha\Delta t$.

At the lowest level ($k = n$) equation (3.68) is modified to include the surface fluxes which are obtained in the surface energy balance routine by averaging over $N_{\rm T}$ tiles:

$$\begin{aligned}A &= \frac{1}{\triangle p_n}\Big(-K^*_{n-\frac{1}{2}} + M^*_{n-1}\Big) \\ B &= \frac{1}{\triangle p_n}\Big(+K^*_{n-\frac{1}{2}} - M^*_n\Big) + 1 + C_{\rm tofd}|\vec{U}|\alpha\Delta t + \beta_{\rm so}\alpha\Delta t \\ C &= 0 \\ RHS &= \frac{\phi^t_n}{\alpha} + \frac{1}{\triangle p_n}M^*_{n-1}\frac{\phi_{u,n-1}}{\alpha} - \frac{1}{\triangle p_n}M^*_n\frac{\phi_{u,n}}{\alpha} + \Delta\phi_{\rm dyn} + \Delta\phi_{\rm rad} + \alpha_{\rm so}\Delta t - \frac{g\Delta t}{\Delta p_n}\bar{J}_\phi\end{aligned} \tag{3.69}$$

where the surface flux is a weighted average over the tiles

$$\frac{g}{\Delta p_n}\bar{J}_\phi = +\sum_{i=1}^{N_{\rm T}} F_i\frac{C^*_{\phi i}}{\alpha\Delta p_n}\{A_{ni}\hat{\phi}_n - A_{{\rm surf}i}\hat{\phi}_{{\rm surf}i}\} \tag{3.70}$$

with $C^*_{\phi i} = C^{t-1}_{\phi i}|U_n|\mathrm{g}\rho\alpha\Delta t$ and

$$\begin{array}{llll} \phi = 0 & A_n = 1 & A_{\mathrm{surf}} = 1 & N_{\mathrm{T}} = 1 \text{ for } \phi = \mathrm{u, v} \\ \phi_{\mathrm{surf}i} = s_{\mathrm{skin}i} & A_{ni} = 1 & A_{\mathrm{surf}i} = 1 & N_{\mathrm{T}} = 8 \text{ for } \phi = \mathrm{s} \\ \phi_{\mathrm{surf}i} = q_{\mathrm{sat}}(T_{\mathrm{skin}i}) & A_{ni} = \alpha_{ni} & A_{\mathrm{surf}i} = \alpha_{\mathrm{surf}i} & N_{\mathrm{T}} = 8 \text{ for } \phi = \mathrm{q} \end{array} \tag{3.71}$$

The downward elimination of the tridiagonal matrix results in linear relations between the lowest model level dry static energy and specific humidity and their fluxes

$$\begin{aligned} \hat{s}_n &= A_{\mathrm{s}}\bar{J}_{\mathrm{s}} + B_{\mathrm{s}} \\ \hat{q}_n &= A_{\mathrm{q}}\bar{J}_{\mathrm{q}} + B_{\mathrm{q}} \end{aligned} \tag{3.72}$$

Coefficients (A's and B's) are passed to the surface energy balance computation for the different tiles, and the resulting weighted fluxes are returned to the tridiagonal solver for upward back-substitution (see Section 3.7).

At the top of the atmosphere ($k = 1$) turbulent fluxes are set to zero resulting in a modification of equation (3.68) as

$$\begin{aligned} A &= 0 \\ B &= \frac{1}{\triangle p_1}\left(K^*_{1+\frac{1}{2}} - M^*_1\right) + 1 + C_{\mathrm{tofd}}|\vec{U}|\alpha\Delta t + \beta_{\mathrm{so}}\alpha\Delta t \\ C &= \frac{1}{\triangle p_1}\left(-K^*_{1+\frac{1}{2}}\right) \\ RHS &= \frac{\phi^t_1}{\alpha} - \frac{1}{\triangle p_1}M^*_1\frac{\phi_{u,1}}{\alpha} + \Delta\phi_{\mathrm{dyn}} + \Delta\phi_{\mathrm{rad}} + \alpha_{\mathrm{so}}\Delta t \end{aligned} \tag{3.73}$$

The tridiagonal matrix equation is solved by a downward elimination scan followed by back substitution in an upward scan (Press *et al.*, 1992, pp 42–43).

To safeguard against instabilities for the mass-flux term a relaxed CFL criteria for M is enforced:

$$M < f\rho\frac{\triangle z}{\triangle t} \tag{3.74}$$

As there is no strict stability analysis available for the EDMF equations, the factor f=2 is determined by experimentation.

3.7 THE SURFACE ENERGY BALANCE

The surface energy balance is satisfied independently for each tile by calculating its skin temperature. The skin layer represents the vegetation layer, the top layer of the bare soil, or the top layer of the snow pack, has no heat capacity and therefore responds instantaneously to changes in, e.g. radiative forcing. In order to calculate the skin temperature, the surface energy balance equation is linearized for each tile leading to an expression for the skin temperature. This procedure is equivalent to the Penmann–Monteith approach which can be derived by eliminating the skin temperature from the surface energy balance equation assuming that the net radiation minus ground heat flux is known (e.g. Brutsaert, 1982). The approach followed here is an extension to the Penmann–Monteith derivation in the sense that it allows for coupling with the underlying soil (or snow, ice). Because of the short time scale associated with the skin layer, the equation for its temperature is solved implicitly together with the vertical turbulent transport in the boundary layer. In a fully implicit approach, the skin temperatures depend on each other and can not be solved independently. We follow the approach suggested by Best *et al.* (2004) which allows for such a solution. The coupling strategy of Best *et al.* (2004) also provides a well defined (universal) interface between atmosphere and land surface models, making it possible to have a stand alone library of the land surface code.

The following general discussion applies to each tile but the parameters are tile dependent as discussed in the land surface part of the documentation (Chapter 8). The surface energy balance equation can be

written as:

$$\mathfrak{R}_{\rm SW} + \mathfrak{R}_{\rm LW} + H + LJ_q = \Lambda_{\rm skin}(T_{\rm sk} - T_{\rm s}) \tag{3.75}$$

where $\mathfrak{R}_{\rm SW}$ and $\mathfrak{R}_{\rm LW}$ are the net short-wave and long-wave radiation fluxes at the surface and the right-hand side represents the ground heat flux through coupling with the underlying soil, snow or ice with temperature T_s. The turbulent sensible and latent heat fluxes are

$$H = J_{\rm s} \tag{3.76}$$

$$J_{\rm s} = \rho C_{\rm H}|U_n|\{s_n - s_{\rm sk}\} \tag{3.77}$$

$$J_{\rm q} = \rho C_{\rm Q}|U_n|\{\alpha_n q_n - \alpha_{\rm surf} q_{\rm sat}(T_{\rm sk})\} \tag{3.78}$$

The equations for $J_{\rm s}$ and $J_{\rm q}$ are linearized

$$J_{\rm s} = \rho C_{\rm H}|U_n|\{(\hat{s}_n - \hat{s}_{\rm sk}) \tag{3.79}$$

$$J_{\rm q} = \rho C_{\rm Q}|U_n|\left\{\alpha_n \hat{q}_n - \alpha_s q_{\rm sat}(T^t_{\rm sk}) - \alpha_s \frac{dq_{\rm sat}}{dT}\left(\frac{\hat{s}_{\rm sk}}{c^t_p} - T^t_{\rm sk}\right)\right\} \tag{3.80}$$

and written as

$$\begin{aligned} J_{\rm s} &= C_{Js1}S_n + C_{Js2}q_n + C_{Js3}S_{\rm sk} + C_{Js4} \\ J_{\rm q} &= C_{Jq1}S_n + C_{Jq2}q_n + C_{Jq3}S_{\rm sk} + C_{Jq4} \end{aligned} \tag{3.81}$$

with coefficients

$$\begin{aligned} C_{Js1} &= \rho C_{\rm H}|U_n|\,, & C_{Jq1} &= 0 \\ C_{Js2} &= 0\,, & C_{Jq2} &= \rho C_{\rm Q}|U_n|\alpha_n \\ C_{Js3} &= -\rho C_{\rm H}|U_n|\,, & C_{Jq3} &= \rho C_{\rm Q}|U_n|\alpha_s \tfrac{dq_{\rm sat}}{dT} c_p^{-1}\,, \\ C_{Js4} &= 0\,, & C_{Jq4} &= -\rho C_{\rm Q}|U_n|\alpha_s(q_{\rm sat}(T^t_{\rm sk}) - \tfrac{dq_{\rm sat}}{dT}T^t_{\rm sk}) \end{aligned}$$

Substitution of the expression for dry static energy and moisture fluxes in the surface energy balance equation, and linearization of the long wave radiation leads to the following expressions

$$\mathfrak{R}_{\rm SW} + \mathfrak{R}_{\rm LW} + J_{\rm s} + LJ_{\rm q} = \Lambda_{\rm skin}(\hat{T}_{\rm sk} - T_{\rm s}) \tag{3.82}$$

$$\begin{aligned} R_{\rm SW} + R^{\rm trad}_{\rm LW} + \frac{dR_{\rm LW}}{dT_{\rm sk}}(\hat{s}_{\rm sk}/c^t_p - T^{\rm trad}_{\rm sk}) + C_{Js1}\hat{s}_n + C_{Js3}\hat{s}_{\rm sk} + +L(C_{Jq2}\hat{q}_n + C_{Jq3}\hat{s}_{\rm sk} + C_{Jq4}) \\ = \Lambda_{\rm sk}(\hat{T}_{\rm sk} - T_{\rm s}) \end{aligned} \tag{3.83}$$

which is written in the following form

$$\hat{s}_{\rm sk} = D_{ss1}\hat{s}_n + D_{ss2}\hat{q}_n + D_{ss4} \tag{3.84}$$

The coefficients are (using $\hat{s}_{\rm sk} = c^t_p \hat{T}_{\rm sk}$)

$$\begin{aligned} D_{ss1} &= -C_{Js1}Z^{-1} \\ D_{ss2} &= -C_{Jq2}LZ^{-1} \\ D_{ss4} &= (-R_{\rm SW} - R^{-\rm trad}_{\rm LW} + \frac{dR_{\rm LW}}{dT_{\rm sk}}T^{\rm trad}_{\rm sk} - LC_{Jq4} - \Lambda_{\rm sk}T_{\rm s})Z^{-1} \\ Z &= (\frac{dR_{\rm LW}}{dT_{\rm sk}} - \Lambda_{\rm sk})c_p^{-1} + C_{Js3} + LC_{Jq3} \end{aligned} \tag{3.85}$$

With (3.83), $\hat{s}_{\rm sk}$ can be eliminated and the flux equations can be written in the following form.

$$\begin{aligned} J_{\rm s} &= D_{Js1}\hat{s}_n + D_{Js2}\hat{q}_n + D_{Js4} \\ J_{\rm q} &= D_{Jq1}\hat{s}_n + D_{Jq2}\hat{q}_n + D_{Jq4} \end{aligned} \tag{3.86}$$

with

$$\begin{aligned} D_{Js1} &= C_{Js1} + C_{Js3}D_{ss1}\,, & D_{Jq1} &= C_{Jq1} + C_{Jq3}D_{ss1} \\ D_{Js2} &= C_{Js2} + C_{Js3}D_{ss2}\,, & D_{Jq2} &= C_{Jq2} + C_{Jq3}D_{ss2} \\ D_{Js4} &= C_{Js3}D_{ss4} + C_{Js4}\,, & D_{Jq4} &= C_{Jq3}D_{ss4} + C_{Jq4} \end{aligned}$$

With equation (3.86), a linear expression of fluxes is available in terms of lowest model level variables. The grid box average can be obtained by taking the weighted average of the coefficients over the tiles.

$$\begin{aligned}\bar{J}_{\mathrm{s}} &= \hat{s}_n \sum_i Fr^i D^i_{Js1} + \hat{q}_n \sum_i Fr^i D^i_{Js2} + \sum_i Fr^i D^i_{Js4}\,,\\ \bar{J}_{\mathrm{q}} &= \hat{s}_n \sum_i Fr^i D^i_{Jq1} + \hat{q}_n \sum_i Fr^i D^i_{Jq2} + \sum_i Fr^i D^i_{Jq4}\,.\end{aligned} \tag{3.87}$$

The over-bar indicates the grid box average of the fluxes. Equation (3.87) can be written as

$$\begin{aligned}\bar{J}_s &= E_{Js1}\hat{s}_n + E_{Js2}\hat{q}_n + E_{Js4}\,,\\ \bar{J}_q &= E_{Jq1}\hat{s}_n + E_{Jq2}\hat{q}_n + E_{Jq4}\,.\end{aligned} \tag{3.88}$$

where the E-coefficients are the grid box averages of the D-coefficients. After the downward elimination of the tridiagonal solver of the vertical turbulent transport a linear relation exists between the lowest model level $\hat{s}_n$, $\hat{q}_n$ and the surface fluxes in the form of equation (3.72).

Together with equation (3.88) it is straightforward to solve for $\bar{J}_{\mathrm{s}}$,$\bar{J}_{\mathrm{q}}$, $\hat{s}_n$, and $\hat{q}_n$. With the latter two, back substitution can be started in an upward scan of the vertical turbulent transport equation.

With the lowest model level dry static energy and specific humidity known, it is also possible to solve for all the tile dependent fluxes and skin temperatures using (3.85) and (3.86).

3.8 TRACER DIFFUSION

Tracers are diffused in the same way as heat and moisture, but no mass flux term is used. The surface boundary condition consists of an externally specified flux. The implicitness factor is set to 1, because a higher value is not necessary for stability. As for momentum, heat and moisture the implicit solver uses the dynamics term as source terms to obtain balance and small time step dependence for long time steps. It can be demonstrated that implicitness factors larger than 1 can lead to negative tracer concentrations due to the combination with the dynamics source term.

3.9 TENDENCY CALCULATIONS AND ENERGY DISSIPATION

Total tendencies for wind and total water after the vertical transport (including diffusion and mass-flux terms and also dynamics, radiation, TOFD, and sub-grid orography tendencies) are

$$\begin{aligned}\frac{\partial u}{\partial t} &= \frac{u^{t+1}-u^t}{\Delta t}\\ \frac{\partial v}{\partial t} &= \frac{v^{t+1}-v^t}{\Delta t}\\ \frac{\partial q_{\mathrm{t}}}{\partial t} &= \frac{q_{\mathrm{t}}^{t+1}-q_{\mathrm{t}}^t}{\Delta t}\end{aligned} \tag{3.89}$$

The tendencies and model level fluxes are also computed separately for each process for diagnostic purposes. The surface fluxes of turbulent diffusion plus total TOFD (vertically integrated) are post-processed as turbulent surface drag. The vertically integrated tendency of the sub-grid orography scheme is post-processed as gravity wave stress.

The kinetic energy loss by the mean flow through the diffusion process, and TOFD (E_{diss}), is

$$E_{\mathrm{turb}} = 2\Delta t \left.\frac{\partial u}{\partial t}\right|_{\mathrm{turb+TOFD}} \left(\frac{u^{t+1}+u^t}{2}\right) + 2\Delta t \left.\frac{\partial v}{\partial t}\right|_{\mathrm{turb+TOFD}} \left(\frac{v^{t+1}+v^t}{2}\right) \tag{3.90}$$

The kinetic energy lost is assumed to be transformed locally into internal energy. This procedure bypasses the sub-grid scale energy cascade, but it allows a closed energy cycle in the model (the term is generally small). Therefore

$$\left.\frac{\partial s_l}{\partial t}\right|_{\mathrm{turb+dyn+rad}} = \frac{s_l^{t+1}+E_{\mathrm{diss}}-s_l^t}{\Delta t} \tag{3.91}$$

3.10 SHORTER TIME STEP IN THE VERTICAL TURBULENT TRANSPORT SCHEME

The vertical turbulent transport scheme is called two times in every physics time step, with a time step of 1/2 of the standard time step.

3.11 DIAGNOSTIC COMPUTATIONS FOR POST-PROCESSING

3.11.1 Diagnostic boundary layer height

Because of its importance for applications (e.g. in air pollution modelling), the boundary layer height is diagnosed and made available for post-processing. The parametrization of the mixed layer (and entrainment) uses a boundary layer height from an entraining parcel model. But in order to get a continuous field, also in neutral and stable situations the bulk Richardson method proposed by Troen and Mahrt (1986) is used as a diagnostic, independent of the turbulence parametrization. Boundary layer height $h_{\rm BL}$ is defined as the level where the bulk Richardson number, based on the difference between quantities at that level and the lowest model level, reaches the critical value $Ri_{\rm cr} = 0.25$. The bulk Richardson is computed from the following set of equations.

$$\begin{aligned}
|\Delta U|^2 &= (u_{\rm hbl} - u_n)^2 + (v_{\rm hbl} - v_n)^2 \\
s_{{\rm v}n} &= c_p T_n (1 + \varepsilon q_n) + g z_n + 0.5{\rm K} \\
s_{\rm vhbl} &= c_p T_{\rm hbl} (1 + \varepsilon q_{\rm hbl}) + g h_{\rm bl} \\
\Delta s &= 8.5 c_p Q_{0{\rm v}} / w_s \\
w_{\rm s} &= \{u_*^3 + 0.6 (g/T) Q_{0{\rm v}} h_{\rm bl}\}^{1/3} \quad \text{unstable} \\
w_{\rm s} &= u_* \quad \text{stable} \\
Ri_{\rm b} &= h_{\rm bl} \frac{2g(s_{\rm vhbl} - s_{{\rm v}n} - \Delta s)}{(s_{\rm vhbl} + s_{{\rm v}n} - g h_{\rm bl} - g z_n)|\Delta U|^2}
\end{aligned} \tag{3.92}$$

where index n indicates the lowest model level and $h_{\rm bl}$ indicates the boundary layer height i.e the level where $Ri_{\rm b} = Ri_{\rm cr}$. The virtual dry static energy from the lowest level $s_{{\rm v}n}$ is increased with a turbulent part Δs and compared to the virtual dry static energy at boundary layer height $h_{\rm bn}$. The boundary layer height is found by a vertical scan from the surface upwards. If the boundary layer height is found to be between two levels a linear interpolation is done to find the exact position. Since the boundary layer height is needed for $w_{\rm s}$, the upward scan is done twice. The first one uses $h_{\rm BL} = 1000$ m in the expression for $w_{\rm s}$; the second scan uses the result of the first scan.

3.11.2 Wind at 10 m level

Wind at the 10 m level is computed for post-processing because it is the standard level for SYNOP observations. It can be obtained rather easily by vertical interpolation between the lowest model level and the surface, making use of profile functions (3.9) and (3.10). This procedure is appropriate over the ocean or in areas where the surface is smooth and homogeneous. However, the postprocess-ed field is meant to be comparable to wind from SYNOP observations and for observations over land WMO requires SYNOP stations to be in open terrain in order to be well exposed to wind. So the SYNOP wind observations are not necessarily compatible with the wind that is representative for a large area (i.e. a grid box from the model). Over inhomogeneous terrain, the problem can be particularly serious, because the "aerodynamic roughness length" in the model is adjusted to provide sufficient drag at the surface which is dominated by the rough elements. This approach leads to a low area-averaged wind speed which is not comparable to the "open-terrain" wind speed as observed by WMO stations.

In order to make the postprocess-ed wind compatible with SYNOP observations, the concept of exposure correction is introduced. The open-terrain wind is obtained by taking the wind information from such a height above the surface that it is less influenced by the underlying terrain. This height is called the blending height $h_{\rm blend}$ and for the interpolation to 10 m an aerodynamic roughness length is used that is typical for open terrain with grassland.

The interpolation procedure is as follows. First the blending height and the interpolation roughness length are set dependent on the model roughness length field using

$$\begin{array}{llll} h_{\rm blend}=75 & z_{\rm 0MWMO}=0.03 & F_{\rm blend}=(u^2_{\rm blend}+v^2_{\rm blend})^{1/2} & \text{if } z_{0M}>0.03 \\ h_{\rm blend}=z_n & z_{\rm 0MWMO}=z_{\rm 0M} & F_{\rm blend}=(u^2_n+v^2_n)^{1/2} & \text{if } z_{\rm 0M}<0.03 \end{array} \tag{3.93}$$

$$F_{10}=F_{\rm blend}\frac{\log\left(\frac{z_{10}+z_{\rm 0MWMO}}{z_{\rm 0MWMO}}\right)-\Psi_{\rm M}\left(\frac{z_{10}+z_{\rm 0MWMO}}{\mathcal{L}}\right)+\Psi_{\rm M}\left(\frac{z_{\rm 0MWMO}}{\mathcal{L}}\right)}{\log\left(\frac{z_{\rm blend}+z_{\rm 0MWMO}}{z_{\rm 0MWMO}}\right)-\Psi_{\rm M}\left(\frac{z_{\rm blend}+z_{\rm 0MWMO}}{\mathcal{L}}\right)+\Psi_{\rm M}\left(\frac{z_{\rm 0MWMO}}{\mathcal{L}}\right)} \tag{3.94}$$

where $z_{10}=10$ m, $F_{\rm blend}$ is the horizontal wind speed at the blending height either interpolated from model levels to 75 m or copied from the lowest model level, and F_{10} is the resulting horizontal wind speed at 10 m. The wind speed from (3.94) is converted to components making use of the wind direction from the lowest model level.

3.11.3 Temperature and humidity at the 2 m level

Computation of temperature and moisture at the 2 m level is based on interpolation between the lowest model level and the surface making use of the same profile functions as in the parametrization of the surface fluxes. The expressions derived from equations (3.11) and (3.12) are

$$s_2=s_{\rm surf}+(s_n-s_{\rm surf})\frac{\log\left(\frac{z_2+z_{\rm 0MWMO}}{z_{\rm 0HWMO}}\right)-\Psi_{\rm H}\left(\frac{z_2+z_{\rm 0MWMO}}{\mathcal{L}}\right)+\Psi_{\rm H}\left(\frac{z_{\rm 0HWMO}}{\mathcal{L}}\right)}{\log\left(\frac{z_n+z_{\rm 0MWMO}}{z_{\rm 0HWMO}}\right)-\Psi_{\rm H}\left(\frac{z_n+z_{\rm 0MWMO}}{\mathcal{L}}\right)+\Psi_{\rm H}\left(\frac{z_{\rm 0HWMO}}{\mathcal{L}}\right)} \tag{3.95}$$

$$q_2=q_{\rm surf}+(q_n-q_{\rm surf})\frac{\log\left(\frac{z_2+z_{\rm 0MWMO}}{z_{\rm 0QWMO}}\right)-\Psi_{\rm H}\left(\frac{z_2+z_{\rm 0MWMO}}{\mathcal{L}}\right)+\Psi_{\rm H}\left(\frac{z_{\rm 0QWMO}}{\mathcal{L}}\right)}{\log\left(\frac{z_n+z_{\rm 0MWMO}}{z_{\rm 0QWMO}}\right)-\Psi_{\rm H}\left(\frac{z_n+z_{\rm 0MWMO}}{\mathcal{L}}\right)+\Psi_{\rm H}\left(\frac{z_{\rm 0QWMO}}{\mathcal{L}}\right)} \tag{3.96}$$

with $z_2=2$ m, $z_{\rm 0HWMO}=z_{\rm 0QWMO}=0.003$ if $z_{\rm 0M}>0.03$, and otherwise $z_{\rm 0HWMO}=z_{\rm 0H}$ and $z_{\rm 0QWMO}=z_{\rm 0Q}$. Temperature T_2 is derived from s_2 with (3.5). Also the dew point is computed from q_2 and surface pressure. The dew point uses the saturation formulation with respect to water to be consistent with WMO reporting practise. If the resulting dew point is lower than temperature T_2, the dew point is set equal to temperature.

3.11.4 Wind gusts

The computation of gusts is intended to be compatible with WMO observing practise for wind extremes. In order to get uniform observations, WMO defines a wind gust as the maximum of the wind averaged over 3 second intervals.

To simulate gusts, the standard deviation of the horizontal wind is estimated on the basis of the similarity relation by Panofsky *et al.* (1977)

$$\begin{array}{lll} \sigma_{\rm u}= & 2.29u_*\left(1-\frac{0.5}{12}\frac{z_{\rm i}}{\mathcal{L}}\right)^{1/3} & \text{for } \mathcal{L}<0 \\ \sigma_{\rm u}= & 2.29u_* & \text{for } \mathcal{L}>0 \end{array} \tag{3.97}$$

with $z_{\rm i}=1000$ m. The difference between the gust and F_{10} is proportional to $\sigma_{\rm u}$, where the multiplier has been determined from universal turbulence spectra for a 50% exceeding probability of the three-second wind gust (see Beljaars, 1987). The resulting wind gust is

$$F_{\rm gust}=F_{10}+C_{\rm ugn}u_* \tag{3.98}$$

with parameter $C_{\rm ugn}=7.71$ and u_* from the surface stress as computed in the vertical turbulent transport code.

From the controlling parameters it is clear that the effects of surface friction (through surface roughness) and stability are captured. However, the approach is not adequate for gusts in baroclinic situations and where gusts are due to strong convective events. Therefore, in the presence of deep convection, a

convective contribution as a function of the vertical wind shear (Bechtold and Bidlot, 2009) is added to the turbulence gustiness (3.98) so that the total gustiness becomes

$$F_{\rm gust} = F_{10} + C_{\rm ugn} u_* + C_{\rm conv} \max(0, U_{850} - U_{950}) \tag{3.99}$$

where the convective mixing parameter $C_{\rm conv} = 0.6$, and U_{850} and U_{950} are the wind speeds at 850 and 950 hPa, respectively. Parameter $F_{\rm gust}$ is computed every time step and its maximum since the last post-processing is written out for archiving.

3.12 CODE

Vertical turbulent transports, which affect temperature, velocities and specific humidity, is performed in subroutine VDFMAIN called by VDFOUTER which, in turn, is called by CALLPAR. VDFOUTER calls VDFMAIN two times with 1/2 of the normal time step (these two routines have identical arguments so VDFMAIN can be called directly if the vertical turbulent transports is only needed once per time step). All the routines for the surface energy balance and for the interaction between the lowest model level and the surface, are in the SURF library. Transfer of information between the IFS and the SURF library is limited to a few interaction routines. The other SURF routines can not be called by the IFS.

At the start of the model integration the following setup routines are called to initialize modules specific to the vertical transport code:

- SUVDF. Setup routine for a number of parametrization constants.
- SUVDFS. Setup routine for constants and tables related to the stability functions. Stability functions are included as statement functions from fcvds.h.
- SUSVEG. Is part of the SURF library and sets a number of vegetation and tile parameters.

The main subroutine (VDFMAIN) does a sequence of computations and subroutine calls:

- SURFEXCDRIVER. This is the first call to the SURF library to prepare all the necessary parameters for exchange with the surface. The tiled surface fluxes and tiled skin temperatures are cycled from time step to time step (fluxes are needed for the first guess of stability parameters), but are not available at the start of the forecast. For the first time step, neutral transfer coefficients are used to estimate momentum fluxes, the tiled skin temperatures are set equal to the grid box averaged skin temperature from the initial condition, and the sensible and latent heat fluxes needed as a first guess for the Obukhov length computation are set to zero. SURFEXCDRIVER calls a number of subroutines from the SURF library.
  - VUPDZ0. This routine computes roughness lengths for momentum, heat and moisture over ocean surfaces according to (3.26). It also computes surface buoyancy flux and Obukhov length from the fluxes of the previous time level.
  - VSURF. This routine prepares the surface boundary conditions for temperature and humidity and is called for every tile. The following quantities are computed: the surface specific humidity at saturation, the derivative of the saturation humidity curve at the surface, surface dry static energy, and vegetation stomatal resistances (see Chapter 8).
  - VEXCS. This routine determines the transfer coefficients between the surface and the lowest model level with the thermal stability expressed as function of the Obukhov length. It is called for every tile. The implicit relation between $z/\mathcal{L}$ and the Richardson number $Ri_{\rm bulk}$ is solved iteratively (using the Newton method with the derivative approximated in finite differences). Pre-computed tables defined in subroutine SUVDFS are used to obtain the first guess in stable conditions ($Ri > 0$) at the first time step. Transfer coefficients are multiplied by a constant factor $\alpha\rho g \frac{\Delta t}{\Delta z}$.
  - VEVAP. This routine computes for each tile the equivalent evapo-transpiration efficiency and the corresponding parameters a_n and $a_{\rm surf}$ defined by the land surface scheme (see chapter 8). Dry static energy at the surface at time level t is estimated as well.

  - VSFLX. This routine computes surface fluxes for each tile (heat flux, evaporation, momentum flux and virtual heat flux) at time t for later use in similarity functions and for the estimation of the diagnostic boundary layer depth.
- CLOUDVAR. This routine calculates the variance of total water from the humidity and cloud water using a symmetrical beta distribution. This value of total water variance is used as input value for the vertical turbulent transport.
- COVER. This routine diagnoses cloud fraction, water vapor, cloud liquid water and cloud ice from total water, total water variance and temperature. This first call diagnoses input reference values of cloud parameters.
- VDFDPBL. This routine diagnoses the boundary layer height for time level t. This boundary layer height is for post-processing only and is not used by the parametrization.
- VDFHGHTN. This routine uses an entraining plume model to determine updraught properties, mass-flux, cloud base and PBL top.
- VDFEXCU. This routine determines the turbulent diffusion coefficients between the model levels above the surface layer.
- VDFTODC. This routine computes coefficients for turbulent orographic form drag.
- VDFDIFM. This routine solves the diffusion equation for momentum, by Gaussian elimination of the tridiagonal matrices.
- VDFDIFH. This routine solves the EDMF equations for total water and liquid water static energy. A downward elimination scan is done through the tridiagonal matrices, and coefficients A_s, B_s, A_q, and B_q are computed. Then, a call is made to SURF routine SURFSEB to compute the surface fluxes for heat and moisture. Also the tiled fluxes are returned.
- VDFDIFC. Routine solves the diffusion equations for passive tracers. A specified flux at the surface is used as a boundary condition.
- VDFINCR. This routine computes the tendencies of the prognostic variables and estimates the kinetic energy dissipation.
- VDFFBLEND. This routine computes the blending height.
- SURFPP. This is the routine from the SURF library for the interpolation of SYNOP parameters. It calls:
  - SPPCFL. This routine computes the surface 2 metre temperature and humidity (dew point and specific humidity), and the wind at 10 m.
  - SPPGUST. This routine computes wind gusts as they are typically observed by standard WMO SYNOP stations.
- COVER. This routine diagnoses cloud fraction, water vapor, cloud liquid water and cloud ice from total water, total water variance and temperature. This second call diagnoses final values of cloud variables. Differences of final and initial values provide the output tendencies.

APPENDIX A. LIST OF SYMBOLS

a_{u}	updraught fraction
C_{H}	transfer coefficient for heat
C_{M}	transfer coefficient for momentum (drag coefficient)
C_{Q}	transfer coefficient for moisture
c_p	specific heat at constant pressure of moist air
E_{diss}	kinetic energy lost by the diffusion process
f	Coriolis parameter
F_{blend}	horizontal wind speed at blending height (for pp of 10 m wind)
F_{10}	horizontal wind speed at 10 m level (for pp)
g	acceleration of gravity
h_{BL}	diagnosed boundary layer height
h_{blend}	blending height (for pp of 10 m wind)
J_ϕ	vertical turbulent flux of ϕ
J_{q}	surface humidity flux
J_{s}	surface flux of dry static energy

J_{M}	surface momentum flux
K_{ϕ}	turbulent exchange coefficient for ϕ
K_{H}	turbulent exchange coefficient for heat
K_{M}	turbulent exchange coefficient for momentum
K_{Q}	turbulent exchange coefficient for moisture
$\mathcal{L}$	Obukhov length
L_{c}	latent heat of condensation
L_{d}	latent heat of deposition
l_{H}	mixing length for heat
l_{M}	mixing length for momentum
M	mass flux
N_{T}	number of tiles
p	pressure
Pr	Prandtl number
q	specific humidity
q_l	specific liquid water
q_{i}	specific ice water
q_{t}	specific total water $= q + q_l + q_{\mathrm{i}}$
q_{sat}	saturated specific humidity
q_*	$= J_{\mathrm{q}}/(\rho u_*)$
ΔR	radiative flux jump at cloud top
$Q_{0\mathrm{v}}$	virtual temperature flux in the surface layer
R_{dry}	gas constant for dry air
R_{vap}	gas constant for water vapour
$\mathfrak{R}_{\mathrm{LW}}$	net long-wave radiation at the surface
$\mathfrak{R}_{SW}$	net short-wave radiation at the surface
RH_{surf}	relative humidity at the surface
Ri	local Richardson number
Ri_{bulk}	bulk Richardson number for the surface layer
s	dry static energy
s_l	generalized liquid water static energy
s_{v}	virtual dry static energy
s_*	$= J_{\mathrm{s}}/(\rho u_*)$
T	temperature
t	time
$\lvert U\rvert$	horizontal wind speed
u, v	horizontal wind components
u_*	friction velocity $= (J_{\mathrm{M}}/\rho)^{1/2}$
w_*	free convection velocity scale
$z_{0\mathrm{M}}$	roughness length for momentum (aerodynamic roughness length)
$z_{0\mathrm{H}}$	roughness length for heat
$z_{0\mathrm{Q}}$	roughness length for moisture
z_{i}	scale height of the boundary layer
z_n	height of the lowest model level n
$z_{0\mathrm{MWMO}}$	roughness length for momentum at SYNOP station
$z_{0\mathrm{HWMO}}$	roughness length for heat at SYNOP station
$z_{0\mathrm{QWMO}}$	roughness length for moisture at SYNOP station
z_2	height of screen level observation (2 m)
z_{10}	height of surface wind observation (10 m)
α	implicitness factor for diffusion equation
α_{Ch}	Charnock parameter
β	scaling parameter for asymptotic mixing length
Δt	time step
Δz	vertical grid length
ε	$= (R_{\mathrm{vap}}/R_{\mathrm{dry}}) - 1$

ε	parcel entrainment
$\theta_{\rm v}$	virtual potential temperature
κ	Von Kármán's constant
λ	asymptotic mixing length
$\Lambda_{\rm skin}$	conductivity of
ν	kinematic viscosity
ρ	density
$\sigma_{\rm qt}$	standard deviation of total water
$\sigma_{\rm u}$	standard deviation of horizontal wind
$\sigma_{\rm w}$	standard deviation of vertical wind
ζ	$= z/\mathcal{L}$
ϕ	symbolic reference to a conservative quantity
$\Phi_{\rm M}$	universal gradient stability function for wind
$\Phi_{\rm H}$	universal gradient stability function for temperature
$\Phi_{\rm Q}$	universal gradient stability function for moisture
$\Psi_{\rm M}$	universal profile stability function for wind
$\Psi_{\rm H}$	universal profile stability function for temperature
$\Psi_{\rm Q}$	universal profile stability function for moisture

Subscripts:

i	tile index
k	level index (counted from model top downwards)
n	referring to lowest model level
skin	referring to the skin layer
surf	referring to the surface
u	referring to the updraught
e	referring to the environment

Superscripts:

t	index for old time level, indicating beginning of time step
$t+1$	index for new time level, indicating end of time step
trad	index referring to the latest full radiation time step

Special symbols:

$\hat{\phi}$	implicit variable ϕ defined by equation (3.65)

Chapter 4
Subgrid-scale orographic drag

Table of contents

4.1 GENERAL PRINCIPLES

The subgrid-scale orography intersects model levels, and consequently influences the momentum of the atmosphere, and hence other parts of the physics. In the model stably stratified flow over the subgrid-scale orography creates drag through a combination of low-level flow blocking (i.e. blocked-flow drag) and the absorption and/or reflection of vertically propagating gravity waves (i.e. gravity-wave drag). The parameteriation scheme is described in detail in Lott and Miller (1997).

The scheme is based on ideas presented by Baines and Palmer (1990), combined with ideas from bluff-body dynamics. The assumption is that the mesoscale-flow dynamics can be described by two conceptual models, whose relevance depends on the non-dimensional height of the mountain via

$$H_{\mathrm{n}} = \frac{NH}{|U|} \tag{4.1}$$

where H is the maximum height of the obstacle, U is the wind speed and N is the Brunt–Väisälä frequency of the incident flow.

At small H_{n} most of the flow goes over the mountain and gravity waves are forced by the vertical motion of the fluid. Suppose that the mountain has an elliptical shape and a height variation determined by a parameter b in the along-ridge direction and by a parameter a in the cross-ridge direction, such that the mountain anisotropy $\gamma = a/b \leq 1$, then the geometry of the mountain can be written in the form

$$h(x,y) = \frac{H}{1 + x^2/a^2 + y^2/b^2} \tag{4.2}$$

In the simple case when the incident flow is at right angles to the ridge the surface stress due to the gravity wave has the magnitude

$$\tau_{\mathrm{wave}} = \rho_0 bGB(\gamma)NUH^2 \tag{4.3}$$

provided that the Boussinesq and hydrostatic approximations apply. In (4.3) G is a function of the mountain sharpness (Phillips, 1984), and for the mountain given by (4.2), $G \approx 1.23$. The term $B(\gamma)$ is a function of γ, and can vary from $B(0) = 1$ for a two-dimensional ridge to $B(1) = \pi/4$ for a circular mountain.

At large H_n, the vertical motion of the fluid is limited and part of the low-level flow is blocked and goes around the mountain. The depth, Z_{blk}, of this blocked layer, when U and N are independent of height, can be expressed as

$$Z_{blk} = H \times \max\left(0, \frac{H_n - H_{n_{crit}}}{H_n}\right) \tag{4.4}$$

where $H_{n_{crit}}$ is a critical non-dimensional mountain height of order unity. The depth Z_{blk} can be viewed as the upstream elevation of the isentropic surface that is raised exactly to the mountain top. At each level below Z_{blk} the flow streamlines divide around the obstacle, and it is supposed that flow separation occurs on the obstacle's flanks. Then, the drag, $D_{blk}(z)$, exerted by the obstacle on the flow at these levels can be written as

$$D_{blk}(z) = -\rho_0 C_d l(z) \frac{U|U|}{2} \tag{4.5}$$

Here $l(z)$ represents the horizontal width of the obstacle as seen by the flow at an upstream height $z < Z_{blk}$, and for an elliptical mountain is given by,

$$l(z) = 2b\left(\frac{Z_{blk} - z}{z}\right)^{1/2} \tag{4.6}$$

C_d represents the drag coefficient, which according to the free streamline theory of jets in ideal fluids is a constant having a value close to 1 (Kirchoff, 1876; Gurevitch, 1965). However, observations show C_d can be nearer 2 in value when suction effects occur in the rear of the obstacle (Batchelor, 1967). Here, this drag is applied to the flow, level by level, and will be referred to as the 'blocked-flow drag', D_{blk}. Unlike the gravity-wave drag computation (4.3), the total stress exerted by the mountain on the 'blocked' flow does not need to be known *a priori*.

In (4.6), it is assumed that the level Z_{blk} is raised up to the mountain top, with each layer below Z_{blk} raised by a factor H/Z_{blk}. This leads, effectively, to a reduction of the obstacle width, as seen by the flow when compared with the case in which the flow does not experience vertical motion as it approaches the mountain. Then applying (4.5) to the fluid layers below Z_{blk}, the stress due to the blocked-flow drag is obtained by integrating from $z = 0$ to $z = Z_{blk}$, viz.

$$\tau_{blk} \approx C_d \pi b \rho_0 Z_{blk} \frac{U|U|}{2} \tag{4.7}$$

Moreover, the blocked layer results in a reduction of the mountain height which produces gravity waves, meaning the mountain height used in (4.3) is replaced with a lower effective (or cut-off) mountain height, i.e.

$$H_{eff} = 2(H - Z_{blk}) \tag{4.8}$$

The factor 2 was added later (in Cy32r2) because diagnostics indicated that without the factor 2, the gravity wave activity was too weak. In the present scheme the value of C_d is allowed to vary with the aspect ratio of the obstacle, as in the case of separated flows around immersed bodies (Landweber, 1961), while at the same time setting the critical number $H_{n_{crit}}$ equal to 0.5 as a constant intermediate value.

4.2 DESCRIPTION OF THE SCHEME

Following Baines and Palmer (1990), the subgrid-scale orography over one grid-point region is represented by four parameters μ, γ, σ and θ which stand for the standard deviation, the anisotropy, the slope and the geographical orientation of the orography, respectively. These four parameters have been calculated from the GTOPO30 data set at $30''$ (about 1000 m) resolution (Gesch and Larson, 1998), averaged to $2'30''$ resolution so as to remove scales less than 5000m. At sub-grid horizontal scales less than 5000 m, small surface obstacles generate additional turbulence or turbulent orographic form drag (TOFD).

The scheme uses values of wind velocity, U_H, Brunt–Väisälä frequency, N_H, and fluid density, ρ_H, which are evaluated by averaging between μ and 2μ above the model mean orography, i.e. representative of flow incident to the subgrid-scale orography. Following Wallace *et al.* (1983), 2μ is interpreted as the envelope

of the subgrid-scale mountain peaks above the model orography. The evaluation of the blocking height $Z_{\rm blk}$ is based on a very simple interpretation of the non-dimensional mountain height $H_{\rm n}$. To first order in the mountain amplitude, the obstacle excites a wave, and the sign of the vertical displacement of a fluid parcel is controlled by the wave phase. If a fluid parcel ascends the upstream mountain flank over a height large enough to significantly modify the wave phase, its vertical displacement can become zero, and it will not cross the mountain summit. In this case $Z_{\rm blk}$ is the highest level located below the mountain top for which the phase change between $Z_{\rm blk}$ and the mountain top exceeds a critical value $H_{\rm n_{crit}}$, i.e.

$$\int_{Z_{\rm blk}}^{3\mu} \frac{N}{U_{\rm p}} {\rm d}z \geq H_{\rm n_{crit}} \tag{4.9}$$

In the inequality (4.9), the wind speed, $U_{\rm p}(z)$, is calculated by resolving the wind, $U(z)$, in the direction of the flow U_H. Then, if the flow veers or backs with height, (4.9) will be satisfied when the flow becomes normal to U_H. Levels below this 'critical' altitude define the low-level blocked flow. The inequality (4.9) will also be satisfied below inversion layers, where the parameter N is very large. These two properties allow the new parametrization scheme to mimic the vortex shedding observed when pronounced inversions occur (Etling, 1989). The upper limit in the equality (4.9) was chosen to be 3μ, which is above the subgrid-scale mountain tops. This ensures that the integration in equality (4.9) does not lead to an underestimation of $Z_{\rm blk}$, which can occur because of the limited vertical resolution when using 2μ as an upper limit (a better representation of the peak height), but this upper limit could be relaxed given better vertical resolution.

In the following subsection the drag amplitudes will be estimated combining formulae valid for elliptical mountains with real orographic data. Considerable simplifications are implied and the calculations are, virtually, scale analyses relating the various amplitudes to the sub-grid parameters.

4.2.1 Blocked-flow drag

Within a given layer located below the blocking level $Z_{\rm blk}$, the drag is given by (4.5). At a given altitude z, the intersection between the mountain and the layer approximates to an ellipse with eccentricity of

$$(a', b') \approx (a, b)\left(\frac{Z_{\rm blk} - z}{z + \mu}\right)^{\frac{1}{2}} \tag{4.10}$$

where, by comparison with (4.6), it is also supposed that the level $z = 0$ (i.e. the model mean orography) is at an altitude μ above the mountain valleys. If the flow direction is taken into account, the length $l(z)$ can be written approximately as

$$l(z) \approx 2\,\max(b\cos\psi, a\sin\psi)\left(\frac{Z_{\rm blk} - z}{z + \mu}\right)^{\frac{1}{2}} \tag{4.11}$$

where ψ is the angle between the incident flow direction θ. For one grid-point region and for uniformly distributed subgrid-scale orography, the incident flow encounters $L/(2a)$ obstacles is normal to the ridge ($\psi = 0$), whereas if it is parallel to the ridge ($\psi = \pi/2$) it encounters $L/(2b)$ obstacles, where L is the length scale of the grid-point region. If we sum up these contributions, the dependence of (4.11) on a and b can be neglected, and the length $l(z)$ becomes

$$l(z) = L\left(\frac{Z_{\rm blk} - z}{z + \mu}\right)^{\frac{1}{2}} \tag{4.12}$$

Furthermore, the number of consecutive ridges (i.e. located one after the other in the direction of the flow) depends on the obstacle shape: there are approximately $L/(2b)$ successive obstacles when the flow is along the ridge, and $L/(2a)$ when it is normal to the ridge. If we take this into account, together with the flow direction, then

$$l(z) = \frac{L^2}{2}\left(\frac{Z_{\rm blk} - z}{z + \mu}\right)^{\frac{1}{2}} \max\left(\frac{\cos\psi}{a}, \frac{\sin\psi}{b}\right) \tag{4.13}$$

Relating the parameters a and b to the subgrid-scale orography parameters $a \approx \mu/\sigma$ and $a/b \approx \gamma$ and, allowing the drag coefficient to vary with the aspect ratio of the obstacle as seen by the incident flow, we

have

$$r = \frac{\cos^2\psi + \gamma \sin^2\psi}{\gamma \cos^2\psi + \sin^2\psi} \tag{4.14}$$

and the drag per unit area and per unit height can be written as

$$D_{\rm blk}(z) = -C_{\rm d} \max\left(2 - \frac{1}{r}, 0\right) \rho \frac{\sigma}{2\mu} \left(\frac{Z_{\rm blk} - z}{z + \mu}\right)^{\frac{1}{2}} \max(\cos\psi, \gamma \sin\psi) \frac{U|U|}{2} \tag{4.15}$$

The drag coefficient is modulated by the aspect ratio of the obstacle to account for the fact that $C_{\rm d}$ is twice as large for flow normal to an elongated obstacle as it is for flow round an isotropic obstacle. The drag tends to zero when the flow is nearly along a long ridge because flow separation is not expected to occur for a configuration of that kind. It can be shown that the term $\max(\cos\psi, \gamma \sin\psi)$ is similar to a later form used for the directional dependence of the gravity-wave stress. For simplicity, this later form has been adopted, so that

$$D_{\rm blk}(z) = C_{\rm d} \max\left(2 - \frac{1}{r}, 0\right) \rho \frac{\sigma}{2\mu} \left(\frac{Z_{\rm blk} - z}{z + \mu}\right)^{\frac{1}{2}} (B \cos^2\psi + C \sin^2\psi) \frac{U|U|}{2} \tag{4.16}$$

with the constants (Phillips, 1984)

$$B = 1 - 0.18\gamma - 0.04\gamma^2, \; C = 0.48\gamma + 0.3\gamma^2 \tag{4.17}$$

The difference between (4.15) and (4.16) has been shown to have only a negligible impact on all aspects of the model's behaviour.

In practice, (4.16) is suitably resolved and applied to the component from of the horizontal momentum equations. This equation is applied level by level below $Z_{\rm blk}$ and, to ensure numerical stability, a quasi-implicit treatment is adopted whereby the wind velocity U in (4.16) is evaluated at the updated time $t + {\rm d}t$, while the wind amplitude, $|U|$, is evaluated at the previous time step.

4.2.2 Gravity-wave drag

This gravity-wave part of the scheme is based on the work of Miller *et al.* (1989) and Baines and Palmer (1990), and takes into account some three-dimensional effects in the wave stress amplitude and orientation. For clarity and convenience, a brief description is given here. On the assumption that the subgrid-scale orography has the shape of one single elliptical mountain, the gravity wave surface stress (4.3) can be written as (Phillips, 1984)

$$(\tau_1, \tau_2) = \rho_H U_H N_H H_{\rm eff}^2 b G (B \cos^2\psi_H + C \sin^2\psi_H, (B - C) \sin\psi \cos\psi_H) \tag{4.18}$$

where ψ_H is the mean value between $z = \mu$ and $z = 2\mu$. Furthermore, when b or a are significantly smaller than the length L, characteristic of the gridpoint region size, there are, typically, $L^2/(4ab)$ ridges inside the grid-point region. Summing all the associated forces we find the stress per unit area, viz.

$$(\tau_1, \tau_2) = \rho_H U_H N_H (H_{\rm eff}^2/4)(\sigma/\mu) G \{B \cos^2\psi_H + C \sin^2\psi_H, (B - C) \sin\psi_H \cos\psi_H\} \tag{4.19}$$

where a has been replaced by μ/σ.

It is worth noting that, since the basic parameters ρ_H, U_H, N_H are evaluated for the layer between μ and 2μ above the mean orography that defines the model's lower boundary, there will be much less diurnal cycle in the stress than in previous formulations that used the lowest model levels for this evaluation. The vertical distribution of the gravity-wave stress will determine the levels at which the waves break and slow down the synoptic flow. Since this part of the scheme is active only above the blocked flow, this stress is now constant from the bottom model level to $Z_{\rm blk}$. Above this height, up to the top of the model, the stress is constant until the waves break (by the top of the model the gravity wave must have broken completely). This occurs when the total Richardson number, Ri, falls below a critical value $Ri_{\rm crit}$, which is of order unity. When the non-dimensional mountain height is close to unity, this algorithm will usually predict wave breaking at relatively low levels (i.e. immediately above the 'blocked' layer).

This is not surprising since the linear theory of mountain gravity waves predicts low-level breaking waves at large non-dimensional mountain heights (Miles and Huppert, 1969). In reality, the depth over which gravity-wave breaking occurs is more likely to be related to the vertical wavelength of the waves. For this reason, when low-level wave breaking occurs in the scheme, the corresponding drag is distributed (above the blocked flow), over a layer of thickness Δz, equal to a quarter of the vertical wavelengths of the waves, i.e.

$$\int_{Z_{\rm blk}}^{Z_{\rm blk}+\Delta z} \frac{N}{U_{\rm p}} {\rm d}z \approx \frac{\pi}{2} \tag{4.20}$$

Above the height $Z_{\rm blk}+\Delta z$ are waves with an amplitude such that $Ri > Ri_{\rm crit}$. The remaining part of the momentum flux above 9.9 Pa is spread between this level and the top of the model.

4.3 SPECIFICATION OF SUBGRID-SCALE OROGRAPHY

For completeness, the following describes how the subgrid-scale orography fields were computed by Baines and Palmer (1990). The mean topographic height above mean sea level over the grid-point region is denoted by $\bar{h}$, and the coordinate z denotes elevation above this level. Then the topography relative to this height $h(x,y)-\bar{h}$ is represented by four parameters, as follows.

(i) The net variance, or standard deviation, μ, of $h(x,y)$ in the grid-point region. This is gives a measure of the amplitude and 2μ approximates the physical envelope of the peaks.
(ii) A parameter γ which characterizes the anisotropy of the topography within the grid-point region.
(iii) An angle ψ, which denotes the angle between the direction of the low-level wind and that of the principal axis of the topography.
(iv) A parameter σ which represents the mean slope within the grid-point region.

The parameters γ and ψ may be defined from the topographic gradient correlation tensor

$$H_{ij} = \overline{\frac{\partial h}{\partial x_i}\frac{\partial h}{\partial x_j}}$$

where $x_1 = x$, and $x_2 = y$, and where the terms be calculated (from the USN data-set) by using all relevant pairs of adjacent gridpoints within the grid-point region. This symmetric tensor may be diagonalized to find the directions of the principal axes and the degree of anisotropy. If

$$K = \frac{1}{2}\left\{\overline{\left(\frac{\partial h}{\partial x}\right)^2} + \overline{\left(\frac{\partial h}{\partial y}\right)^2}\right\}, \quad L = \frac{1}{2}\left\{\overline{\left(\frac{\partial h}{\partial x}\right)^2} - \overline{\left(\frac{\partial h}{\partial y}\right)^2}\right\} \quad \text{and} \quad M = \overline{\frac{\partial h}{\partial x}\frac{\partial h}{\partial y}} \tag{4.21}$$

the principal axis of H_{ij} is oriented at an angle θ to the x-axis, where θ is given by

$$\begin{aligned} \theta &= \frac{1}{2}\arctan(M/L) \quad if \quad L>0 \\ \theta &= \frac{1}{2}\arctan(M/L) + \pi/2 \quad if \quad L<0 \; and \; M>0 \\ \theta &= \frac{1}{2}\arctan(M/L) - \pi/2 \quad if \quad L<0 \; and \; M<0 \end{aligned} \tag{4.22}$$

This gives the direction where the topographic variations, as measured by the mean-square gradient, are largest. The corresponding direction for minimum variation is at right angles to this. Changing coordinates to x', y' which are oriented along the principal axes $x' = x\cos\theta + y\sin\theta$ and $y' = y\cos\theta - x\sin\theta$, the new values of K, L, and M relative to these axes, denoted K', L' and M', are given by

$$K' = K, \quad L' = (L^2+M^2)^{\frac{1}{2}} \quad \text{and} \quad M' = 0$$

where K, L and M are given by (4.21). The anisotropy of the orography or 'aspect ratio'. γ is then defined by the equations

$$\gamma^2 = \overline{\left(\frac{\partial h}{\partial y'}\right)^2} \Big/ \overline{\left(\frac{\partial h}{\partial x'}\right)^2} = \frac{K'-L'}{K'+L'} = \frac{K-(L^2+M^2)^{1/2}}{K+(L^2+M^2)^{1/2}} \tag{4.23}$$

If the low-level wind vector is directed at an angle φ to the x-axis, then the angle ψ is given by

$$\psi = \theta - \varphi \tag{4.24}$$

The slope parameter, σ, is defined as

$$\sigma^2 = \overline{\left(\frac{\partial h}{\partial x'}\right)^2} \tag{4.25}$$

which is the mean-square gradient along the principal axis.

4.4 CODE

The principal routine is GWDRAG, which is called from CALLPAR. GWDRAG first calls GWSETUP to define all the basic input values required for the evaluation of the blocking drag and gravity wave stress. It then computes the surface gravity wave stress and calls GWPROFIL to calculate its vertical distribution. GWDRAG then computes the momentum tendency coefficients (rather than the actual momentum tendencies). The coefficients are passed back to CALLPAR where they are solved in the vertical diffusion scheme as a joint implicit calculation with TOFD momentum tendency coefficients. The joint implicit calculation introduces some degree of dependency into these coupled processes, and so reduces the time step sensitivity which would have existed if each scheme had evaluated its tendencies independently (Beljaars *et al.*, 2004b).

4.4.1 GWSETUP

This routine defines various reference model levels for controlling the vertical structure of the calculations, and sets up a number of derived atmospheric variables and geometric calculations required to run the scheme.

(i) The definition of the Brunt–Väisälä frequency on half levels

$$N^2_{k-1/2} = \frac{2g^2}{c_{p_{\rm dry}}(T_k + T_{k-1})}\left\{1 - c_{p_{\rm dry}}\rho_{k-1/2}\frac{(T_k - T_{k-1})}{(p_k - p_{k-1})}\right\} \tag{4.26}$$

(ii) The definition of the mean wind components in the layer $\mu < z < 2\mu$

$$U_{\rm LOW} = \frac{\sum_{k=\mu}^{k=2\mu} U_k \Delta p_k}{\sum_{k=\mu}^{k=2\mu} \Delta p_k} \tag{4.27}$$

and similarly for $V_{\rm LOW}$; likewise the mean static stability, $N_{\rm LOW}$, and the mean density, $\rho_{\rm LOW}$ are calculated.

(iii) The calculation of necessary geometry pertaining to geographical orientation of subgridscale orography and wind direction,

$$\varphi_k = \tan^{-1}\left(\frac{V_k}{U_k}\right) \tag{4.28}$$

$$\psi_k = \theta - \varphi_k \tag{4.29}$$

$$\bar{\varphi} = \tan^{-1}\left(\frac{V_{\rm LOW}}{U_{\rm LOW}}\right) \tag{4.30}$$

and $\bar{\psi} = \theta - \bar{\varphi}$. Also computed are the parameters B and C (4.17).

(iv) The calculation of the vertical wind-profile in the plane of the gravity wave stress. Defining

$$\hat{U}_k = \frac{U_{\rm LOW}}{|\mathbf{V}_{\rm LOW}|}U_k + \frac{V_{\rm LOW}}{|\mathbf{V}_{\rm LOW}|}V_k$$

and similarly for $\hat{V}_k$, where $\mathbf{V}_{\rm LOW} = (U_{\rm LOW}, V_{\rm LOW})$, then the wind profile is defined level-by-level as

$$V^{\rm G}_k = \frac{(\hat{U}_k D_1 + \hat{V}_k D_2)}{\sqrt{(D_1^2 + D_2^2)}} \tag{4.31}$$

where $D_1 = B - (B - C)\sin^2\bar{\psi}$ and $D_2 = (B - C)\sin\bar{\psi}\cos\bar{\psi}$; the values of V_k^{G} are also used to compute half level values $V_{k+1/2}^{\mathrm{G}}$ etc. by linear interpolation in pressure.

(v) The calculation of basic flow Richardson Number

$$\overline{Ri}_{k-1/2} = N_{k-1/2}^2 \left\{ \frac{p_k - p_{k-1}}{g\rho_{k-1/2}(V_k^G - V_{k-1}^G)} \right\}^2$$

(vi) The calculation of the blocked layer depth (4.4), given by the value of Z_{blk} that is the solution to the finite-difference form of the equation

$$\int_{Z_{\mathrm{blk}}}^{3\mu} \frac{N_k}{\hat{U}_k}\,\mathrm{d}z \geq H_{\mathrm{n_{crit}}} \tag{4.32}$$

(vii) The calculation of the layer in which low-level wave-breaking occurs (if any). This is given by the value of Δz that is the solution to the finite difference form of the equation

$$\int_{Z_{\mathrm{blk}}}^{Z_{\mathrm{blk}}+\Delta z} \frac{N_k}{\hat{U}_k}\,\mathrm{d}z = \frac{\pi}{2} \tag{4.33}$$

the value of $(Z_{\mathrm{blk}} + \Delta z)$ is not allowed to be less than 4μ.

(viii) The calculation of the assumed vertical profile of the sub-grid scale orography needed for the 'blocking' computations (4.10), for $z < Z_{\mathrm{blk}}$,

$$z_k^{\mathrm{DEP}} = \sqrt{\frac{Z_{\mathrm{blk}} - z_k}{z_k + \mu}} \tag{4.34}$$

4.4.2 GWPROFIL

This routine computes the vertical profile of gravity-wave stress by constructing a local wave Richardson number which attempts to describe the onset of turbulence due to the gravity waves becoming convectively unstable or encountering critical layers. This local Richardson number can be written in the form

$$\tilde{R}i = \overline{Ri}\left\{ \frac{1-\alpha}{(1 + \overline{Ri}^{1/2}\alpha)^2} \right\}$$

where $\overline{Ri}$ is the Richardson number of the basic flow. The parameter $\alpha = N|\delta z|/V_k^{\mathrm{G}}$ in which $|\delta z|$ represents the amplitude. By requiring that $\tilde{R}i$ never falls below a critical value $\tilde{R}i_{\mathrm{crit}}$ (currently equal to 0.25), values of wave stress are defined progressively from the top of the blocked layer upwards.

When low-level breaking occurs the relevant depth is assumed to be related to the vertical wavelength. Hence a linear (in pressure) decrease of stress is included over a depth Δz given by the solution of (4.33). The linear decrease of gravity wave stress is written as

$$\tau_{wave_{p_k}} = \tau_{wave_{z_{\mathrm{blk}}}} + (\tau_{wave_{z_{\mathrm{blk}}+\Delta z}} - \tau_{wave_{z_{\mathrm{blk}}}}) \frac{p_k - p_{z_{\mathrm{blk}}}}{p_{z_{\mathrm{blk}}+\Delta z} - p_{z_{\mathrm{blk}}}} \tag{4.35}$$

4.4.3 GWDRAG

This is the main routine. The total (TOT) tendency due the dynamics (DYN), vertical diffusion (VDF), wave drag, and blocking drag is given by

$$\left(\frac{\partial u}{\partial t}\right)_{\mathrm{TOT}} = \left(\frac{\partial u}{\partial t}\right)_{\mathrm{wave}} + \left(\frac{\partial u}{\partial t}\right)_{\mathrm{blk}} + \left(\frac{\partial u}{\partial t}\right)_{\mathrm{DYN+VDF}} = \alpha_{\mathrm{u}} - \beta u^{n+1} + \left(\frac{\partial u}{\partial t}\right)_{\mathrm{DYN+VDF}} \tag{4.36}$$

where α_{u} and β are the explicit gravity wave drag tendency coefficient and implicit blocking drag tendency coefficient respectively. A similar equation is apparent for the v component. As stated above, these tendencies are computed in the vertical diffusion routine.

(a) Gravity wave drag component

Using (4.19) the surface gravity-wave stress is computed in the form,

$$\tau_{\text{wave}} = \rho_{\text{LOW}}(H_{\text{eff}}^2/9)(\sigma/\mu)G(U_{\text{LOW}}^2 + V_{\text{LOW}}^2)^{1/2}(D_1^2 + D_2^2)^{1/2}N_{\text{LOW}} \tag{4.37}$$

where G is a function of the mountain sharpness. As Z_{blk} is able to reach a maximum height of 3μ (4.32), we must choose $H = 3\mu$. However, the surface stress must be scaled to a mountain height of 2μ, so the denominator of (4.37) is divided by 9 rather than 4 (4.19) (i.e. for $Z_{\text{blk}} = 0$ both equations are identical). Following this, GWPROFIL is called to compute the vertical profile of gravity wave stress.

For $z > Z_{\text{blk}}$ the gravity wave tendency coefficient is defined level by level as, ¿¿¿¿ ORIGINAL //depot/user/paa/paa$_C$Y33R1$_D$OC$_a$nton$_f$or36R1/IFSdoc/4$_P$hysical$_P$rocesses/Chapter$_4$/p4c04.tex1

==== THEIRS //depot/user/paa/paa$_C$Y33R1$_D$OC$_a$nton$_f$or36R1/IFSdoc/4$_P$hysical$_P$rocesses/Chapter$_4$/p4c04.tex2 == YOURS//client$_n$e3$_C$Y33R1$_N$EW/IFSdoc/4$_P$hysical$_P$rocesses/Chapter$_4$/p4c04.tex <<<<

$\left(\frac{\partial u}{\partial t}\right)_{\text{wave}} = -g\frac{\tau_{wave_{k+1}} - \tau_{wave_k}}{p_{k+1} - p_k} f_{\text{u}}(\psi) = \alpha_{\text{u}}$(4.39)where $f_{\text{u}}(\psi)$ is the necessary geometric function to generate components. A similar equation exists for α_{v}. Here $\beta = 0$.

To avoid excessive tendencies at the top of the model, the remaining momentum flux above 9.9 Pa is spread over the layer between 9.9 Pa and the top of the model according to the following expression

$$\left(\frac{\partial u}{\partial t}\right)_{\text{wave}} = -g\frac{\tau_{wave_{ktop}} - \tau_{wave_1}}{p_{ktop} - p_1}^2 (p_{k+1} - p_k) f_{\text{u}}(\psi) \tag{4.40}$$

where *ktop* is the index of the first level above 9.9 Pa.

(b) Blocking drag component

For $z \le Z_{\text{blk}}$ the blocking drag tendency is defined level by level as

$$\left(\frac{\partial u}{\partial t}\right)_{\text{blk}} = -C_{\text{d}} \max\left(2 - \frac{1}{r}, 0\right)\frac{\sigma}{2\mu}\sqrt{\frac{Z_{\text{blk}} - z}{z + \mu}}(B\cos^2\psi + C\sin^2\psi)\frac{U|U|}{2} \tag{4.41}$$

Here $\alpha_{\text{u,v}} = 0$. This equation is evaluated in the following partially implicit manner by writing it in the form

$$\left(\frac{\partial u}{\partial t}\right)_{\text{blk}} = \frac{U^{n+1} - U^n}{\Delta t} = -A|U^n|U^{n+1} = -\beta_{\text{u}}U^{n+1}$$

with $U^{n+1} = U^n/(1 + \beta)$ and $\beta = \beta_{\text{u}}\Delta t$, with $\beta_{\text{u}} = A|U^n|$. Here

$$\beta_{\text{u}} = C_{\text{d}} \max\left(2 - \frac{1}{r}, 0\right)\frac{\sigma}{2\mu}\sqrt{\frac{Z_{\text{blk}} - z}{z + \mu}}(B\cos^2\psi + C\sin^2\psi)\frac{|U|}{2} \tag{4.42}$$

(c) Evaluation of tendencies

The tendency coefficients are passed to CALLPAR where they are jointly implicitly computed in the vertical diffusion code with momentum tendency coefficients from the TOFD scheme. The actual tendencies are given as

$$\left(\frac{\partial u}{\partial t}\right)_{\text{wave+blk}} = \left(\frac{\partial u}{\partial t}\right)_{\text{TOT}} - \left(\frac{\partial u}{\partial t}\right)_{\text{DYN+VDF}} \tag{4.43}$$

Finally the tendencies are incremented. Local dissipation heating is calculated in the form

$$\left(\frac{\partial u}{\partial t}\right)_{\text{wave+blk}} = \frac{1}{c_p}\frac{DISS}{\Delta t}$$

with $DISS = 0.5((U^n)^2 + (V^n)^2 - \hat{U}^2 - \hat{V}^2)$, where $\hat{U} = U^n + \Delta t(\partial u/\partial t)_{\text{wave+blk}}$ and $\hat{V} = V^n + \Delta t(\partial v/\partial t)_{\text{wave+blk}}$.

APPENDIX A. LIST OF SYMBOLS

a	half mountain width in the cross-ridge or x-direction
B, C	functions of the mountain anisotropy
b	half mountain width in the along-ridge or y-direction
$C_{\rm d}$	drag coefficient
$c_{p_{\rm dry}}$	specific heat capacity
$D_{\rm blk}$	blocked-flow drag
g	gravitational accleration
G	function of the mountain sharpness
H	maximum mountain height
$H_{\rm eff}$	effective mountain height
$h(x, y)$	mountain height profile
$H_{\rm n}$	non-dimensional mountain height ($= NH/\|U\|$)
$H_{\rm n_{crit}}$	critical non-dimensional mountain height
L	length scale of the grid-point region
$l(z)$	horizontal width of mountain seen by the upstream flow
N	Brunt–Väisälä frequency
$N_{\rm H}$	($=N_{\rm LOW}$) mean Brunt–Väisälä frequency of low-level flow between $z = \mu$ and $z = 2\mu$
$p_{\rm k}$	model level air pressure
$\overline{Ri}$	Richardson number of the basic flow
$\tilde{R}i$	local Richardson number
$\tilde{R}i_{\rm crit}$	critical Richardson number
T	temperature
U	wind speed
$U_{\rm LOW}, V_{\rm LOW}$	horizontal components of mean low-level flow between $z = \mu$ and $z = 2\mu$
$U_{\rm H}$	mean wind speed of low-level flow between $z = \mu$ and $z = 2\mu$
$U_{\rm p}$	component of the wind speed in the direction of U_H
U_τ	component of wind speed in the direction of the stress τ
u, v	horizontal wind components
$U_{\rm k}, V_{\rm k}$	level-by-level horizontal wind components
$V_{\rm k}^{\rm G}$	level-by-level wind profile in the plane of gravity wave stress
$Z_{\rm blk}$	depth of blocked layer
$\alpha_{\rm u,v}$	explicit gravity wave tendency coefficient
β	($= \beta_u \Delta t$) implicit blocking drag tendency coefficient
γ	anisotropy of the orography ($= a/b \leq 1$)
θ	orientation of the orography
μ	standard deviation of orography
$\rho_{\rm k}$	model level air density
ρ_0	density of air at the surface
$\rho_{\rm H}$	($=\rho_{LOW}$) mean density of low-level flow between $z = \mu$ and $z = 2\mu$
σ	slope of the orography
$\tau_{\rm blk}$	stress due to blocked flow
$\tau_{\rm wave}$	surface stress due to gravity waves
ψ	angle between incident flow and orographic principal axis
$\bar{\psi}$	($= \psi_{\rm H}$) mean value of ψ between $z = \mu$ and $z = 2\mu$
φ	angle between low-level wind and the x-axis
$\bar{\varphi}$	mean value of φ between $z = \mu$ and $z = 2\mu$

Chapter 5
Non-orographic gravity wave drag

Table of contents

5.1 INTRODUCTION

Gravity waves have an important influence on the climate of the middle atmosphere, comprising the stratosphere and the mesosphere. The middle atmosphere is dominated by a westerly jet in the winter hemisphere and an easterly jet in the summer hemisphere, and a meriodional circulation with upwelling in the tropics and downwelling over the winter pole, referred to as the Brewer-Dobson circulation. This circulation is driven by the momentum deposited by breaking Rossby and small-scale non-orographic gravity waves. Furthermore, non-orographic gravity waves form the dominant source of momentum in the mesosphere and the thermosphere, and are also important in driving the variability of the tropical stratosphere, most prominent are the quasi-biennial oscilation and the semi-annual oscillation.

Non-orographic gravity waves are forced by dynamical motions such as convection, frontogenesis, and jet stream activity (e.g Fritts and Nastrom, 1980). They have vertical wavelengths which vary from less than one to many tens of kilometres and horizontal wavelengths which vary from tens to thousands of kilometres (Ern *et al.*, 2004). Thus these waves are generally unresolved or under-resolved by the model as the generating process is often poorly represented, and therefore have to be parametrized.

Prior to Cy35r3 (September 2009) the effect of small-scale non-orographic gravity waves has been parametrized in the simplest possible manner by Rayleigh friction above the stratopause, which is formulated as a drag force proportional to the mean flow. The parametrization scheme adopted since then is that of Scinocca (2003). The description is kept short and the effects of the parametrization on the middle atmosphere circulation in the IFS are not discussed as all material is described in detail, inluding an extensive literature list, in Orr *et al.* (2010).

5.2 HISTORY

The Scinocca (2003) scheme, hereafter referred to as S03 scheme, is a spectral scheme that follows from the Warner and McIntyre (1996) scheme which represents the three basic wave mechanisms that are conservative propagation, critical level filtering, and non-linear dissipation. However, the full non-hydrostatic and rotational wave dynamics considered by Warner and McIntyre (1996) is too costly for operational models, and therefore only hydrostatic and non-rotational wave dynamics is employed.

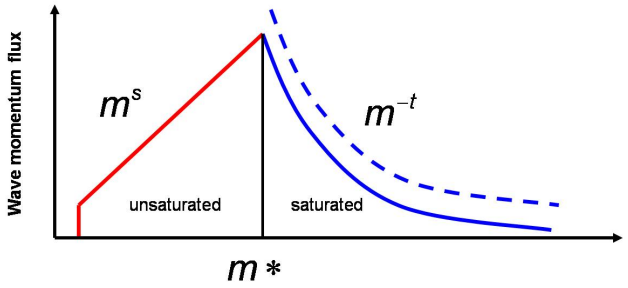

Figure 5.1 *Schematic of the gravity wave spectrum as a function of vertical wavenumber at constant intrinsic frequency $\tilde{\omega}$ showing the different spectral shapes, seperated by $m_\star$ for large and small m. The saturation spectrum is denoted by the dashed line.*

5.3 LAUNCH SPECTRUM

The dispersion relation for a hydrostatic gravity wave in the absence of rotation is

$$m^2 = \frac{k^2 N^2}{\tilde{\omega}^2} = \frac{N^2}{\tilde{c}^2} \tag{5.1}$$

where k, m are horizontal and vertical wavenumbers, $\tilde{\omega} = \omega - kU$ and $\tilde{c} = c - U$ are the intrinsic frequency and phase speed (with c the ground based phase speed and U the background wind speed in the direction of propagation), and N is the Brunt–Väisälä frequency (here expressed in height coordinate z for a better tangent-linear approximation and not in pressure coordinates as in the original code)

$$N^2 = \frac{g^2}{c_p T} + \frac{g\partial T}{T\partial z}; \qquad N \geq 10^{-12} \tag{5.2}$$

with g the gravity constant and c_p the specific heat of dry air at constant volume.

The launch spectrum is given by the total wave energy per unit mass in each azimuth ϕ following Fritts and Nastrom (1993), and is globally uniform and constant

$$\tilde{E}(m, \tilde{\omega}, \phi) = \mathrm{B}\left(\frac{m}{m_\star}\right)^{\mathrm{s}} \frac{N^2 \tilde{\omega}^{-\mathrm{p}}}{1 - \left(\frac{m}{m_\star}\right)^{\mathrm{s}+3}} \tag{5.3}$$

where B, s and p are constants, and $m_\star = 2\pi/L$ is a transitional wavelength (see Section 5.8 for an overview of the parameter settings).

Observation and theory suggest p values in the range $1 \leq \mathrm{p} \leq 2$. The spectrum is separable in terms of both m and $\tilde{\omega}$ and is displayed in Fig. 5.1 for a given value of $\tilde{\omega}$.

However, instead of the total wave energy the momentum flux spectral density $\rho\tilde{F}(m, \tilde{\omega}, \phi)$ is required, where ρ is the air density. It is obtained through the group velocity rule

$$\rho\tilde{F}(m, \tilde{\omega}, \phi) = \rho c_{\mathrm{g}} \frac{k}{\tilde{\omega}} E(m, \tilde{\omega}, \phi) \tag{5.4}$$

where $c_{\mathrm{g}} = \partial\tilde{\omega}/\partial m = \tilde{\omega}/m$ is the group velocity for hydrostatic dynamics. However as shown in S03, in the $(m, \tilde{\omega})$ coordinate framework the wave momentum flux is not conserved in the absence of dissipative processes as the spectrum propagates vertically through height varying background winds and buoyancy frequencies, but it is conserved in the (k, ω) coordinate framework. Performing a coordinate transformation on (5.4) and using the dispersion relation (5.1), one obtains the expression of the unscaled momentum flux density or Eliassen-Palm flux density as a function of the independent variable c

$$\rho F^{\star}(\hat{c},\phi) = \rho \frac{\hat{c}-\hat{U}}{N}\left(\frac{\hat{c}-\hat{U}}{\hat{c}}\right)^{2-\mathrm{p}} \frac{1}{1+\left(\frac{m_{\star}(\hat{c}-\hat{U})}{N}\right)^{s+3}} \tag{5.5}$$

where $\hat{U} = U^{(\phi)} - U_0^{(\phi)}$ and $\hat{c} = c - U_0^{(\phi)}$, with $U^{(\phi)} = u\cos(\phi) + v\sin(\phi)$ the velocity in the direction of the azimuth ϕ and the subscript 0 referring to the launch level. Note that at the launch level $\hat{U} = 0$ so that the transformation renders the wave flux independent of azimuth. In the current formulation the departure spectrum is globally constant, therefore identical for each model column.

The final result for the scaled momentum or Eliassen-Palm flux density (having units ρ m^{2}s$^{-1}/d\hat{c} = \rho$ ms^{-1}) at the launch level $\hat{F}$ is obtained through scaling with $\rho_0 F_{\mathrm{launch}}$ which is the imposed launch momentum flux, and the most important free model parameter

$$\rho\hat{F}(\hat{c},\phi) = \rho F^{\star}(\hat{c},\phi) * A; \qquad A = (\rho_0 F_{\mathrm{launch}}) / \int (\rho F^{\star}(\hat{c},\phi_1))d\hat{c} \tag{5.6}$$

5.4 DISCRETISATION

The wave fluxes are defined at half model levels. Therefore, all variables like U, N (temperature) etc. required in the computation of the fluxes have to be interpolated to half-levels.

The wave spectrum is discretised in n_c phase speed bins, and n_ϕ equally spaced azimuths. The wave momentum flux is initialised at the model level just below the launch level height p_{launch}.

As it is the small-m portion of the spectrum which is associated with large values of momentum flux it is important to apply a coordinate stretch in order to obtain higher resolution and better accuracy at large phase speeds (i.e. small m). The problem is solved in the space of the transformed variable $\bar{X}$ having uniform resolution $d\bar{X}$. Taking as untransformed variable

$$X = \frac{1}{\hat{c}} \tag{5.7}$$

the coordinate stretch under the constraint $X_{\min} \le X \le X_{\max}$ is defined by

$$X = B_1 e^{(\bar{X}-X_{\min})/\Gamma} + B_2 \tag{5.8}$$

and

$$B_1 = \frac{X_{\max}-X_{\min}}{e^{(X_{\max}-X_{\min})/\Gamma}-1}; \qquad B_2 = X_{\min} - B_1 \tag{5.9}$$

The free parameters are the half-width of the stretch Γ, as well as $\hat{c}_{\min}$ with $X_{\min} = 1/\hat{c}_{\min}$, and $\hat{c}_{\max}$ with $X_{\max} = 1/\hat{c}_{\max}$. In discretised space this means one uses $\bar{X}_i = X_{\min} + (X_{\max} - X_{\min})(i/n_c)$ instead of $\hat{c}_i = \hat{c}_{\min} + (\hat{c}_{\max} - \hat{c}_{\min})(i/n_c)$, and the space element $d\hat{c}$ then becomes

$$d\hat{c} = \frac{d\hat{c}}{dX}\frac{dX}{d\bar{X}} = X^{-2}\frac{B_1}{\Gamma}e^{(\bar{X}-X_{\min})/\Gamma} \tag{5.10}$$

5.5 CRITICAL LEVEL FILTERING

Waves that encounter critical levels are filtered from the wave spectrum, depositing their momentum to the mean flow in this layer. In practice one checks for each azimuth bin in each layer z above the departure level and for each phase speed. Critical level filtering is encountered if U increases such with height that $\hat{U}_1 > \hat{U}_0$ and $\hat{U}_0 >\leq \hat{c} \le \hat{U}_1$. Then all momentum flux in the corresponding $(\hat{c},\phi)$ bin is removed from $\rho\bar{F}(\hat{c},\phi)$. Note that at the departure level $\hat{U}_0 = 0$ which sets an aboslute lower bound for critical filtering of $\hat{c} = \hat{c}_{\min}$.

The consequence of critical level filtering is that, as the waves propagate vertically through stratospheric westerlies (easterlies) as in the middle latitude winter (summer) hemisphere, the spectrum becomes more and more asymmetric with height leaving only the easterly (westerly) phase speed component. In contrast, in the tropical atmosphere winds change from easterlies to westerlies or vice versa and both wind directions are filtered, leaving little zonal momentum flux.

The portions of the wave spectrum that survive critical level filtering undergo conservative propagation to the next model level where they are checked for nonlinear dissipation.

5.6 NONLINEAR DISSIPATION

Nonlinear dissipation is simply modelled by assuming that waves are dissipative in nature and employing 'saturation' theory (Lindzen, 1981) such that the amplitude of the parametrized wave field is limited to some treshold value (thought to be associated with the onset of instability). This is dealt with empricially by limiting the growth of the gravity wave spectrum at large-m (short wavelengths) so as not to exceed the observed m^{-3} dependence. The saturation momentum flux is written as

$$\rho\hat{F}^{\rm sat}(\hat{c},\phi) = \rho C^{\star} A \frac{\hat{c}-\hat{U}}{N}\left(\frac{\hat{c}-\hat{U}}{\hat{c}}\right)^{2-{\rm p}} \tag{5.11}$$

where $C^{\star}$ is a tuning parameter introduced by McLandress and Scinocca (2005). The saturation momentum flux is depicted in Fig. 5.1. It decreases with height as a consequence of decreasing density, iit is therefore not conserved. Nonlinear dissipation is formulated as the constraint $\rho\hat{F}(\hat{c},\phi) \leq \rho\hat{F}^{\rm sat}(\hat{c},\phi)$. When the wave momentum flux exceeds the saturated value $\rho\hat{F}(\hat{c},\phi)$ is set equal to $\rho\hat{F}^{\rm sat}$ meaning that the excess momentum flux is deposited to the flow. Increasing the parameter $C^{\star}$ means pushing the onset of nonlinear dissipation to higher amplitudes and therefore to greater heights.

Finally, at the model top momentum conservation is achieved by depositing any remaining momentum from the wave field to the mean flow, i.e. the upper boundary condition is zero wave momentum flux.

5.7 TENDENCIES

The tendencies for the u, v wind components are given by the divergence of the net eastward $\rho\bar{F}_{\rm E}$, and northward, $\rho\bar{F}_{\rm N}$ momentum fluxes, which are obtained through summation of the total momentum flux (i.e. integrated over all phase speed bins) in each azimuth ϕ_i projected onto the east and north directions, respectively.

$$\left.\begin{aligned} \frac{\partial u}{\partial t} &= g\frac{\partial(\rho\bar{F}_{\rm E})}{\partial p}; \qquad \bar{F}_{\rm E} = \sum_{i=1}^{n_\phi}(\rho\hat{F}(\phi_i))\cos\phi_i \\ \frac{\partial v}{\partial t} &= g\frac{\partial(\rho\bar{F}_{\rm N})}{\partial p}; \qquad \bar{F}_{\rm N} = \sum_{i=1}^{n_\phi}(\rho\hat{F}(\phi_i))\sin\phi_i \end{aligned}\right\} \tag{5.12}$$

The dissipation of the non-orographic gravity waves (an external wave source) is also taken into account as a heat source for the model

$$\frac{\partial T}{\partial t} = -\frac{1}{c_p}\left(u\frac{\partial u}{\partial t} + v\frac{\partial v}{\partial t}\right) \tag{5.13}$$

5.8 PARAMETER SETTINGS

- $\hat{c}_{\rm min} = 0.25$ m s^{-1}, $\hat{c}_{\rm max} = 100$ m s^{-1}: minimum and maximum intrinsic phase speed
- $\Gamma = 0.25$: half width of the stretch in (5.8)
- $L = 2000$ m: transitional wavelength
- $p = 1$: the $\tilde{\omega}$ exponent in (5.5) and (5.11)

- $s = 1$: the small m spectral slope in (5.5) and (5.11)
- p_{launch}=450 hPa: launch elevation (Pa)
- n_ϕ=4 (=N, S, E, W): number of equally spaced azimuths
- n_c=25: number of spectral intervals for phase speed
- $C^\star$=1: non-dimensional constant for saturation spectrum in (5.11)
- $\rho_0 F_{\text{launch}} = 3.75 \times 10^{-4}$ (Pa): launch momentum flux

The most important tuning for future applications (in particular higher horizontal resolutions) would require a reduction of the amplitude of the launch momentum flux with increasing resolution so that as the resolved gravity wave momentum flux increases the parametrised flux decreases, and the total flux remains fairly constant. A reduction of the launch momentum flux would also increase the period of the models 'Quasi-Biennial Oscillation' which is currently too short. Further tuning could also include a time-dependent and horizontally variable amplitude of the launch momentum flux, but this is probably fairly difficult to achieve.

5.9 CODE

The principal routine is GWDRAG_WMS, which is called from CALLPAR. The tunable parameters are defined in the setup routine SUGWWMS which is called from SUPHEC. To save computing time routine GWDRAG_WMS is not called every time step, but typically every few time steps (i.e. every hour for spectral truncations >255 and every 2 hours for truncations < 255. Therefore, the tendencies due to non-orographic gravity wave dissipation are stored in buffers (GFL arrays), and the total physics tendencies are incremented every time step inside routine GWDRAG_WMS.

APPENDIX A. LIST OF SYMBOLS

A	scaling factor for momentum flux density
B	formal dimensional constant, not actually used
c	phase speed
$\tilde{c}$	intrinsic phase speed $= c - U$
$\hat{c}$	intrinsic phase speed using departure level Doppler shift$= c - U_0$
c_{g}	group velocity
$\hat{c}_{\text{max}}$	maximum intrinsic phase speed
$\hat{c}_{\text{min}}$	minimum intrinsic phase speed
c_p	specific heat at constant pressure
$C_\star$	parameter
F	wave momentum flux (without density factor)
F^{sat}	saturation value of wave momentum flux
g	gravity constant
Γ	parameter
k	horizontal wavenumber
L	transitional wavelength
m	vertial wavenumber
n_c	number of phase speed bins
n_ϕ	number of azimuth bins
N	Brunt–Väisälä frequency
p	constant, the ω exponent
p	pressure
s	constant, the small m spectral slope
t	time
T	temperature
u	west-east component of wind speed
U	wind speed in direction of wave
v	south-north component of wind speed
z	height

ϕ azimuthal direction
ω frequency

Chapter 6
Convection

Table of contents

6.1 INTRODUCTION

Cumulus convection is parametrized by a bulk mass flux scheme which was originally described in Tiedtke (1989). The scheme considers deep, shallow and mid-level convection. Clouds are represented by a single pair of entraining/detraining plumes which describes updraught and downdraught processes. Momentum and tracer transport is also included.

6.2 LARGE-SCALE BUDGET EQUATIONS

The contributions from cumulus convection to the large-scale budget equations of heat moisture, momentum, and chemical tracers are

$$\left.\begin{aligned}
\left(\frac{\partial \bar{s}}{\partial t}\right)_{\rm cu} &= g\frac{\partial}{\partial p}[M_{\rm up}s_{\rm up} + M_{\rm down}s_{\rm down} - (M_{\rm up}+M_{\rm down})\bar{s}] \\
&\quad +L(c_{\rm up} - e_{\rm down} - e_{\rm subcld}) - (L_{\rm subl} - L_{\rm vap})(M_{\rm elt} - F_{\rm rez}) \\
\left(\frac{\partial \bar{q}}{\partial t}\right)_{\rm cu} &= g\frac{\partial}{\partial p}[M_{\rm up}q_{\rm up} + M_{\rm down}q_{\rm down} - (M_{\rm up}+M_{\rm down})\bar{q}] \\
&\quad -(c_{\rm up} - e_{\rm down} - e_{\rm subcld}) \\
\left(\frac{\partial \bar{u}}{\partial t}\right)_{\rm cu} &= g\frac{\partial}{\partial p}[M_{\rm up}u_{\rm up} + M_{\rm down}u_{\rm down} - (M_{\rm up}+M_{\rm down})\bar{u}] \\
\left(\frac{\partial \bar{v}}{\partial t}\right)_{\rm cu} &= g\frac{\partial}{\partial p}[M_{\rm up}v_{\rm up} + M_{\rm down}v_{\rm down} - (M_{\rm up}+M_{\rm down})\bar{v}] \\
\left(\frac{\partial \bar{C}^i}{\partial t}\right)_{\rm cu} &= g\frac{\partial}{\partial p}[M_{\rm up}C^i_{\rm up} + M_{\rm down}C^i_{\rm down} - (M_{\rm up}+M_{\rm down})\bar{C}^i]
\end{aligned}\right\} \tag{6.1}$$

where $M_{\rm up}$, $M_{\rm down}$ are the net contributions from all clouds to the updraught and downdraught mass fluxes, $c_{\rm up}$ and $e_{\rm down}$ are the condensation/sublimation in the updraughts, and the evaporation in the downdraughts. $s_{\rm up}$, $s_{\rm down}$, $q_{\rm up}$, $q_{\rm down}$, $u_{\rm up}$, $u_{\rm down}$, $v_{\rm up}$, $v_{\rm down}$, $C^i_{\rm up}$ and $C^i_{\rm down}$ are the weighted averages of the dry static energy $\bar{s}$, the specific humidity $\bar{q}$, the horizontal wind components $\bar{u}$ and $\bar{v}$ and the passive chemical tracer $\bar{C}^i$ from all updraughts and downdraughts within a grid box (although individual convective elements are not considered) obtained from the bulk cloud model described below. $L_{\rm subl}$ and $L_{\rm vap}$ are latent heats of sublimation and vaporization, and L is the effective latent heat for an ice–water mix (an empirical function of temperature). $e_{\rm subcld}$ is the evaporation of precipitation in the unsaturated sub-cloud layer, $M_{\rm elt}$ is the melting rate of snow and $F_{\rm rez}$ is the freezing rate of condensate in the convective updraught. In addition to (6.1) the precipitation fluxes are defined as

$$P^{\rm rain}(p) = \int_{P{\rm top}}^{p}(G^{\rm rain} - e^{\rm rain}_{\rm down} - e^{\rm rain}_{\rm subcld} + M_{\rm elt})\frac{dp}{g};\; P^{\rm snow}(p) = \int_{P{\rm top}}^{p}(G^{\rm snow} - e^{\rm snow}_{\rm down} - e^{\rm snow}_{\rm subcld} - M_{\rm elt})\frac{dp}{g} \tag{6.2}$$

where $P^{\rm rain}$ and $P^{\rm snow}$ are the fluxes of precipitation in the forms of rain and snow at level p. $G^{\rm rain}$ and $G^{\rm snow}$ are the conversion rates from cloud water into rain and cloud ice into snow, and $M_{\rm elt}$ denotes melted precipitation. The evaporation of precipitation in the downdraughts $e_{\rm down}$, and below cloud base $e_{\rm subcld}$, have been split into water and ice components, $e^{\rm rain}_{\rm down}$, $e^{\rm snow}_{\rm down}$, $e^{\rm rain}_{\rm subcld}$, and $e^{\rm snow}_{\rm subcld}$. The microphysical terms in (6.1) and (6.2) referring to the updraught are explained in detail in Section 6.6, those referring to the downdraught are defined in (6.16).

6.3 CLOUD MODEL EQUATIONS

6.3.1 Updraughts

The updraught of the cloud ensemble is assumed to be in a steady state. Then the bulk equations for mass, heat, moisture, cloud water content, momentum and tracers are

$$\left.\begin{aligned}
-g\frac{\partial M_{\rm up}}{\partial p} &= E_{\rm up} - D_{\rm up} \\
-g\frac{\partial (M_{\rm up}s_{\rm up})}{\partial p} &= E_{\rm up}\bar{s} - D_{\rm up}s_{\rm up} + Lc_{\rm up}, \quad -g\frac{\partial (M_{\rm up}q_{\rm up})}{\partial p} = E_{\rm up}\bar{q} - D_{\rm up}q_{\rm up} - c_{\rm up} \\
-g\frac{\partial (M_{\rm up}l_{\rm up})}{\partial p} &= -D_{\rm up}l_{\rm up} + c_{\rm up} - G, \quad -g\frac{\partial (M_{\rm up}r_{\rm up})}{\partial p} = -D_{\rm up}r_{\rm up} + G - S_{\rm fallout} \\
-g\frac{\partial (M_{\rm up}u_{\rm up})}{\partial p} &= E_{\rm up}\bar{u} - D_{\rm up}u_{\rm up}, \quad -g\frac{\partial (M_{\rm up}v_{\rm up})}{\partial p} = E_{\rm up}\bar{v} - D_{\rm up}v_{\rm up} \\
-g\frac{\partial (M_{\rm up}C^i_{\rm up})}{\partial p} &= E_{\rm up}\bar{C}^i - D_{\rm up}C^i_{\rm up}
\end{aligned}\right\} \tag{6.3}$$

where $E_{\rm up}$ and $D_{\rm up}$ are the rates of mass entrainment and detrainment, $l_{\rm up}$ is the updraught cloud water/ice content, and $r_{\rm up}$ is precipitating rain and snow. The vertical integration of (6.3) requires knowledge of the cloud-base mass flux and of the mass entrainment and detrainment rates. the cloud-base mass flux is determined for the various types of convection from the closure assumptions discussed in Section 6.4.

Entrainment of mass into convective plumes is assumed to occur (1) through turbulence exchange of mass through the cloud edges, and (2) through organized inflow; and detrainment is assumed to occur (1) through turbulent exchange and (2) through organized outflow at cloud top. The superscripts (1) and (2) are used to denote the components of the entrainment and detrainment due to turbulent and organized exchanges, respectively

$$E_{\rm up} = E^{(1)}_{\rm up} + E^{(2)}_{\rm up}, \quad D_{\rm up} = D^{(1)}_{\rm up} + D^{(2)}_{\rm up} \tag{6.4}$$

(a) Entrainment and detrainment rates

Turbulent entrainment and detrainment rates ($\rm s^{-1}$) are parametrized as

$$E^{(1)}_{\rm up} = \varepsilon^{(1)}_{\rm up} \frac{M_{\rm up}}{\bar{\rho}} f^{(1)}_{\rm scale} \quad D^{(1)}_{\rm up} = \delta^{(1)}_{\rm up} \frac{M_{\rm up}}{\bar{\rho}} \tag{6.5}$$

where the fractional entrainment/detrainment ($\rm m^{-1}$) depend inversely on cloud radii in the updraughts ($R_{\rm up}$) (Simpson and Wiggert, 1969; Simpson, 1971) so that

$$\varepsilon^{(1)}_{\rm up} = \frac{0.2}{R_{\rm up}}, \quad f^{(1)}_{\rm scale} = 4\left(\frac{q_{\rm sat}(\bar{T})}{q_{\rm sat}(\bar{T}_{\rm base})}\right)^2 \tag{6.6}$$

By assuming typical cloud sizes for the various types of convection, average values of fractional entrainment/detrainment are defined

$$\varepsilon^{(1)}_{\rm up} = \begin{cases} 0.8 \times 10^{-4}\ \rm m^{-1} & \text{for penetrative and midlevel convection} \\ 3.0 \times 10^{-4}\ \rm m^{-1} & \text{for shallow convection} \end{cases}$$
$$\delta^{(1)}_{\rm up} = 1.2 \times \varepsilon^{(1)}_{\rm up} \tag{6.7}$$

(6.7) implies an updraught (base) radius of roughly 625 m for deep convective clouds, and 150 m for shallow convection, with the latter value being typical for the larger trade wind cumuli (Nitta, 1975). In (6.5) we have also included a vertical scaling function $f^{(1)}_{\rm scale}$ in order to mimick the effects of a cloud ensemble. As the scaling function strongly decreases with height the detrainment rate will become eventually larger than the entrainment rate, and the mass flux starts to decrease with height.

(b) Organized entrainment and detrainment

Organized entrainment is applied to positively buoyant deep convection only.Observations show that mid-tropospheric relative humidity strongly controls the cloud top heights, in particular over the tropical oceans. It turned out that the simplest way to represent this sensitivity and to increase the mass fluxes in unstable buoyant situation, is a formulation depending on the environmental relative humidity RH

$$E^{(2)}_{\rm up} = \varepsilon^{(2)}_{\rm up} \frac{M_{\rm up}}{\bar{\rho}} \Big(1.3 - RH\Big) f^{(2)}_{\rm scale}, \quad \varepsilon^{(2)}_{\rm up} = 0.8 \times 10^{-3} \rm m^{-1}, \quad f^{(2)}_{\rm scale} = \left(\frac{q_{\rm sat}(\bar{T})}{q_{\rm sat}(\bar{T}_{\rm base})}\right)^3 \tag{6.8}$$

The formulation (6.5)-(6.8) produce on average a vertical distribution of the convective mass flux that broadly follows that of the large-scale ascent which is partly supported by diagnostic studies for tropical convection (e.g. Cheng *et al.*, 1980; Johnson, 1980). Finally, note that in cycles prior to 32r3 the organized entrainment has been linked to the the large-scale moisture convergence as first advocated by Lindzen (1981). However, the imposed strong coupling between the large-scale and the convection had a detrimental effect on the forecasts ability to represent tropical variability. Only since Cy32r3, using entrainment rates scaled by a vertical function together with a relative humidity based organized entrainment, and a varibale convective adjustment time-scale (see below), the model is able to maintain a realistic level of tropical variability.

Organized detrainment is estimated from the vertical variation of the updraught vertical velocity $w_{\rm up}$, which is estimated from the budget equation for the updraught kinetic energy written in height coordinates

$$\frac{\partial K_{\rm up}}{\partial z} = -\frac{\mu_{\rm up}}{M_{\rm up}}(1+\beta C_{\rm d})2K_{\rm up} + \frac{1}{f(1+\gamma)}g\frac{T_{\rm v,up}-\bar{T}_{\rm v}}{\bar{T}_{\rm v}} \tag{6.9}$$

with

$$K_{\rm up} = \frac{w_{\rm up}^2}{2} \tag{6.10}$$

where $K_{\rm up}$ is the updraught kinetic energy, $T_{\rm v,up}$ is the virtual temperature of the updraught and $\bar{T}_{\rm v}$ the virtual temperature of the environment. $\mu_{\rm up}$ is a mixing coefficient which is equal to the entrainment rate (E_{up}), or the detrainment rate (D_{up}) if this is larger. As entrainment is set to zero in the upper part of the cloud layer, use of detrainment in this region better represents the effect of mixing and vertical pressure gradients in the upper part of deep convective clouds, reducing vertical velocity and reducing overshoot of convective towers into the lower stratosphere.

$\gamma = 0.5$ is the virtual mass coefficient (Simpson and Wiggert, 1969), the factor $f = 2$ is introduced because the flow is highly turbulent (Cheng *et al.*, 1980) and for the drag coefficient a value of $C_{\rm d} = 0.506$ is used (Simpson and Wiggert, 1969). The value for β is 1.875. The cloud base value of the updraught velocity is chosen as 1 m s^{-1}.

$w_{\rm up}$ enters the scheme in several ways: (i) for the generation and fallout of rain (Section 6.6), (ii) to determine the penetration above the zero-buoyancy level and the top of cumulus updraughts (where $w_{\rm up}$ reduces to zero), and (iii) to specify detrainment below the top of the updraught.

Organized detrainment is estimated by equating the decrease in updraught vertical velocity due to negative buoyancy at the top of the cloud to the decrease in mass flux with height:

$$\frac{M_{\rm up}(z)}{M_{\rm up}(z+\Delta z)} = \sqrt{\frac{K_{\rm up}(z)}{K_{\rm up}(z+\Delta z)}} \tag{6.11}$$

This assumes that the cloud area remains constant in the detraining layer. (6.11) defines the reduction of mass flux with height, which combined with the updraught continuity equation (see (6.3)) gives the organised detrainment rate.

6.3.2 Downdraughts

Downdraughts are considered to be associated with convective precipitation from the updraughts and originate from cloud air influenced by the injection of environmental air. Following Fritsch and Chappell (1980) and Foster (1958), the Level of Free Sinking (LFS) is assumed to be the highest model level (below the level of minimum moist static energy) where a mixture of equal parts of cloud and saturated environmental air at the wet-bulb temperature becomes negative buoyant with respect to the environmental air. The downdraught mass flux is assumed to be directly proportional to the upward mass flux. Following Johnson (1976, 1980) the mass flux at the LFS is specified from the updraught mass flux at cloud base as

$$(M_{\rm down})_{\rm LFS} = -\eta(M_{\rm up})_{\rm base} \quad \text{with} \quad \eta = 0.3 \tag{6.12}$$

The vertical distribution of the downdraught mass flux, dry static energy, moisture, horizontal momentum and passive tracers below the LFS are determined by entraining/detraining plume equations similar to

those for the updraught:

$$\left.\begin{aligned} g\frac{\partial M_{\rm down}}{\partial p} &= E_{\rm down} - D_{\rm down} \\ g\frac{\partial (M_{\rm down} s_{\rm down})}{\partial p} &= E_{\rm down}\bar{s} - D_{\rm down} s_{\rm down} + Le_{\rm down} \\ g\frac{\partial (M_{\rm down} q_{\rm down})}{\partial p} &= E_{\rm down}\bar{q} - D_{\rm down} q_{\rm down} - e_{\rm down} \\ g\frac{\partial (M_{\rm down} u_{\rm down})}{\partial p} &= E_{\rm down}\bar{u} - D_{\rm down} u_{\rm down} \\ g\frac{\partial (M_{\rm down} v_{\rm down})}{\partial p} &= E_{\rm down}\bar{v} - D_{\rm down} v_{\rm down} \\ g\frac{\partial (M_{\rm down} C^i_{\rm down})}{\partial p} &= E_{\rm down}\bar{C}^i - D_{\rm down} C^i_{\rm down} \end{aligned}\right\} \tag{6.13}$$

$e_{\rm down}$ is the evaporation of convective rain to maintain a saturated descent; the moistening and cooling of the environmental air injected at the LFS is also due to evaporating rain.

Entrainment and detrainment in downdraughts are highly uncertain as relevant data are not available. As for the updraught, both turbulent and organized entrainment/detrainment are considered.

(a) *Turbulent entrainment and detrainment*

For turbulent mixing

$$\varepsilon^{(1)}_{\rm down} = \delta^{(1)}_{\rm down} = 2 \times 10^{-4}\ {\rm m}^{-1} \tag{6.14}$$

(b) *Organized entrainment and detrainment*

Organized entrainment for the downdraught is based upon a formulation suggested by Nordeng (1994) so that

$$\varepsilon^{(2)}_{\rm down} = \frac{\left\{ g\frac{T_{\rm v,down} - T_{\rm down} r_{\rm down} - \bar{T}_{\rm v}}{\bar{T}_{\rm v}} \right\}}{(w^{\rm LFS}_{\rm down})^2 - \int_{z_{\rm LFS}}^{z} \left\{ g\frac{T_{\rm v,down} - T_{\rm down} r_{\rm down} - \bar{T}_{\rm v}}{\bar{T}_{\rm v}} \right\} {\rm d}z} \tag{6.15}$$

where $w^{\rm LFS}_{\rm down}$ is the vertical velocity in the downdraught at the LFS (set to -1 ms^{-1}). The total evaporation rate in the downdraft corresponds to the total downdraft precipitation rate that is simply given as

$$\sum_{k={\rm LFS}}^{\rm nlev} e_{\rm down} = \sum_{k={\rm LFS}}^{\rm nlev} \frac{g}{\Delta p}(q_{\rm down,k} - \hat{q}_{\rm down,k}) M_{\rm down,k} \tag{6.16}$$

where $q_{\rm down,k}$ is the value of the downdraft humidity computed from (6.13) without saturation adjustment, and $\hat{q}_{\rm down,k}$ is the humidity after the saturation adjustment. The value of the rain water content in the downdraft used in (6.15) is estimated as $r_{\rm down} = e_{\rm down} g/(\Delta p M_{\rm up})$, for the definition of the pressure thickness Δp of layer k see (6.49).

Organized detrainment from the downdraught occurs when either the downdraught becomes positively buoyant or approaches the surface. If the downdraught remains negatively buoyant until it reaches the surface then the mass flux is decreased linearly over the lowest 60 hPa of the atmosphere. However, if a downdraught becomes positively buoyant during its descent, it is detrained over one level, except where this occurs at cloud base. In this case the downdraught fluxes are decreased linearly (deep convection) or quadratically (mid-level convection) to zero at the surface.

6.4 CONVECTION INITIATION AND CONVECTIVE TYPES

The first important task of a convection parameterization is to decide if convection is active or not in a model grid column. This is done in a very simplified "first-guess" updraught computation that implies the determination of the cloud base level, i.e. the Lifting Condensation Level (LCL), and of the properties

of the cloud (updraught) at cloud base. Furthermore, in using a bulk mass flux scheme, as opposed to a scheme which considers an ensemble of convective clouds (such as that of Arakawa and Schubert, 1974), some determination of convective cloud type must be made so that appropriate choices can be made for the cloud properties.

The scheme first tests for the occurrence of shallow convection by computing the ascent of a surface parcel. The following simplified updraught equation is applied

$$\frac{\partial \phi_{\rm up}}{\partial z} = \varepsilon_{\rm up}^{\rm ini}(\bar{\phi} - \phi_{\rm up}) \tag{6.17}$$

where ϕ stands either for the dry static energy or the total water specific humidity. As proposed by Jakob and Siebesma (2003) the entrainment rate for the test parcel for shallow convection is set to $\varepsilon_{\rm up}^{\rm ini} = 0.5(\frac{0.55}{z} + 1 \times 10^{-4})$. Additionally, a temperature $\Delta T_{\rm up}$ and moisture excess $\Delta q_{\rm up}$ with respect to the environment is given to the test parcel at the lowest model level depending on the surface sensible and latent turbulent heat fluxes

$$\Delta T_{\rm up}^{\rm shal} = -1.5\frac{J_s}{\bar{\rho} c_p w_*} \quad \text{and} \quad \Delta q_{\rm up}^{\rm shal} = -1.5\frac{J_q}{\bar{\rho} L w_*} \tag{6.18}$$

where the convective-scale velocity w_* is given as

$$w_* = 1.2\left(u_*^3 - 1.5\frac{gz\kappa}{\bar{\rho}\bar{T}}\left[\frac{J_s}{c_p} + 0.61\bar{T}\frac{J_{\rm v}}{L}\right]\right)^{\frac{1}{3}} \tag{6.19}$$

with $\kappa = 0.4$ the von Kármán constant; the friction velocity u_* is set to a constant value of 0.1 $\rm ms^{-1}$. The convective-scale velocity w_* is also used to initialise the updraft vertical velocity at the first model level. A grid column is then identified as shallow convective if a LCL is found for the surface parcel, if the updraft vertical velocity at the LCL (obtained by solving the kinetic energy equation (6.9)) is positive, and if the cloud thickness is smaller than 200 hPa.

Next, the occurrence of deep convection is tested for by repeating the updraught computations but starting at the next higher model level. However, the entrainment rate is now set as for the first full updraught computation (6.7), i.e. $\varepsilon_{\rm up}^{\rm ini} = \varepsilon_{\rm up}^{(1)}$, simplified microphysics is taken into account by removing at each level 50% of the condensed water; the initial parcel perturbations are specified as

$$\Delta T_{\rm up}^{\rm deep} = 0.2 \text{ K} \quad \text{and} \quad \Delta q_{\rm up}^{\rm deep} = 1 \times 10^{-4} \text{ kg kg}^{-1} \tag{6.20}$$

and the updraught vertical velocity at the departure level is initialised to 1 $\rm ms^{-1}$. Furthermore, in the lowest 60 hPa of the atmosphere that typically correspond to the mixed-layer depth over oceanic regions, the updraught values of the dry static energy (or humidity) at the departure level k are initialised as $s_{{\rm up},k} = \tilde{s}_k + c_p \Delta T_{\rm up}^{\rm deep}$, where the tilde symbol represents a 50 hPa layer average, instead of $s_{{\rm up},k} = \bar{s}_k + c_p \Delta T_{\rm up}^{\rm deep}$ as for departure levels above the assumed 60 hPa mixed-layer. The idea behind is that deep convection requires a sufficiently deep source layer, this procedure also avoids spurious convection in the early morning hours when the surface-layer undergoes strong heating. A grid-column is then identified as deep-convective, if a LCL is found and the resulting cloud (the top being defined as the level where the updraught vertical velocity vanishes) is thicker than 200 hPa. If this criterion is verified the cloud is identified as deep and the results obtained for the shallow convective test parcel are ignored (only one cloud type can exist). If no deep convective cloud is found for the given departure level, the procedure is repeated starting from the next higher model level and so on until the departure level of the test parcel is more than 350 hPa above ground. A summary of this procedure, and a discussion of the consequences for the simulation of the diurnal cycle of convection over land is given in Bechtold *et al.* (2004).

Finally, if neither deep nor shallow convection has been found, elevated (or mid-level) convection is tested for (see Subsection 6.4.3). Also, at the end of this procedure and if a column has been identified as convective, the computed values of the updraught vertical velocity, dry static energy, liquid water and specific humidity at cloud base are used to initialise the following full updraught computation at cloud base. The updraught values of the horizontal wind components at cloud base are simply set to the environmental values at the level just below (see Section 6.9).

In the following, the determination of the convective activity (as controlled by the cloud-base mass flux) is discussed separately for each type of convection.

6.4.1 Deep convection

Following Fritsch and Chappell (1980) and Nordeng (1994), the cloud base mass flux for deep convection is estimated from assuming that convection acts to reduce the convective available potential energy (CAPE) towards zero over a specified time scale τ. Therefore

$$\frac{\partial \mathrm{CAPE}}{\partial t} = -\frac{\mathrm{CAPE}}{\tau} = \int_{z_{\mathrm{base}}}^{z_{\mathrm{top}}} \frac{g}{\bar{T}_{\mathrm{v}}} \left(\frac{\partial \bar{T}_{\mathrm{v}}}{\partial t}\right)^{\mathrm{cum}} \mathrm{d}z \approx \int_{z_{\mathrm{base}}}^{z_{\mathrm{top}}} \frac{M_{\mathrm{cld}}}{\bar{\rho}} \frac{g}{\bar{T}_{\mathrm{v}}} \left(\frac{\partial \bar{T}_{\mathrm{v}}}{\partial z}\right) \mathrm{d}z \tag{6.21}$$

where

$$M_{\mathrm{cld}} = M_{\mathrm{up}} + M_{\mathrm{down}} = \alpha [M_{\mathrm{up}}]_{\mathrm{base}} + \beta [M_{\mathrm{down}}]_{\mathrm{LFS}} \tag{6.22}$$

where α and β describe the vertical variation of the updraught and downdraught mass flux due to entrainment and detrainment and the subscript 'base' refers to cloud-base quantities. As the downdraught mass flux at the LFS is linked to the updraught mass flux at cloud base (see (6.12)) then

$$M_{\mathrm{cld}} = [M_{\mathrm{up}}]_{\mathrm{base}} (\alpha - \beta\eta) \tag{6.23}$$

Using (6.23) in (6.21) results in an expression for the "final" cloud base mass flux given by

$$[M_{\mathrm{up}}]_{\mathrm{base}} = \frac{\frac{CAPE}{\tau}}{g \int_{z_{\mathrm{base}}}^{z_{\mathrm{top}}} (\alpha - \beta\eta) \frac{g}{\bar{\rho}\bar{T}_{\mathrm{v}}} \frac{\partial \bar{T}_{\mathrm{v}}}{\partial z} \mathrm{d}z} = \frac{\frac{CAPE}{\tau}}{g \int_{z_{\mathrm{base}}}^{z_{\mathrm{top}}} \frac{M_{\mathrm{cld}}^{n-1}}{M_{\mathrm{base}}^{n-1}} \frac{1}{\bar{\rho}\bar{T}_{\mathrm{v}}} \frac{\partial \bar{T}_{\mathrm{v}}}{\partial z} \mathrm{d}z} \tag{6.24}$$

where M_{cld}^{n-1} is the cloud mass flux from the first full updraught (n − 1 = 1) computation that has been initialised with a unit cloud base mass flux $M_{\mathrm{base}}^{n-1} = 0.1\Delta p_{\mathrm{base}}/(g\Delta t)$, with Δt the model time step, and where CAPE is estimated from the parcel ascent incorporating the effects of water loading,

$$\mathrm{CAPE} = \int_{z_{\mathrm{base}}}^{z_{\mathrm{top}}} g \left(\frac{T_{\mathrm{v,up}} - \bar{T}_{\mathrm{v}}}{\bar{T}_{\mathrm{v}}} - l_{\mathrm{up}}\right) \mathrm{d}z \tag{6.25}$$

Using these estimates the updraught mass flux at cloud base is recomputed and downdraught mass fluxes are rescaled. A second updraught ascent is then computed to revise the updraught properties.

The closure is complete with the specification of the adjustment time scale τ. In cycles prior to 32r3 it was set close to or larger than the model time step (τ=3600 s at T159, 1200 s at T511 and 600 s at T799). In cylce 32r3 it is set proportional to a convective turnover time scale

$$\tau = \bar{w}_{\mathrm{up}}^{H} \quad \alpha_{n_T}, \qquad \alpha_{n_T} = (1 + 264/n_T), \qquad \Delta t <= \tau <= 10800 \text{ s} \tag{6.26}$$

where H is the cloud depth, $\bar{w}_{\mathrm{up}}^{H}$ is the cloud average updraught velocity. α_{n_T} is a proportionality factor depending on horizontal resolution (model truncation n_T) so that the adjustment time scale varies by roughly a factor of two between model truncations T799 and T159.

6.4.2 Shallow convection

Here we consider cumulus convection, which predominantly occurs in undisturbed flow, that is in the absence of large-scale convergent flow. Typical examples are trade-wind cumuli under a subsidence inversion, convection occurring in the ridge region of tropical easterly waves and daytime convection over land. This type of convection seems to be effectively controlled by sub-cloud layer turbulence. In fact, most of the diagnostic studies carried out for trade-wind cumuli show that the net upward moisture flux at cloud-base level is nearly equal to the turbulent moisture flux at the surface (Le Mone and Pennell, 1976). In regions of cold air flowing over relatively warm oceans the strong sensible heat flux has been found to be of significant importance. We therefore derive the mass flux at cloud base on a balance assumption for the sub-cloud layer based on the moist static energy budget given by

$$[M_{\mathrm{up}}(h_{\mathrm{up}} - \bar{h})]_{\mathrm{base}} = -\int_{\mathrm{surf}}^{\mathrm{base}} \left(\bar{\mathbf{V}} \cdot \nabla \bar{h} + \bar{\omega} \frac{\partial}{\partial p} \bar{h} - c_p \left(\frac{\partial}{\partial t} \bar{T}\right)_{\mathrm{rad}} + \frac{\partial}{\partial p} (\overline{\omega' h'})_{\mathrm{turb}}\right) \frac{dp}{g} \tag{6.27}$$

with

$$\bar{h} = c_p\bar{T} + L\bar{q} + gz \tag{6.28}$$

The moisture supply to the shallow cumulus is largely through surface evaporation as the contributions from large-scale convergence are either small or even negative, such as in the undisturbed trades where dry air is transported downward to lower levels.

An initial estimate for the updraught base mass flux is obtained using (6.27). If downdraughts occur (relatively rare for shallow convection due to the low precipitation rates), then a revised estimate is made accounting for the impact of downdraughts upon the sub-cloud layer, the l.h.s. of (6.27) being replaced by

$$[M_{\rm up}(h_{\rm up} - \bar{h})]_{\rm base} + [M_{\rm down}(h_{\rm down} - \bar{h})]_{\rm base} = [M_{\rm up}(h_{\rm up} - \bar{h})]_{\rm base} - [\beta\eta M_{\rm up}(h_{\rm down} - \bar{h})]_{\rm base} \tag{6.29}$$

Again downdraught properties are obtained using the original estimate of the updraught base mass flux and then rescaled by the revised value. For the updraught a second ascent is calculated using the revised value of the base mass flux.

No organized entrainment is applied to shallow convection. As turbulent entrainment and detrainment rates are equal, the mass flux remains constant with height until reducing at cloud top by organized detrainment.

6.4.3 Mid-level convection

Mid-level convection, that is, convective cells which have their roots not in the boundary layer but originate at levels above the boundary layer, often occur at rain bands at warm fronts and in the warm sector of extratropical cyclones (Browning *et al.*, 1973; Houze *et al.*, 1976; Herzegh and Hobbs, 1980). These cells are probably formed by the lifting of low level air until it becomes saturated (Wexler and Atlas, 1959) and the primary moisture source for the clouds is from low-level large-scale convergence (Houze *et al.*, 1976). Often a low-level temperature inversion exists that inhibits convection from starting freely from the surface; therefore convection seems to be initiated by lifting low-level air dynamically to the level of free convection. This occurs often in connection with mesoscale circulations which might be related to conditionally symmetric instability (Bennets and Hoskins, 1979; Bennets and Sharp, 1982) or a wave-CISK mechanism (Emanuel, 1982).

Although it is not clear how significant the organization of convection in mesoscale rain bands is for the large- scale flow, a parametrization should ideally account for both convective and mesoscale circulations. Such a parametrization, however, is presently not available and we must therefore rely on simplified schemes. Here we use a parametrization which in a simple way considers the finding of the diagnostic studies mentioned above. We assume that mid-level convection can be activated in a height range between 5×10^2 m $< z < 1 \times 10^4$ m when there is a large-scale ascent, and the environmental air is sufficiently moist, i.e. of relative humidity in excess of 80%.

The convective mass flux at cloud base is set equal to the vertical mass transport by the large-scale flow at that level:

$$\bar{\rho}_{\rm base}\bar{w}_{\rm base} = (M_{\rm up})_{\rm base} + (M_{\rm down})_{\rm base} = (M_{\rm up})_{\rm base}(1 - \beta\eta) \tag{6.30}$$

following the notation of Subsection 6.4.1 above. Again two estimates of the updraught base mass flux are made; first neglecting downdraughts, followed by a revised estimate if downdraughts occur. The closure ensures that the amount of moisture which is vertically advected through cloud base by the large-scale ascent is fully available for generation of convective cells.

6.5 SUB-CLOUD LAYER

The first level at which convective mass, momentum and thermodynamic fluxes are estimated is cloud base. To represent the effects of convective updraughts on the sub-cloud layer a simple scaling of cloud base fluxes is applied in which they decrease to zero at the surface through the sub-cloud layer.

Care must be taken to ensure that fluxes of liquid water are zero below cloud base. Through the cloud base level an interpolation of the fluxes of liquid water static energy and total water content is used to

estimate fluxes of dry static energy and water vapour mixing ratio in the level immediately below cloud base;

$$\begin{aligned}(Ms)_{\rm up}^{\rm base+1} &= (Z^n)(Ms)_{\rm up}^{\rm base} - L(Ml)_{\rm up}^{\rm base}\\ (Mq)_{\rm up}^{\rm base+1} &= (Z^n)(Mq)_{\rm up}^{\rm base} + (Ml)_{\rm up}^{\rm base}\\ (Ml)_{\rm up}^{\rm base+1} &= 0\end{aligned} \tag{6.31}$$

where $\phi^{\rm base+1}$ refers to the value of ϕ at the level immediately below cloud base. Z is given by

$$Z = \left(\frac{p_{\rm surf} - p_{\rm base+1}}{p_{\rm surf} - p_{\rm base}}\right)^m \tag{6.32}$$

and $p_{\rm surf}$ is the surface pressure.

For deep and shallow convection m is set to 1 (implying a linear decrease in the flux with pressure below cloud base) while for mid-level convection m is equal to 2 (implying a quadratic reduction in flux below cloud base).

For the remainder of the sub-cloud layer, fluxes at level 'B + 1' are reduced to zero at the surface using Z recomputed as

$$Z = \left(\frac{p_{\rm surf} - p_k}{p_{\rm surf} - p_{\rm base+1}}\right)^m \tag{6.33}$$

where p_k is the pressure at level model k.

The cloud-mass and momentum fluxes in the sub-cloud layer are treated in a similar manner.

6.6 CLOUD MICROPHYSICS

6.6.1 Condensation rate in updraughts

The updraught condensation rate $c_{\rm up}$ is computed through a saturation adjustment

$$c_{\rm up} = \frac{g}{\Delta p}(q_{\rm up} - \hat{q}_{\rm up})M_{\rm up} \tag{6.34}$$

where $q_{\rm up}$ is the value of the specific humidity before the saturation adjustment, and $\hat{q}_{\rm up}$ is the specific humidity at saturation after the adjustment.

6.6.2 Freezing in convective updraughts

We assume that condensate in the convective updraughts freezes in the temperature range 250.16 K $< T <$ 273.16 K maintaining a mixed phase within that range according to (7.6) (see Chapter 7 'Clouds and large-scale precipitation').

6.6.3 Generation of precipitation

The conversion from cloud water/ice to rain/snow is treated in a consistent way with that in the large-scale precipitation scheme by using a formulation following Sundqvist (1978)

$$G^{\rm precip} = \frac{M_{\rm up}}{\bar{\rho}}\frac{c_0}{0.75 w_{\rm up}} l_{\rm up}[1 - \exp\{-(l_{\rm up}/l_{\rm crit})^2\}] \tag{6.35}$$

where $c_0 = 1.4 \times 10^{-3}$ s^{-1} and $l_{\rm crit} = 0.5$ g kg^{-1}. $w_{\rm up}$ is the updraught vertical velocity and is limited to a maximum value of 10 m s^{-1} in (6.35). Conversion only proceeds if $l_{\rm up}$ is greater than a threshold liquid water content of 0.3 g kg^{-1} to prevent precipitation generation from small water contents. The value of the autoconversion coefficient is higher than in previous cycles where it was around $c_0 = 1 \times 10^{-3}$ s^{-1}. With this value the updraft condensate content is probably still overestimated. However, with even larger values of the conversion coefficient the precipitation efficiency of the convection scheme would be too high, and the detrainment of cloud condensate too low.

Sundqvist (1978) takes into account the Bergeron–Findeisen process for temperatures below −5°C through a temperature dependent modification of c_0 and $l_{\rm crit}$ given by

$$\begin{aligned} c_0' &= c_0 c_{\rm BF} \\ l_{\rm crit}' &= l_{\rm crit}/c_{\rm BF} \end{aligned} \tag{6.36}$$

where

$$\begin{aligned} c_{\rm BF} &= 1 + 0.5\sqrt{\min(T_{\rm BF} - T_{\rm up}, T_{\rm BF} - T_{\rm ice}} \quad \text{for } T < T_{\rm BF} \\ c_{\rm BF} &= 1 \quad \text{for } T > T_{\rm BF} \end{aligned} \tag{6.37}$$

with $T_{\rm BF} = 268.16$ K and $T_{\rm ice} = 250.16$ K.

Equation (6.35) is integrated analytically in the vertical using the generic differential equation $dl/dz = -al + b$, where l is the cloud water, $a = G^{\rm precip}\bar{\rho}/(l_{up}M_{\rm up})$, and $b = c_{\rm up}\Delta t$. The analytical solution is then given by $l = l_0 \exp^{-az} + b/a(1 - \exp^{-az})$.

6.6.4 Fallout of precipitation

The fallout of rain water/snow is parametrized as (e.g. Kuo and Raymond, 1980)

$$S_{\rm fallout} = \frac{g}{\Delta p} M_{\rm up} \frac{V}{w_{\rm up}} r_{\rm up} \tag{6.38}$$

where Δp is the model layer depth. The terminal velocity V is parametrized as (Liu and Orville, 1969)

$$V = 21.18 r_{\rm up}^{0.2} \tag{6.39}$$

Since the fall speed of ice particles is smaller than that of water droplets, only half the value of V calculated with (6.39) is used for ice. In estimating the fallout of precipitation in the mixed phase region of the cloud a weighted mean of the fall speed for ice and water precipitation is used. Equation (6.38) is integrated in the vertical with the same analytical framework as(6.35).

6.6.5 Evaporation of rain

The evaporation rate of convective rain below cloud base is activated when the relative humidity RH in the environment drops below 80%. It is parametrized following Kessler (1969), where the evaporation is assumed to be proportional to the saturation deficit $(\bar{q}_{\rm sat} - \bar{q})$ and to be dependent on the density of rain $\rho_{\rm rain}$ $({\rm gm}^{-3})$

$$e_{\rm subcld} = \alpha_1 ({\rm RH}\bar{q}_{\rm sat} - \bar{q}) \rho_{\rm rain}^{13/20} \tag{6.40}$$

where α_1 is a constant being zero for $\bar{q} > RH\bar{q}_{\rm sat}$.

As the density of rain $\rho_{\rm rain}$ is not given by the model it is convenient to express it in terms of the precipitation flux $P({\rm kg\ m^{-2}\ s^{-1}})$ as

$$P = \rho_{\rm rain} V_{\rm rain} \tag{6.41}$$

where $V_{\rm rain}$ is the mean fall speed of rain drops which again is parametrized following Kessler (1969).

$$V_{\rm rain} = \alpha_2 \rho_{\rm rain}^{1/8} / \sqrt{p/p_{\rm surf}} \tag{6.42}$$

(Note that this is different from the formulation used in the estimation of the fallout of precipitation.)

Considering that the convective rain takes place only over a fraction $C_{\rm conv}$ of the grid area, the evaporation rate at level k becomes

$$e_{\rm subcld} = C_{\rm conv}\alpha_1 (RH\bar{q}_{\rm sat} - \bar{q}) \left[\frac{\sqrt{p/p_{\rm surf}}}{\alpha_2} \frac{P}{C_{\rm conv}} \right]^{\alpha_3} \tag{6.43}$$

where the constants have the following values (Kessler, 1969)

$$\alpha_1 = 5.44 \times 10^{-4}\ {\rm s}^{-1} \quad \alpha_2 = 5.09 \times 10^{-3} \quad \alpha_3 = 0.5777$$

and where for the fractional area of precipitating clouds a constant value of $C_{\rm conv} = 0.05$ is assumed.

6.6.6 Melting and freezing of precipitation

Melting of snow falling across the freezing level T_0 is parameterized by a simple relaxation towards T_0 so that

$$M_{\rm elt} = \frac{c_p}{L_{\rm f}} \frac{(\bar{T} - T_0)}{\tau} \Delta p \tag{6.44}$$

where $M_{\rm elt}$ is the rate of melting and $\tau_{\rm melt}$ is a relaxation time scale which decreases with increasing temperature

$$\tau_{\rm melt} = \frac{\tau_m}{\{1 + 0.5(\bar{T} - \bar{T}_0)\}} \tag{6.45}$$

where $\tau_m = 11800$ s. The parametrization may produce melting over a deeper layer than observed (Mason, 1971) but this has been intentionally introduced to account implicitly for the effects of vertical mixing which may develop in response to the production of negative buoyancy.

6.7 LINK TO CLOUD SCHEME

Before the introduction of the prognostic cloud scheme (see Chapter 7 'Clouds and large-scale precipitation') water detrained from convection ($D_{\rm up} l_{\rm up}$) was evaporated instantaneously. However with the prognostic cloud scheme water detrained from convection is a source of cloud mass increasing the cloud fraction and water content of clouds. Therefore

$$\begin{aligned} \frac{\partial a}{\partial t} &= D_{\rm up} \\ \frac{\partial \bar{l}}{\partial t} &= D_{\rm up} l_{\rm up} \end{aligned} \tag{6.46}$$

where a is the cloud fraction and $\bar{l}$ the grid-box mean cloud water.

6.8 MOMENTUM TRANSPORT

Equation set (6.3) includes a treatment of the vertical transport of horizontal momentum by convection. Studies have shown that for deep convection momentum transports are overestimated by the plume models unless the effects of cloud scale horizontal pressure gradients are included (Gregory *et al.*, 1997). For unorganised convection the effects of the pressure gradients are to adjust the in-cloud winds towards those of the large-scale flow. This can be represented by an enhanced turbulent entrainment rate in the cloud momentum equations. To ensure mass continuity the turbulent detrainment rate is also increased by an equivalent amount.

Hence for deep and mid-level convection the turbulent entrainment and detrainment used in the updraught momentum equation are

$$\begin{aligned} \varepsilon_{\rm up}^{(1),(u,v)} &= \varepsilon_{\rm up}^{(1)} + \lambda \delta_{\rm up}^{(1)} \\ \delta_{\rm up}^{(1),(u,v)} &= \delta_{\rm up}^{(1)} + \lambda \delta_{\rm up}^{(1)} \end{aligned} \tag{6.47}$$

where $\delta_{\rm up}^{(1)}$ is given by (6.7).

For deep and mid-level conevction $\lambda = 2$, while for shallow convection $\lambda = 0$. Gregory (1997) suggests that the above formulation provides an adequate description of the effects of cloud scale pressure gradients in cases of deep convection. For shallow convection and downdraughts it is assumed that the effects of the pressure gradient term can be neglected and no enhancement of the entrainment rates in the momentum equations is applied. This formulation limits the momentum transports to be downgradient. Upgradient transports by highly organized convective systems (e.g. African squall lines) are not captured by this method.

The definition of the horizontal wind in the updraught and downdraught at and below cloud base and LFS is not well known. For the updraught, the value at cloud base is set to the environmental value at the departure level. For the downdraught, the initial values at the LFS are set equal to the average values of the winds in the updraught and those of the large-scale flow. The updraught values below cloud base are

derived asuming a linear decrease of the fluxes from their cloud base value to zero at the surface. Finally, in order to correct for an apparent low-bias in the near surface wind speeds with the present linear flux relation (quasi-linear in case of an implicit time discretisation see Section 6.10), the updraught velocities are decreased by a constant perturbation $u_{\rm pert}$=0.3 m s^{-1}

$$\begin{aligned} u_{\rm up} &= u_{\rm up} - u_{\rm pert}\ {\rm sign}(\overline{u}) \\ v_{\rm up} &= v_{\rm up} - u_{\rm pert}\ {\rm sign}(\overline{v}). \end{aligned} \tag{6.48}$$

6.9 VERTICAL DISCRETIZATION OF THE MODEL EQUATIONS

The flux divergence in the large-scale budget equations (6.1) and in the cloud equations (6.3) and (6.13) are approximated by centred finite differences as

$$g\frac{\partial(M\phi)}{\partial p} = \frac{g}{\Delta p}(M_{k+1/2}\phi_{k+1/2} - M_{k-1/2}\phi_{k-1/2}), \quad \Delta p = p_{k+1/2} - p_{k-1/2} \tag{6.49}$$

Furthermore, the updraught/downdraught equations (6.3) and (6.13) including the entrainment/ detrainment terms are discretized as

$$\begin{aligned} \frac{g}{\Delta p}(M_{{\rm up},k-1/2}\phi_{{\rm up},k-1/2} - M_{{\rm up},k+1/2}\phi_{{\rm up},k+1/2}) &= E_{\rm up}\bar{\phi}_{k+1/2} - D_{\rm up}\phi_{{\rm up},k+1/2} \\ \frac{g}{\Delta p}(M_{{\rm down},k+1/2}\phi_{{\rm down},k+1/2} - M_{{\rm down},k-1/2}\phi_{{\rm down},k-1/2}) &= E_{\rm down}\bar{\phi}_{k-1/2} - D_{\rm down}\phi_{{\rm down},k-1/2} \end{aligned} \tag{6.50}$$

The updraught equation is solved for $\phi_{{\rm up},k-1/2}$ and the downdraught equation for $\phi_{{\rm down},k+1/2}$. Note that with the definition (6.5) the terms $E_{\rm down}$ and $D_{\rm down}$ are negative. For the horizontal wind components and for tracers, the half-level environmental values are defined as shifted full-level values, i.e. $\bar{\phi}_{k+1/2} = \bar{\phi}_k$ and $\bar{\phi}_{k-1/2} = \bar{\phi}_{k-1}$. For temperature (dry static energy) and humidity, the half-level environmental values are determined by downward extrapolation from the next full level above along a cloud-ascent through that level giving

$$\left.\begin{aligned} \bar{T}_{k+1/2} &= \bar{T}_k + \left(\frac{\partial\bar{T}}{\partial p}\right)_{h_{\rm sat}}(p_{k+1/2} - p_k) \\ \bar{q}_{k+1/2} &= \bar{q}_k + \left(\frac{\partial\bar{q}}{\partial p}\right)_{h_{\rm sat}}(p_{k+1/2} - p_k) \end{aligned}\right\} \tag{6.51}$$

where $h_{\rm sat} = c_pT + gz + Lq_{\rm sat}$ is the saturation moist static energy. Using an extrapolation like (6.51) for calculating the subsidence of environmental air assures smooth profiles, and is also more consistent with the calculation of the updraughts where cloud air is transported upwards through level $k+1/2$ with the thermal state below that level and equally with the downdraughts which depend only on values of s and q above that level. Similarly, because of (6.49) the subsidence of environmental air through the same level accounts now only for thermal properties above that level. The choice of a moist adiabat for extrapolation is dictated by the property of the moist static energy which is, by convection in the absence of downdraughts, only changed through the fluxes of moist static energy

$$\left(\frac{\partial\bar{h}}{\partial t}\right)_{\rm cu} = g\frac{\partial}{\partial p}[M_{\rm up}(h_{\rm up} - \bar{h})] \tag{6.52}$$

As the lines of the saturation moist static energy $h_{\rm sat}$ through point $(p_{k+1/2}, \bar{T}_{k-1/2})$ and the updraught moist static energy are almost parallel, apart from entrainment effects, the difference $h_{\rm up} - \bar{h}$ is little affected by the vertical discretization.

The ascent in the updraughts is obtained by vertical integration of (6.3). Starting at the surface the condensation level (equal to the lowest half-level which is saturated or supersaturated and where updraught velocity is positive) is determined from an adiabatic ascent. The cloud profile above cloud base is determined layer by layer by first doing a dry adiabatic ascent with entrainment and detrainment included and then adjusting temperature and moisture towards a saturated state, taking into account condensation and freezing processes. The buoyancy of the parcel is calculated taking into account the

effects of cloud and precipitation water loading so that

$$B = T_{\rm up}(1+0.608q_{\rm up}-l_{\rm up}-r_{\rm up}) - \bar{T}(1+0.608q_{\rm e}) \tag{6.53}$$

Special care has to be taken in the discretization of (6.9) because of overshooting effects. A centred differencing scheme is used so that

$$\begin{aligned}\frac{K_{{\rm up},k-1/2}-K_{{\rm up},k+1/2}}{z_{k-1/2}-z_{k+1/2}} &= \frac{E_{{\rm up},k}}{M_{{\rm up},k+1/2}}(1+\beta C_{\rm d})\{K_{{\rm up},k-1/2}+K_{{\rm up},k+1/2}\} \\ &+ \frac{1}{f(1+\gamma)}\frac{1}{2}g\left[\frac{\{T_{\rm v,up}-\bar{T}_{\rm v}\}_{k-1/2}}{\{T_{\rm v}\}_{k-1/2}}+\frac{\{T_{\rm v,up}-\bar{T}_{\rm v}\}_{k+1/2}}{\{T_{\rm v}\}_{k+1/2}}\right]\end{aligned} \tag{6.54}$$

Finally, we mention that for numerical reasons the environmental air must not be convectively unstably stratified so

$$\bar{s}_{k-1/2} \geq \bar{s}_{k+1/2} \tag{6.55}$$

In fact, one of the forecasts with the ECMWF global model became numerically unstable when (6.55) was not imposed.

6.10 TEMPORAL DISCRETIZATION

The convective tendencies for the environmental values are obtained by an explicit solution of the advection equation (6.1) written in flux form

$$\left(\frac{\partial\bar{\phi}}{\partial t}\right)_{\rm cu} = \frac{\bar{\phi}_k^{\rm n+1}-\bar{\phi}_k^{\rm n}}{\Delta t} = \frac{g}{\Delta p}[M_{\rm up}\phi_{\rm up}+M_{\rm down}\phi_{\rm down}-(M_{\rm up}+M_{\rm down})\bar{\phi}^{\rm n}]|_{k-1/2}^{k+1/2} \tag{6.56}$$

as the tendency (or the new environmental value $\bar{\phi}$ at time n + 1) only depends on quantities known at time step n. However, in order for the explicit solution to be stable it must satisfy the Courant–Friedrich–Levy (CFL) criterion, and therefore the mass flux values should be limited to

$$M_{\rm up}+M_{\rm down} \leq \frac{\Delta p}{g\Delta t} \tag{6.57}$$

It turned out that this mass flux limit is frequently reached in the case of shallow convection and long model time steps of order $\Delta t > 1800$ s, and that the application of this mass flux limiter contributed to a sensitivity of model results to the model time step. Therefore, from model cycle Cy26r3 onwards it was decided to relax this mass flux limiter to three times the value given by the CFL criterion in the case of shallow convection and for model time steps $\Delta t > 1800$ s – as a further restriction this relaxed mass flux limiter is only applied to temperature and humidity, but not to the horizontal winds.

With cycle Cy31r1 onwards the convective transports are solved implicitly for chemical tracers and horizontal winds, whereas a semi-implicit formulation is used for specific humidity and dry static energy. The implicit formulation for tracers or momentum reads

$$\left(\frac{\partial\bar{\phi}}{\partial t}\right)_{\rm cu} = \frac{\bar{\phi}_k^{\rm n+1}-\bar{\phi}_k^{\rm n}}{\Delta t} = \frac{g}{\Delta p}[M_{\rm up}\phi_{\rm up}+M_{\rm down}\phi_{\rm down}-(M_{\rm up}+M_{\rm down})\bar{\phi}^{\rm n+1}]|_{k-1/2}^{k+1/2} \tag{6.58}$$

With the "shifted" vertical discretization for Tracers and horizontal winds $\bar{\phi}_{k+1/2}=\bar{\phi}_k$ and $\bar{\phi}_{k-1/2}=\bar{\phi}_{k-1}$, this equation constitutes a bi-diagonal linear system with unknowns $\bar{\phi}_k^{\rm n+1}$ and $\bar{\phi}_{k-1}^{\rm n+1}$.

However, the implicit formulation for specific humidity and dry static energy (temperature) is less straightforward, as the half-level values are non-linear functions of the full-level values (6.51). However, expressing the half-level values as a linear function of the full-level values

$$\begin{aligned}\bar{s}_{k-1/2}^{n+1} &= \bar{s}_{k-1}^{n+1}+\alpha_{k-1/2}^{(s)}\bar{s}_k^n \\ \bar{q}_{k-1/2}^{n+1} &= \bar{q}_{k-1}^{n+1}+\alpha_{k-1/2}^{(q)}q_{\rm sat}(\overline{T}_k^n),\end{aligned} \tag{6.59}$$

with the coefficients $\alpha^{(s)}$ and $\alpha^{(q)}$ precomputed from

$$\begin{aligned}\overline{s}^n_{k-1/2} &= \overline{s}^n_{k-1} + \alpha^{(s)}_{k-1/2}\overline{s}^n_k \\ \overline{q}^n_{k-1/2} &= \overline{q}^n_{k-1} + \alpha^{(q)}_{k-1/2} q_{\rm sat}(\overline{T}^n_k)\end{aligned} \tag{6.60}$$

the same bi-diagonal linear equation system as for tracers and momentum is obtained. Note that only the temperature and not the geopotential term of the dry static energy is formulated implicitly, and that the saturation specific humidity $q_{\rm sat}(\overline{T}^n_k)$ has been prefered to q^n_k as it is smoother and positive definit. Overall the implicit solution provides a stable solution, and smoother and non-local vertical profiles of tendencies through its inherent diffusivity. With Cy32r3 onward the mass flux CFL limit for temperature and humidity is set to 5 for horizontal resolutions below T511, and to 3 for all higher resolutions. For momentum a CFL limit of 1 is retained in order to prevent too strong surface winds.

6.11 DIAGNOSTICS FOR POSTPROCESSING: CAPE

As the CAPE computed in the convection routines is only computed for convectively active model columns, but taking into account lateral entrainment and liquid water loading (6.21) it was decided to provide to forecasters a CAPE product that is horizontally more homogeneous and close in line with the actual WMO definition (i.e the CAPE corresponding to a pseudo-adiabatic ascent)

$$\text{CAPE} = \int_{z_{\rm base}}^{z_{\rm top}} g\left(\frac{T_{\rm up} - \bar{T}}{\bar{T}}\right) {\rm d}z \approx \int_{z_{\rm base}}^{z_{\rm top}} g\left(\frac{\theta_{\rm e,up} - \bar{\theta}_{\rm esat}}{\bar{\theta}_{\rm esat}}\right) {\rm d}z \tag{6.61}$$

For reasons of numerical efficiency the CAPE has been approximated using the updraught equivalent potential temperature $\theta_{\rm e} = T\left(\frac{p_0}{p}\right)^{R/c_p} \exp\left(\frac{{\rm L q}}{{\rm c_p T}}\right)$ which is conserved during pseudo-adiabatic ascent, and the environmental saturated $\theta_{\rm e}$ which is a function of the environmental temperature only; a more accurate formulation of $\theta_{\rm e}$ could have been used using e.g. the temperature at the LCL and taking into account glaciation processes, but the present simple definition is of sufficient accuracy for the diagnostic purpose.

The above integral is evaluated for parcels ascending from model levels in the lowest 350 hPa initialising $\theta_{\rm e,up} = \bar{T}_k\left(\frac{p_0}{\bar{p}_k}\right)^{R/c_p} \exp\left(\frac{{\rm L}\bar{\rm q}_{\rm k}}{{\rm c_p}\bar{\rm T}_{\rm k}}\right)$ at a given "departing" model level k; for parcels ascending in the lowest 30 hpa, mixed layer values are used. The CAPE value retained is the maximum value from the different ascents.

6.12 STRUCTURE OF CODE

The parameterization of cumulus convection is performed in subroutines shown in Fig. 6.1.

CUCALLN: Provides interface of routines for cumulus parametrization. It takes the input values through arguments from CALLPAR and returns updated tendencies of T, q, l, u, v and chemical Tracers, as well as convective precipitation rates.

CUMASTRN: Master routine for convection scheme. Also performs the convective closure and with Cy32r3 computes the momentum in the convective draughts.

CUININ: Initializes variables for convection scheme (including vertical interpolation to the half model levels).

CUBASEN: First Guess updraught. Calculates condensation level, and sets updraught base variables and first guess cloud type.

CUASCN: Calculates ascent in updraughts. Before Cy32r3 CUASCN has been called twice as part of an iterative procedure. With ccyle 32r3 CUASCN is only called once and the mass flux scaling is done in routine CUMASTRN. Routines CUENTR and CUBASMCN are called from CUASCN.

CUENTR: Calculates turbulent entrainment and detrainment rates.

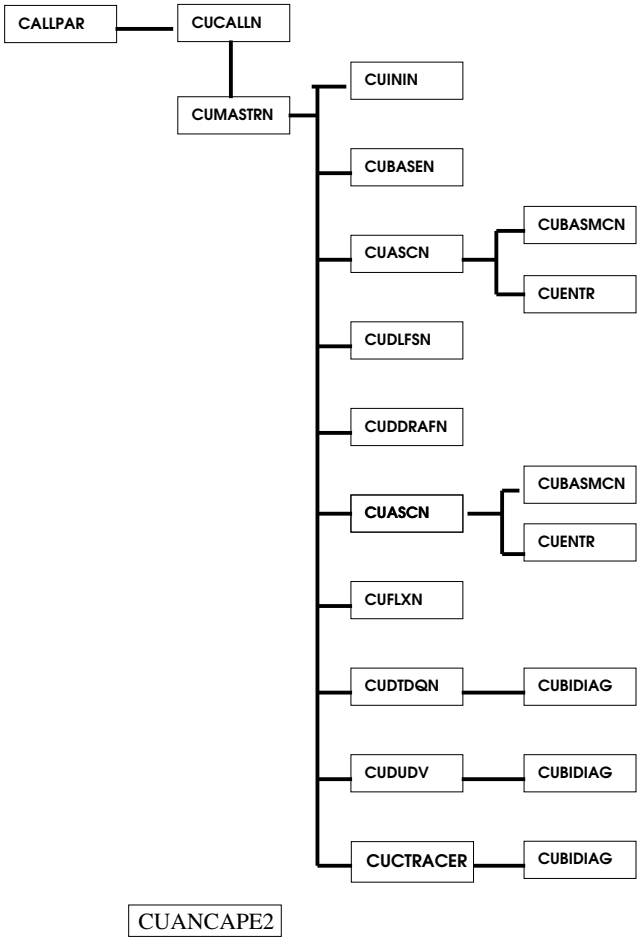

Figure 6.1 *Structure of convection scheme.*

CUBASMCN: Calculates cloud base properties of mid-level convection.

CUDLFSN: Calculates the level of free sinking for downdraughts.

CUDDRAFN: Calculates the downdraught descent.

CUFLXN: Calculates final convective fluxes and surface precipitation rates taking into account of melting/freezing and the evaporation of falling precipitation.

CUDTDQN: Calculates the tendencies of T and q from convection.

CUDUDV: Calculates the tendencies of u and v from convection.

CUADJTQ: Calculates super/sub saturation and adjusts T and q accordingly.

CUCTRACER: Calculates convective tendencies for chemical Tracers.

CUBIDIAG: Solver for bi-diagonal linear equation system.

CUANCAPE2: Computes CAPE diagnostics.

EXTERNALS

Subroutine SATUR for calculating saturation mixing ratio.

PARAMETERS

Defined in subroutine SUCUM called from INIPHY.

APPENDIX A. LIST OF SYMBOLS

CAPE	Convective available potential energy
C^i	Convective chemical Tracer no i
$C^i_{\rm down}$	Convective Tracer concentration in updraught
$C^i_{\rm down}$	Convective Tracer concentration in downdraught
$C_{\rm d}$	Drag coefficient
$C_{\rm conv}$	Fraction of grid square occupied by convection
c_p	Specific at constant pressure for dry air
$c_{\rm up}$	Condensation/sublimation in the updraughts
c_0	Autoconversion coefficient
$D_{\rm up}$	Rate of mass detrainment in the updraughts
$D_{\rm down}$	Rate of mass detrainment in the downdraughts
$E_{\rm up}$	Rate of mass entrainment in the updraughts
$E_{\rm down}$	Rate of mass entrainment in the downdraughts
$e^{\rm rain}$	Evaporation of rain
$e_{\rm down}$	Evaporation of precipitation (rain and snow) in the downdraughts
$e^{\rm rain}_{\rm down}$	Evaporation of rain in the downdraughts
$e^{\rm snow}_{\rm down}$	Evaporation of snow in the downdraughts
$\tilde{e}_{\rm subcld}$	Evaporation of precipitation (rain and snow) in the unsaturated sub-cloud layer
$f_{\rm scale}$	vertical scaling function for the entrainment
$\tilde{e}^{\rm rain}_{\rm subcld}$	Evaporation of rain in the unsaturated sub-cloud layer
$\tilde{e}^{\rm snow}_{\rm subcld}$	Evaporation of snow in the unsaturated sub-cloud layer
$F_{\rm rez}$	Freezing rate of condensate in the updraughts
g	gravity constant
$G^{\rm precip}$	Conversion rate from cloud (water+ice) into precipitation (rain+snow)
$G^{\rm rain}$	Conversion rate from cloud water into rain
$G^{\rm snow}$	Conversion rate from cloud ice into snow
$\bar{h}$	Moist static energy ($= c_p\bar{T} + L\bar{q} + gz$) in the environment
$\bar{h}_{\rm sat}$	Saturated moist static energy in the environment
$h_{\rm up}$	Moist static energy in the updraughts
$h_{\rm down}$	Moist static energy in the downdraughts
J_s	Surface turbulent sensible heat flux
J_q	Surface turbulent latent heat flux
k	model level
$K_{\rm up}$	Kinetic energy in the updraughts
L	Effective latent heat for an ice/water mix
$L_{\rm fus}$	Latent heat of fusion
$L_{\rm subl}$	Latent heat of sublimation
$L_{\rm vap}$	Latent heat of vaporization
LCL	Lifting Condensation Level
CFL	Courant–Friedrich–Levy criterium
$l_{\rm up}$	Cloud water/ice content in the updraughts
$l_{\rm crit}$	Cloud water/ice content above which autoconversion occurs
$M_{\rm elt}$	Melting rate of snow
$M_{\rm cld}$	Net mass flux in the convective clouds (updraughts + downdraughts)
$M_{\rm up}$	Net mass flux in the downdraughts
$M_{\rm down}$	Net mass flux in the downdraughts
n	index for time dsicretization
n_T	horizontal truncation (global wavenumber)
nlev	number of vertical model levels (nlev denotes the first layer above surface)
$P^{\rm rain}$	Net flux of precipitation in the form of rain
$P^{\rm snow}$	Net flux of precipitation in the form of snow
p	Pressure
p_0	Reference pressure=1000 hPa
$\bar{q}$	Specific humidity of the environment

$q_{\rm up}$	Specific humidity in the updraughts
$q_{\rm down}$	Specific humidity in the downdraughts
R	Rain intensity
RH	Relative humidity
$r_{\rm up}$	Precipitation (rain+snow) in the updraughts
$r_{\rm down}$	Precipitation (rain+snow) in the downdraughts
$S_{\rm fallout}$	Fall-out of rain/snow
$\bar{s}$	Dry static energy in the environment
$s_{\rm up}$	Dry static energy in the updraughts
$s_{\rm down}$	Dry static energy in the downdraughts
$\bar{T}_{\rm v}$	Virtual temperature in the environment
$T_{\rm v,up}$	Virtual temperature in the updraughts
$\bar{u}$	u component of wind in the environment
$u_{\rm up}$	u component of wind in the updraughts
$u_{\rm down}$	u component of wind in the downdraughts
$u_{\rm pert}$	additional updraught perturbation velocity
V	Mean terminal velocity of precipitation (rain+snow)
$V_{\rm rain}$	Mean terminal velocity of rain drops
$\bar{v}$	v component of wind in the environment
$v_{\rm up}$	v component of wind in the updraughts
$v_{\rm down}$	v component of wind in the downdraughts
$\bar{w}$	Vertical velocity in the environment
$w_{\rm up}$	Vertical velocity in the updraughts
w_*	Convective velocity scale
$\alpha_1, \alpha_2, \alpha_3$	Microphysical constants
α_n	Horizontal resolution dependency of the deep convective adjustment time
$\alpha^{(s)}, \alpha^{(q)}$	Interpolation coefficients for half-level values
δ	Detrainment per unit length
ε	Entrainment per unit length
η	Updraught mass flux fraction to initialise downdraught
κ	von Karman constant
ρ	Density of air
$\rho_{\rm rain}$	Density of rain
τ	Adjustment time scale
ω	Omega (large-scale) vertical velocity
Δp	Pressure difference between two model half-levels
Δt	Model time step

Chapter 7
Clouds and large-scale precipitation

Table of contents

7.1 THEORY

Cloud and large-scale precipitation processes are described by prognostic equations for cloud liquid water/ice and cloud fraction and diagnostic relations for precipitation. The scheme is described in detail in Tiedtke (1993).

7.1.1 Definitions

(*a*) *Specific cloud water content and cloud fraction*

The grid-mean specific cloud water/ice content (kg kg^{-1})is defined as

$$l = \frac{1}{V}\int_V \frac{\rho_w}{\rho}\,dV \tag{7.1}$$

where ρ_w is the density of cloud water (kg m^{-3}), ρ is the density of moist air (kg m^{-3}) and V is the volume of the grid box (m^{-3}). The fraction of the grid box covered by clouds is defined as

$$a = \frac{1}{V}\int_V \delta\,dV, \delta = \begin{cases} 1, & \text{in clouds} \\ 0, & \text{otherwise} \end{cases} \tag{7.2}$$

Furthermore, the definition of the specific cloud water content per cloud area (in-cloud water/ice content) is

$$l_{cld} = \frac{l}{a} \tag{7.3}$$

(*b*) *Saturation specific humidity*

The saturation specific humidity is expressed as a function of saturation water vapour pressure as

$$q_{sat} = \frac{\frac{R_{dry}}{R_{vap}} e_{sat}(T)}{p - \left(1 - \frac{R_{dry}}{R_{vap}}\right) e_{sat}(T)} \tag{7.4}$$

where the saturation water vapour pressure is expressed with the Teten's formula

$$e_{\mathrm{sat}}(T) = a_1 \exp\left\{a_3\left(\frac{T-T_0}{T-a_4}\right)\right\} \tag{7.5}$$

with the parameters set according to Buck (1981) for saturation over water ($a_1 = 611.21$ Pa, $a_3 = 17.502$ and $a_4 = 32.19$ K) and to the AERKi formula of Alduchov and Eskridge (1996) for saturation over ice ($a_1 = 611.21$ Pa, $a_3 = 22.587$ and $a_4 = -20.7$ K), with $T_0 = 273.16$ K.

(*c*) *Mixed phase*

In the scheme only one variable for condensed water species is used. The distinction between the water and ice phase is made as a function of temperature. The fraction of water in the total condensate is described as

$$\begin{aligned} \alpha &= 0 && T \le T_{\mathrm{ice}} \\ \alpha &= \left(\frac{T-T_{\mathrm{ice}}}{T_0-T_{\mathrm{ice}}}\right)^2 && T_{\mathrm{ice}} < T < T_0 \\ \alpha &= 1 && T \ge T_0 \end{aligned} \tag{7.6}$$

T_{ice} and T_0 represent the threshold temperatures between which a mixed phase is allowed to exist and are chosen as $T_{\mathrm{ice}} = 250.16$ K and $T_0 = 273.16$ K. The saturation thermodynamics are calculated according to the mixture of water and ice obtained with (7.6) so that the saturation specific humidity becomes

$$q_{\mathrm{sat}} = \alpha q_{\mathrm{sat(w)}} + (1-\alpha) q_{\mathrm{sat(i)}} \tag{7.7}$$

where $q_{\mathrm{sat(w)}}$ and $q_{\mathrm{sat(i)}}$ are the saturation specific humidities with respect to water and ice, respectively. The latent heat of phase changes is described as

$$L = \alpha L_{\mathrm{vap}} + (1-\alpha) L_{\mathrm{subl}} \tag{7.8}$$

7.1.2 Basic equations

With these definitions and the usual assumption that clouds encountered extend vertically over the whole model layer depth the equations for the time change of the grid-box averaged cloud water/ice content and the cloud fraction are obtained as

$$\frac{\partial l}{\partial t} = A(l) + S_{\mathrm{conv}} + S_{\mathrm{strat}} - E_{\mathrm{cld}} - G_{\mathrm{prec}} \tag{7.9}$$

and

$$\frac{\partial a}{\partial t} = A(a) + \delta a_{\mathrm{conv}} + \delta a_{\mathrm{strat}} - \delta a_{\mathrm{evap}} \tag{7.10}$$

The terms on the right-hand side of (7.9) and (7.10) represent the following processes:

(i) $A(l), A(a)$ – rate of change of cloud water/ice and cloud area due to transport through the boundaries of the grid volume.
(ii) $S_{\mathrm{conv}}, \delta a_{\mathrm{conv}}$ – rate of formation of cloud water/ice and cloud area by convective processes.
(iii) $S_{\mathrm{strat}}, \delta a_{\mathrm{strat}}$ – rate of formation of cloud water/ice and cloud area by stratiform condensation processes.
(iv) E_{cld} – rate of evaporation of cloud water/ice.
(v) G_{prec} – rate of generation of precipitation from cloud water/ice.
(vi) δa_{evap} – rate of decrease of cloud area due to evaporation.

The large-scale budget equations for specific humidity q, and dry static energy $s = c_p T + gz$ after introduction of the scheme are modified to

$$\frac{\partial q}{\partial t} = A(q) - S_{\mathrm{strat}} + E_{\mathrm{cld}} + E_{\mathrm{prec}} \tag{7.11}$$

and

$$\frac{\partial s}{\partial t} = A(s) + L(S_{\text{strat}} - E_{\text{cld}} - E_{\text{prec}}) - L_{\text{fus}} M + c_p\{(1-\alpha)R_{\text{clear}} + aR_{\text{cld}}\} \tag{7.12}$$

where $A(q)$ and $A(s)$ represent all processes except those related to clouds and radiation. L_{fus} is the latent heat of freezing, M is the rate of snow-melt, R_{clear} and R_{cld} are the radiative heating rates in cloud-free and cloudy areas. The flux-divergence terms represent the effects of cloud top entrainment.

7.1.3 Definition of the source and sink terms

(a) Convection

Clouds formed by convective processes are parametrized by considering them to be condensates produced in cumulus updraughts and detrained into the environmental air. This approach, besides being part of the cloud parametrization, represents also an important extension of the model's cumulus parametrization. It is applied for all types of convection, namely deep, shallow and mid-level. The source of cloud water/ice content is

$$S_{\text{conv}} = D_{\text{up}} l_{\text{up}} + \frac{M_{\text{up}}}{\rho}\frac{\partial l}{\partial z} \tag{7.13}$$

and the source of cloud area is described as

$$\delta a_{\text{conv}} = D_{\text{up}} + \frac{M_{\text{up}}}{\rho}\frac{\partial a}{\partial z} \tag{7.14}$$

where D_{up} is the detrainment of mass from cumulus updraughts, l_{up} is the specific cloud water/ice content in cumulus updraughts and M_{up} is the updraught mass flux (see Chapter 6). The first term in (7.13) and (7.14) represents the detrainment of cloud from the convective updraughts and the second term represents the advection of cloud in the vertical due to compensating subsidence in the environmental air. The evaporation due to this subsidence is represented by term E_1 described in subsection *(d)* below.

(b) Formation of stratiform clouds

Here the formation of clouds by non-convective processes (e.g. large-scale lifting of moist air, radiative cooling etc.) is considered. The parametrization is based on the principle that condensation processes are determined by the rate at which the saturation specific humidity decreases. This rate is linked to vertical motions and diabatic cooling through

$$\frac{\mathrm{d}q_{\text{sat}}}{\mathrm{d}t} = \left(\frac{\mathrm{d}q_{\text{sat}}}{\mathrm{d}p}\right)_{\text{ma}} (\bar{w} + gM_{\text{Cu}}) + \left(\frac{\mathrm{d}q_{\text{sat}}}{\mathrm{d}T}\right)\left(\frac{\mathrm{d}T}{\mathrm{d}t}\right)_{\text{diab}} \tag{7.15}$$

where $(\mathrm{d}q_{\text{sat}}/\mathrm{d}p)_{\text{ma}}$ is the change of q_{sat} along a moist adiabat through point (p, T), $\bar{w}$ is the area-mean generalized vertical velocity, gM_{Cu} is the cumulus-induced subsidence between the updraughts, and $(\mathrm{d}T/\mathrm{d}t)_{\text{diab}}$ is the net temperature tendency due to radiative and turbulent processes. Two cases of condensation are distinguished.

(i) In already existing clouds.
(ii) The formation of new clouds.

$$S_{\text{strat}} = C_1 + C_2 \tag{7.16}$$

The condensation rate in already existing clouds is described as

$$C_1 = -a\frac{\mathrm{d}q_{\text{sat}}}{\mathrm{d}t} \quad \frac{\mathrm{d}q_{\text{sat}}}{\mathrm{d}t} < 0 \tag{7.17}$$

New clouds are assumed to form, when the grid-averaged relative humidity exceeds a threshold value which is defined as a function of height as

$$\begin{aligned} RH_{\rm crit} &= RH_{\rm c} + (1-RH_{\rm c})\left(\frac{\sigma-\sigma_1}{1-\sigma_1}\right)^2 && \sigma_1 < \sigma \\ RH_{\rm crit} &= RH_{\rm c} && \sigma_{\rm trop} + (\Delta\sigma)_{\rm d} < \sigma < \sigma_{\rm d} \\ RH_{\rm crit} &= RH_{\rm c} + (1-RH_{\rm c})\left(\frac{\sigma_{\rm trop}+(\Delta\sigma)_{\rm d}-\sigma}{(\Delta\sigma)_{\rm d}}\right)^2 && \sigma_{\rm trop} < \sigma < \sigma_{\rm trop} + (\Delta\sigma)_{\rm d} \\ RH_{\rm crit} &= 1 && \sigma < \sigma_{\rm trop} \end{aligned} \tag{7.18}$$

where $RH_{\rm c} = 0.8$, $\sigma = p/p_{\rm surf}$ with p being the pressure and $p_{\rm surf}$ the pressure at the surface, $\sigma_1 = 0.8$, $\sigma_{\rm trop}$ is the height of the tropopause in σ-coordinates and $(\Delta\sigma)_{\rm d} = 0.2$. The increase in cloud cover is determined by how much of the cloud-free area exceeds saturation in one time step which in turn depends on the moisture distribution in the cloud-free area and how fast saturation is approached. The vapour is assumed to be evenly distributed within the range $[\{q^{\rm env} - (q_{\rm sat} - q^{\rm env})\}, q_{\rm sat}]$ around the mean environmental value $q^{\rm env}$, while the approach to saturation is determined by $\mathrm{d}q_{\rm sat}/\mathrm{d}t$. The rate of increase in cloud cover then becomes

$$\delta a_{\rm strat} = \frac{1}{2}\frac{-(1-a)}{(q_{\rm sat}-q^{\rm env})}\frac{\mathrm{d}q_{\rm sat}}{\mathrm{d}t} \qquad \frac{\mathrm{d}q_{\rm sat}}{\mathrm{d}t} < 0 \tag{7.19}$$

which can be expressed in terms of grid averages (using the definition $q = aq_{\rm sat} + (1-a)q^{\rm env}$) as

$$\delta a_{\rm strat} = \frac{-(1-a)^2}{2}\frac{1}{(q_{\rm sat}-q)}\frac{\mathrm{d}q_{\rm sat}}{\mathrm{d}t} \qquad \frac{\mathrm{d}q_{\rm sat}}{\mathrm{d}t} < 0 \tag{7.20}$$

For the application of (7.20) at values of q close to saturation, the constraint $\delta a_{\rm strat} < (1-a)/\Delta t$ is imposed to ensure realistic values of a.

The generation rate of cloud water/ice in newly formed clouds is then

$$C_2 = -\frac{1}{2}\delta a_{\rm strat}\Delta t\frac{\mathrm{d}q_{\rm sat}}{\mathrm{d}t} \qquad \frac{\mathrm{d}q_{\rm sat}}{\mathrm{d}t} < 0 \tag{7.21}$$

where $\delta a_{\rm strat}$ is the rate of increase of cloud cover given by (7.20).

(c) *Supersaturation in pure ice phase*

Ice crystal nucleation contrasts sharply with the equivalent process for liquid cloud droplets, since the nucleation process is not activated at small supersaturations with respect to the ice saturation vapour pressure. At cold temperatures, where the difference between the liquid water and ice saturation vapour pressures is large, the relative humidity (RH) with respect to ice can exceed 150% before the onset of the nucleation process, and supersaturations with respect to ice are commonly observed by in-situ and remote sensing techniques (e.g. Heymsfield *et al.*, 1998; Gierens *et al.*, 1999, 2000, 2004; Spichtinger *et al.*, 2003).

In the pure ice phase, the cloud scheme therefore modifies the formulation for cloud generation outlined above to allow supersaturation in the clear sky portion of grid-cell. The scheme assumes ice nucleation initiates when the RH measured with respect to ice saturation *locally* reaches the threshold $RH_{\rm homo}$ specified by Kärcher and Lohmann (2002):

$$RH_{\rm homo} = 2.583 - \frac{T}{207.8} \tag{7.22}$$

However, as in the warm phase, the clear-sky humidity fluctuations are assumed to be uniformly distributed with a fixed constant variance. Thus nucleation can occur when the grid-mean RH exceeds a threshold that is lower than this local criterion, and is given by $RH_{\rm crit} \times RH_{\rm homo}$. For temperatures close to $T_{\rm ice}$, the liquid water saturation mixing ratio can be lower. Thus the cloud formation occurs when

$$RH > RH_{\rm crit} \times MIN\left(RH_{\rm homo}, \frac{q_{\rm sat}^{\rm liq}}{q_{\rm sat}^{\rm ice}}\right) \tag{7.23}$$

Once ice is present, the deposition process is considered to be sufficiently rapid relative to the model time-step that it can be approximated by a diagnostic adjustment to exactly saturated conditions inside the cloud. This assumption is necessary, since to allow supersaturation both within the cloud and in the clear sky environment would either require a separate prognostic variable to monitor the evolution of the water vapour inside the cloud, or a diagnostic assumption would have to be used to divide the grid-mean humidity between the two regions, which can generate large- artificial horizontal sub-grid humidity fluxes (see Tompkins *et al.*, 2007, for more detail). In any case, this assumption appears to be reasonably justified in a wide range of updraught situations by modelling of the homogeneous nucleation process (Khvorostyanov and Sassen, 1998). The obvious drawback is that clouds may not exist in subsaturated conditions, and no information concerning the ice crystal number concentration is available.

Thus, if $T < T_{\rm ice}$ and the relative humidity exceeds the threshold given by (7.23), the scheme calculates the increase in cloud fraction from (7.20). The associated change in cloud ice mass is calculated in two stages. The first source term is derived using (7.21). This generation term for ice mass reduces RH back to threshold given by (7.23), and leaves the newly generated cloudy region in a supersaturated state. This is then corrected by clipping the grid-mean humidity to the limit of

$$q_v^{max} = q_s(a + (1-a)RH_{homo}). \tag{7.24}$$

This clipping term has the effect of reducing the in-cloud humidity to the saturated value within one time-step. Again, with RH_{homo} equal to unity when T >250K a standard clipping to the saturation value is used.

Tompkins *et al.* (2007) show that the supersaturation scheme, while simple, reproduces very well the climatological PDF of upper tropospheric RH derived from MOZAIC aircraft observations (Gierens *et al.*, 1999), as well as the geographical distribution of ice supersaturation given by MLS retrievals (Spichtinger *et al.*, 2003).

(*d*) *Evaporation of cloud water/ice*

The scheme describes evaporation of clouds by two processes in connection with large-scale and cumulus-induced descent and diabatic heating and by turbulent mixing of cloud air with unsaturated environmental air.

$$E_{\rm cld} = E_1 + E_2 \tag{7.25}$$

The first process is accounted for in the same way as stratiform cloud formation except that $\mathrm{d}q_{\rm sat}/\mathrm{d}t > 0$. Hence

$$E_1 = a\frac{\mathrm{d}q_{\rm sat}}{\mathrm{d}t} \quad \frac{\mathrm{d}q_{\rm sat}}{\mathrm{d}t} > 0 \tag{7.26}$$

Assuming a homogeneous horizontal distribution of liquid water in the cloud, the cloud fraction remains unaltered by this process except at the final stage of dissipation where it reduces to zero.

$$\delta a_{\rm evap} = \frac{a}{\Delta t} \quad \text{if } l \to 0 \tag{7.27}$$

The parametrization of cloud dissipation as cloud air mixes with environmental air is described as a diffusion process proportional to the saturation deficit of the air:

$$E_2 = aK(q_{\rm sat} - q) \tag{7.28}$$

where the diffusion coefficient is

$$K = 2.10^{-6}\ \mathrm{s}^{-1} \tag{7.29}$$

The rate of decrease in cloud cover is parametrized as

$$\delta a_{\rm evap} = \frac{E_2}{l_{\rm cld}} \tag{7.30}$$

where $l_{\rm cld}$ is the specific cloud water/ice content per cloud area as defined in (7.3). Note that because of (7.3) the parametrizations (7.28) and (7.30) imply a reduction in cloud area while $l_{\rm cld}$ remains unchanged.

(e) *Precipitation processes*

Similar to radiation, precipitation processes are treated separately in clear and cloudy skies. This owes to the fact that the microphysical processes in these two regions are very distinct from each other, with conversion, collection and accretion processes being relevant in clouds whereas evaporation of precipitation is the relevant process outside clouds. Therefore the precipitation flux is written as

$$P = P^{\mathrm{cld}} + P^{\mathrm{clr}} \tag{7.31}$$

with

$$P^{\mathrm{cld}} \equiv \frac{1}{A}\int P \cdot H(l)\, dA \tag{7.32}$$

and

$$P^{\mathrm{clr}} \equiv \frac{1}{A}\int P \cdot (1 - H(l))\, dA \tag{7.33}$$

where the step function, $H(l)$, marks the portion of the grid-cell containing cloud with a condensate specific humidity $l > 0$ and A is the area of the grid-cell.

The precipitation fraction in the grid-box is then described as

$$a_p = a_p^{\mathrm{cld}} + a_p^{\mathrm{clr}} \tag{7.34}$$

with

$$a_P^{\mathrm{cld}} \equiv \frac{1}{A}\int H(l)H(P)\, dA \tag{7.35}$$

and

$$a_P^{\mathrm{clr}} \equiv \frac{1}{A}\int (1 - H(l))H(P)\, dA \tag{7.36}$$

Rain and snow is removed from the column immediately but can evaporate, melt and interact with the cloud water in the layers it passes through.

(i) *Rain and snow autoconversion.* For the autoconversion process from liquid cloud water to rain, and also from ice cloud to snow, a parametrization following Sundqvist (1978) is used. The rate of generation of precipitation is written as

$$G_{\mathrm{prec}} = a c_0 l_{\mathrm{cld}} \left[1 - \exp\left\{-\left(\frac{l_{\mathrm{cld}}}{l_{\mathrm{crit}}}\right)^2\right\}\right] \tag{7.37}$$

where c_0^{-1} represents a characteristic time scale for conversion of cloud liquid droplets or ice crystals into raindrops or snow, respectively, and l_{crit} is a typical cloud water content at which the generation of precipitation begins to be efficient. In the mixed and warm phases, these disposable parameters are adjusted as follows

$$c_0 = c_0^* F_1 F_2 \tag{7.38}$$

and

$$l_{\mathrm{crit}} = \frac{l_{\mathrm{crit}}^*}{F_1 F_2} \tag{7.39}$$

to take into account the effect of collection of cloud droplets by raindrops falling through the cloud (F_1) and the Bergeron–Findeisen mechanism (F_2). Here F_1 and F_2 are defined as

$$F_1 = 1 + b_1\sqrt{P_{\mathrm{loc}}} \tag{7.40}$$

and

$$F_2 = 1 + b_2\sqrt{(T_{\mathrm{BF}} - T)} \quad \text{if } T_{\mathrm{ice}} < T < T_{\mathrm{BF}} \tag{7.41}$$

where P_{loc} is the local cloudy precipitation rate ($P_{\mathrm{loc}} = P^{\mathrm{cld}}/a_P^{\mathrm{cld}}$) and T_{BF} is the temperature at which the Bergeron–Findeisen mechanism starts to enhance the precipitation. The values for the constants are $T_{\mathrm{BF}} = 268$ K, $b_1 = 100$ (kg m^{-2} s^{-1})$^{-0.5}$, $b_2 = 0.5$ K$^{-0.5}$, $c_0^* = 1.67 \times 10^{-4}$ s^{-1}, and $l_{\mathrm{crit}}^* = 0.3$ g kg^{-1}.

For ice to snow autoconversion, the rate coefficient (c_0) is based on Lin *et al.* (1983) (equation 21), as

$$c_0 = 10^{-3} e^{0.025(T-273.15)} \tag{7.42}$$

where T is the temperature in Kelvin. For this process, Lin *et al.* (1983) set l_{crit} to 10^{-3}kg kg^{-1} in their cloud resolving model (note they were using a Kessler-type scheme rather than the Sundqvist form, but the sensitivities to c_0 and l_{crit} are likely to be similar in both schemes). A lower value is appropriate for a GCM sized grid box (unless sub-grid cloud variability is explicitly taken into account Rotstayn, 2000; Pincus and Klein, 2000), and based on model tuning l_{crit} is set to 3×10^{-5}kg kg^{-1}.

(ii) *Ice sedimentation.* Before Cy31r1 the ice sedimentation treatment only allowed ice to fall through one vertical grid box in a single timestep, and ice falling into a clear sky region according to the vertical overlap rules was converted into snow. The use of the sedimentation process as a proxy for autoconversion in this way, and its numerical implementation, resulted in a strong dependency to model vertical resolution. Thus, this treatment was altered at Cy31r1 to treat sedimentation with an implicit upstream approach, and a separate autoconversion term was introduced to handle the conversion of ice to snow, as described above.

The numerical treatment of the sedimentation term is described below. With ice allowed to settle through many model layers in a single timestep, using an ice-mass related ice fall speed was found to lead to numerical 'shocks' when long timesteps are necessary. Thus the ice fallspeed is set to a constant ($w_{\rm ice0} = 15$ cm s^{-1}) to avoid this. However, the fallspeed is adjusted to account for variations in temperature and pressure as derived by Heymsfield and Iaquinta (2000),

$$w_{\rm ice} = w_{\rm ice0} \left(\frac{p}{p_{\rm ice0}} \right)^{-0.178} \left(\frac{T}{T_{\rm ice0}} \right)^{-0.394} \tag{7.43}$$

where $p_{\rm ice0} = 30000$ Pa and $T_{\rm ice0} = 233$ K.

(iii) *Evaporation of precipitation.* The parametrization of rain and snow evaporation follows Kessler (1969) with evaporation occurring only in the clear air part of the grid-box. The evaporation rate is assumed to be proportional to the saturation deficit $(q_{\rm sat} - q^{\rm env})$ and dependent on the density of rain in the clear air $\rho^{\rm clr}_{\rm rain}$ (gm^{-3}),

$$E_{\rm prec} = \alpha_1 (q_{\rm sat} - q^{\rm env}) (\rho^{\rm clr}_{\rm rain})^{13/20} \tag{7.44}$$

where α_1 is a constant.

As the density of rain is not given by the model, it is convenient to express it in terms of the precipitation flux $P^{\rm clr}$(kg m^{-2} s^{-1}) as

$$P^{\rm clr} = \rho^{\rm clr}_{\rm rain} V_{\rm rain} \tag{7.45}$$

where $V_{\rm rain}$ is the mean fall speed of rain drops which again is parametrized following Kessler (1969).

$$V_{\rm rain} = \alpha_2 (\rho^{\rm clr}_{\rm rain})^{1/8} / \sqrt{p/p_0} \tag{7.46}$$

Considering that the evaporation only takes place in the clear-sky precipitation fraction $a^{\rm clr}_P$, the evaporation rate becomes

$$E_{\rm prec} = a^{\rm clr}_P \alpha_1 (q_{\rm sat} - q^{\rm env}) \left[\frac{\sqrt{p/p_0}}{\alpha_2} \frac{P^{\rm clr}}{a^{\rm clr}_P} \right]^{\alpha_3} \tag{7.47}$$

where the constants have the following values (Kessler, 1969)

$$\alpha_1 = 5.44 \times 10^{-4} \text{ s}^{-1} \quad \alpha_2 = 5.09 \times 10^{-3} \quad \alpha_3 = 0.5777$$

Evaporation of rain/snow only takes place when the grid mean relative humidity is below a threshold value. The choice of the threshold value is not straightforward for numerical reasons. Here, the

assumption is made that the clear-sky relative humidity (= grid mean relative humidity in the absence of clouds) that can be reached by evaporation of precipitation is a function of the fractional coverage with precipitation of the clear sky part of the grid-box. Hence, the threshold value is parametrized as

$$RH_{\mathrm{crit},E_P} = 0.7 + 0.3\frac{a_P^{\mathrm{clr}}}{(1-a)} \tag{7.48}$$

(iv) *Melting of snow.* The melting of snow is parametrized by allowing the part of the grid box that contains precipitation to cool to T_{melt} over a time scale τ, that is

$$M = (a_P^{\mathrm{cld}} + a_P^{\mathrm{clr}})\frac{c_p}{L_{\mathrm{fus}}}\frac{T_w - T_{\mathrm{melt}}}{\tau} \tag{7.49}$$

where $T_{\mathrm{melt}} = 0°\mathrm{C}$, T_w is the wet-bulb temperature and

$$\tau = \frac{\tau_m}{1 + 0.5(T_w - T_{\mathrm{melt}})}$$

where $\tau_m = 11800$ s (decreased at CY35R1 from 27000 s to reduce the occurrence of snow at warmer temperatures). The wet-bulb temperature is used in order to account for the thermal (cooling) effect of evaporation on the melting process in sub-saturated air. The evaporation counteracts the latent heating due to melting and allows snow particles to survive to slightly warmer temperatures when the relative humidity of the air is low. The wet-bulb temperature is approximated as in Wilson and Ballard (1999)

$$T_w = T_d - (q_s - q)(A + B(p - C) - D(T_d - E)) \tag{7.50}$$

where $A = 1329.31$, $B = 0.0074615$, $C = 0.85 \times 10^5$, $D = 40.637$, and $E = 275$.

7.2 NUMERICS

7.2.1 Integration of the equations for cloud water/ice and cloud cover

As cloud processes are rapidly varying in time, care must be taken when (7.9) and (7.10) are integrated over the relatively large model time steps. Therefore terms that depend linearly on a and l are integrated analytically. Equations (7.9) and (7.10) for a cloud variable ϕ, (liquid water or cloud cover) including a flux form term for transport at a velocity V (consisting of ice sedimentation, advection due to convective subsidence etc.) can be written as

$$\frac{d\phi}{dt} = C + D\phi + \frac{1}{\rho}\frac{d(\rho V\phi)}{dp}. \tag{7.51}$$

Here fast processes (relative to the model timestep) are treated in the $D\phi$ implicit term, while slow processes are explicitly treated in the C term. Before Cy31r1 the exact analytical solution was used. However, it was found that this method, combined with the way ice settling and ice to snow autoconversion were treated, lead to a vertical resolution sensitivity.

Therefore at Cy31r1 a simple forward-in-time upstream implicit solver was introduced for the cloud variables, using a mass flux form for the advection term to ensure conservation. The handling of the cloud-top entrainment term by the vertical diffusion scheme simplifies the problem from a tridiagonal to bidiagonal system of equations, since all the advective fluxes act in a downwards direction. If subscript j refers to the grid level and superscript n to the time level, the discretised form is

$$\frac{\phi_j^{n+1} - \phi_j^n}{\Delta t} = C + \frac{\rho_{j-1}V_{j-1}\phi_{j-1}^{n+1}}{\rho_j \Delta Z} + \left(D - \frac{\rho_j V_j}{\rho_j \Delta Z}\right)\phi_j^{n+1} \tag{7.52}$$

This is rearranged to give the solution

$$\phi_j^{n+1} = \frac{C\Delta t + \frac{\rho_{j-1}V_{j-1}\phi_{j-1}^{n+1}}{\rho_j \Delta Z}\Delta t + \phi_j^n}{1 - D\Delta t + \frac{\rho_j V_j}{\rho_j \Delta Z}\Delta t} \tag{7.53}$$

Once ϕ_j^{n+1} is known, the contributions of each process can be calculated from (7.52). Note that if sink terms reduce ϕ to zero over a timestep, only the linear and advective source terms are assumed to operate, since $D\phi_j^{n+1}$ is also zero (likewise for the advective loss term). This is in contrast to the post-Cy25r3 numerics which attempted to divide the loss between all linear and nonlinear terms appropriately.

Fast processes are considered implicitly. Further details are provided below, but briefly the processes that are now treated implicitly for cloud cover are:

(i) Convective detrainment
(ii) Generation by cooling
(iii) Destruction by turbulent mixing

For the cloud water the implicit processes are:

(i) Advection by convective subsidence
(ii) Generation/destruction by cooling/warming
(iii) Sedimentation of ice
(iv) Warm and mixed phase precipitation generation

It should be noted that the choice of numerical treatment is often based on pragmatism, and no perfect solution exists for a model such as the IFS using high vertical resolution with relatively long timesteps.

7.2.2 Calculation of $\mathrm{d}q_{\mathrm{sat}}/\mathrm{d}t$

Special care has to be taken in the numerical calculation of $\mathrm{d}q_{\mathrm{sat}}/\mathrm{d}t$ from (7.15). Since the saturation water vapour pressure depends exponentially on temperature, straightforward numerical integration of (7.15) would produce large truncation errors. Therefore the average of $\mathrm{d}q_{\mathrm{sat}}/\mathrm{d}t$ over the time step is determined by the means of moist adjustment (e.g. Haltiner and Williams, 1980). This is achieved by first extrapolating the cloud temperature to time-level $t + \Delta t$ and then adjusting temperature and moisture toward saturation conditions.

7.2.3 Convective cloud source

The vertical discretisation of (7.13) and (7.14) is achieved with a simple upstream scheme, that is

$$S_{\mathrm{conv}} = D_{\mathrm{up},k} l_{\mathrm{up},k+1/2} - gM_{\mathrm{up},k-1/2} \frac{l_{k-1} - l_k}{P_{k-1} - P_k} \tag{7.54}$$

and

$$\delta a_{\mathrm{conv}} = D_{\mathrm{up},k} - gM_{\mathrm{up},k-1/2} \frac{a_{k-1} - a_k}{P_{k-1} - P_k}. \tag{7.55}$$

Although two of the terms in (7.54) depend linearly on l_k, the convective source is treated explicitly to ensure conservation. As stated above, cloud fraction is treated implicitly.

7.2.4 Precipitation fractions

The method to determine a_P^{cld} and a_P^{clr} is as follows. If precipitation is generated in a level through the processes of autoconversion or ice sedimentation, it is assumed to be generated at all portions of the cloud uniformly and thus at the base of level k, $a_{P,k}^{\mathrm{cld}} = a_k$. The precipitation generated in this cloudy region is given by

$$\Delta P_k^{\mathrm{cld}} \equiv \frac{1}{A} \int \left(\frac{1}{g} \int_{P_{k-1/2}}^{p_{k+1/2}} G_{\mathrm{prec}} \cdot H(l)\, dp' \right) dA \tag{7.56}$$

and the cloudy precipitation flux at the base of level k is given by $P_k^{\mathrm{cld}} = \tilde{P}_k^{\mathrm{cld}} + \Delta P_k^{\mathrm{cld}}$, where the twiddle symbol indicates the value of P^{cld} at the top of level k. Because the cloud is assumed to be internally homogenous, (7.56) simplifies to $a_k G_{\mathrm{prec}}(p_{k+1/2} - p_{k-1/2})/g$, where G_{prec} is the generation rate of precipitation inside the cloud. If only accretion occurs in the clouds of level k, $a_{P,k}^{\mathrm{cld}}$ equals $\tilde{a}_{P,k}^{\mathrm{cld}}$, the fractional area that contains cloudy precipitation flux at the top of level k.

Because the clear precipitation flux is assumed to be horizontally uniform, evaporation does not alter the area containing clear precipitation flux such that $a^{\rm clr}_{P,k} = \tilde{a}^{\rm clr}_{P,k}$. Only in the case that all of the clear precipitation flux evaporates in level k does $a^{\rm clr}_{P,k} = 0$. The clear-sky precipitation flux at the base of level k is given by $P^{\rm clr}_k = \tilde{P}^{\rm clr}_k + \Delta P^{\rm clr}_k$, where $\tilde{P}^{\rm clr}_k$ is the clear-sky precipitation flux at the top of level k, and

$$\Delta P^{\rm clr}_k = \frac{1}{A}\int\left(\frac{1}{g}\int_{pk-1/2}^{p_{k+1/2}} E_{\rm prec}\cdot(1-H(l))\,dp'\right)dA = \tilde{a}^{\rm clr}_{P,k}E_{\rm prec}(p_{k+1/2}-p_{k-1/2})/g \tag{7.57}$$

where $E_{\rm prec}$ represents precipitation evaporation. Note that precipitation evaporation is a function of $\tilde{P}^{\rm clr}_k$ guaranteeing that precipitation generated in a level cannot evaporate in the same level. This will guarantee consistency with the assumption that clouds where present fill the vertical extent of the grid cell and that horizontal transfer of precipitation mass from cloudy to clear regions of the grid cell is not possible.

At the interfaces between levels, precipitation mass that is in cloud of the upper level may fall into clear air of the lower level, or precipitation mass that is in clear air of the upper level may fall into cloud of the lower level. Thus at level interfaces an algorithm is needed to transfer precipitation and its area between the cloudy and clear portions of the grid box. The algorithm is constructed by determining the amount of area associated with each transfer and then transferring precipitation fluxes between clear and cloudy components according to the assumption that the precipitation flux is horizontally uniform but with different values in the clear and cloudy regions containing precipitation.

There are four possible areas to be defined (see schematic in Figure 1 of Jakob and Klein, 2000): the area in which cloudy precipitation flux falls into cloud of the lower level, the area in which cloudy precipitation flux falls into clear air of the lower level, the area in which clear precipitation flux falls into clear air of the lower level, and the area in which clear precipitation flux falls into cloud of the lower level. To determine these areas, the cloud overlap assumption is applied to determine the relative horizontal placements of clouds in the upper and lower levels. The cloud overlap assumption is expressed in terms of an equation which relates the total horizontal area C_k covered by clouds in levels 1 to k (where $k=1$ is the top level of the model), to the total horizontal area cover by clouds in levels 1 to $k-1$. Therefore

$$(1-C_k) = (1-C_{k-1})\cdot\frac{1-\max(a_k,a_{k-1})}{1-\min(a_{k-1},1-\delta)} \tag{7.58}$$

where δ is a tiny number set to 10^{-6}. Equation (7.58) gives maximum overlap for clouds in adjacent levels and random overlap for clouds separated by clear levels. From this equation, one can determine the portion of clouds of the lower level which is not overlapped by clouds at all higher levels; this area, $\Delta C = C_k - C_{k-1}$, cannot have any precipitation falling into it. Using this assumption, the area for which cloudy precipitation flux falls into clear air of the level below is given by

$$\Delta a_{\rm cld\to clr} = a^{\rm cld}_{P,k-1} - \min(a_k - \Delta C, a^{\rm cld}_{P,k-1}) \tag{7.59}$$

Equation (7.59) makes the further assumption that there is maximum overlap between the area covered by cloudy precipitation at the base of the upper level and the portion of the lower level cloud which lies beneath clouds in higher levels, $a_k - \Delta C$. With the assumption that the precipitation flux is horizontally uniform, the amount of cloudy precipitation flux of the upper level that falls into clear air of the level below is

$$\Delta P_{\rm clr\to clr} = \frac{\Delta a_{\rm cld\to clr}}{a^{\rm cld}_{P,k-1}}\cdot P^{\rm cld}_{k-1} \tag{7.60}$$

The area in which clear precipitation flux of the upper level falls into cloud of the level below is

$$\Delta a_{\rm clr\to cld} = \max(0.,\min(a^{\rm clr}_{P,k-1}, a_k - \Delta C - a_{k-1})) \tag{7.61}$$

which assumes maximum overlap between the portion of the cloud in the lower level k which has cloud at some higher level other than $k-1$, and the area covered by the clear precipitation flux. Again, with the assumption that the precipitation flux is horizontally uniform, the amount of clear precipitation flux of the upper level that falls into cloud of the level below is

$$\Delta P_{\rm clr\to cld} = \frac{\Delta a_{\rm clr\to cld}}{a^{\rm clr}_{P,k-1}}\cdot P^{\rm clr}_{k-1} \tag{7.62}$$

Finally, the areas and fluxes at the top of level k can be related to those at the base of level $k-1$ by

$$\tilde{a}^{\rm cld}_{P,k} = a^{\rm cld}_{P,k-1} + \Delta a_{\rm clr\to cld} - \Delta a_{\rm cld\to clr} \tag{7.63}$$

$$\tilde{a}^{\rm clr}_{P,k} = a^{\rm clr}_{P,k-1} - \Delta a_{\rm clr\to cld} + \Delta a_{\rm cld\to clr} \tag{7.64}$$

$$\tilde{P}^{\rm cld}_{k} = P^{\rm cld}_{k-1} + \Delta P_{\rm clr\to cld} - \Delta P_{\rm cld\to clr} \tag{7.65}$$

$$\tilde{P}^{\rm clr}_{k} = P^{\rm clr}_{k-1} - \Delta P_{\rm clr\to cld} + \Delta P_{\rm cld\to clr} \tag{7.66}$$

From these equations it is obvious that total precipitation area, $a_P^{\rm cld} + a_P^{\rm clr}$, and precipitation flux, $P^{\rm cld} + P^{\rm clr}$, are conserved at level interfaces.

7.2.5 Evaporation of precipitation

Since the evaporation of precipitation has a threshold value of relative humidity at which the process should cease to exist (see (7.48)) an implicit treatment is applied when solving (7.47). If (7.47) is written as

$$\frac{\partial q}{\partial t} = \beta(q_{\rm s} - q) \tag{7.67}$$

the implicit solution becomes

$$\Delta q = \frac{\beta \Delta t (q^n_{\rm s} - q^n)}{1 + \beta \Delta t \left[1 + \frac{L}{c_p}\left(\frac{dq_{\rm s}}{dT}\right)^n\right]} \tag{7.68}$$

where n refers to the time level at the beginning of timestep Δt. The implicit solution ensures that evaporation of precipitation never leads to $q^{n+1} > q^{n+1}_{\rm s}$. To ensure the maximum relative humidity after evaporation does not exceed the threshold value defined in (7.48) the maximum change in specific humidity is calculated as

$$(\Delta q)_{\rm max} = \frac{RH_{{\rm crit},E_p} \cdot q^n_{\rm s} - q^n}{1 + RH_{{\rm crit},E_p} \frac{L}{C_p}\left(\frac{dq_{\rm s}}{dT}\right)^n} \tag{7.69}$$

The smaller of the values given by (7.68) and (7.69) is then used.

7.2.6 Final moist adjustment

In the case where semi-Lagrangian advection is not used, a final test for supersaturation is performed after the calculation of the liquid water/ice tendency and the corresponding tendencies of temperature and moisture. If any supersaturation is found the grid box is re-adjusted to saturation (using the moist adjustment formulation) and the moisture excess is converted into precipitation. When the semi-Lagrangian advection scheme is utilized however, this final supersaturation check is performed by a separate routine that is applied on the effective profiles of temperature and humidity after all physical and explicit dynamical contributions have been computed. See Section 3.10 of Chapter 3 "Semi-Lagrangian formulation" for a more detailed description of the applied saturation check. Note, that small amounts of non-physical supersaturation due to numerical approximations may remain in the postprocessed fields.

7.3 CODE

The parametrization of cloud and large-scale precipitation processes is performed in the following routines.

CLDPP

This routine calculates total, high, mid-level and low cloud cover for postprocessing diagnostics. These are obtained using a generalised cloud overlap assumption between maximum and random (Hogan and Illingworth, 2000; Mace and Benson-Troth, 2002), where the degree of randomness between two cloudy layers increases with increasing vertical separation distance between the layers. The algorithm to apply the generalised overlap is the same as used in the IFS McICA radiation scheme (Chapter 2) and is based on the stochastic cloud generator described in Räisänen *et al.* (2004). The cloud cover diagnostics are calculated over the relevant vertical atmospheric slab. In sigma coordinates these slabs are defined as follows.

(i) Low clouds: $p > 0.8p_s$
(ii) Medium clouds: $0.45p_s \leq p \leq 0.8p_s$
(iii) High clouds: $p < 0.45p_s$

where p is the pressure and p_s is the surface pressure.

CLOUDSC

This routine carries out all calculations necessary to solve (7.9) and (7.10). As stated above, recent developments in the numerical treatment has allowed the code to be greatly modularized. The calculations are carried out in the following order.

(i) Section 1: Calculate initial input profiles
(ii) Section 2: Setup
- initial setup including calculation of q_{sat}, tropopause height for (7.18)

(iii) Section 3: Sources and sinks
- convective source terms including freezing if different mixed phase assumptions are used for convection and large-scale processes ((7.13) and (7.14))
- erosion of clouds by turbulent mixing ((7.28) and (7.30))
- calculation of dq_{sat}/dt (see Subsection 7.2.2)
- large-scale evaporation (7.26)
- large-scale cloud formation ((7.17), (7.20) and (7.21))

(iv) Section 4: Precipitation generation
- precipitation overlap
- ice sedimentation
- warm rain and mixed phased processes

(v) Section 5: Solvers for cloud cover and water
- analytical integration of the equation for a
- analytical integration of the equation for l
- apply limiters calculation modified cloud advection processes

(vi) Section 6: Solver-dependent physics
- mixing due to cloud-top entrainment of static energy and horizontal winds
- melting of snow (7.49)
- evaporation of precipitation (7.47)

(vii) Section 7: Update tendencies
- final tendency calculations of all thermodynamic quantities

(viii) Sections 8: Flux calculations for diagnostics

APPENDIX A. LIST OF SYMBOLS

$A(\ )$	advective transport through the boundaries of the grid box
a	fraction of grid box covered by clouds
a_{prec}	fraction of grid box covered by precipitation
a_{up}	fractional area of updraughts
c_p	specific heat at constant pressure
D_{up}	detrainment in the cumulus updraughts (s^{-1})
E_{cld}	rate of evaporation of cloud water/ice
E_{prec}	rate of evaporation of precipitation
e_{sat}	saturation water vapour
F_{LW}	longwave radiative flux divergence

F_q	moisture transport by clouds
g	acceleration of gravity
G_{fallout}	generation of precipitation that falls out from one level to another
G_{prec}	generation of precipitation from cloud water/ice
G_{rain}	generation of precipitation in the form of rain
G_{snow}	generation of precipitation in the form of snow
H	mixed-layer height
J_q	surface humidity flux
K	diffusion coefficient
L	latent heat
L_{fus}	latent heat of fusion
L_{subl}	latent heat of sublimation
L_{vap}	latent heat of vaporization
l	grid-mean specific cloud liquid-water and ice content
l_{cld}	specific cloud water content per cloud area
l_{down}	specific cloud water/ice content in the cumulus downdraughts
l_{up}	specific cloud water/ice content in the cumulus updraughts
M	rate of snowmelt
M_{Cu}	cumulus-induced subsidence mass flux
P	precipitation rate
P_{loc}	local precipitation rate
p	pressure
q^{env}	environmental specific humidity (kg kg^{-1})
q_{down}	specific humidity in the convective downdraughts (kg kg^{-1})
q_{sat}	saturation specific humidity (kg kg^{-1})
$q_{\text{sat(i)}}$	saturation specific humidity with respect to ice (kg kg^{-1})
$q_{\text{sat(w)}}$	saturation specific humidity with respect to water (kg kg^{-1})
q_{up}	specific humidity in the convective updraughts (kg kg^{-1})
R_{cld}	radiative heating rate in cloudy air
R_{clear}	radiative heating rate in cloud-free air
R_{dry}	gas constant for dry air
R_{vap}	gas constant for water vapour
RH_c	$= 0.8$
RH_{crit}	threshold value of the relative humidity
RH_{homo}	threshold relative humidity for homogenous nucleation
S_{conv}	formation of cloud water/ice by convective processes
S_{strat}	formation of cloud water/ice by stratiform condensation processes
S_{bl}	formation of cloud water/ice by boundary-layer processes
s	dry static energy
s_{v}	virtual dry static energy
T	temperature
T_0	$= 273.16$ K
T_{BF}	$= 268$ K temperature at which the Bergeron–Findeison enhances the precipitation
T_{ice}	$= 250.16$ K
T_{melt}	$= 0°$ C
$\bar{w}$	area-mean generalized vertical velocity
$\hat{w}$	$\rho\hat{w} = \rho a_{\text{up}} w_{\text{up}}$ is the cloud mass flux
w_{e}	entrainment velocity
w_{ice}	terminal fall speed of ice particles
w_{up}	updraught velocity
α	fraction of condensate held as liquid water
δa_{bl}	rate of increase of cloud area by boundary-layer processes
δa_{conv}	rate of increase of cloud area by convective processes
δa_{strat}	rate of increase of cloud area by stratiform condensation processes
δa_{evap}	rate of decrease of cloud area due to evaporation

ρ	density of moist air (kg m^{-3})
ρ_{w}	density of cloud water (kg m^{-3})
ρ_{rain}	density of rain in air (kg m^{-3})

Chapter 8
Surface parametrization

Table of contents

8.1 INTRODUCTION

The parametrization scheme described in this chapter represents the surface fluxes of energy and water and, where appropriate, corresponding sub-surface quantities. Fig. 8.1 summarizes the main features of the land part of the model; hereafter the scheme will be referred to as the TESSEL (Tiled ECMWF Scheme for Surface Exchanges over Land) scheme. At the interface between the surface and the atmosphere, each grid-box is divided into fractions (tiles), with up to 6 fractions over land (bare ground, low and high vegetation, intercepted water, shaded and exposed snow) and up to 2 fractions over sea and freshwater bodies (open and frozen water). Each fraction has its own properties defining separate heat and water fluxes used in an energy balance equation solved for the tile skin temperature. Special attention is devoted to the different physical mechanisms limiting evaporation of bare ground and vegetated surfaces. A revised land surface Hydrology (hereafter referred as HTESSEL), has been introduced to address shortcomings of the previous land surface scheme version, specifically the lack of surface runoff and the choice of a

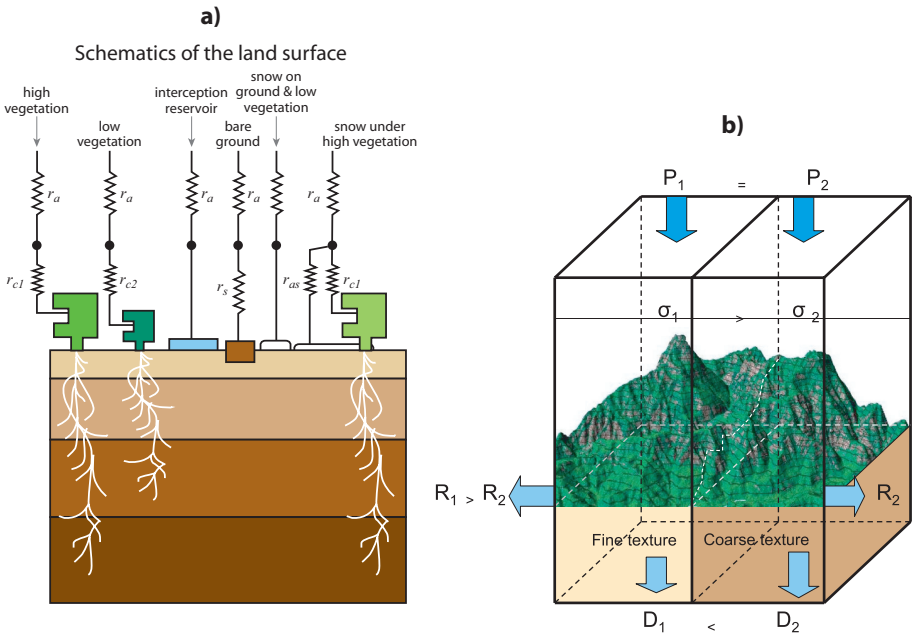

Figure 8.1 *Schematic representation of the structure of (a) TESSEL land-surface scheme and (b) spatial structure added in HTESSEL (for a given precipitation $P_1 = P_2$ the scheme distributes the water as surface runoff and drainage with functional dependencies on orography and soil texture respectively).*

global uniform soil texture. New infiltration and runoff schemes are introduced with a dependency on the soil texture and standard deviation of orography. A new formulation for the snow-pack is introduced to improve the thermal insulation properties, add the interception of liquid rain and revise the albedo and metamorphism aging processes.

Over land, the skin temperature is in thermal contact with a four-layer soil or, if there is snow present, a single layersnow mantle overlying the soil. The snow temperature varies due to the combined effect of top energy fluxes, basal heat flux and the melt energy. The soil heat budget follows a Fourier diffusion law, modified to take into account the thermal effects of soil water phase changes. The energy equation is solved with a net ground heat flux as the top boundary condition and a zero-flux at the bottom.

Snowfall is collected in the snow mantle, which in turn is depleted by snowmelt, contributing to surface runoff and soil infiltration, and evaporation. A fraction of the rainfall is collected by an interception layer, where the remaining fraction (throughfall) is partitioned between surface runoff and infiltration. Subsurface water fluxes are determined by Darcy's law, used in a soil water equation solved with a four-layer discretization shared with the heat budget equation. Top boundary condition is infiltration plus surface evaporation, free drainage is assumed at the bottom; each layer has an additional sink of water in the form of root extraction over vegetated areas.

Finally, open water points have a fixed surface temperature. When present, frozen water occupies a fraction of the grid box, with a prognostic ice temperature evolving in the forecast following the heat budget of a four-layer ice model in thermal contact with an underlying ocean at freezing temperature.

8.2 TILES AND SURFACE FLUXES

8.2.1 Tile and vegetation characteristics

Grid-box surface fluxes are calculated separately for the different subgrid surface fractions (or "tiles"), leading to a separate solution of the surface energy balance equation and skin temperature for each of these tiles. This is an analogue of the "mosaic" approach of Koster and Suarez (1992). Note that the tiles at the interface soil-atmosphere are in energy and hydrological contact with one single atmospheric profile above and one single soil profile below. Each grid box is divided into 8 fractions: two vegetated fractions (high and low vegetation without snow), one bare soil fraction, three snow/ice fractions (snow

on bare ground/low vegetation, high vegetation with snow beneath, and sea-ice, respectively), and two water fractions (interception reservoir, ocean/lakes). The tile for "high vegetation with snow beneath" is a combined tile with a separate energy balance and evaporation model for the high vegetation and the underlying snow. A mixture of land and water (ocean/inland water) tiles is not allowed, i.e. a grid box is either 100% land or 100% sea.

In each grid box two vegetation types are present: a high and a low vegetation type. An external climate database, based on the Global Land Cover Characteristics (GLCC) data that has been derived using one year of Advanced Very High Resolution Radiometer (AVHRR) data and ancillary information (Loveland *et al.*, 2000; http://edcdaac.usgs.gov/glcc/glcc.html; see also Chapter 11). The nominal resolution is 1 km. The data used provides for each pixel a biome classification based on the Biosphere-Atmosphere Transfer Scheme (BATS) model (Dickinson *et al.*, 1993), and four parameters have been derived for each grid box: dominant vegetation type, $T_{\rm H}$ and $T_{\rm L}$, and the area fraction, $A_{\rm H}$ and $A_{\rm L}$, for each of the high- and low-vegetation components, respectively.

The coverage C_i for the tile i depends on the type and relative area of low and high vegetation, and the presence of snow and intercepted water. In the absence of snow and interception, the vegetation coverage of high ($c_{\rm H}$) and low ($c_{\rm L}$) vegetation are calculated as $A_{\rm H}c_{\rm veg}(T_{\rm H})$ and $A_{\rm L}c_{\rm veg}(T_{\rm L})$, respectively, with $c_{\rm veg}$ a vegetation type dependent coverage (see Table 8.1). The bare ground fraction $c_{\rm B}$ is the residual.

$$\begin{aligned} c_{\rm H} &= A_{\rm H}c_{\rm veg}(T_{\rm H}) \\ c_{\rm L} &= A_{\rm L}c_{\rm veg}(T_{\rm L}) \\ c_{\rm B} &= (1 - c_{\rm H} - c_{\rm L}) \end{aligned} \tag{8.1}$$

Each vegetation type is characterized by a series of (fixed) parameters as detailed in Table 8.1.

(i) A minimum canopy resistance, $r_{\rm s,min}$.
(ii) A leaf area index, LAI.
(iii) A vegetation coverage, $c_{\rm veg}$.
(iv) A coefficient, $g_{\rm D}$, for the dependence of the canopy resistance, $r_{\rm c}$, on water vapour pressure deficit.
(v) The root distribution over the soil layers, specified by an exponential profile involving attenuation coefficients, $a_{\rm r}$, and $b_{\rm r}$.

The numerical values for the parameters of Table 8.1 are based both on experiments conducted as described in Van den Hurk *et al.* (2000) and on literature review, in particular Mahfouf *et al.* (1995), Manzi and Planton (1994), Giard and Bazile (2000), Dorman and Sellers (1989), Bonan (1994), Pitman *et al.* (1991), and Zeng *et al.* (1998a).

The presence of snow and intercepted water dynamically modifies the coverage fractions. The coverage of snow, $c_{\rm sn}$, has been revised to be linearly dependent from the snow depth $D_{\rm sn}$ (units m), therefore taking into account both the snow mass S (units (kg m^{-2})) and the snow density $\rho_{\rm sn}$ (units (kg m^{-3})), to account for the hysteresis characterizing snow accumulation and melting processes.

The interception reservoir fraction, c_1, is given by $W_1/W_{1\rm m}$, with $W_{1\rm m}$, the maximum value for the intercepted water in the grid box, defined from the leaf area index contributions from the high and low vegetation tiles. The water contents of the interception reservoir, W_1 (units m), and S are prognostic quantities in the model. Snow cover is assumed to be overlying vegetation and bare ground with the same fraction. The interception reservoir occupies an identical fraction of all snow-free tiles.

$$\begin{aligned} c_{\rm sn} &= \min\left(1, \frac{S/\rho_{\rm sn}}{D_{\rm cr}}\right) \\ W_{1\rm m} &= W_{\rm lmax}[c_{\rm B} + c_{\rm H} \cdot LAI(T_{\rm H}) + c_{\rm L} \cdot LAI(T_{\rm L})] \\ c_1 &= \min\left(1, \frac{W_{\rm l}}{W_{\rm lm}}\right) \end{aligned} \tag{8.2}$$

In the expressions above the minimum snow depth that ensures complete coverage of the grid box is $D_{\rm cr} = 0.10$m and the maximum water over a single layer of leaves or over bare ground is $W_{1\ \rm max} = 0.0002$m.

Table 8.1 *Vegetation types and parameter values (see text). H/L refer to the distinction between high and low vegetation.*

Index	Vegetation type	H/L	$r_{s,min}$ (sm^{-1})	LAI (m^2m^{-2})	c_{veg}	g_D (hPa^{-1})	a_r	b_r
1	Crops, mixed farming	L	180	3	0.90	0	5.558	2.614
2	Short grass	L	110	2	0.85	0	10.739	2.608
3	Evergreen needleleaf trees	H	500	5	0.90	0.03	6.706	2.175
4	Deciduous needleleaf trees	H	500	5	0.90	0.03	7.066	1.953
5	Deciduous broadleaf trees	H	175	5	0.90	0.03	5.990	1.955
6	Evergreen broadleaf trees	H	240	6	0.99	0.03	7.344	1.303
7	Tall grass	L	100	2	0.70	0	8.235	1.627
8	Desert	–	250	0.5	0	0	4.372	0.978
9	Tundra	L	80	1	0.50	0	8.992	8.992
10	Irrigated crops	L	180	3	0.90	0	5.558	2.614
11	Semidesert	L	150	0.5	0.10	0	4.372	0.978
12	Ice caps and glaciers	–	–	–	–	–	–	–
13	Bogs and marshes	L	240	4	0.60	0	7.344	1.303
14	Inland water	–	–	–	–	–	–	–
15	Ocean	–	–	–	–	–	–	–
16	Evergreen shrubs	L	225	3	0.50	0	6.326	1.567
17	Deciduous shrubs	L	225	1.5	0.50	0	6.326	1.567
18	Mixed forest/woodland	H	250	5	0.90	0.03	4.453	1.631
19	Interrupted forest	H	175	2.5	0.90	0.03	4.453	1.631
20	Water and land mixtures	L	150	4	0.60	0	–	–

The leaf area index LAI, is specified in Table 8.1 as a function of surface type. The full set of fractional tile coverages is given by (8.3) and (8.4), where the indexing of the tiles is detailed in Table 8.2. Since a mixture of land and ocean tiles is not allowed, a grid box is either 100% water (open water and ice, with ice fraction c_i):

$$\begin{aligned} C_1 &= 1 - c_i \\ C_2 &= c_i \\ C_i &= 0, i \in [3, N_T] \end{aligned} \tag{8.3}$$

or 100% land (tiles 3 to N_T, where $N_T = 8$ is the number of tiles):

$$\begin{aligned} C_1 &= C_2 = 0 \\ C_3 &= (1 - c_{sn}) \cdot c_1 \\ C_4 &= (1 - c_{sn}) \cdot (1 - c_1) \cdot c_L \\ C_5 &= c_{sn} \cdot (1 - c_H) \\ C_6 &= (1 - c_{sn}) \cdot (1 - c_1) \cdot c_H \\ C_7 &= c_{sn} \cdot c_H \\ C_8 &= (1 - c_{sn}) \cdot (1 - c_1) \cdot (1 - c_L - c_H) \end{aligned} \tag{8.4}$$

Apart from the fractional gridbox coverage, each tile has a couple of additional parameters (see Table 8.2).

(i) The skin conductivity, Λ_{sk}, provides the thermal connection between the skin level and the soil or snow deck. For high vegetation, Λ_{sk}, is different for a stable and unstable stratification of the temperature gradient between the skin level and the upper soil or snow layer. This difference is considered to represent the asymmetric coupling between the ground surface and the tree canopy layer: an effective convective transport within the tree trunk space for unstable conditions, and a limited turbulent exchange for stable stratification (Bosveld *et al.*, 1999).

(ii) A small fraction f_{R_s} of net short-wave radiation that is transmitted directly to the top soil or snow layer. The remaining fraction of the short-wave radiation $(1 - f_{R_s})$ is absorbed by the skin layer.

Table 8.2 *Tile specific values.*

Index	Tile	Λ_{sk} unstable ($Wm^{-2}K^{-1}$)	Λ_{sk} stable ($Wm^{-2}K^{-1}$)	f_{R_s}	Resistance scheme
1	Open water	∞	∞	0	Potential
2	Ice water	58	58	0	Potential
3	Interception reservoir	10	10	0.05	Potential
4	Low vegetation	10	10	0.05	Resistance
5	Snow on low vegetation/bare ground	7	7	0	Potential
6	High vegetation	$\Lambda_{a,u}+5$	$\Lambda_{a,s}+5$	0.03	Resistance
7	High vegetation with snow beneath	$\Lambda_{a,u}+5$	$\Lambda_{a,s}+5$	0.03	Canopy and snow resistance
8	Bare ground	15	15	0	Resistance

The resistance scheme describes the way of coupling with the atmosphere: *Potential* denotes atmospheric resistance only; *Resistance* denotes aerodynamic resistance in series with a canopy or soil resistance; *Canopy and snow resistance* denotes a canopy resistance for the vegetation and an extra aerodynamic coupling to the snow surface (see Figs 8.1–8.2 and Subsection 8.2.2). For tiles 6 and 7, $\Lambda_{a,u} = 15$W m^{-2}K^{-1} and $\Lambda_{a,s} = 10$W m^{-2}K^{-1} represent the aerodynamic coupling between the canopy and the soil in the unstable and stable cases, respectively, and the factor 5 represents the long-wave radiative exchanges. *Unstable/stable* refers to the temperature gradient between the skin layer and the top soil or snow layer.

Finally, the surface albedo, α_i, is similar for all land tiles within a grid box except for those covered with snow (see the snow scheme description below). The climate database provides the snow-free background albedo on a monthly basis. Long-wave emissivity, ε, outside the window region is equal to 0.99 for all tiles; emissivity in the window region is tile dependent and varies between 0.93 and 0.98 (see Table 2.5 in Section 2.8.5 for more details). The remaining surface characteristics (roughness length for momentum, z_{0m}, and heat, z_{0h}) are similar for all land tiles within a grid box and specified in the climate database (Chapter 11).

8.2.2 Surface heat and evaporation fluxes

A resistance parameterization is used to calculate the turbulent fluxes. Momentum exchange is parameterized with the same roughness length for all tiles, but with a different stability correction for each tile. The resistance scheme for water vapour and heat exchanges is different for different tiles (see Fig. 8.2). For ocean, sea ice and snow on low vegetation, the turbulent fluxes of heat and water vapour are given by

$$H_i = \rho_a c_p |U_L| C_{H,i}(T_L + g z_L/c_p - T_{sk,i}) \tag{8.5}$$

$$E_i = \rho_a |U_L| C_{H,i}[q_L - q_{sat}(T_{sk,i})] \tag{8.6}$$

with ρ_a the air density, c_p the heat capacity of moist air, g the acceleration of gravity, $|U_L|$, T_L, q_L, z_L the wind speed, temperature, humidity and height of the lowest atmospheric model level, and $C_{H,i}$ the turbulent exchange coefficient, that varies from tile to tile because of different atmospheric stabilities. See Chapter 3 for a description of the exchange coefficients where different roughness lengths for heat and momentum are assumed and a Monin–Obukhov formulation is adopted for the stability dependence.

For high and low vegetation, an additional canopy resistance r_c is added with

$$E_i = \frac{\rho_a}{r_a + r_c}[q_L - q_{sat}(T_{sk,i})] \tag{8.7}$$

with $r_a = (|U_L| C_{H,i})^{-1}$ and i indicating the high or low vegetation tiles. r_c is a function of downward short-wave radiation R_s, leaf area index LAI, average unfrozen root soil water $\bar{\theta}$, atmospheric water

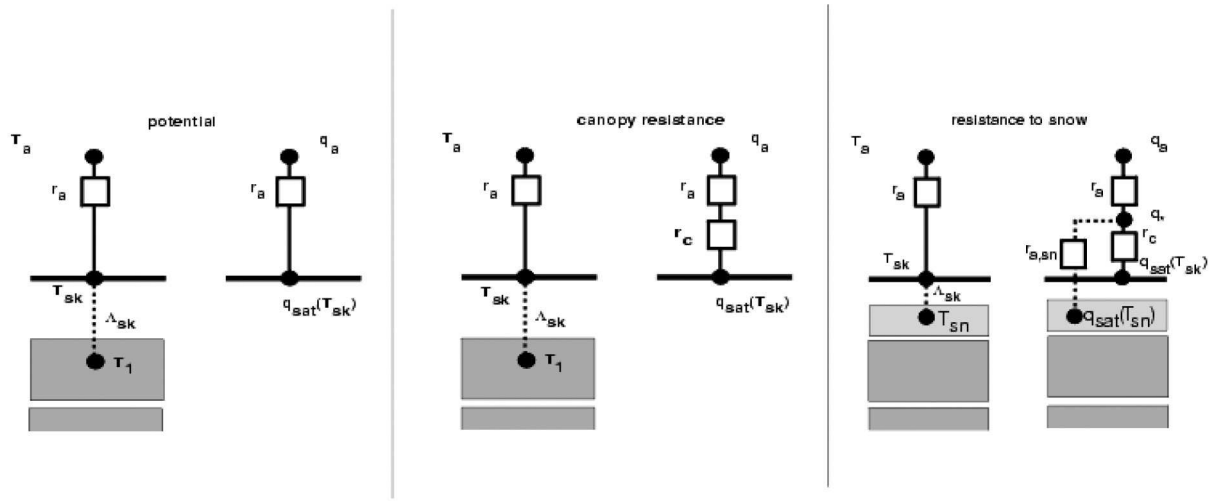

Figure 8.2 *Resistance scheme for three categories of coupling. Potential refers to ocean, sea ice and snow on low vegetation; (Canopy) resistance to dry low and dry high vegetation, bare soil, and interception reservoir when potential evaporation exceeds the maximum reservoir content; Resistance to snow to snow under high vegetation.*

vapour deficit D_a and a minimum stomatal resistance $r_{\mathrm{s,min}}$, following Jarvis (1976) given by

$$r_\mathrm{c} = \frac{r_{\mathrm{S,min}}}{LAI} f_1(R_\mathrm{s}) f_2(\bar{\theta}) f_3(D_\mathrm{a}) \tag{8.8}$$

f_1 is a hyperbolic function of downward short-wave radiation only so that

$$\frac{1}{f_1(R_\mathrm{s})} = \min\left[1, \frac{bR_\mathrm{s}+c}{a(bR_\mathrm{s}+1)}\right] \tag{8.9}$$

where $a = 0.81$, $b = 0.004$ W^{-1}m^2 and $c = 0.05$.

Function f_2 is defined as

$$\frac{1}{f_2(\bar{\theta})} = \begin{cases} 0 & \bar{\theta} < \theta_{\mathrm{pwp}} \\ \dfrac{\bar{\theta}-\theta_{\mathrm{pwp}}}{\theta_{\mathrm{cap}}-\theta_{\mathrm{pwp}}} & \theta_{\mathrm{pwp}} \le \bar{\theta} \le \theta_{\mathrm{cap}} \\ 0 & \bar{\theta} > \theta_{\mathrm{cap}} \end{cases} \tag{8.10}$$

where the soil moisture at permanent wilting point and at field capacity, θ_{pwp} and θ_{cap}, respectively, are defined in Table 8.6. $\bar{\theta}$ is a weighted average of the unfrozen soil water given by

$$\bar{\theta} = \sum_{k=1}^{4} R_k \max[f_{\mathrm{liq},k}\theta_k, \theta_{\mathrm{pwp}}] \tag{8.11}$$

where R_k is the fraction of roots in layer k and the fraction of unfrozen soil water, $f_{\mathrm{liq},k} = 1 - f_{\mathrm{fr}}(T_k)$, is a parameterized function of the soil temperature of layer k, T_k, as specified in Subsection 8.5.2. Table 8.1 lists the coefficients a_r and b_r which are used to calculate the root fraction R_k according to Zeng *et al.* (1998a):

$$R_k = 0.5[\exp(-a_\mathrm{r} z_{k-1/2}) + \exp(-b_\mathrm{r} z_{k-1/2}) - \exp(-a_\mathrm{r} z_{k+1/2}) - \exp(-b_\mathrm{r} z_{k+1/2})] \tag{8.12}$$

where $z_{k+1/2}$ is the depth of the bottom of layer k (in m; $z_{1/2} = 0$ m). Contributions from levels exceeding the column depth are added to the deepest soil layer in order to ensure that $\sum R_k = 1$. Table 8.3 lists the distribution of the roots over the four soil layers.

A dependence on atmospheric humidity deficit ($D_\mathrm{a} = e_{\mathrm{sat}}(T_\mathrm{L}) - e_\mathrm{L}$, with e the vapour pressure) is included according to

$$\frac{1}{f_3(D_\mathrm{a})} = \exp(-g_\mathrm{D} D_\mathrm{a}) \tag{8.13}$$

Table 8.3 *Root distribution per vegetation type (in %) over the four layers. Vegetation indexes refer to Table 8.1.*

Vegetation index	1	2	3	4	5	6	7	8	9	10	11	13	16	17	18	19
Layer 1	24	35	26	26	24	25	27	100	47	24	17	25	23	23	19	19
Layer 2	41	38	39	38	38	34	27	0	45	41	31	34	36	36	35	35
Layer 3	31	23	29	29	31	27	27	0	8	31	33	27	30	30	36	36
Layer 4	4	4	6	7	7	14	9	0	0	4	19	11	11	11	10	10

where g_D depends on the vegetation type (Table 8.1), and is non-zero for high vegetation only.

Evaporation from the interception reservoir is given by (8.6) only when the amount of water in the interception reservoir, W_1, is sufficient to sustain potential evaporation during the entire time step Δt. If W_1 is limited, an additional resistance r_1, analogue to r_c in (8.7), is introduced. r_1 is calculated from the potential evaporation of the previous time step. Note that this type of flux-limiter is a time-step dependent feature of the model numerics.

Bare-soil evaporation uses a resistance approach, an analogue to the canopy transpiration formulation (see (8.7)). The soil evaporation resistance, r_{soil}, is

$$r_{soil} = r_{soil,min} f_2(f_{liq}\theta_1) \tag{8.14}$$

with f_2 given by (8.10), and $r_{soil,min} = 50$ s m^{-1}. By this parameterization, evaporation from bare ground is treated similar to a single leaved canopy with a minimum resistance $r_{soil,min}$, extracting water from the upper soil layer only, and not experiencing any additional stress due to limited radiation or dry air. Equation (8.14) shuts off evaporation when the top soil moisture reaches permanent wilting point. When compared to observations over semi-arid areas, an alternative relative humidity formulation (Mahfouf and Noilhan, 1991; Viterbo and Beljaars, 1995), that does not have a similar limitation, gave excessive evaporation (Van den Hurk *et al.*, 2000).

A special treatment is included in the calculation of evaporation over high vegetation with snow underneath (see Fig. 8.2). Evaporation takes place from both the canopy component in the tile ($E_{veg,7}$) and from the snow lying under the vegetation. The canopy evaporation uses a canopy resistance and saturation specific humidity at the canopy skin temperature, while the snow evaporation $E_{sn,7}$ is parameterized with an additional constant aerodynamic resistance $r_{a,sn}$ and saturation specific humidity at snow temperature T_{sn}. The evaporation from tile 7 is the combination of the canopy transpiration and the snow evaporation so that

$$E_7 = \rho_a \frac{q_L - q_*}{r_a} = \rho_a \frac{q_* - q_{sat}(T_{sn})}{r_{a,sn}} + \rho_a \frac{q_* - q_{sat}(T_{sk})}{r_c} \tag{8.15}$$

where q_* is the humidity at the connection point of the three resistances (Fig. 8.2). After elimination of q_*, E_7 can be rewritten as

$$E_7 = \rho_a \frac{q_L - q_{sat}(T_{sk})}{r_a + r_c + r_c \frac{r_a}{r_{a,sn}}} + \rho_a \frac{q_L - q_{sat}(T_{sn})}{r_a + r_{a,sn} + r_{a,sn} \frac{r_a}{r_c}} \tag{8.16}$$

The first term in the equation above is interpreted as $E_{veg,7}$ and is treated in the standard way (i.e., implicit in the tile skin temperature). The second term is interpreted as evaporation from snow ($E_{sn,7}$) and is handled explicitly. The values of $r_{a,sn}$ depend on the stability of the subcanopy layer and are functions of $\Lambda_{a,u}$ and $\Lambda_{a,s}$ (see Table 8.2); $r_{a,sn} = 67$ sm^{-1} and $r_{a,sn} = 220$ s m^{-1} for an unstable and stable subcanopy layer, respectively. In spring, the latent heat flux of that tile, $L_v E_{veg,7} + L_s E_{sn,7}$ will be dominated by snow evaporation since the frozen soil under the snow deck will lead to very large values of r_c.

The grid box total sensible and latent heat fluxes are expressed as an area weighted average:

$$H = \sum_{i=1}^{8} C_i H_i \tag{8.17}$$

$$E = \sum_{i=1}^{8} C_i E_i \tag{8.18}$$

with H_i given by (8.5), and E_i by (8.6) for ocean, sea-ice and snow on low vegetation, (8.7) for dry high and low vegetation, the interception reservoir (with r_c replaced by r_1) and for bare soil (with r_c replaced by r_{soil}) and (8.16) for high vegetation with underlying snow.

8.3 THE SURFACE ENERGY BALANCE AND COUPLING TO THE SOIL

A skin temperature T_{sk} forms the interface between the soil and the atmosphere. As detailed in Section 3.7, it is calculated for each grid box tiles separately, by scanning the surface energy balance solver over the 8 tiles, assuming a complete coverage of the specific tile. For a single tile, this procedure is very similar to the derivation of the Penman–Monteith equation in which the skin temperature is eliminated from the surface energy balance equation. The numerical approach used in (H)TESSEL has the advantage that the feedback of skin temperature on net radiation and ground heat flux is included (see Section 3.7). The input radiation and reference atmospheric temperature (T_L), specific humidity (q_L) and wind speed (U_L) are identical for each tile. The surface fluxes "seen" by the atmosphere are calculated as an area-weighted average over the tiles (see (8.17) and (8.18)). For the high vegetation with snow underneath, the skin temperature is that of the high vegetation; the temperature of the underlying snow is calculated separately.

The energy balance equation solved for each tile takes into account partial absorption of net short-wave radiation, $1 - f_{Rs,i}$, in the skin layer (see Table 8.2). The remaining energy is directly passed to the soil or snow so that

$$(1 - f_{Rs,i})(1 - \alpha_i)R_s + \varepsilon(R_T - \sigma T_{sk,i}^4) + H_i + L_{v,s}E_i = \Lambda_{sk,i}(T_{sk,i} - T_1) \tag{8.19}$$

where i denotes the tile index, R_s and R_T are downward short-wave radiation and long-wave radiation, respectively, σ is the Stefan–Bolzman constant, T_1 the temperature of the upper soil or snow layer, H_i the sensible heat flux, and $L_{v,s}E_i$ the latent heat flux from the skin layer, and $\Lambda_{sk,i}$, the skin conductivity for tile i. Latent heat of evaporation, L_v, is used for all evaporation terms except snow evaporation, while L_s, the latent heat of sublimation, is used for evaporation of snow (i.e., tile 5 and the contribution $E_{sn,7}$ from tile 7, defined by (8.16)).

The tiled surface is thermally coupled to the snow deck, when present, and to a single soil profile. The net flux into the soil is a weighted average of the flux from each tile.

The solution of (8.19) is performed inside the code for turbulent exchanges in the atmosphere (Chapter 3). The atmospheric vertical diffusion equations yield a tridiagonal system of equations, with the coupling to the skin temperature given by the matrix row corresponding to the lowest model level. The first step for the solution of the system of equations, an LU decomposition, is followed by the solution of (8.19) before back-substitution. Details of the computations can be found in Chapter 3.

8.4 SNOW

The snow scheme represents an additional "layer" on top of the upper soil layer, with an independent, prognostic, thermal and mass contents. The snow pack is represented by a single snow temperature, T_{sn} and the snow mass per unit area (snow mass for short) S. The net energy flux at the top of the snow pack, G_{sn}^T, is the residual of the skin energy balance from the snow covered tiles and the snow evaporation from the tile with high vegetation over snow (see (8.15)). The basal heat flux, G_{sn}^B, is given by equation a resistance formulation modified in case of melting. The absorbed energy is used to change the snow

temperature or melt the snow, when $T_{\rm sn}$ exceeds the melting point. Liquid water whithin the snow pack is diagnosed from snow temperature, snow mass and snow density. Liquid water coexists in the snowpack leading to internal phase changes (freezing/melting), and rainfall can ben intercepted.

The heat capacity of the snow deck is a function of its depth, and snow density, and is modified in the presence of liquid water. The snow thermal conductivity changes with changing snow density. Snow density changes due to overburden and thermal metamorphisms (Anderson, 1976; Boone and Etchevers, 2001) and compaction related to melt water retained in the snowpack, adapted from Lynch-Stieglitz (1994) . The snow albedo changes exponentially with snow age. For snow on low vegetation it ranges between 0.50 for old snow and 0.85 for fresh snow. The albedo for high vegetation with snow underneath depends on vegetation type adapted from Moody *et al.* (2007). The details of the snow scheme and its validation can be found in Dutra *et al.* (2009) and Dutra *et al.* (2010).

8.4.1 Snow mass and energy budget

The snow energy budget in the presence of snow liquid water reads as

$$\begin{aligned}(\rho C)_{\rm sn} D_{\rm sn} \frac{\partial T_{\rm sn}}{\partial t} &= R^{\rm N}_{\rm sn} + L_s E_{\rm sn} + H_{\rm sn} - G^{\rm B}_{\rm sn} - L_f M_{\rm sn} - Q^{\rm INT}_{\rm sn} \\ Q^{\rm INT}_{\rm sn} &= L_f M^{\rm INT}_{\rm sn} = L_f \frac{\partial S_{\rm l}}{\partial t}\end{aligned} \tag{8.20}$$

where $(\rho C)_{\rm sn}$ is the snow volumetric heat capacity (J m^{-3}K^{-1}), $D_{\rm sn}$ is the snowpack depth (m), $T_{\rm sn}$ is the snow temperature (K), and the energy fluxes $R^{\rm N}_{\rm sn}$, $H_{\rm sn}$ and $G^{\rm B}_{\rm sn}$ are the net radiation (shortwave and longwave), sensible heat flux and basal heat flux (W m^{-2}), respectively. The mass fluxes $E_{\rm sn}$ and $M_{\rm sn}$ are the snow sublimation and melting (kg m^{-2}s^{-1}), respectively, that are associated with the latent heat of sublimation L_s and fusion L_f (J kg^{-1}). The superscript INT denotes internal phase changes, where $Q^{\rm INT}_{\rm sn}$ is the heat change associated with internal phase changes, and S_l the snow liquid water content (SLW) (kg m^{-2}). Whithout loss of generality, it can be assumed that for the grid box characteristic of NWP models, the following expression is valid

$$S_l = S_l(T_{\rm sn}, S) \approx f(T_{\rm sn}) S^c_l(S, \rho_{\rm sn}) \tag{8.21}$$

where S^c_l (kg m_{-2}) is the snow liquid water capacity, S is the sum of snow and water in the snowpack (also referred as SWE) and $\rho_{\rm sn}$ is the snow density (kg m_{-3}). The snow temperature function is prescribed in an analytical form - following a similar approach described by Viterbo *et al.* (1999) for soil phase changes

$$f_(T_{\rm sn}) = \left\{ \begin{array}{ll} 0 & T_{\rm sn} < T_f - d/2 \\ 1 + \sin\left\{ \dfrac{\pi(T_{\rm sn} - T_f)}{d} \right\} & T_{\rm sn} \geq T_f - d/2 \end{array} \right\} \tag{8.22}$$

where T_f is the triple-point temperature for water and d is a characteristic temperature difference, with respect to T_f, limiting the phase change regime. In the numerical implementation, $d = 4K$ was chosen. Snow liquid water capacity is approximated as a function of S and $\rho_{\rm sn}$, following Anderson (1976)

$$S^c_l = S[r_{\rm l,min} + (r_{\rm l,max} - r_{\rm l,min}) \max(0, \rho_{\rm sn,l} - \rho_{\rm sn})/\rho_{\rm sn,l}] \tag{8.23}$$

with the constants $r_{\rm l,min}$ =0.03, $r_{\rm l,max}$ =0.1 and $\rho_{\rm sn,l}$ =200 kg m^{-3}. This equation is a simple parameterization of a very complex phenomenon and has been used recently in other snow schemes, for example, Boone and Etchevers (2001).

Combining (8.20) and (8.21) results in a modified snow energy budget equation,

$$\left[(\rho C)_{\rm sn} D_{\rm sn} + L_f S^c_l \frac{\partial f(T_{\rm sn})}{\partial T_{\rm sn}} \right] \frac{\partial T_{\rm sn}}{\partial t} = R^{\rm N}_{\rm sn} + L_s E_{\rm sn} + H_{\rm sn} - G^{\rm B}_{\rm sn} - L_f M_{\rm sn} \tag{8.24}$$

with one extra term in the lhs of the equation, that can be interpreted as an additional snow heat capacity - or heat capacity barrier. In compacted snowpacks, the representation of SLW as a diagnostic increases

the snow heat capacity by a factor of up to five. This increase acts as a heat barrier near T_f, representing the increased snow temperature inertial due to freeze-melt events. The snow heat capacity in (8.20),(8.24) is aproximated as

$$(\rho C)_{\rm sn} \approx \frac{(\rho C)_{\rm i}}{\rho_{\rm i}} \rho_{\rm sn} \tag{8.25}$$

This diagnostic approach for SLW also allows the representation of rainfall interception. The snow mass balance reads as

$$\frac{\partial S}{\partial t} = F + c_{\rm sn} F_l + c_{\rm sn} E_{\rm sn} - R_{\rm sn}, \tag{8.26}$$

where F, F_l, and $R_{\rm sn}$ are the mass fluxes of snowfall, rainfall and runoff (kg m^{-2} s^{-1}) and $c_{\rm sn}$ is the snow cover fraction. Rainfall is considered to reach the snowpack at T_f, and latent heat released by the freezing of the intercepted rainfall, if $T_{\rm sn} < T_f$, is also accounted in the energy-balance solution. Runoff is defined as the rate at which liquid water leaves the snowpack and parameterized as follows:

$$R_{\rm sn} = c_{\rm sn} M_{\rm sn} + \max\left(c_{\rm sn} F_l - \frac{S_l^c (1 - f(T_{\rm sn}))}{\Delta}, 0 \right) \tag{8.27}$$

Liquid water is generated by melting ($M_{\rm sn}$) and by rainfall interception (F_l). When snow liquid water content exceeds the snow liquid water capacity (defined in (8.22)) runoff is generated.

In this section, all fluxes are per unit area and apply only to the snow area (i.e. tile 5 and 7). The snow mass S applies to the entire grid square, as weel as the snowfall flux from the atmospheric model. As a general rule, all quantitites with subscript *sn* refer to the snow area. Snow evaporation (8.24,8.26) is defined as

$$c_{\rm sn} E_{\rm sn} = c_5 E_5 + c_7 E_{\rm sn,7} \tag{8.28}$$

Snow mass and snow depth are related by

$$D_{\rm sn} = \frac{1}{\rho_{\rm sn}} \frac{S}{c_{\rm sn}} \tag{8.29}$$

where $D_{\rm sn}$ is snow depth for the snow-covered area (units m; note that $D_{\rm sn}$ is not a grid-averaged quantity) and $\rho_{\rm sn}$ is the snow density (units kg $\rm m^{-3}$).

8.4.2 Prognostic snow density and albedo

Snow density is assumed to be constant with depth, and the rate of density change is parameterized as

$$\frac{1}{\rho_{\rm sn}} \frac{\partial \rho_{\rm sn}}{\partial t} = \frac{\sigma_{\rm sn}}{\eta_{\rm sn}(T_{\rm sn}, \rho_{\rm sn})} + \xi_{\rm sn}(T_{\rm sn}, \rho_{\rm sn}) + \frac{\max(0, Q_{\rm sn}^{\rm INT})}{L_f (S - S_l)} \tag{8.30}$$

where the first two terms in (8.30) represent overburden and thermal metamorphism (Anderson, 1976; Boone and Etchevers, 2001), respectively, and the last term represents the compaction related to meltwater retained in the snowpack, adapted from Lynch-Stieglitz (1994). In the overburden term (first term on the rhs of (8.30)), $\sigma_{\rm sn}$ and $\eta_{\rm sn}$ are the pressure of the overlying snow (Pa) and snow viscosity (Pa s), repectively. Melted water retained in the snowpack leads to a decrease of snow depth while keeping S constant. In snowfall conditions a weighted average is taken between the current snow density and the density of snowfall

$$\rho_{\rm sn}^* = \frac{S \rho_{\rm sn}^t + \Delta t F \rho_{\rm new}}{S + \Delta t F} \tag{8.31}$$

where $\rho_{\rm sn}^*$ is an updated snow density. Snowfall density $\rho_{\rm new}$ is given by an expression from CROCUS (Brun *et al.*, 1989, 1992) were fresh snow density is a function of near surface air temperature and wind speed

$$\rho_{\rm new} = a_{\rm sn} + b_{\rm sn}(T_{\rm air} - T_f) + c_{\rm sn}(V_a)^{1/2} \tag{8.32}$$

where $T_{\rm air}$ and V_a are the near surface air temperature (K) and wind speed (m s^{-1}),repectively. The coefficients are $a_{\rm sn}$=109 kg m^{-3}, $b_{\rm sn}$=6 kg $m^{-3}K^{-1}$, and $c_{\rm sn}$=26 kg $m^{-7/2}s^{1/2}$. Snow density is constrained to be between 50 to 450 kg m^{-3}.

The snow viscosity in (8.30) is formulated following Anderson (1976)

$$\eta_{\rm sn} = \eta_0 \exp\Big(a_\eta(T_f - T_{\rm sn}) + b_\eta \rho_{\rm sn}\Big) \tag{8.33}$$

where η_0=3.7 10^7 (Pa s), a_η=8.1 $10^{-2}K^{-1}$ and b_η=1.8 $10^{-2}m^3kg^{-1}$. The pressure of the overlying snow is given by $\sigma_{\rm sn} = \frac{1}{2}Sg$, where g is the standard gravity (m^2s^{-2}).

The thermal metamorphim (second term in the rhs of (8.30)) is parameterized as

$$\xi_{\rm sn} = a_\xi \exp\Big[-b_\xi(T_f - T_{\rm sn}) - c_\xi \max(0, \rho_{\rm sn} - \rho_\xi)\Big] \tag{8.34}$$

using the constant values of Anderson (1976): a_ξ=2.8 $10^{-6}s^{-1}$, b_ξ=4.2 10^{-2}, c_ξ=460 m^3kg^{-1}, and ρ_ξ=150 kg m^{-3}.

Snow albedo in exposed areas evolves according to the formulation of Baker *et al.* (1990), Verseghy (1991), Douville *et al.* (1995) and Dutra *et al.* (2010). For melting and non melting-conditions:

$$\alpha_{\rm sn}^{\rm t+1} = \begin{cases} \alpha_{\rm sn}^{\rm t} - \tau_a \Delta t/\tau_1 & M_{\rm sn} = 0 \\ (\alpha_{\rm sn}^{\rm t} - \alpha_{\rm min})\exp(-\tau_f \Delta t/\tau_1) + \alpha_{\rm min} & M_{\rm sn} > 0 .or. T_{\rm sn} \geq T_f - d/2 \end{cases} \tag{8.35}$$

where $\tau_{\rm a} = 0.008$, which will decrease the albedo by 0.1 in 12.5 days, $\alpha_{\rm min} = 0.5$ and $\alpha_{\rm max} = 0.85$. The timescales $\tau_1 = 86400$ s, and $\tau_{\rm f} = 0.24$ corresponding to an e-folding time of about 4 days (see table 8.4).

A continuous reset is applied to snow albedo after snowfall events:

$$\alpha_{\rm sn}^{\rm t+1} = \alpha_{\rm sn}^{\rm t} + \min\Big(1, \frac{F\Delta t}{10}\Big)(\alpha_{\rm max} - \alpha_{\rm sn}^{\rm t}) \tag{8.36}$$

This formulation assumes that 10 kg m^{-2} of fresh snowfall are needed to reset the snow albedo to its maximum value ($\alpha_{\rm max} = 0.85$).

The above formulae are inadequate to describe the evolution of the surface albedo of snow cover with high vegetation. Observations suggest a dependence on forest type but, by and large, the albedo changes from a value around 0.3 just after a heavy snowfall to a value around 0.2 after a few days (see Betts and Ball (1997) and the discussion in Viterbo and Betts (1999)). This change reflects the disappearance of intercepted snow, due to melt (for sufficiently warm temperatures) or wind drift (for cold temperatures). Ways of describing those two mechanisms would involve either a separate albedo variable for the snow in the presence of high vegetation, or the introduction of an interception reservoir for snow. In the absence of any of the two, a vegetation-type-dependent albedo adapted from Moody *et al.* (2007) is used (see table 8.5). Moody *et al.* (2007) provide a 5-year (2000–04) climatological statistic of northern hemisphere broadband (0.–5.0 μm) white-sky albedo for the 16 IGBP ecosystem classes when accompanied by the presence of snow on the ground.

8.4.3 Additional details

(*a*) *Limiting of snow depth in the snow energy equation*

Initial experimentation with the snow model revealed that the time evolution of snow temperature was very slow over Antarctica. The reason is rather obvious; the snow depth over Antarctica is set to a climatological value of 10 m which can respond only very slowly to the atmospheric forcing due to its large thermal inertia. In previous model versions, the properties of layer 1 were replaced by snow properties when snow was present, which kept the timescale short. A limit is put on the depth of the

Table 8.4 *Snow-related parameters.*

Symbol	Parameter	Value
$D_{\rm sn}^{\rm max}$	Maximum snow thermal depth	1.00 m
$D_{\rm cr}$	Threshold value for grid box coverage of snow	0.1 m
$\alpha_{\rm min}$	Minimum albedo of exposed snow	0.50
$\alpha_{\rm max}$	Maximum albedo of exposed snow	0.85
$\lambda_{\rm i}$	Ice heat conductivity	2.2 W $\rm m^{-1}K^{-1}$
$\rho_{\rm i}$	Ice density	920 k $\rm gm^{-3}$
$(\rho C)_i$	Ice volumetric heat capacity	2.05×10^6 J $\rm m^{-3}K^{-1}$
$\tau_{\rm a}$	Linear coefficient for decrease of albedo of non-melting snow	0.008
$\tau_{\rm f}$	Coefficient for exponential decrease of snow density and melting snow albedo	0.24
τ_1	Length of day	86400 s

Table 8.5 *Mean values of Northern Hemisphere broadband surface albedo (in presence of snow) aggregated by high vegetation type.*

Index	Vegetation type	Albedo
3	Evergreen needle leaf trees	0.27
4	Deciduous needle leaf trees	0.33
5	Deciduous broad leaf trees	0.31
6	Evergreen broad leaf trees	0.38
18	Mixed forest / woodland	0.29
19	Interrupted forest	0.29

snow layer in the thermal budget, $D_{\rm sn}^{\rm max} = 1.0$ m. The energy equation reads

$$\left[(\rho C)_{\rm sn} D_{\rm sn}^{*} + L_f S_l^{c} \frac{\partial f(T_{\rm sn})}{\partial T_{\rm sn}}\right] \frac{\partial T_{\rm sn}}{\partial t} = R_{\rm sn}^{\rm N} + L_s E_{\rm sn} + H_{\rm sn} - G_{\rm sn}^{\rm B} - L_f M_{\rm sn}$$
$$D_{\rm sn}^{*} = \min(D_{\rm sn}, D_{\rm sn}^{\rm max}) \tag{8.37}$$

A physical solution will be explored in a future scheme with a multilayer snow model, with e.g. four layers to represent timescales from one day to a full annual cycle.

(*b*) *Basal heat flux and thermal coefficients*

The heat flux at the bottom of the snow pack is written as a finite difference using

$$G_{\rm sn}^{\rm B} = \frac{T_{\rm sn} - T_1}{r_{\rm sn}} \tag{8.38}$$

where $r_{\rm sn}$ is the resistance between the middle of the snow pack and the middle of soil layer 1, with two components: the resistance of the lower part of the snow pack and the resistance of the top half of soil layer 1. Therefore

$$r_{\rm sn} = 0.5 \frac{D_{\rm sn}^{*}}{\lambda_{\rm sn}} + \frac{1}{\Lambda_{\rm sk,8}} \tag{8.39}$$

where the second term is the skin layer conductivity for bare soil (tile 8), which can be seen as an approximation of $0.5(D_1/\lambda_{\rm T})$. The snow thermal conductivity, is related to the ice thermal conductivity according to Douville *et al.* (1995) given by

$$\lambda_{\rm sn} = \lambda_{\rm i} \left(\frac{\rho_{\rm sn}}{\rho_{\rm i}}\right)^{1.88} \tag{8.40}$$

Table 8.4 contains the numerical values of the ice density and ice heat conductivity.

(c) Numerical solution for non-melting situations

The net heat flux that goes into the top of the snow deck is an output of the vertical diffusion scheme

$$H_{\rm sn}^{\rm N} = R_{\rm sn}^{\rm N} - L_{\rm s}E_{\rm sn} - H_{\rm sn} \tag{8.41}$$

In the absence of melting, the solution of (8.37) is done implicitly. The preliminary snow temperature, prior to the checking for melting conditions, $T_{\rm sn}^*$, is given by

$$A_1\frac{T_{\rm sn}^* - T_{\rm sn}^t}{\Delta t} = H_{\rm sn}^{\rm N} - \frac{T_{\rm sn}^* - T_1}{r_{\rm sn}} \tag{8.42}$$

$$\begin{aligned} A_1 &= \min\left[\frac{(\rho C)_{\rm i}}{\rho_{\rm i}c_{\rm sn}}S, A_1^{\max}\right] + L_f S_l^c \frac{\partial f(T_{\rm sn})}{\partial T_{\rm sn}}\bigg|_{T_{\rm sn}^t} \\ A_1^{\max} &= \frac{(\rho C)_{\rm i}}{\rho_i}\rho_{\rm sn}D_{\rm sn}^{\max} \end{aligned} \tag{8.43}$$

where superscript t refers to the current time step and superscript * to the preliminary value at the next time step. The solution for $T_{\rm sn}^*$ is obtained from

$$T_{\rm sn}^*\left(1 + \frac{\Delta t}{r_{\rm sn}A_1}\right) = T_{\rm sn}^t + \frac{\Delta t}{A_1}\left(H_{\rm sn}^{\rm N} + \frac{T_1^t}{r_{\rm sn}}\right) \tag{8.44}$$

The basal snow heat flux to be used as input for the thermal budget of the soil (in the snow covered fraction only) is

$$G_{\rm sn}^{\rm B} = \frac{T_{\rm sn}^* - T_1}{r_{\rm sn}} \tag{8.45}$$

Finally, a preliminary new value for the snow mass, S^*, is computed from snow fall and snow evaporation using

$$\frac{S^* - S^t}{\Delta t} = F + c_{\rm sn}E_{\rm sn} \tag{8.46}$$

8.4.4 Treatment of melting

(a) No melting occurs

If $T_{\rm sn}^* < T_0$ no melting occurs and the preliminary values $T_{\rm sn}^*$ and S^* become the $t+1$ values, while the basal heat flux is given by (8.45).

(b) Melting conditions

If $T_{\rm sn}^* > T_0$, snow melting occurs and the time step is divided in two fractions, $\Delta t = \Delta_1 t + \Delta_2 t$, where the first fraction, $\Delta_1 t$ brings the temperature to T_0 with no melting so that

$$\Delta_1 t = \frac{A_1(T_0 - T_{\rm sn}^t)}{H_{\rm sn}^{\rm N} - (T_0 - T_1^t)/r_{\rm sn}} \tag{8.47}$$

while, during the second fraction, $\Delta_2 t$, melting occurs with no resultant warming of the snow so that

$$\begin{aligned} T^{t+1} &= T_0 \\ Q_{\rm sn} &= H_{\rm sn}^{\rm N} - G_{\rm sn}^{\rm B} \\ \frac{S^{t+1} - S^*}{\Delta_2 t} &= -c_{\rm sn}M_{\rm sn} = -c_{\rm sn}\frac{Q_{\rm sn}}{L_{\rm f}} = -c_{\rm sn}\frac{H_{\rm sn}^N - G_{\rm sn}^{\rm B}}{L_{\rm f}} \end{aligned} \tag{8.48}$$

If not all the snow melts, i.e., if $S^{t+1} > 0$, the heat flux passed to the soil is

$$G_{\rm sn}^{\rm B} = \frac{T_0 - T_1}{r_{\rm sn}} \tag{8.49}$$

Table 8.6 *Parameters in the land-surface scheme. See Table 8.4 for snow-related parameters.*

Symbol	Parameter	Value
b_I	Interception efficiency	0.25
D_1	Depth of soil layer 1	0.07 m
D_2	Depth of soil layer 2	0.21 m
D_3	Depth of soil layer 3	0.72 m
D_4	Depth of soil layer 4	1.89 m
$F_{\rm cv}$	Fraction of gridbox covered by convective rainfall	0.5
k	Heterogeneity factor for convective precipitation	0.5
$T_{\rm f1}$	Highest temperature for existence of ice water	T_0+1
$T_{\rm f2}$	Lowest temperature for existence of liquid water	T_0-3
$w_{1\,\max}$	Maximum water amount on single leaf	0.0002 m

When all the snow melts, i.e., if $S^{t+1}<0$, the melting time step is redefined as

$$\begin{aligned} S^{t+1} &= 0 \\ \Delta_2 t &= L_{\rm f}\frac{S^*}{c_{\rm sn}(H^{\rm N}_{\rm sn}-G^{\rm B}_{\rm sn})} \\ \Delta_3 t &= 1-(\Delta_1 t+\Delta_2 t) \end{aligned} \tag{8.50}$$

and the basal heat flux is redefined as

$$G^{\rm B}_{\rm sn} = \frac{\Delta_1 t+\Delta_2 t}{\Delta t}\frac{T_0-T^t_1}{r_{\rm sn}}+\frac{\Delta_3 t}{\Delta t}H^{\rm N}_{\rm sn} \tag{8.51}$$

8.5 SOIL HEAT TRANSFER

In the absence of internal phase changes, the soil heat transfer is assumed to obey the following Fourier law of diffusion

$$(\rho C)_{\rm soil}\frac{\partial T}{\partial t} = \frac{\partial}{\partial z}\left[\lambda_T\frac{\partial T}{\partial z}\right] \tag{8.52}$$

where $(\rho C)_{\rm soil}$ is the volumetric soil heat capacity (J m^{-3}K^{-1}), T is the soil temperature (units K), z is the vertical coordinate—the distance from the surface, positive downwards—(units m), and $\lambda_{\rm T}$ is the thermal conductivity (W m^{-1}K^{-1}). The above equation assumes that heat fluxes are predominantly in the vertical direction, that the effects of phase changes in the soil and the heat transfer associated with the vertical movement of water in the soil can be neglected (De Vries, 1975), and that the effects of hysteresis can be neglected (Milly, 1982).

The boundary condition at the bottom, no heat flux of energy, is an acceptable approximation provided that the total soil depth is large enough for the time-scales represented by the model or, in other words, the bottom of the soil is specified at a depth where the amplitude of the soil heat wave is a negligible fraction of its surface amplitude (see De Vries (1975) and next Section 8.6).

8.5.1 Discretization and choice of parameters

For the solution of (8.52) the soil is discretized in four layers, of depths D_k, $(k=1,2,3,4)$, the temperatures are defined at full layers (T_k), and the heat fluxes, at half layers ($G_{k+1/2}$ is the heat flux, positive downwards, units W m^{-1}, at the interface between layer k and $k+1$). An energy-conserving implicit algorithm is used, leading to a tridiagonal system of equations with solution detailed in Section 8.9.

The boundary condition at the bottom is

$$G_{4+1/2}=0 \tag{8.53}$$

At the top, the boundary condition is the soil heat flux at the surface, computed as a weighted average over the tiles. For the snow free tiles, the flux into the soil consists of two parts. Apart from the diffusion

of heat governed by $\Lambda_{\mathrm{sk},i}(T_{\mathrm{sk},i} - T_1)$ (see (8.19)), the net short-wave radiation not absorbed by the skin layer ($f_{\mathrm{Rs},i}$) provides energy to the soil. Table 8.2 lists the values of $\Lambda_{\mathrm{sk},i}$ and $f_{\mathrm{Rs},i}$ for each of the tiles. For the snow tiles, the heat flux into the soil is the snow basal flux, calculated using a resistance formulation and modified in the case of partial melting (see (8.38), (8.45), (8.49), and (8.51)).

The net heat flux into the soil is given by

$$G_{1/2} = \sum_i C_i[\Lambda_{\mathrm{sk},i}(T_{\mathrm{sk},i} - T_1) + f_{\mathrm{Rs},i}(1-\alpha_i)R_{\mathrm{s}}] + c_{\mathrm{s}}G^{\mathrm{B}}_{\mathrm{sn}} \tag{8.54}$$

where the summation scans all snow free tiles.

The volumetric soil heat capacity is assumed constant, with value 2.19×10^6 J m^{-3}K^{-1} (see Table 8.6 for a list of constants used by the model). The heat conductivity, λ, depends on the soil-water content following Peters-Lidard *et al.* (1998) (see also Farouki, 1986; Johansen, 1975) and is given by a combination of dry λ_{dry} and saturated λ_{sat} values, weighted by a factor known as the Kersten number, K_{e}, so that

$$\lambda = K_{\mathrm{e}}(\lambda_{\mathrm{sat}} - \lambda_{\mathrm{dry}}) + \lambda_{\mathrm{dry}} \tag{8.55}$$

where $\lambda_{\mathrm{dry}} = 0.190$ W m^{-1} K^{-1} and

$$\lambda_{\mathrm{sat}} = \lambda_{\mathrm{sm}}^{1-\theta_{\mathrm{sat}}}\lambda_{\mathrm{w}}^{\theta} \tag{8.56}$$

where the heat conductivity of the soil matrix, $\lambda_{\mathrm{sm}} = 3.44$ W m^{-1} K^{-1} and the thermal conductivity of water is $\lambda_{\mathrm{w}} = 0.57$ W m^{-1} K^{-1}. Equation (8.56) represents a simplification of Peters-Lidard formulation, neglecting the changes in conductivity due to ice water and assuming the quartz content typical of a loamy soil. Finally, the Kersten number for fine soils was selected in Peters-Lidard *et al.* (1998) as

$$K_e = \log_{10}\left[\max\left(0.1, \frac{\theta}{\theta_{\mathrm{sat}}}\right)\right] + 1 \tag{8.57}$$

The depths of the soil layers are chosen in an approximate geometric relation (see Table 8.6), as suggested in Deardorff (1978). Warrilow *et al.* (1986) have shown that four layers are enough for representing correctly all timescales from one day to one year. Using the numerical values of the heat capacity and soil depths defined in Table 8.6, the amplitude and phase response of the numerical solution of (8.52) were analysed by Viterbo and Beljaars (1995) for typical values of soil moisture in (8.55), and for harmonic forcings at the surface with periods ranging from half a day to two years. The analysis points to an error in the numerical solution of less than 20% in amplitude and 5% in phase for forcing periods between one day and one year.

8.5.2 Soil-water phase changes

At high and mid latitudes the phase changes of water in the soil have an important effect on the water and energy transfer in the soil. A proper consideration of the solid phase of soil water requires modifications including, in order of importance, the following.

(i) The thermal effects related to the latent heat of fusion/freezing (e.g. Rouse, 1984).
(ii) Changes in the soil thermal conductivity due to the presence of ice (e.g. Penner, 1970, not included in TESSEL as mentioned in the previous section).
(iii) Suppression of transpiration in the presence of frozen ground (e.g. Betts *et al.*, 1998) and already described in (8.11).
(iv) Soil water transfer dependent on a soil water potential including the effects of frozen water (e.g. Lundin, 1989), represented in a proxy way by (8.79).

The latent-heat effects are described in the following. The main impact will be to delay the soil cooling in the beginning of the cold period, and to delay the soil warming in spring, although the latter effect is less important because it occurs when the solar forcing is significant. Both effects make the soil temperatures less responsive to the atmospheric forcing and damp the amplitude of the annual soil temperature cycle. More details on the soil-freezing scheme and its impact on forecasts and the model climate are described in Viterbo *et al.*, 1999.

The soil energy equation, (8.52), is modified in the presence of soil water phase changes as

$$(\rho C)_{\text{soil}}\frac{\partial T}{\partial t}=\frac{\partial}{\partial z}\left[\lambda_T\frac{\partial T}{\partial z}\right]+L_{\text{fus}}\rho_{\text{w}}\frac{\partial \theta_{\text{I}}}{\partial t} \tag{8.58}$$

where θ_{I} is the volumetric ice-water content. Without loss of generality, for the grid squares characteristic of NWP models it can be assumed that

$$\theta_{\text{I}}=\theta_{\text{I}}(\theta,T)=f(T)\theta \tag{8.59}$$

where θ is the total soil-water content (liquid + ice), and

$$\begin{array}{ll} f_{\text{fr}}(T)=0 & T>T_{\text{f1}} \\ 0<f_{\text{fr}}(T)<1 & T_{f1}\le T\le T_{\text{f2}} \\ f_{\text{fr}}(T)=1 & T<T_{\text{f2}} \end{array} \tag{8.60}$$

where T_{f1} and T_{f2} are characteristic temperatures limiting the phase change regime. In reality, the values of T_{f1} and T_{f2} and the function $f_{\text{fr}}(T)$ have complicated dependencies on soil texture and composition (see e.g. Williams and Smith, 1989), but here they are approximated in a simple way. For an idealized homogeneous, one-component soil, $f_{\text{fr}}(T)$ would be a step-function. According to Williams and Smith (1989) physical reasons for having an interval over which melting/freezing is active, rather than a threshold temperature, include the following.

(i) Adsorption, resulting from forces between the mineral parts of the soil and the water.
(ii) Capillarity, related to the fact that the water-free surface is not plane.
(iii) Depression of the freezing point due to the effect of dissolved salts.
(iv) Soil heterogeneity.

To avoid an undesirable coupling between the temperature and water equations in the soil, (8.59) is simplified to

$$\theta_{\text{I}}=f_{\text{fr}}(T)\theta_{\text{f}} \tag{8.61}$$

where θ_{f} is a constant, representing the amount of soil water that can be frozen (thawed). For simplicity, $\theta_{\text{f}}=(c_{\text{H}}+c_{\text{L}})\theta_{\text{cap}}$. The scaling with the vegetated fractions is the simplest way of distinguishing between dry (vegetation-sparse areas, e.g. deserts) and wet (vegetated) areas. Combining (8.61) with (8.58) results in

$$\left[(\rho C)_{\text{soil}}-L_{\text{fus}}\rho_{\text{w}}\frac{\partial f_{\text{fr}}}{\partial T}\right]\frac{\partial T}{\partial t}=\frac{\partial}{\partial z}\left[\lambda_T\frac{\partial T}{\partial z}\right] \tag{8.62}$$

showing that the effect of freezing can be interpreted as an additional soil heat capacity, sometimes referred in the literature as the 'heat-capacity barrier' around freezing; not considering the process of soil water freezing/melting can lead to very large artificial temperature changes that do not occur in nature when sufficient soil water is available.

Finally, function $f_{\text{fr}}(T)$, is given by

$$f_{\text{fr}}(T)=\begin{cases} 0 & T>T_{\text{f1}} \\ 0.5\left\{1-\sin\left[\dfrac{\pi(T-0.5T_{\text{f1}}-0.5T_{\text{f2}})}{T_{\text{f1}}-T_{\text{f2}}}\right]\right\} & T_{\text{f2}}\ge T\ge T_{\text{f1}} \\ 1 & T<T_{\text{f2}} \end{cases} \tag{8.63}$$

with $T_{\text{f1}}=T_0+1, T_{\text{f1}}=T_0-3$.

8.6 SOIL-WATER BUDGET

The vertical movement of water in the unsaturated zone of the soil matrix obeys the following equation (see Richards (1931), Philip (1957), Hillel (1982), and Milly (1982) for the conditions under which (8.64)

and (8.65) are valid) for the volumetric water content θ:

$$\rho_{\mathrm{w}} \frac{\partial \theta}{\partial t} = -\frac{\partial F_{\mathrm{w}}}{\partial z} + \rho_{\mathrm{w}} S_\theta \tag{8.64}$$

ρ_{w} is the water density (kg m^{-3}), F_{w} is the water flux in the soil (positive downwards, kg m^{-2}s^{-1}), and S_θ is a volumetric sink term (m^{3}m$^{-3}s^{-1}$), corresponding to root extraction. Using Darcy's law, F_{w} can be specified as

$$F_{\mathrm{w}} = \rho_{\mathrm{w}} \left(\lambda \frac{\partial \theta}{\partial z} - \gamma \right) \tag{8.65}$$

λ (m^2 s^{-1}) and γ (m s^{-1}) are the hydraulic diffusivity and hydraulic conductivity, respectively.

Replacing (8.65) in (8.64), specifying $S_\theta = S_\theta(\theta, z)$, and defining parametric relations for λ and γ as functions of soil water, a partial differential equation for θ is obtained; it can be numerically integrated if the top boundary condition is precipitation minus evaporation minus surface runoff. The bottom boundary condition assumes free drainage. Abramopoulos *et al.* (1988) specified free drainage or no drainage, depending on a comparison of a specified geographical distribution of bedrock depth, with a model-derived water-table depth. For the sake of simplicity the assumption of no bedrock everywhere has been adopted.

8.6.1 Interception

The interception reservoir is a thin layer on top of the soil/vegetation, collecting liquid water by the interception of rain and the collection of dew, and evaporating at the potential rate. The water in the interception reservoir, W_1, obeys

$$\rho_{\mathrm{w}} \frac{\partial W_l}{\partial t} = c_1 E_1 + D + I \tag{8.66}$$

where $C_1 E_1$ is the water evaporated by the interception reservoir (or dew collection, depending on its sign), D represents the dew deposition from other tiles, and I (kg m^{-2} s^{-1}) is the interception—the fraction of precipitation that is collected by the interception reservoir and is later available for potential evaporation. Because the interception reservoir has a very small capacity (a maximum of the order of 1 mm, see (8.2)), it can fill up or evaporate completely in one time step; special care has to be taken in order to avoid numerical problems when integrating (8.66). In addition, since E_1 is defined in the vertical diffusion code, it might impose a rate of evaporation that depletes entirely the interception layer in one time step. In order to conserve water in the atmosphere-intercepted water–soil continuum, the mismatch of evaporation of tile 3 plus dew deposition from the other tiles (which is not explicitly dealt with by the vertical diffusion) as seen by the vertical diffusion and the intercepted water has to be fed into the soil.

The equation is solved in three fractional steps: evaporation, dew deposition, and rainfall interception. The solver provides the following as outputs.

(i) Interception layer contents at time step $n+1$, W_{i}^{n+1}.
(ii) Throughfall (i.e. rainfall minus intercepted water).
(iii) The evaporation effectively seen by the intercepted layer in each tile i.

First, the upward evaporation ($E_1 < 0$) contribution is considered; because $C_1 E_1$ depends linearly on W_1 (see (8.2)), an implicit version of the evaporating part of (8.66) is obtained by linearizing $C_1(W_1)E_1$ giving

$$\rho_{\mathrm{w}} \frac{W_1^* - W_1^t}{\Delta t} = C_1(W_1^t)E_1 + \frac{E_1}{W_{1\mathrm{m}}}(W_1^* - W_1^t) \tag{8.67}$$

where W_1^* is the new value of interception-reservoir content after the evaporation process has been taken into account. After solving for W_1^*, a non-negative value of evaporation is obtained and the evaporation seen by this fractional time step is calculated

$$\begin{aligned} W_1^1 &= \max(0, W_1^*) \\ E^1 &= \rho_{\mathrm{w}} \frac{W_1^1 - W_1^t}{\Delta t} \end{aligned} \tag{8.68}$$

The dew deposition is dealt with explicitly for each non-snow tile in succession, for tiles 3, 4, 6, 7, 8, where tile 7 is also considered because in the exposed snow tile, the canopy is in direct evaporative contact with the atmosphere. When the evaporative flux is downwards ($E_1 > 0$)

$$\begin{aligned} W^2 &= W^1 + \min\left(W_{1\mathrm{m}} - W^1, \frac{\Delta t}{\rho_\mathrm{w}} c_i D_i\right) \\ D_i &= \rho_\mathrm{w} \frac{W^2_{1,i} - W^1_1}{\Delta t} \end{aligned} \tag{8.69}$$

where superscript 2 denotes the final value at the end of the this fractional time step.

The interception of rainfall is considered by applying the following set of equations to large-scale and convective rainfall

$$\begin{aligned} W^3_1 &= W^2_1 + \min\left(W_{1\mathrm{m}} - W^2_1, \frac{\Delta t}{\rho_\mathrm{w}} b_I (c_\mathrm{H} + c_\mathrm{L}) R_{1\mathrm{s}}\right) \\ T_{1\mathrm{s}} &= R_{1\mathrm{s}} - \rho_\mathrm{w} \frac{W^3_1 - W^2_1}{\Delta t} \\ W^{t+1}_1 &= W^3_1 + \min\left(W_{1\mathrm{m}} - W^3_1, \frac{\Delta t}{\rho_\mathrm{w}} b_I (c_\mathrm{H} + c_\mathrm{L}) \frac{R_\mathrm{cv}}{F_\mathrm{cv}}\right) \\ T_\mathrm{cv} &= R_\mathrm{cv} - \rho_\mathrm{w} \frac{W^{t+1}_1 - W^3_1}{\Delta t} \end{aligned} \tag{8.70}$$

$R_\mathrm{cv}/F_\mathrm{cv}$ is a modified convective rainfall flux, computed by applying the heterogeneity assumption that convective rainfall only covers a fraction $F_\mathrm{cv} = 0.5$ of the grid box, $b_I = 0.25$ is a coefficient of efficiency of interception of rain. The total evaporation seen by the interception reservoir is D_i for tiles 4, 6, 7, and 8 and $c_l E_l + D_i$ for tile 3.

The interception reservoir model described in this section is probably the simplest water-conserving formulation based on Rutter's original proposition (Rutter *et al.*, 1972, 1975). For more complicated formulations still based on the Rutter concept see, for instance, Mahfouf and Jacquemin (1989), Dolman and Gregory (1992) and Ridder (2001).

8.6.2 Soil properties

Integration of (8.64) and (8.65) requires the specification of hydraulic conductivity and diffusivity as a function of soil-water content. In TESSEL the parametric relations of Clapp and Hornberger (1978) (see also Cosby *et al.*, 1984) were adopted (still available as option). These are given by

$$\begin{aligned} \gamma &= \gamma_\mathrm{sat} \left(\frac{\theta}{\theta_\mathrm{sat}}\right)^{2b+3} \\ \lambda &= \frac{b \gamma_\mathrm{sat} (-\psi_\mathrm{sat})}{\theta_\mathrm{sat}} \left(\frac{\theta}{\theta_\mathrm{sat}}\right)^{b+2} \end{aligned} \tag{8.71}$$

where b is a non-dimensional exponent, γ_sat and ψ_sat are the values of the hydraulic conductivity and matric potential at saturation, respectively. A minimum value is assumed for λ and γ corresponding to permanent wilting-point water content.

Cosby *et al.* (1984) tabulate best estimates of $b, \gamma_\mathrm{sat}, \Psi_\mathrm{sat}$ and θ_sat, for the 11 soil classes of the US Department of Agriculture (USDA) soil classification, based on measurements over large samples. Since the model described here specifies only one soil type everywhere, and because the determination of the above constants is not independent of the values of θ_cap and θ_pwp, the following procedure is adopted.

A comprehensive review of measurements of θ_cap and θ_pwp may be found in Patterson (1990). Starting from Patterson's estimates of θ_cap and θ_pwp for the 11 USDA classes, a mean of the numbers corresponding

Table 8.7 *Van Genuchten soil parameters.*

Texture	α	l	n	γ_{sat}
Units	m^{-1}	-	-	$10^{-6}m/s$
Coarse	3.83	1.250	1.38	6.94
Medium	3.14	-2.342	1.28	1.16
Medium-Fine	0.83	-0.588	1.25	0.26
Fine	3.67	-1.977	1.10	2.87
Very Fine	2.65	2.500	1.10	1.74
Organic	1.30	0.400	1.20	0.93

Table 8.8 *Values for the volumetric soil moisture in Van Genuchten and Clapp-Hornberger (CH, loamy; bottom row), at saturation, θ_{sat}, field capacity, θ_{cap}, and permanent wilting point, θ_{pwp}. Last column reports the plant available soil moisture. Units are $[m^3m^{-3}]$.*

Texture	θ_{sat}	θ_{cap}	θ_{pwp}	$\theta_{cap}-\theta_{pwp}$
Coarse	0.403	0.244	0.059	0.185
Medium	0.439	0.347	0.151	0.196
Medium-Fine	0.430	0.383	0.133	0.251
Fine	0.520	0.448	0.279	0.170
Very Fine	0.614	0.541	0.335	0.207
Organic	0.766	0.663	0.267	0.396
Loamy (CH)	0.472	0.323	0.171	0.151

to the medium-texture soils (classes 4, 5, 7, and 8, corresponding to silt loam, loam, silty clay loam and clay loam, respectively) is taken. The resulting numbers are $\theta_{\rm cap} = 0.3\dot{2}3{\rm m}^3\ {\rm m}^{-3}$ and $\theta_{\rm pwp} = 0.171{\rm m}^3\ {\rm m}^{-3}$. Averaging the values of Cosby *et al.* (1984) for soil moisture and soil-water conductivity at saturation for the same classes gives the numerical values $\gamma_{\rm sat} = 0.57 \times 10^{-6}$ m s^{-1} and $\theta_{\rm sat} = 0.472$ m^3 m^{-3} . The Clapp and Hornberger expression for the matric potential is

$$\psi = \psi_{\rm sat}\left(\frac{\theta}{\theta_{\rm sat}}\right)^{-b} \tag{8.72}$$

is used with $\psi(\theta_{\rm pwp}) = -153$ m (-15 bar) and $\psi(\theta_{\rm cap}) = -3.37$ m (-0.33 bar) (see Hillel, 1982; Jacquemin and Noilhan, 1990) to find the remaining constants b and $\psi_{\rm sat}$. The results are $b = 6.04$ and $\Psi_{\rm sat} = -0.338$ m. The above process ensures a soil that has an availability corresponding to the average value of medium-texture soils, and yields a quantitative definite hydraulic meaning to $\theta_{\rm cap}$ and $\theta_{\rm pwp}$ compatible with the Van Genuchten relations (see Table 8.7 for a summary of the soil constants).

The van Genuchten (1980) formulation provides a closed-form analytical expression for the conductivity, given as a function of the pressure head, h, as

$$\gamma = \gamma_{\rm sat}\frac{[(1+\alpha h^n)^{1-1/n} - \alpha h^{n-1}]^2}{(1+\alpha h^n)^{(1-1/n)(l+2)}} \tag{8.73}$$

where α, n and l are soil-texture dependent parameters. Pressure head h is linked to the soil moisture by the expression

$$\theta(h) = \theta_r + \frac{\theta_{sat}-\theta_r}{(1+\alpha h)^{1-1/n}} \tag{8.74}$$

The VG scheme is recognized among soil physicists as capable of reproducing both the soil water retention and the hydraulic conductivity, and has shown good agreement with observations in intercomparison studies (Shao and Irannejad, 1999). Table 8.7 lists parameter values for six soil textures for the VG scheme. HTESSEL uses the dominant soil texture class for each gridpoint. This information is taken from the FAO (FAO, 2003) dataset as detailed in chapter 11. The permanent wilting point and the soil field capacity are obtained by a specified matric potential of $\psi(\theta_{\rm pwp}) = -15$bar and $\psi(\theta_{\rm cap}) = -0.10$bar, respectively. In Table 8.8 the volumetric soil moistures associated with each soil class are shown for saturation, field capacity and wilting point. Also shown is the plant available water content and the percentage of land points in each class. The last row shows the corresponding values for the single loamy

soil used in the CH formulation in TESSEL. Note that the plant available soil water is greater for all the new soil classes in HTESSEL. Figure 8.3 shows the soil hydraulic diffusivity and conductivity for

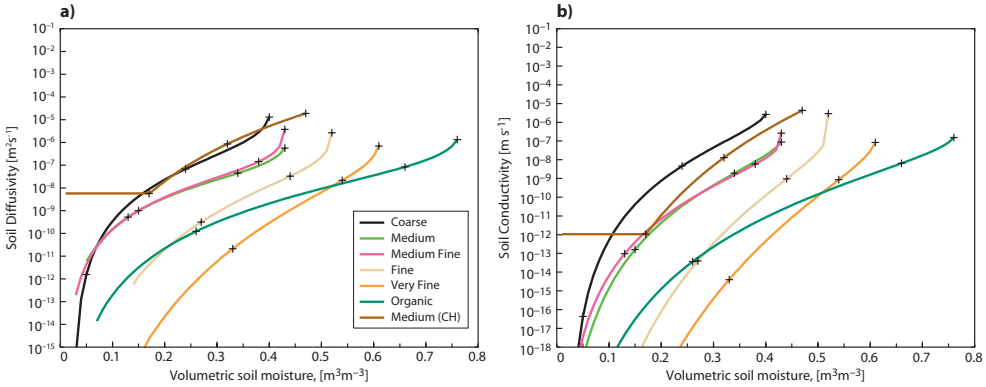

Figure 8.3 *Hydraulic properties of TESSEL and HTESSEL: (a) Diffusivity and (b) conductivity. The (+) symbols on the curves highlight (from high to low values) saturation, field capacity permanent wilting point.*

the TESSEL CH formulation and the six VG soil texture classes in HTESSEL. In TESSEL those were not allowed to fall below their wilting point values. At saturation, TESSEL has the highest diffusivity and conductivity. The reduced values for fine soils in HTESSEL reduces the infiltration of water and consequently the baseflow.

8.6.3 Runoff

In general when the water flux at the surface exceeds the maximum infiltration rate, the excess water is put into surface runoff. A general formulation of surface runoff can be written as:

$$R = T + M - I_{\max} \tag{8.75}$$

where $I_{\max}$ is the maximum infiltration rate, T the throughfall precipitation and M the snow melting. Different runoff schemes differ in the formulation of the infiltration. In TESSEL a maximum infiltration

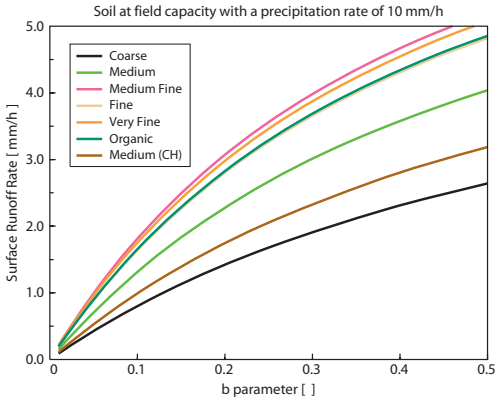

Figure 8.4 *Surface runoff generation (rate mm/h) as a function of the b parameter (accounting for sub-grid effects of orography), when exposed to a precipitation rate of* 10 *mm/h.*

rate at the surface, defined by the maximum downward diffusion from a saturated surface was used to define the runoff term. The maximum infiltration rate $I_{\max}$ is calculated as

$$I_{\max} = \rho_w \left(\frac{b_c \gamma_{\text{sat}}(-\psi_{\text{sat}})}{\theta_{\text{sat}}} \frac{\theta_{\text{sat}} - \theta_1}{z_1/2} + \gamma_{\text{sat}} \right) \tag{8.76}$$

where ρ_w is the water density, and z_1 is the depth of the first soil model layer (7 cm). At typical NWP model resolutions this scheme is active only in the presence of frozen soil, when downward soil water transfer is inhibited, otherwise it hardly ever produces runoff, as shown in Boone *et al.* (2004).

In HTESSEL A variable infiltration rate, first introduced in the so-called Arno scheme by Dümenil and Todini (1992), accounts for the sub-grid variability related to orography and considers that the runoff can (for any precipitation amount and soil condition) occur on a fraction s of the grid-point area S.

$$\frac{s}{S} = 1 - \left(1 - \frac{W}{W_{\text{sat}}}\right)^b \qquad b = \frac{\sigma_{or} - \sigma_{\min}}{\sigma_{or} + \sigma_{\max}} \tag{8.77}$$

where W and W_{sat} are vertically integrated soil water contents (θ and θ_{sat}) over the first 50 cm of soil defined as an effective depth for surface runoff. Parameter b is spacially variable, depends on standard deviation of orography (σ_{or}), and is allowed to vary between 0.01 and 0.5. The parameters $\sigma_{\min}$ and $\sigma_{\max}$ are set to 100 m and 1000 m respectively as in Van den Hurk and Viterbo (2003).

The surface runoff is obtained by the Hortonian runoff formulation by integrating Eq. 8.77 over the gridbox.

$$I_{\max} = (W_{\text{sat}} - W) + \max\left[0, W_{\text{sat}}\left[\left(1 - \frac{W}{W_{\text{sat}}}\right)^{\frac{1}{b+1}} - \left(\frac{T+M}{(b+1)W_{\text{sat}}}\right)\right]^{b+1}\right] \tag{8.78}$$

Whenever rain or snow melt occurs, a fraction of the water is removed as surface runoff. The ratio runoff/precipitation scales with the standard deviation of orography, and therefore depends on the complexity represented in the gridbox, as well as on soil texture and soil water content via W and W_{sat}.

In Figure 8.4 the response to a 10 mm/h rain rate for the six VG soil types and for the CH case in TESSEL is shown as a function of the b parameter. At field capacity, the surface runoff may vary from roughly 1% to 50% of the rainfall (snow melting) rate, generally increasing with finer textures and orographic complexity.

8.6.4 Water transport in frozen soil

Finally, the water transport is limited in the case of a partially frozen soil, by considering the effective hydraulic conductivity and diffusivity to be a weighted average of the values for total soil water and a very small value (for convenience, taken as the value of (8.71) at the permanent wilting point) for frozen water.

8.6.5 Discretization and the root profile

A common soil discretization is chosen for the thermal and water soil balance for ease of interpretation of the results, proper accounting of the energy involved in freezing/melting soil water, and simplicity of the code. Equations (8.64) and (8.65) are discretized in space in a similar way to the temperature equations, i.e., soil water and root extraction defined at full layers, θ_k and $\rho_{\text{water}} S_{\theta,k}$, and $F_{k+1/2}$ the flux of water at the interface between layer k and $k+1$. The resulting system of equations represents an implicit, water-conserving method.

For improved accuracy, the hydraulic diffusivity and conductivity are taken as (see Mahrt and Pan, 1984)

$$\begin{aligned} \lambda_{k+1/2} &= (1 - f^*_{\text{fr}})\lambda[\max(\theta^n_k, \theta^n_{k+1})] + f^*_{\text{fr}}\lambda(\theta_{\text{pwp}}) \\ \lambda_{k+1/2} &= (1 - f^*_{\text{fr}})\gamma[\max(\theta^n_k, \theta^n_{k+1})] + f^*_{\text{fr}}\gamma(\theta_{\text{pwp}}) \end{aligned} \tag{8.79}$$

where $f^*_{\text{fr}} = \min[f_{\text{fr}}(\theta_k), f_{\text{fr}}(\theta_{k+1})]$. The boundary conditions are given by

$$\begin{aligned} F_{4+1/2} &= \rho_{\text{w}}\gamma_4 \\ F_{1/2} &= T + M_{\text{sn}} - y_{\text{sfc}} + E_{1/2} \end{aligned} \tag{8.80}$$

The difference between throughfall T and surface runoff $Y_{\rm sfc}$ (kg m^{-2} s^{-1}) is the soil infiltration at the surface:

$$\begin{aligned} T &= T_{\rm ls} + T_{\rm cv} \\ y_{sfc} &= \max(0, T_{\rm ls} + M_{\rm sn} - I_{\rm f,mx}) + \frac{\max(0, F_{\rm cv} + T_{\rm cv} - I_{\rm f,mx})}{F_{\rm cv}} \\ I_{\rm f,mx} &= \rho_{\rm w}\left[\lambda_{1/2}\frac{(\theta_{\rm sat} - \theta_1)}{0.5D_1} + \gamma_{1,2}\right] \end{aligned} \tag{8.81}$$

and $\lambda_{1/2} = f^*_{\rm fr}\lambda(\theta_{\rm pwp}) + (1 - f^*_{\rm fr})\lambda(\theta_{\rm sat})$, with a similar equation for $\gamma_{1/2}$. The evaporation at the top of the soil layer, $E_{1/2}$, is computed as the sum of the evaporations of tile 8 plus the contributions necessary to conserve water with the solver of the interception layer.

(i) Tile 3 mismatch (after the evaporated water used by the interception reservoir for the given tile is subtracted).
(ii) When the evaporative fluxes are downward (i.e., dew deposition), the evaporation for tiles 4, 6 and the canopy evaporation of tile 7.

Root extraction is computed as

$$\rho_{\rm w} S_{\theta,k} = \sum_i C_i \frac{E_i}{D_k}\frac{R_k\theta_k}{\sum_j R_j\theta_j} \tag{8.82}$$

where the sum over tiles i is done for tiles 4, 6, and 7 (for which only the transpiration is used) and the sum over j is done over all soil levels. In case of dew deposition (i.e., tile downward evaporative flux), $S_{\theta,k} = 0$.

8.7 SEA/LAKE ICE

Any non-land point (i.e., a grid point with land cover less or equal 0.5) can have two fractions, open water and ice. A surface analysis defines the ice fraction, c_I, and the temperature of the open water fraction; both quantities are kept constant during the forecast. No distinction is made between surface and skin temperature for the open water fraction (see Table 8.2).

The ice fraction is modelled as an ice slab, with open water underneath and a skin temperature for the thermal contact with the atmosphere. The main caveats in the sea ice parameterization are as follows.

(i) Fixed depth of the slab, which can be relaxed once there is a reliable data set to specify its geographic distribution.
(ii) Fixed fraction, which is a reasonable assumption for a 10-day forecast period, and avoids the need for the momentum balance of the ice and its complex rheology (see, e.g., Flato and Hibler III, 1992) and the definition of the ocean currents.
(iii) No snow accumulation on top of the ice (although one of the main effects of snow, i.e., a markedly different surface albedo, is partially emulated by the prescribed seasonal albedo in Table 2.6).

The ice heat transfer is assumed to obey the following Fourier law of diffusion

$$(\rho C)_{\rm I}\frac{\partial T_{\rm I}}{\partial t} = \frac{\partial}{\partial z}\left[\lambda_{\rm I}\frac{\partial T_{\rm I}}{\partial z}\right] \tag{8.83}$$

where $(\rho C)_{\rm I} = 1.88 \times 10^6$ J m^{-3} K^{-1} is the volumetric ice heat capacity, $T_{\rm I}$ is the ice temperature, $\lambda_{\rm I} = 2.03$ W m^{-1} K^{-1} and is the ice thermal conductivity. The boundary condition at the bottom is the temperature of the frozen water, $T_{\rm fr} = T_0 - 1.7$ and the top boundary condition is the net heat flux at the surface, obtained from the solution of the ice skin thermal budget.

Equation (8.83) is solved with the ice disretized in four layers, with the depth of the top three layers as in the soil model and the depth of the bottom layer defined as

$$D_{\rm I,4} = D_{\rm I} - \sum_{j=1}^{3} D_{{\rm I},j} \tag{8.84}$$

and the total depth of the ice slab, $D_{\rm I}$, is prescribed as 1.5 m. In order to ensure a constant ice fraction, the solution of the ice thermal budget is capped to the ice melting temperature, $T_{\rm m1} = T_0$ at all levels. the details of the numerical discretization can be found in Section 8.9.

8.8 OCEAN BOUNDARY CONDITIONS FOR TEMPERATURE AND SPECIFIC HUMIDITY

In the operational system, the sea surface temperature (SST) is specified from an analysis provided by OSTIA and kept constant during the 10-day forecast. This analysis is a blend of satellite retrievals and in situ observations from ships. The idea is to have a detailed horizontal distribution from satellite and to anchor this temperature fields to the rather sparse ship observations. It means that that the analyzed SST fields are calibrated as if they are ship observations and therefore they represent bulk SST fields (i.e. measured a few metres deep)

The ocean skin temperature is not always the same as the bulk SST. A very shallow layer (less then 1 mm thick) is cooler because of the turbulent and long wave radiative heat loss to the atmosphere which has to be compensated for by the inefficient molecular transport in the water skin. Solar radiation has only a small effect on the cool skin because the solar absorption in such a thin layer is small. However, at low winds, solar radiation can create a so-called warm layer with a depth of a few metres.

Parametrizations of three different near surface ocean effects are included in the code: 1. the cool skin, 2. the warm layer and 3. salinity effects on the saturation specific humidity at the surface. These parametrizations can be controlled through namelist NAEPHY. The namelist parameters are LEOCCO (default:TRUE), LEOCWA (default:TRUE), and LEOCSA (default:TRUE), for the cool skin, the warm layer and salinity effects respectively. So, all 3 effects are activated in this cycle (cool skin and warm layer are activated since Cy35r1). Details of the cool skin and warm layer parametrizations are given in Beljaars (1997) and Zeng and Beljaars (2005).

8.8.1 The cool skin

The cool ocean skin is the result of heat loss to the atmosphere which is balanced by thermal conduction in the quasi-laminar sublayer near the water surface. Scaling arguments for the skin layer lead to the following expression for the temperature difference over the skin layer (cf. Fairall *et al.*, 1996)

$$T_{\rm sk} - T_{-\delta} = \frac{\delta}{\rho_w c_w k_w}(Q + R_s f_s) \tag{8.85}$$

$$\text{with } Q = H + \lambda E + LW \tag{8.86}$$

where $T_{\rm sk}$ is the skin temperature, $T_{-\delta}$ is the temperature below the cool skin, $R_{\rm s}$ is the net solar radiation at the surface, $f_{\rm s}$ is the fraction of solar radiation absorbed in the skin, H is the sensible heat flux, λE is the latent heat flux, LW is the net long wave radiation at the surface, ρ_w (=1025 kgm^{-3}) is the density of water, c_w (=4190 Jkg^{-1}K^{-1}) is the volumetric heat capacity of water, and k_w (=0.6 Wm^{-1}K^{-1}) is the molecular thermal conductivity of water. The fraction of solar absorbed radiation is given by

$$f_{\rm s} = 0.065 + 11\delta - \frac{6.6\,10^{-5}}{\delta}\left(1 - e^{-\delta/0.0008}\right) \tag{8.87}$$

$$\tag{8.88}$$

The thickness of the skin layer δ is (Fairall *et al.*, 1996)

$$\delta = 6\left[1 + \left(\frac{-16 g \alpha_w \nu_w^3}{u_{*w}^4 k_w^2 \rho_w c_w}(Q + R_s f_s)\right)^{3/4}\right]^{-1/3} \tag{8.89}$$

where g is the acceleration of gravity, $\alpha_w = \max(10^{-5}, 10^{-5}(T_{-d} - 273))$ is the thermal expansion coefficient of water and ν_w (=1.0 10^{-6} m^{2}s^{-1}) is the kinematic viscosity.

8.8.2 The warm layer

The near ocean warm layer is caused by solar absorption in the top few meters of the ocean during day time. This warm layer can develop when the wind mixing is not strong enough to prevent a stable layer to build up. The result is a diurnal cycle in the surface temperature which is commonly observed by satellite, but not seen in routine bulk SST observations from ships. The warm layer is typically a few meters deep. Although wind mixing erodes the warm later at night, in very low wind conditions a residual warm layer may survive until the next day, and therfore a prognostic variable is needed. The model variable T_{sk} (which is diagnostic over land) is used as a prognostic variable over the ocean.

In the IFS a simple bulk formulation is used based on similarity temperature profiles. It results in the following differential equation for the difference between the temperature just below the cool skin (less than a mm deep) $T_{-\delta}$ and the ocean bulk temperature a few m deep T_{-d}

$$\frac{\partial(T_{-\delta}-T_{-d})}{\partial t}=\frac{Q+R_s-R(-d)}{d\rho_w c_w \nu/(\nu+1)}-\frac{(\nu+1)ku_{*w}}{d\phi_t(d/L)}(T_{-\delta}-T_{-d}) \tag{8.90}$$

where d (=3 m) is the depth scale of the warm layer, ν (=0.3) is the profile shape parameter and $\phi_t(d/L)$ is the stability function with L for the Obukhov length. The solar radiation at depth $-d$ is

$$R(-d)=R_s\Sigma_{i=1}^{3}a_i e^{-db_i} \tag{8.91}$$

with $(a_1,a_2,a_3)=(0.28,0.27,0.45)$ and $(b_1,b_2,b_3)=(71.5,2.8,0.06\,m^{-1})$. The stability function is

$$\begin{aligned}\phi_t(-z/L) &= 1+5\frac{-z}{L} \qquad for\frac{-z}{L}\geq 0\\ &= (1-16\frac{-z}{L})^{-1/2}\ for\ \frac{-z}{L}<0\end{aligned} \tag{8.92}$$

The Obukhov length is

$$L=\rho_w c_w u_{*w}^3/(kF_d) \tag{8.93}$$

The buoyancy flux F_d is

$$\begin{aligned}F_d &= g\alpha_w[Q+R_s-R(-d)] \qquad for\ (T_{-\delta}-T_{-d})\leq 0\\ &= \left(\frac{\nu g\alpha_w}{5d}\right)^{1/2}\rho_w c_w u_{*w}^2(T_{-\delta}-T_{-d})^{1/2} \quad for\ (T_{-\delta}-T_{-d})>0\end{aligned} \tag{8.94}$$

Equation (8.90) is integrated in time with a fully implicit scheme using $(T_{-\delta}-T_{-d})$ as the prognostic variable. Every time step, the differences $(T_{-\delta}-T_{-d})$ from equation (8.90) and the difference $(T_{sk}-T_{-\delta})$ from equation (8.86) are added to the ocean bulk temperature to obtain the ocean skin temperature T_{sk}. With the schemes switched off (by default), the differences are zero and the skin temperature is equal to the bulk SST.

8.8.3 Salinity effect on q_s

Many models use the saturation specific humidity at ocean surface temperature as boundary condition for humidity. However, salinity reduces the saturation value and a reasonable approximation for a salinity of 34 parts per thousand is (Sverdrup *et al.*, 1942)

$$q_s=0.98\,q_{sat}(T_{sk}) \tag{8.95}$$

The 2% difference due to salinity may look a small effect, but it should be seen as a fraction of the air-sea specific humidity difference, which is typically 15% in relative humidity. So a 2% change in saturation value at the surface is equivalent to a change of 2/0.15=13% in air-sea transfer (see Zeng *et al.*, 1998b for an intercom-parison of schemes).

Table 8.9 *Variables in the generalized soil/ice temperature and water equation.*

Equation	Ψ	C	λ	γ	S_Ψ	UBC	LBC
Soil moisture	θ	1	λ_θ	γ_θ	S_θ	$F_\theta = If - c_8 E_8$	$F_\theta = \gamma_\theta$
Soil temperature	T	$(\rho C)_{\text{eff}}$	λ_T	0	0	$F_T = H^N$	$F_T = 0$
Ice temperature	T_I	$(\rho C)_I$	λ_I	0	0	$F_I = H^N$	$F_{Ns+1} = T_{0,I}$
UBC and LBC stand for upper and lower boundary condition, respectively							

8.9 NUMERICAL SOLUTION OF THE SURFACE EQUATIONS

8.9.1 Recap of the analytical equations

The water budget ((8.64) and (8.65) with boundary conditions given by (8.80)), the soil energy budget ((8.52) with boundary conditions given by (8.53) and (8.54)) and the ice energy budget (8.83) can be rewritten in a generalised form as

$$\frac{\partial \Psi}{\partial t} = \frac{1}{C}\frac{\partial}{\partial z}\left(\lambda \frac{\partial \Psi}{\partial z} - \gamma\right) + S_\Psi \tag{8.96}$$

The meaning of the different variables in each individual equations is summarized Table 8.9, together with the respective upper and lower boundary conditions, F_Ψ.

8.9.2 Implicit numerical solution

Equation (8.96) is time discretized using

$$\frac{\Psi^{t+1} - \Psi^t}{\Delta t} = \frac{1}{C}\frac{\partial}{\partial z}\left(\lambda \frac{\partial \hat{\Psi}}{\partial z} - \gamma\right) + S_\Psi \tag{8.97}$$

where

$$\hat{\Psi} = \alpha_{\text{impl}} \Psi^{t+1} + (1 - \alpha_{\text{impl}})\Psi^t \tag{8.98}$$

and the semi-implicit coefficient, $\alpha_{\text{impl}} = 1$. If the prognostic variable Ψ is defined at full levels and the fluxes F_Ψ are defined at half-levels (the interface between layers), (8.97) can be discretized in space to give

$$\begin{aligned}
\frac{\hat{\Psi} - \Psi^t}{\alpha_{\text{impl}}} &= \frac{\Delta t}{C_k}\left(\frac{\lambda_{k-1/2}(\hat{\Psi}_{k-1} - \hat{\Psi}_k)}{\Delta z_k \Delta z_{k-1/2}} - \frac{\lambda_{k-1/2}(\hat{\Psi}_k - \hat{\Psi}_{k+1})}{\Delta z_k \Delta z_{k+1/2}} + \frac{\gamma_{k-1/2} - \gamma_{k+1/2}}{\Delta z_k}\right) + \Delta t S_{\Psi,k} \qquad k = 2, \ldots, Ns-1 \\
\frac{\hat{\Psi} - \Psi^t}{\alpha_{\text{impl}}} &= \frac{\Delta t}{C_k}\left(\frac{F_\Psi^T}{\Delta z_k} - \frac{\lambda_{k-1/2}(\hat{\Psi}_k - \hat{\Psi}_{k+1})}{\Delta z_k \Delta z_{k+1/2}} + \frac{\gamma_{k-1/2} - \gamma_{k+1/2}}{\Delta z_k}\right) + \Delta t S_{\Psi,k} \qquad k = 1 \\
\frac{\hat{\Psi} - \Psi^t}{\alpha_{\text{impl}}} &= \frac{\Delta t}{C_k}\left(\frac{\lambda_{k-1/2}(\hat{\Psi}_{k-1} - \hat{\Psi}_k)}{\Delta z_k \Delta z_{k-1/2}} - \underbrace{\frac{\lambda_{k-1/2}(\hat{\Psi}_k - \hat{\Psi}_{k+1})}{\Delta z_k \Delta z_{k+1/2}}}_{I} + \frac{\gamma_{k-1/2} - \gamma_{k+1/2}}{\Delta z_k}\right) + \Delta t S_{\Psi,k} \qquad k = Ns
\end{aligned} \tag{8.99}$$

where the horizontal brace means that the term exists only for the ice temperature equation (because of the bottom temperature boundary condition for ice) and Δz_k, z_k, $z_{k-1/2}$, and $z_{k+1/2}$ represent the thickness of layer k, and the depths of its centre, the top and the bottom interface, respectively:

$$\begin{aligned}
\Delta z_k &= D_k = z_{k+1/2} - z_{k-1/2} \\
\Delta z_{k+1/2} &= z_{k+1} - z_k
\end{aligned} \tag{8.100}$$

Equation (8.99) leads to a triadiagonal system of equations

$$
\begin{aligned}
&\frac{\hat{\Psi}_{k-1}}{\alpha_{\text{impl}}}\left(\frac{\hat{\lambda}_{k-1/2}}{C_k\Delta z_k}\right)+\frac{\hat{\Psi}_k}{\alpha_{\text{impl}}}\left(1+\frac{\hat{\lambda}_{k-1/2}}{C_k\Delta z_k}+\frac{\hat{\lambda}_{k+1/2}}{C_k\Delta z_k}\right)-\frac{\hat{\Psi}_{k+1}}{\alpha_{\text{impl}}}\left(\frac{\hat{\lambda}_{k+1/2}}{C_k\Delta z_k}\right)\\
&\quad=\left(\frac{\Psi_k^t}{\alpha_{\text{impl}}}+\Delta t\left(\frac{\gamma_{k-1/2}-\gamma_{k+1/2}}{C_k\Delta z_k}\right)+\Delta t S_{\Psi,k}\right) \qquad k=2,\ldots,Ns-1\\
&\frac{\hat{\Psi}_k}{\alpha_{\text{impl}}}\left(1+\frac{\hat{\lambda}_{k+1/2}}{C_k\Delta z_k}\right)-\frac{\hat{\Psi}_{k+1}}{\alpha_{\text{impl}}}\left(\frac{\hat{\lambda}_{k+1/2}}{C_k\Delta z_k}\right)-\frac{F_\Psi^T}{C_k\Delta z_k}\\
&\quad=\frac{\Psi_k^t}{\alpha_{\text{impl}}}+\Delta t\left(\frac{\gamma_{k-1/2}-\gamma_{k+1/2}}{C_k\Delta z_k}\right)+\Delta t S_{\Psi,k} \qquad k=1\\
&\frac{\hat{\Psi}_{k-1}}{\alpha_{\text{impl}}}\left(\frac{\hat{\lambda}_{k-1/2}}{C_k\Delta z_k}\right)-\frac{\hat{\Psi}_k}{\alpha_{\text{impl}}}\left(1+\frac{\hat{\lambda}_{k-1/2}}{C_k\Delta z_k}+\underbrace{\frac{\hat{\lambda}_{k+1/2}}{C_k\Delta z_k}}_{I}\right)-\underbrace{\frac{\hat{\Phi}_{k+1}}{\alpha_{\text{impl}}}\left(\frac{\hat{\lambda}_{k+1/2}}{C_k\Delta z_k}\right)}_{I}\\
&\quad=\frac{\Psi_k^t}{\alpha_{\text{impl}}}+\Delta t\left(\frac{\gamma_{k-1/2}-\gamma_{k+1/2}}{c_k\Delta z_k}\right)+\Delta t S_{\Psi,k} \qquad k=Ns
\end{aligned}
\tag{8.101}
$$

with the generalized modified diffusivities, $\hat{\lambda}_{k-1/2}$, defined as

$$
\begin{aligned}
&\hat{\lambda}_{k-1/2}=\frac{\Delta t\alpha_{\text{impl}}\lambda_{k-1/2}}{\Delta z_{k-1/2}}\\
&I\begin{cases}\Delta z_{Ns+1/2} & =D_{Ns}/2\\ \hat{\Psi}_{Ns+1} & =T_{0,I}\end{cases}
\end{aligned}
\tag{8.102}
$$

where D_{Ns} is the depth of the deepest soil layer. The discretization above conserves water (energy) and is linearly stable. The coefficients λ and γ are a function of variable at the current time step, Ψ^n.

8.10 CODE

The surface code is fully externalized and it communicates with the rest of the code via interfaces. The architecture of the surface code is organized in modules which contain the parameterizations and normally belong to the surface library only (internal routines).

- ROUTINE_MOD.F90. The module which contains the routine's code ROUTINE with the parameterization.

Routines which need to be called from anywhere outside the surface code are duplicated as externals. For a given external routine there are associated:

- ROUTINE.h. The routine's interface which is needed in the outside routine to call the external surface routine.
- ROUTINE.F90. The external routine which uses the routine's module ROUTINE_CTL_MOD and contains the call to the surface routine ROUTINE_CTL.
- ROUTINE_CTL_MOD.F90. The module which contains the routine's code ROUTINE_CTL with the parameterization.

The external routines, for which the above structure apply, are identified hereafter by ⋆ROUTINE⋆. This structure allows for separately compile and run the surface code (e.g. with prescribed atmospheric forcing). The access to surface parameters and fields is done by dedicated routines (⋆SURF_INQ⋆ allows for enquiry mode for scalars, and ⋆SURFBC⋆ for a given set of surface fields). The surface parametrization computations are shared between the vertical diffusion routine (the routine ⋆SURFEXCDRIVER⋆ called by VDFMAIN, see Chapter 3) and the main surface routine, ⋆SURFTSTP⋆. In ⋆SURFEXCDRIVER⋆,

the tile fluxes and skin temperatures are computed: After the elimination part of the tridiagonal system of equations is computed, the energy budget for each tile is computed before back-substitution.

At the start of the model integration, the ⋆SUSURF⋆ setup routine is called to initialize modules specific to the surface code:

- SUSCST. Setup general constants.
- SUSTHF. Setup thermodynamic function constants.
- SUSRAD. Setup radiation constants.
- SUSSOIL. Setup soil constants.
- SUSVEG. Setup vegetation constants.
- SUVEXC. Setup surface exchange coefficients constants.
- SUVEXCS. Setup static stability constants.

The main subroutine of the surface code (⋆SURFTSTP⋆) is called from CALLPAR, with: (a) values of the surface prognostic equations at time step n, convective and large-scale rainfall and snowfall, tile evaporation, sensible and latent heat fluxes, and temperatures, net surface long-wave flux, tile net short-wave flux as inputs; and (b) tendencies for the surface prognostic variables, plus a comprehensive set of diagnostic arrays as outputs. ⋆SURFTSTP⋆ does a sequence of computations and subroutine calls:

- SRFENE. Computes soil energy in each layer, considering vegetation and snow effects.
- SRFSN_LWIMP. Solution of the snow energy and water budget and computation of the next time step density and albedo fields. Inputs: snow depth, temperature, density and albedo at the current time step, soil temperature, short-wave and long-wave radiation fluxes, snowfall, and tile fluxes. Outputs: snow depth, temperature, density and albedo at the next time step, meltwater flux, and basal heat flux. The formulation include a diagnostic treatment of liquid water reservoir in the snow-pack.
- SRFSN. Same as SRFSN_LWIMP but using the former TESSEL snow formulation (available as an option).
- SRFRCG. Computes apparent soil heat capacity, ie including effects of soil freezing. Inputs: soil temperature and vegetation covers. Output is volumetric heat capacity.
- SRFT. Solution of the soil heat budget. Inputs: Soil temperature, soil moisture, long-wave radiative flux, snow basal heat flux, volumetric heat capacity, tile evaporation, sensible heat flux and short-wave radiative flux. Output: Soil temperature at the next time step. First the modified heat diffusivity, the soil energy per unit area and the right-hand sice of the system of equations are computed. The generalized surface tridiagonal solver, SRFWDIF, is called to solve for the semi-implicit variable, $\hat{T}/\alpha$. The soil temperatures for the next time step are computed at the end.
- SRFI. Solution of the ice heat budget. Inputs: Ice temperature, long-wave radiative flux, tile evaporation, sensible heat flux and short-wave radiative flux. Output: Ice temperature at the next time step. First the modified heat diffusivity, the ice energy per unit area and the right-hand sice of the system of equations are computed. The generalized surface tridiagonal solver, SRFWDIF, is called to solve for the semi-implicit variable, $\hat{T}_I/\alpha$. The ice temperatures for the next time step are computed at the end.
- SRFWL. Solution of the interception layer water budget. Inputs: Interception layer contents, low and high vegetation water cover, maximum capacity of the interception layer, convective and large-scale rainfall, snow evaporation of shaded snow tile, and tile evaporation. Outputs: Interception layer at next time step, convective and large-scale throughfall and tile evaporation collected (or depleting) the interception layer.
- SRFWEXC_VG. First part of the computation of the soil water budget (i.e., computation of the coefficients of the tridiagonal system of equations for $\hat{\theta}$). This includes the partitioning of transpiration into root extraction at the different layers and soil hydraulic coefficients including the effect of frozen water. Inputs: Soil moisture and temperature, convective and large-scale throughfall, snowmelt, tile evaporation, tile evaporation collected (or depleting) the interception layer, and snow evaporation of the shaded snow tile. Outputs: Modified diffusivity for water, right-hand side of the tridiagonal system, and layer depths. Soil properties are defined according to HTESSEL scheme

- SRFWEXC. Same as SRFWEXC_VG but using the former TESSEL soil properties formulation (available as an option).
- SRFWDIF. Generalized surface tridiagonal solver. Inputs: Values of ψ at the current time step, generalized modified diffusivities, soil energy (or water) per unit area, and right-hand side of equations. Output: $\hat{\psi}/\alpha$. The routine computes the coefficients on the left-hand side of the equations and solves the equations using and LU-decomposition and back substitution in one downward scan and one upward scan.
- SRFWINC. Computation of next time step soil water. Inputs: $\hat{\theta}/\alpha$ and current time step soil water. Output: next time step soil water.
- SRFWNG. Bounded-value operator for intercepted water (limited to non-negative values and values below or equal the maximum contents of the interception layer) and soil water (limited to non-negative values and values below or equal saturation). The "soil column" is scanned from top to bottom and the amount of water needed to satisfy physical limits in each layer are borrowed from the layer below. The water exchanged in this way is accounted for as runoff. Inputs: next time step intercepted water and soil water. Output: Bounded values of the same quantities.

In ⋆SURFEXCDRIVER⋆ a set of routines relevant for the vertical diffusion code are called. These are listed below and discussed in full detail in Chapter 3:

- VUPDZ0. Update of roughness lengths for heat and momentum over ocean and setup over land according to vegetation types.
- VSURF. Definition of bare soil resistance, low and high canopy resistances.
- VEXCS. Computation of aerodynamical part of exchange coefficients for heat and moisture, including stability computations.
- VEVAP. Computation of evapotranspiration for each tile.
- VSFLX. Surface fluxes for each tile, defined at time t.
- ⋆SURFSEB⋆. Computation of surface energy balance and skin temperature for each tile.
- ⋆SURFPP⋆. Computation of quantities at the end of vertical diffusion, including post-processed weather elements and gustiness.
- VOSKIN. Computation of warm/cold skin effects over the ocean (called by ⋆SURFPP⋆).

Chapter 9
Methane oxidation

Table of contents

9.1 INTRODUCTION

A study of stratospheric humidity in analyses and multi-year simulations has shown that the ECMWF system prior to 1999 was capable of producing a broadly realistic distribution of water vapour at, and immediately above, the tropopause, and that the slow upward transfer of water vapour in the tropical stratosphere could be captured quite reasonably given sufficiently fine vertical resolution in the model (Simmons *et al.*, 1999). However, values of water vapour in the tropical upper stratosphere, and throughout much of the extratropical stratosphere, were too low. This deficiency has now been remedied by the introduction of a simple parametrization of the upper-stratospheric moisture source due to methane oxidation. A sink representing photolysis in the mesosphere is also included. The scheme was derived as a simplification of an approach adopted by Peter Stott and Anne Pardaens at the Department of Meteorology, University of Edinburgh, notes on which and helpful references were supplied by Bob Harwood.

9.2 METHANE OXIDATION

Methane is produced by natural and anthropogenic sources at the earth's surface, and is well-mixed in the troposphere. Its volume mixing ratio is currently around 1.7 ppmv. It is carried upwards in the tropical stratosphere and decreases in relative density (due to oxidation) to values of around 0.2–0.4 ppmv around the stratopause. Mean stratospheric descent at higher latitudes results in relatively low values of methane at these latitudes in the middle and lower stratosphere.

Brasseur and Solomon (1984) provide an account of the chemistry of carbon compounds in the stratosphere and mesosphere. The long chain of reactions starting from methane (CH_4) ends with the production of water vapour (H_2O) and molecular hydrogen (H_2) in the stratosphere and mesosphere. This occurs such that the sum

$$2[CH_4] + [H_2O] + [H_2]$$

is approximately uniformly distributed in the absence of precipitation, where [ ] denotes a volume mixing ratio. Le Texier *et al.* (1988) provide calculations of the relative amounts of H_2O and H_2, showing that the predominant production is that of water vapour in the vicinity of the stratopause. They indicate, however, that H_2 production in the mesosphere, and relatively strong descent in winter and early spring at high latitudes, may result in the upper stratosphere being relatively dry in these seasons and latitudes.

There is, nevertheless, good observational evidence that over much of the stratosphere the quantity

$$2[CH_4] + [H_2O]$$

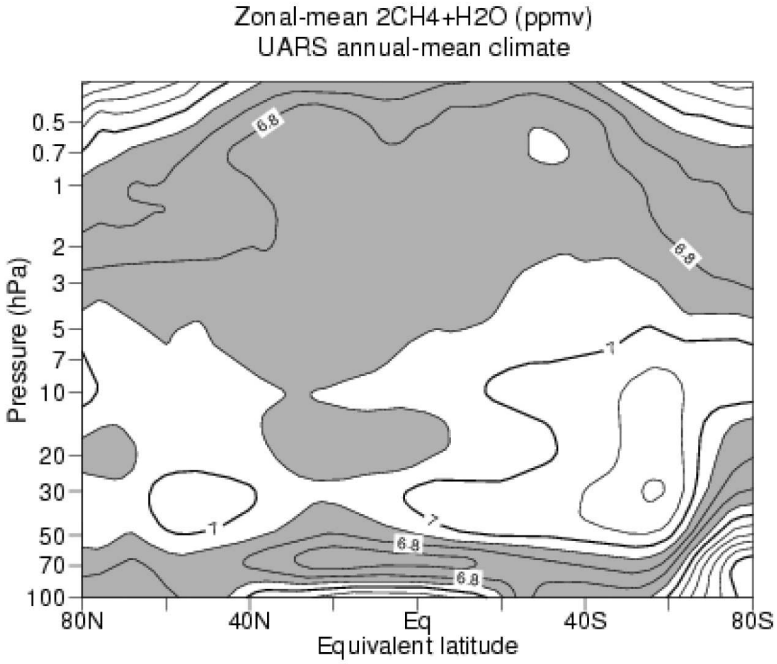

Figure 9.1 *Annual-mean distribution of the sum of twice the volume mixing ratio of methane and of the mixing ratio of water vapour (ppmv) as a function of pressure and potential vorticity (expressed as equivalent latitude), derived from UARS (HALOE, supplemented by CLAES and MLS) data analysed by Randel* et al. *(1998). The contour interval is 0.1 ppmv, and shading denotes the range 6.6–6.9 ppmv.*

is quite uniformly distributed with a value somewhat over 6 ppmv. Jones *et al.* (1986) provide evidence for this from the LIMS and SAMS instruments on the Nimbus 7 satellite launched in 1978, and a particularly clear demonstration is given by Bithell *et al.* (1994) based on HALOE data from the UARS satellite. In a pressure-latitude section at about the austral spring equinox, Bithell *et al.* show the result to fail significantly only below 10 hPa in the high-latitude southern hemisphere due, presumably, to condensation at the very cold temperatures in the Antarctic polar vortex.

Prior to cycle 25r1 of the IFS, the parametrization used the value 6 ppmv for the sum $2[CH_4] + [H_2O]$. This version was used in production of the ERA-40 reanalyses, which have been found to be generally drier in the stratosphere than the climatology derived by Randel *et al.* (1998) from UARS measurements. From cycle 25r1 onwards, the parametrization uses the value 6.8 ppmv, based on Randel *et al.*'s data as presented in Fig. 9.1.

9.3 THE PARAMETRIZATION

9.3.1 Methane oxidation

We assume that the volume mixing ratio of water vapour $[H_2O]$ increases at a rate

$$2k_1[CH_4] \tag{9.1}$$

We further assume that

$$2[CH_4] = 6.8 \text{ ppmv} - [H_2O] \tag{9.2}$$

The rate of increase of volume mixing ratio of water vapour (in ppmv) is thus

$$k_1(6.8 - [H_2O]) \tag{9.3}$$

In terms of specific humidity, q, the source is

$$k_1(Q - q) \tag{9.4}$$

where (having divided by 1.6×10^6 to convert from volume mixing ratio in ppmv to specific humidity) the parameter Q has the value 4.25×10^{-6}, or 4.25 mg/kg.

The rate k_1 could be determined, for example, from a two-dimensional model with comprehensive chemistry, as in the scheme developed at Edinburgh University. However, in this first scheme for use at ECMWF we prescribe a simple analytical form for k_1 which varies only with pressure.

The photochemical life time of water vapour is of the order of 100 days near the stratopause, 2000 days at 10 hPa, and effectively infinite at the tropopause (Brasseur and Solomon, 1984). A prescription of k_1 that gives a reasonable profile up to the stratopause is provided by

$$k_1 = \frac{1}{86400\tau_1} \tag{9.5}$$

where k_1 is given in s^{-1} and the timescale, τ_1, in days, is given in terms of pressure, p, in Pa, by

$$\tau_1 = \begin{cases} 100 & p \le 50 \\ 100\left[1 + \alpha_1 \dfrac{\{\ln(p/50)\}^4}{\ln(10000/p)}\right] & 50 < p < 10000 \\ \infty & p \ge 10000 \end{cases} \tag{9.6}$$

where we define

$$\alpha_1 = \frac{19 \ln 10}{(\ln 20)^4} \tag{9.7}$$

to give a time-scale of 2,000 days at the 10 hPa level.

This parametrization moistens rising air in the tropical stratosphere. This air will earlier have been freeze-dried near the tropopause, where specific humidities can locally fall well below 1 mg/kg. Specific humidities approaching the value Q will be reached near the stratopause. Descent near the poles will bring down air with specific humidity close to Q. Expression (9.4) will then yield a source term that is weaker in polar than in tropical latitudes, so reasonable results may be obtained without imposing a latitudinal variation of k_1. (Strictly, k_1 should vanish in the polar night, where photodissociation does not produce the excited oxygen $O(^1D)$, which in turn produces the OH radical, these two species being intimately involved in the production of water vapour from methane.)

9.3.2 Photolysis in the mesosphere

For model versions with an uppermost level at 0.1 hPa, or lower, there is no strong need to include the sink of water vapour that occurs in the mesosphere and above due to photolysis. However, for completeness we include a simple representation of this effect, modifying the source term (9.4) by adding a decay term $-k_2 q$ above a height of about 60 km. The full source/sink term becomes

$$k_1(Q - q) - k_2 q \tag{9.8}$$

As for k_1 we take k_2 independent of latitude with parameters chosen to match the vertical profile of photochemical lifetime presented by Brasseur and Solomon (1984). Specifically,

$$k_2 = \frac{1}{86400\tau_2} \tag{9.9}$$

with

$$\tau_2 = \begin{cases} 3 & p \le 0.1 \\ \left[\exp\left\{\alpha_2 - 0.5(\ln 100 + \alpha_2)\left(1 + \cos\dfrac{\pi \ln(p/20)}{\ln 0.005}\right)\right\} - 0.01\right]^{-1} & 0.1 < p < 20 \\ \infty & p \ge 20 \end{cases} \tag{9.10}$$

and

$$\alpha_2 = \ln\left(\frac{1}{3} + 0.01\right) \tag{9.11}$$

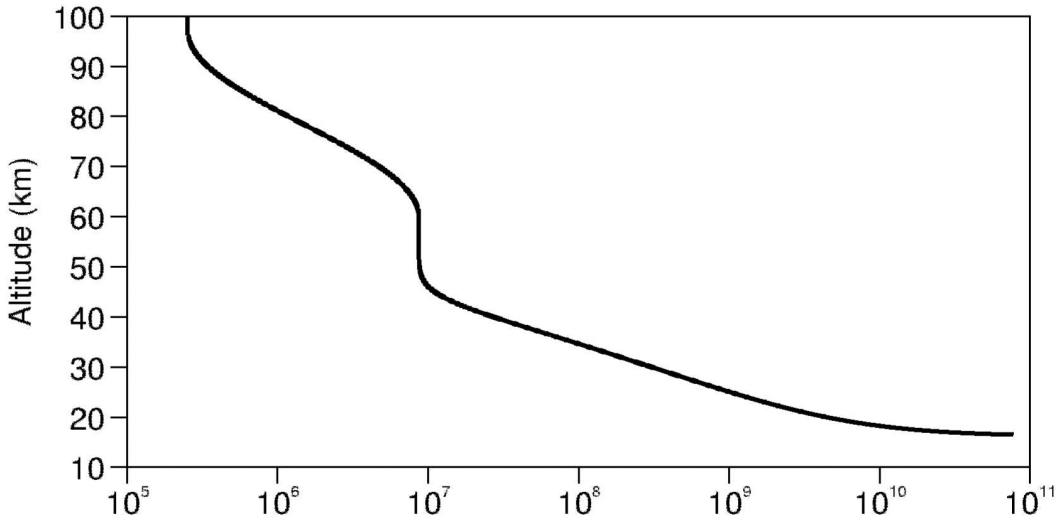

Figure 9.2 *Combined photochemical lifetime,* $(k_1 + k_2)^{-1}$*, as a function of altitude for the analytical specification given by Equations (9.5) to (9.7) and (9.9) to (9.11).*

The vertical profile of the photochemical lifetime of the combined scheme, $(k_1 + k_2)^{-1}$, is shown in Fig. 9.2, in which we have converted to height as a vertical coordinate assuming an isothermal atmosphere with a temperature of 240 K. Comparison of this profile with that for H_2O shown in Fig. 5.21 of Brasseur and Solomon (1984) indicates reasonable agreement.

9.4 CODE

The calculations for methane oxidation and photolysis of water vapour are performed in subroutine METHOX.

This routine calculates the tendency of water vapour due to methane oxidation and due to photolysis following (9.8). The order of the calculations is as follows.

(i) Find time-scale for methane oxidation following (9.6).
(ii) Solve first part of (9.8).
(iii) Find time-scale for water vapour photolysis following (9.10).
(iv) Solve second part of (9.8).

The setup of the constants used in METHOX is performed in SUMETHOX which is called from SUPHEC. The constants are kept in module YOEMETH. The controlling switch for the methane oxidation is LEMETHOX which is part of namelist NAEPHY.

Chapter 10
Ozone chemistry parametrization

Table of contents

10.1 INTRODUCTION

Ozone is fully integrated into the ECMWF forecast model and analysis system as an additional three-dimensional model and analysis variable similar to humidity. The forecast model includes a prognostic equation for the ozone mass mixing ratio (kg/kg) given by

$$\frac{\mathrm{d}\mathrm{O}_3}{\mathrm{d}t} = R_{\mathrm{O}_3} \tag{10.1}$$

where R_{O_3} is a parametrization of sources and sinks of ozone. Without such a source/sink parametrization the ozone distribution would drift to unrealistic values in integrations longer than a few weeks. The source/sink parametrization must maintain a realistic ozone distribution over several years of integration, without reducing the dynamic variability of ozone. In addition, we would like the parametrization to be able to create an Antarctic ozone hole when the conditions are right.

10.2 THE ECMWF OZONE PARAMETRIZATION

The parametrization used in the ECMWF model is an updated version of Cariolle and Déqué (1986), which has been used in the ARPEGE climate model at Météo-France. This parametrization assumes that chemical changes in ozone can be described by a linear relaxation towards a photochemical equilibrium. It is mainly a stratospheric parametrization. The relaxation rates and the equilibrium values have been determined from a photochemical model, including a representation of the heterogeneous ozone hole chemistry. The updated version of the parametrization (with coefficients provided by Pascal Simon, Météo-France) is

$$R_{\mathrm{O}_3} = c_0 + c_1(\mathrm{O}_3 - \overline{O_3}) + c_2(T - \overline{T}) + c_3(\mathrm{O}_3^{\uparrow} - \overline{\mathrm{O}_3^{\uparrow}}) + c_4(\mathrm{Cl}_{\mathrm{EQ}})^2\mathrm{O}_3 \tag{10.2}$$

where

$$\mathrm{O}_3^{\uparrow}(p) = -\int_{p^0} \frac{\mathrm{O}_3(p')}{g}\mathrm{d}p' \tag{10.3}$$

Here ($i = 0, \ldots, 4$) are the relaxation rates and $\overline{T}$, $\overline{\mathrm{O}_3}$ and $\overline{\mathrm{O}_3^{\uparrow}}$ are photochemical equilibrium values, all functions of latitude, pressure, and month. $\mathrm{Cl}_{\mathrm{EQ}}$ is the equivalent chlorine content of the stratosphere for the actual year, and is the only parameter that varies from year to year (see Fig. 10.1). The heterogeneous part is only turned on below a threshold temperature of 195 K. The coefficients for the ozone parametrization (c_0, c_1, c_2, c_3, c_4, $\overline{O_3}$, $\overline{T}$, $\overline{\mathrm{O}_3^{\uparrow}}$) have been developed by Météo-France. Their version 2.3 is used (Cariolle and Teyssèdre, 2007).

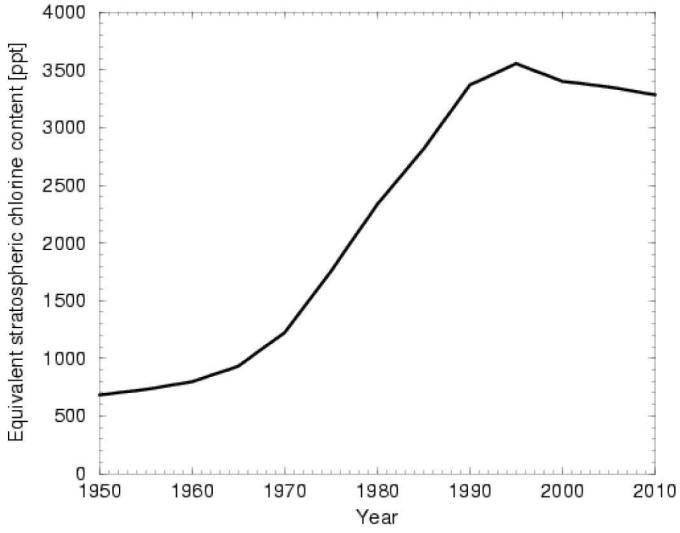

Figure 10.1 *Equivalent chlorine content of the stratosphere in ppt for the heterogeneous chemistry part of the ozone source/sink parametrization (provided by Pascal Simon, Météo-France).*

Chapter 11
Climatological data

Table of contents

11.1 INTRODUCTION

The ECMWF model uses a series of climate fields of different origin which have different resolution and different projections. Brankovic and Van Maanen (1985) describe a set of programs (known as PREPCLIM software) to interpolate the different fields to the requested target resolution. The software handles all the target resolutions that are in use at ECMWF and either full or reduced Gaussian grids. Grid areas at the model resolution are referred to as ECMWF or model grid squares. This chapter describes the different climate fields and the procedures to derive the fields that are needed by the model.

11.2 TOPOGRAPHIC DATA

The model orography and land use fields are based on the terrain elevation data set GTOPO30 at 30″ resolution (Gesch and Larson, 1998), the terrain elevation data for Greenland KMS DEM also at 30″ resolution (Ekholm, 1996) and the Global Land Cover Characteristics (GLCC) data set at 1 km resolution.

The GTOPO30 data set, as used in the IFS, was completed in 1996 through a collaborative effort led by the US Geological Survey's Data Centre (EDC, see
http://edcwww.cr.usgs.gov/landdaac/gtopo30/gtopo30.html)
and was derived from a variety of information sources. It contains terrain elevation above mean sea level at a resolution of 30 arc seconds with -9999 code for sea points. A lake mask is not included.

Greenland KMS DEM replaces GTOPO30 for the Greenland area, because of the better accuracy of the Greenland data.

The Global Land Cover Characteristics (GLCC) data set has been derived from 1 year of Advanced Very High Resolution Radiometer (AVHRR) data, digital elevation models, ecoregions and map data. The nominal resolution is 1 km, and the data comes on a Goode Homolosine global projection. The data base provides for each pixel a biome classification based on several of the popular classifications, including BATS, SiB and SiB2. The BATS classification has been adopted for the IFS because it contains inland water as one of its classes.

Table 11.1 *Land use classification according to BATTS.*

Index	Vegetation type	H/L veg
1	Crops, Mixed Farming	L
2	Short Grass	L
3	Evergreen Needleleaf Trees	H
4	Deciduous Needleleaf Trees	H
5	Deciduous Broadleaf Trees	H
6	Evergreen Broadleaf Trees	H
7	Tall Grass	L
8	Desert	-
9	Tundra	L
10	Irrigated Crops	L
11	Semidesert	L
12	Ice Caps and Glaciers	–
13	Bogs and Marshes	L
14	Inland Water	–
15	Ocean	–
16	Evergreen Shrubs	L
17	Deciduous Shrubs	L
18	Mixed Forest/woodland	H
19	Interrupted Forest	H
20	Water and Land Mixtures	L

Due to their high resolution and global coverage, these data sets are rather big and therefore difficult to handle by the standard PREPCLIM software. Therefore the original data has been converted to an intermediate resolution of $2'30''$ which is much easier to handle by the standard PREPCLIM software. The derived $2'30''$ data set contains the following fields.

- Mean elevation above mean sea level.
- Land fraction.
- Lake fraction.
- Fractional cover for all 20 BATS biome classes (see Table 11.1).

11.3 MEAN OROGRAPHY

Orography, or geopotential height, is derived from the $2'30''$ data by averaging. Source and target grid are overlaid, and weighted averages are computed by considering the fractions of source grid areas that cover the target grid square.

The orography is spectrally fitted to ensure consistency in spectral space between the orography and the model resolution. Smoothing is applied in spectral space with a ∇^4 operator, where damping by a factor 5 is applied to the smallest scales. This applies to all operational resolutions (T95, T159, T255, T399 and T799). Orographic ripples appear as a consequence of the spectral fitting. Fig. 11.1 shows the orography at T799 resolution.

11.4 LAND SEA MASK

Each grid point of the model is provided with a land fraction parameter, derived from the 2'30" data. The model converts this parameter into a mask where grid points that have more than 50% land are considered as land points.

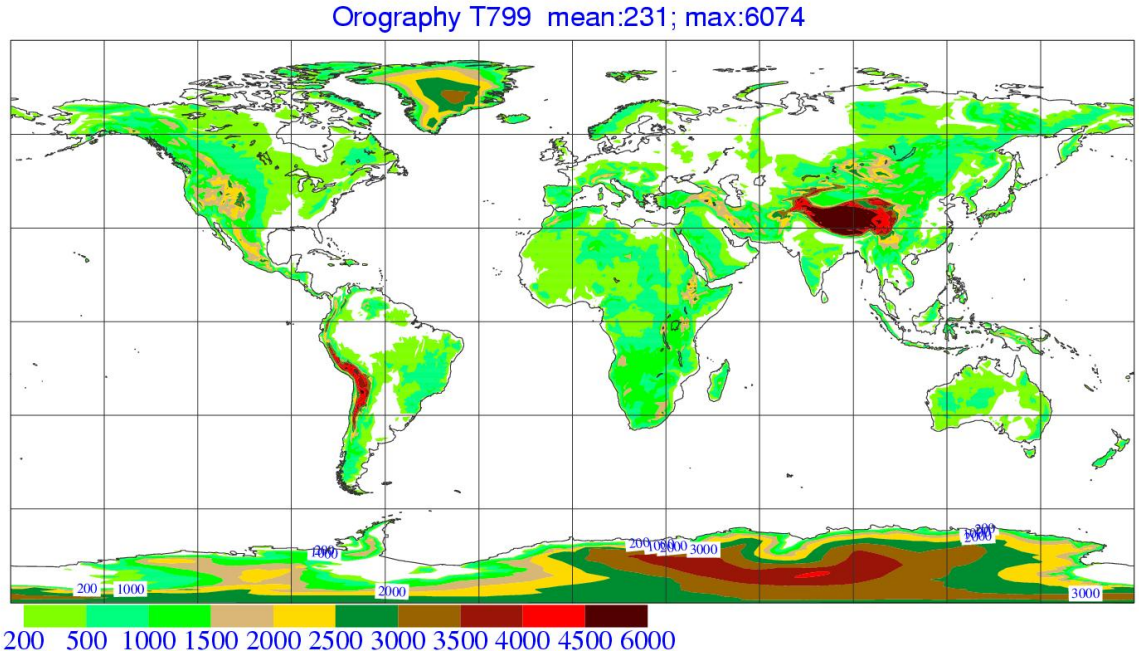

Figure 11.1 *Orography at T799 resolution.*

11.5 STANDARD DEVIATION OF FILTERED OROGRAPHY

To estimate the spectral parameters from the 1 km global data, a band pass filter is applied and the standard deviation of the terrain height is computed from the filtered field. The band pass filter is obtained by using the following smoothing operator two times with different smoothing scales.

$$\begin{aligned} h(r) &= \tfrac{1}{\Delta}, && \text{for } |r| < \Delta/2 - \delta \\ h(r) &= \tfrac{1}{2\Delta} + \tfrac{1}{2\Delta}\cos\pi(r - \Delta/2 + \delta)/2\delta, && \text{for } \Delta/2 - \delta < |r| < \Delta/2 + \delta \\ h(r) &= 0, && \text{for } |r| > \Delta/2 + \delta \end{aligned} \tag{11.1}$$

This smoothing operator is a top hat function with smooth edges. The edges reduce the amplitude of the side lobes in the spectral domain. The filter is applied by convoluting the input field in two dimensions with $h(r)$, where r is the radial distance. Parameter Δ is the width of the filter and δ is the width of the edge. Sardeshmukh and Hoskins (1984) show that a rotation symmetric smoothing is equivalent to filtering of the total wavenumber. The effect of this operation is equivalent to multiplying the spectrum by a filter function $H(k)$ where H is the square of the Fourier transform of $h(r)$.

To compute the standard deviation of the small scale orography for well defined scales all over the globe (also in polar regions where the grid point spacing is much less than 1 km), the 30" field is filtered twice with filter (11.1), shown in Fig. 11.2. The first time, the smallest scales are filtered out by using $\Delta_1 = 2$ km and $\delta_1 = 1$ km. The second filtering is done with $\Delta_2 = 20$ km and $\delta_2 = 1$ km, to isolate the longer scales. The standard deviation of the difference of the two 1 km resolution fields is computed at the resolution of the target model. The resulting field is shown in Fig. 11.4 for the T799 model. In contrast to the mean orography and the other subgrid orography fields, the standard deviation of filtered subgrid orography is based on the 30" resolution GLOBE data set.

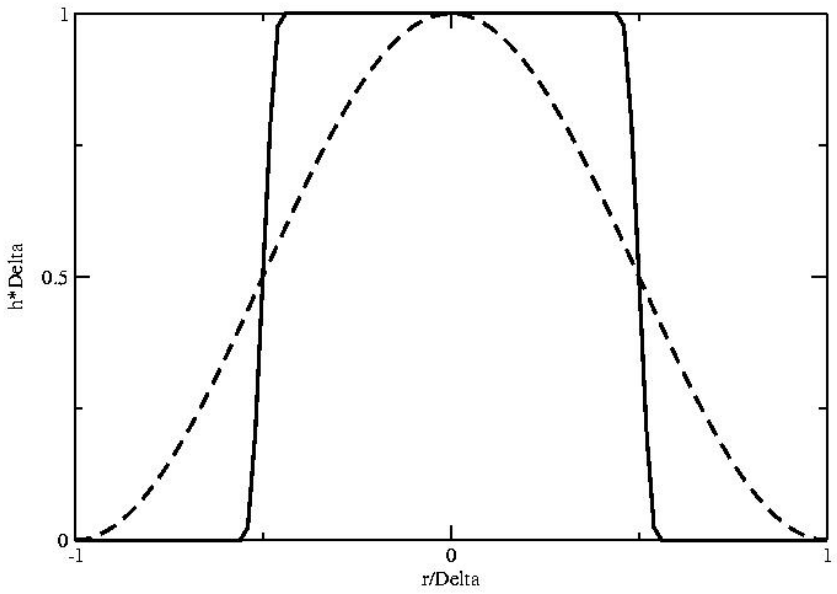

Figure 11.2 *Smoothing operators for $\delta = \Delta/20$ (solid), and $\delta = \Delta/2$ (dashed).*

The spectral filter for the small scale orography corresponding to the procedure described above is

$$
\begin{aligned}
H_{flt}(k) = \quad & \frac{1}{\Delta_1^2}\left\{\frac{\sin(k\Delta_1/2 - k\delta_1)}{k} + \frac{\sin(k\Delta_1/2 + k\delta_1)}{k}\right. \\
& \left. + \frac{\cos(\pi/2 + k\Delta_1/2)\sin(\pi/2 + k\delta_1)}{\pi/(2\delta_1) + k} + \frac{\cos(\pi/2 - k\Delta_1/2)\sin(\pi/2 - k\delta_1)}{\pi/(2\delta_1) - k}\right\}^2 \\
& - \frac{1}{\Delta_2^2}\left\{\frac{\sin(k\Delta_2/2 - k\delta_2)}{k} + \frac{\sin(k\Delta_2/2 + k\delta_2)}{k}\right. \\
& \left. + \frac{\cos(\pi/2 + k\Delta_2/2)\sin(\pi/2 + k\delta_2)}{\pi/(2\delta_2) + k} + \frac{\cos(\pi/2 - k\Delta_2/2)\sin(\pi/2 - k\delta_2)}{\pi/(2\delta_2) - k}\right\}^2
\end{aligned}
\tag{11.2}
$$

The filter of (11.2) is shown in Fig. 11.3. The filter has the shape of a band pass filter with the lower bound determined by Δ_2, and the upper bound by Δ_1. Parameters δ_1 and δ_2 control the level of overshooting. The parameter selection is based on the following ideas. First the filter should drop off quickly near $k = 0.0012$ m^{-1}, because the spectrum has an aliasing tail (see Beljaars *et al.* (2004b)). Secondly we would like to cut off below scales of 5 km because we are interested in scales smaller 5 km for TOFD. However, this leads to a very narrow filter with noisy results. Therefore we select a longer filtering scale of about 20 km. The edges of the filter defined by $H_{flt} = 0.0005$ are $k = 0.00014$ m^{-1} and $k = 0.00112$ m^{-1} respectively. These wave numbers correspond to length scales (half wave length) of 22000 m and 3000 m. The advantage of having a broad filter is that resulting standard deviations will be less noisy.

With an orography spectrum F_o and the band pass filtering with (11.2), the following spectrum is obtained for the small scale orography

$$F_{flt}(k) = F_o(k)H_{flt}(k) \tag{11.3}$$

The variance of the sub-grid orography as computed from the filtered fields is

$$\sigma_{flt}^2 = \int F_o(k)H_{flt}(k)dk \tag{11.4}$$

$$\approx F_o(k_{flt}) \int H_{flt}(k)dk \tag{11.5}$$

$$= F_o(k_{flt})I_H \tag{11.6}$$

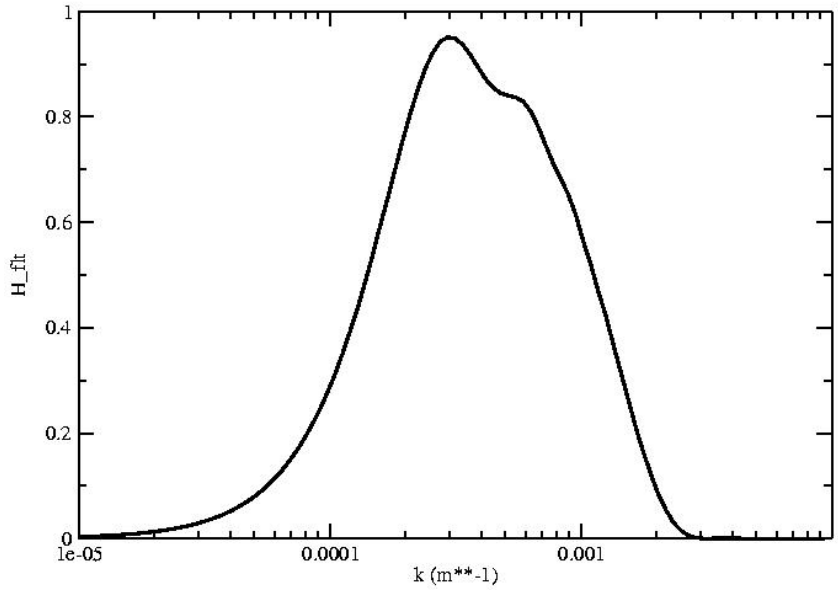

Figure 11.3 *Spectral filter corresponding to difference of two smoothing operations with:* $\Delta_1 = 2000$ *m,* $\Delta_2 = 20000$ *m,* $\delta_1 = 1000$ *m,* $\delta_2 = 1000$ *m.*

The approximation is based on the idea that the band width of the filter is small and that the spectrum of the orography does not change much over the band width of the filter. So, by computing the variance of the small scale orography σ^2_{flt}, an estimate is obtained of the orographic power spectrum at wavelength k_{flt}:

$$F_o(k_{flt}) = \sigma^2_{flt}/I_H \tag{11.7}$$

For a power spectrum with exponent n_1 in the range of the band filter, a filter wave number can be defined that satisfies (11.6) exactly

$$k^{n_1}_{flt} = \left\{ \int k^{n_1} H(k) dk \right\} \left\{ \int H(k) dk \right\}^{-1} \tag{11.8}$$

With the filter parameters $\Delta_1 = 2000$ m, $\delta_1 = 1000$ m, $\Delta_2 = 20000$ m, $\delta_2 = 1000$ m, and $n_1 = -1.9$, the following results are found from numerical integration:

$$I_H = 0.00102\,\mathrm{m}^{-1},\ k_{flt} = 0.00035\,\mathrm{m}^{-1} \tag{11.9}$$

These numbers are used in the parametrization scheme to account for the way the standard deviation of filtered orography was generated.

11.6 PARAMETERS FOR GRAVITY-WAVE AND LOW LEVEL ORGRAPHIC BLOCKING SCHEMES

The following subgrid parameters are needed: standard deviation μ_{GW}, anisotropy γ_{GW}, orientation θ_{GW}, and slope σ_{GW}. They are computed as follows (see Lott and Miller, 1997; Baines and Palmer, 1990).

(i) For every point (index i) of the $2'30''$ data, $(\partial h/\partial x)_i$ and $(\partial h/\partial y)_i$ are computed by central differencing with help of the points to the north, south, east and west. These derivatives are computed after subtracting the mean orography at target resolution to avoid contributions from the slope of the resolved orography. The central differences in the north–south direction use adjacent points; derivatives in the east–west direction use adjacent points in the tropics but use equidistant points rather than equi-longitude points when approaching the polar regions (to maintain a uniform resolution over the globe). Then parameters K, L and M are computed by summation, taking into

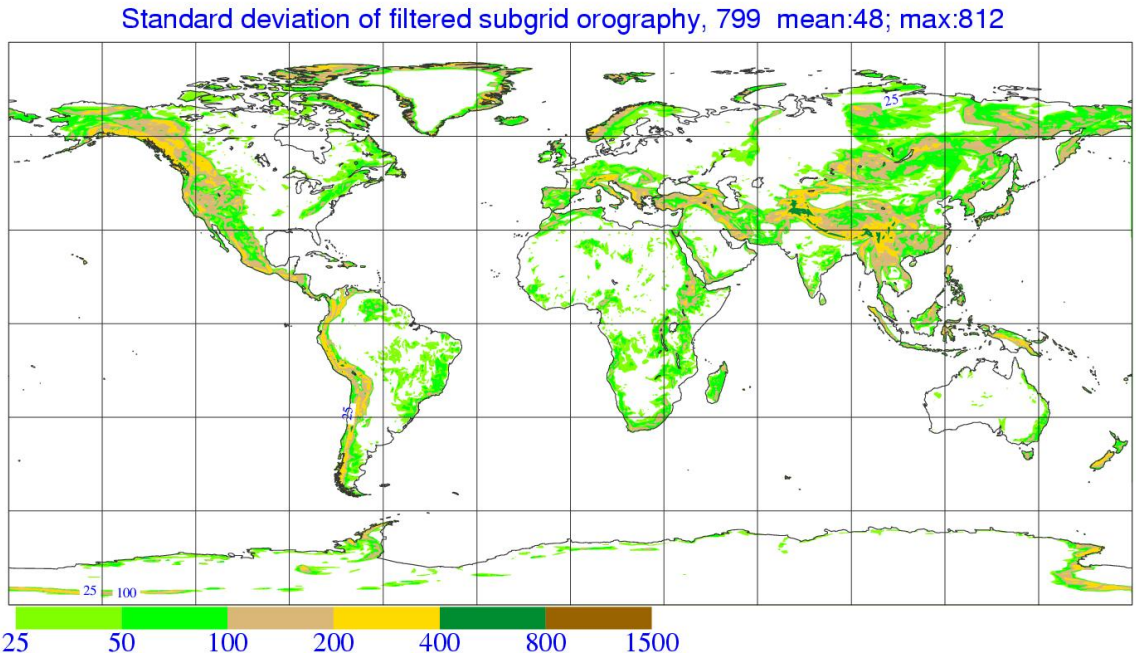

Figure 11.4 *Standard deviation of the filtered orography for the T799 model, to support the TOFD parametrization.*

account the weights p_i of every $10' \times 10'$ area in the ECMWF grid using

$$K = \frac{1}{2}\sum_i p_i \left\{ \left(\frac{\partial h}{\partial x}\right)_i^2 + \left(\frac{\partial h}{\partial y}\right)_i^2 \right\}$$

$$L = \frac{1}{2}\sum_i p_i \left\{ \left(\frac{\partial h}{\partial x}\right)_i^2 - \left(\frac{\partial h}{\partial y}\right)_i^2 \right\}$$

$$M = \sum_i p_i \left\{ \left(\frac{\partial h}{\partial x}\right)_i \left(\frac{\partial h}{\partial y}\right)_i \right\}$$

(ii) Anisotropy γ_{GW}, orientation θ_{GW}, and slope σ_{GW} are computed from K, M and L using

$$\gamma_{\mathrm{GW}}^2 = \frac{K - (L^2 + M^2)^{1/2}}{K + (L^2 + M^2)^{1/2}}$$

$$\theta_{\mathrm{GW}} = \frac{1}{2}\mathrm{atan}\frac{M}{L}$$

$$\sigma_{\mathrm{GW}}^2 = K + \sqrt{L^2 + M^2}$$

and the standard deviation μ_{GW} is

$$\mu_{\mathrm{GW}} = \sum_i p_i h_i^2 - \left(\sum_i p_i h_i\right)^2$$

No further filtering is applied to the fields. Results are shown in Figs 11.5, 11.6, 11.7 and 11.8.

11.7 VEGETATION PARAMETERS

Vegetation is represented by four climatological parameters: vegetation cover of low vegetation, vegetation cover of high vegetation, low vegetation type and high vegetation type. These parameters are derived from the $2'30''$ GLCC data by averaging over the target grid squares. The fractional covers for low and

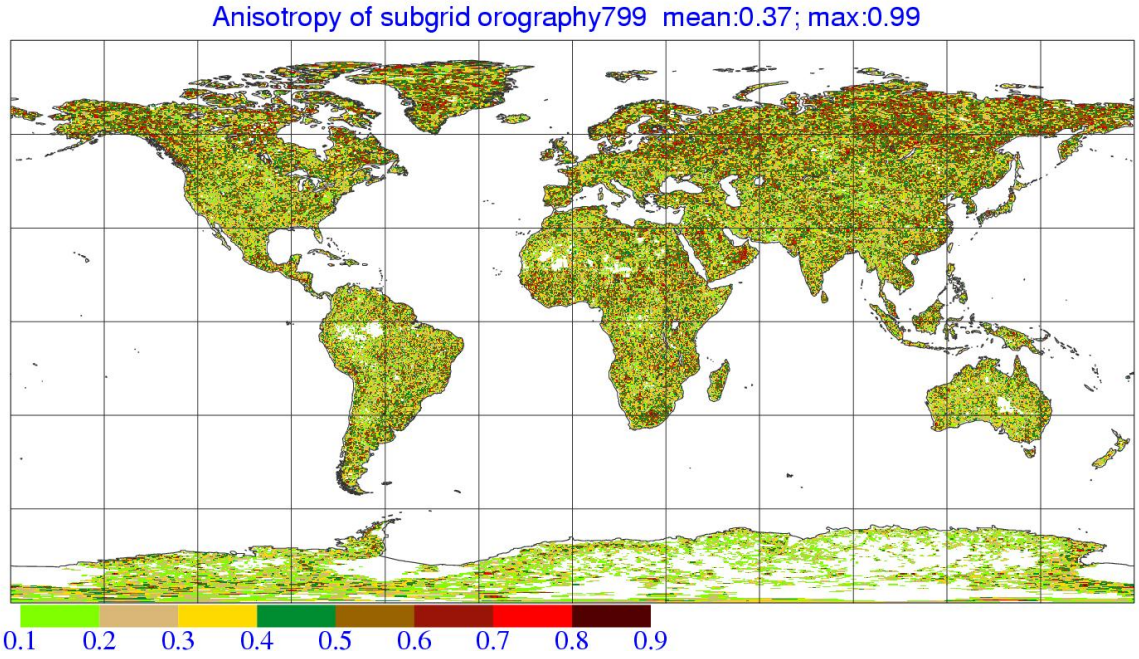

Figure 11.5 *Anisotropy γ_{GW} of subgrid orography (1 indicates isotropic, 0 means maximum anisotropy).*

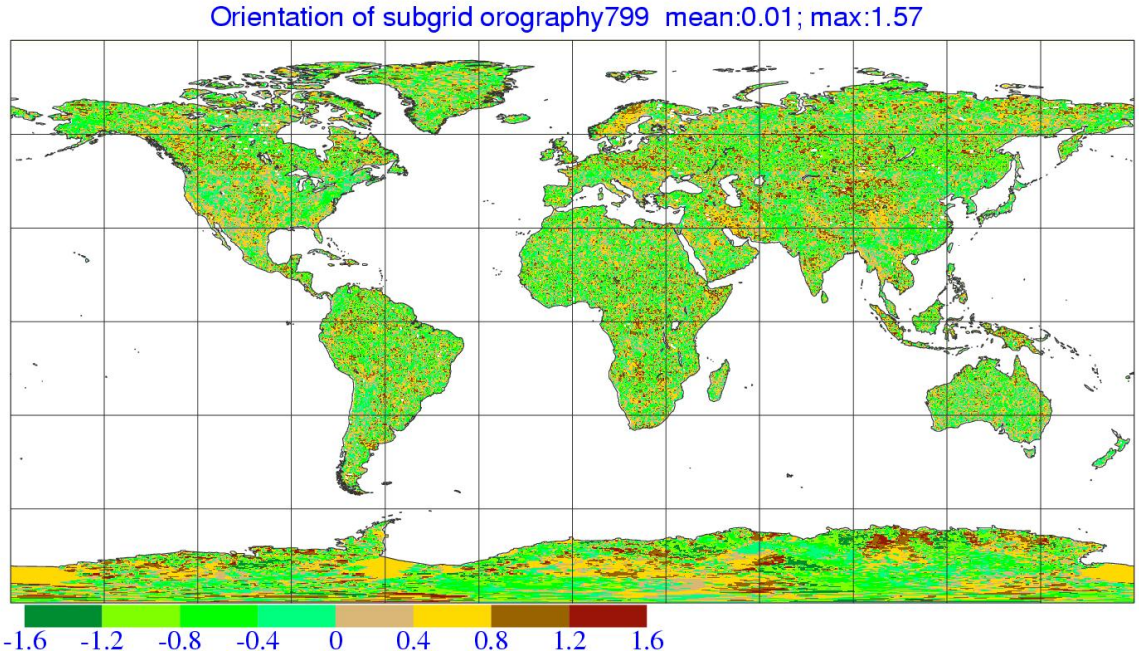

Figure 11.6 *Orientation θ_{GW} of subgrid orography (values between $-\pi$ and π).*

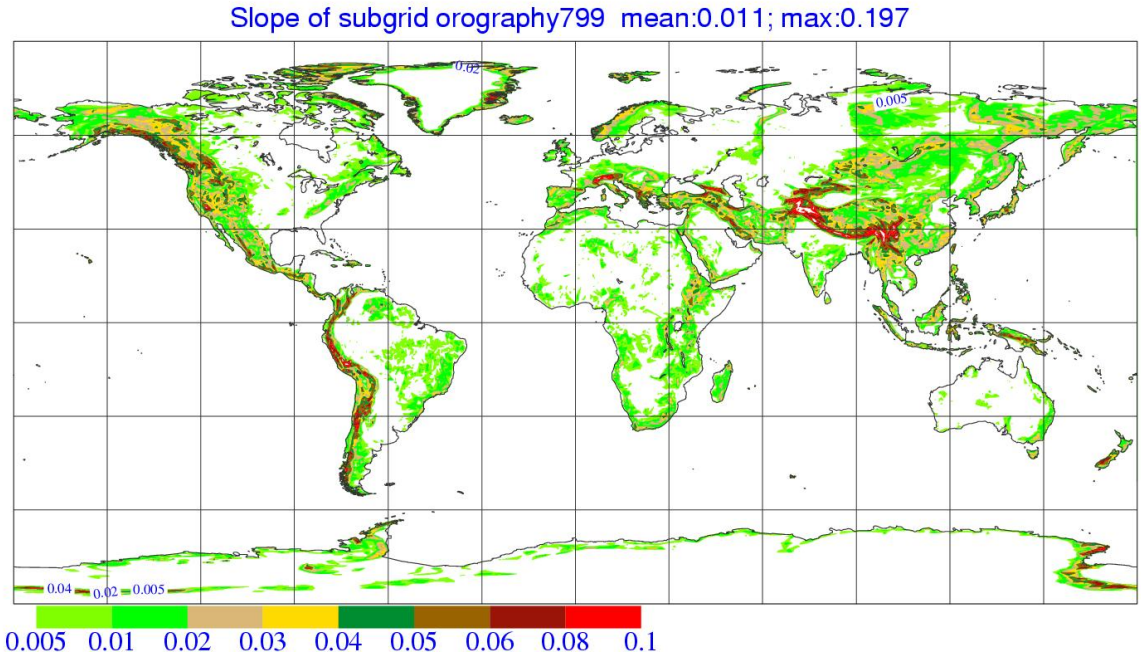

Figure 11.7 *Slope σ_{GW} of subgrid orography.*

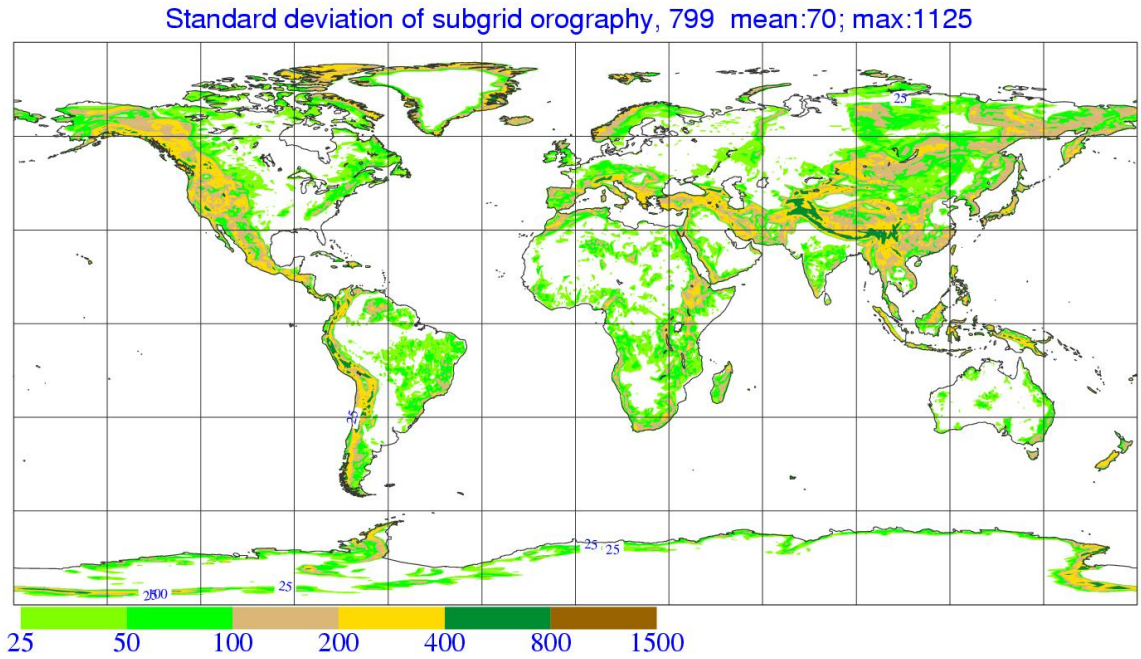

Figure 11.8 *Standard deviation μ_{GW} of subgrid orography.*

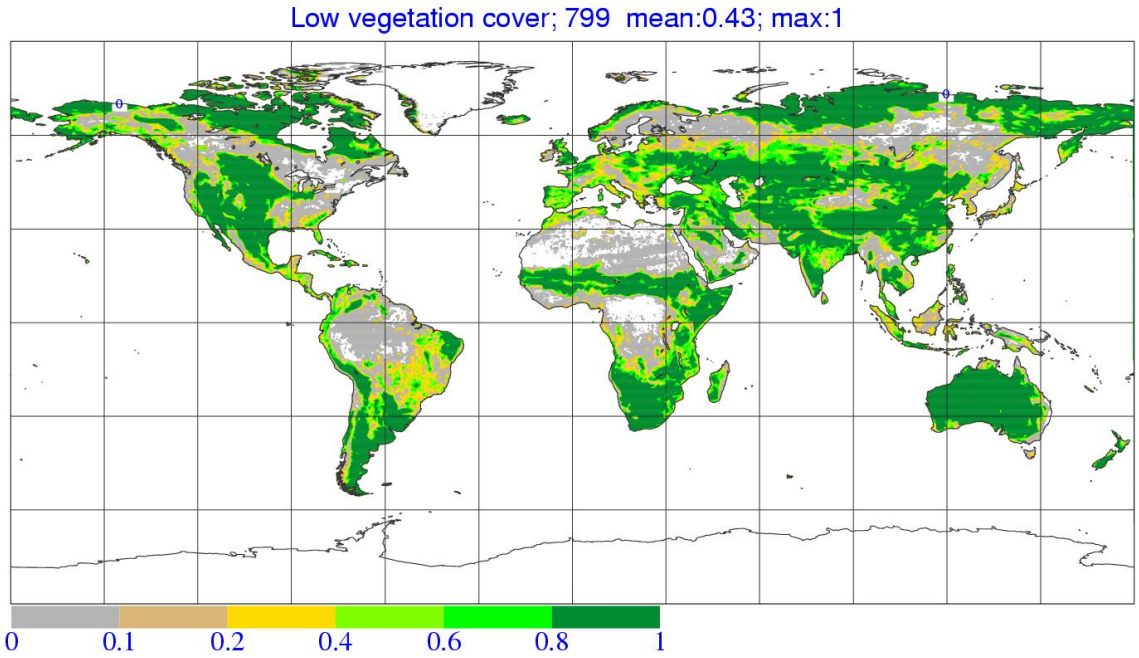

Figure 11.9 *Fractional cover of low vegetation.*

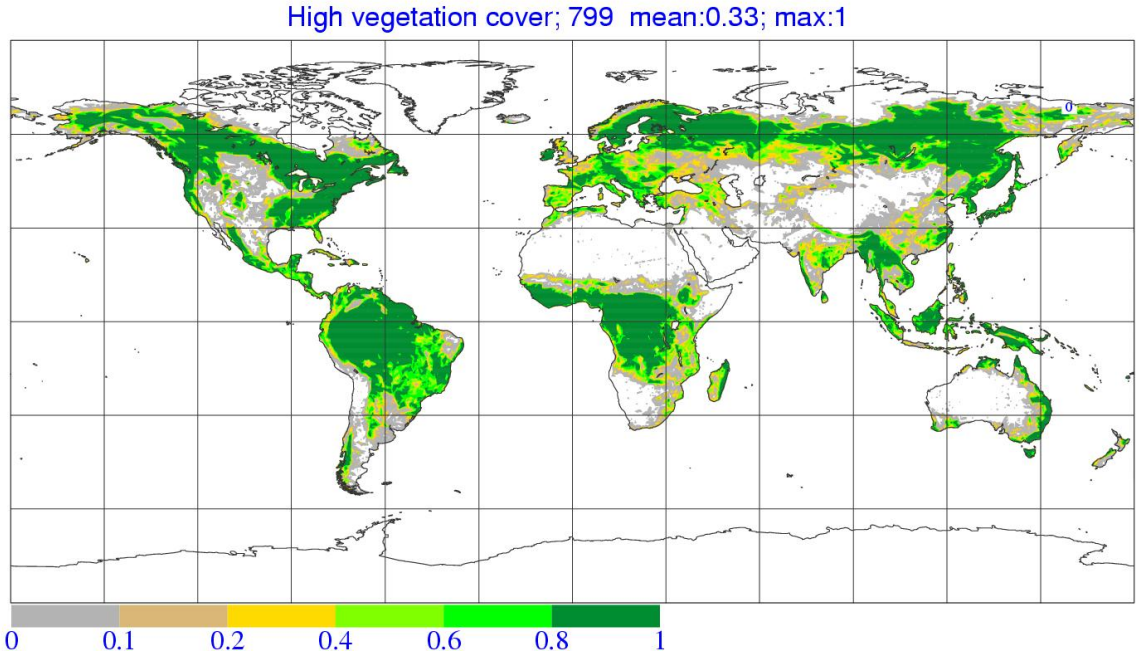

Figure 11.10 *Fractional cover of high vegetation.*

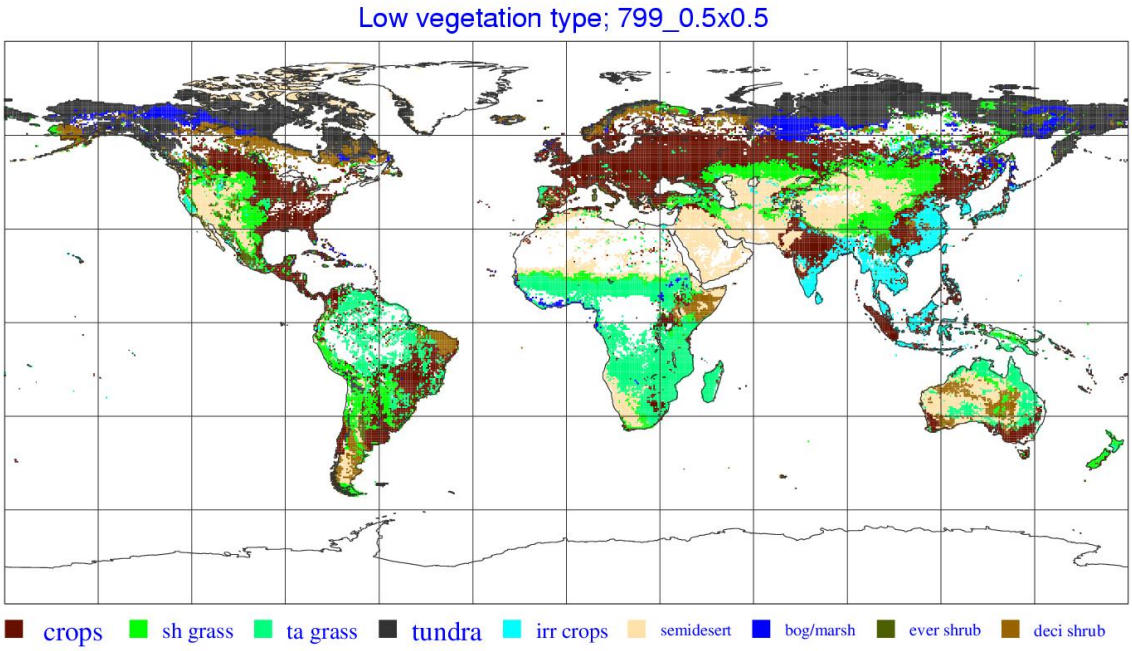

Figure 11.11 *Low vegetation type.*

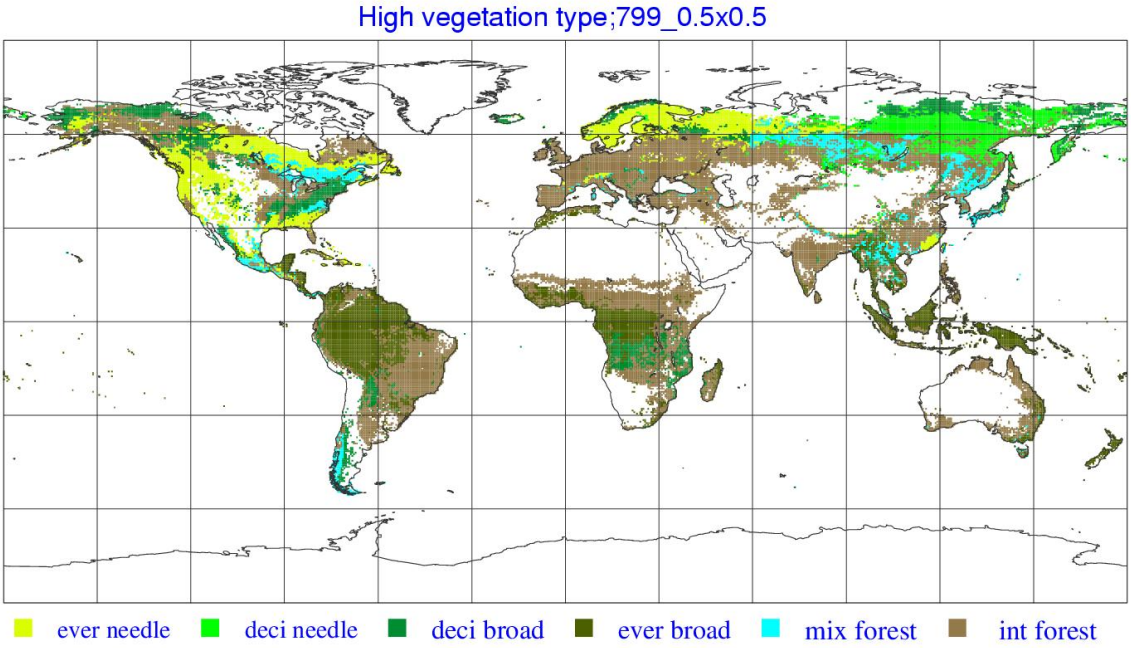

Figure 11.12 *High vegetation type.*

Table 11.2 *Percentage of land points at T799 for each low vegetation type.*

Index	Vegetation type	Percentage of land points
1	Crops, Mixed Farming	19.5
2	Short Grass	9.4
7	Tall Grass	12.1
9	Tundra	7.3
10	Irrigated Crops	3.9
11	Semidesert	12.5
13	Bogs and Marshes	1.8
16	Evergreen Shrubs	1.3
17	Deciduous Shrubs	4.2
20	Water and Land Mixtures	0
-	Remaining land points without low vegetation	27.6

Table 11.3 *Percentage of land points at T799 for each high vegetation type.*

Index	Vegetation type	Percentage of land points
3	Evergreen Needleleaf Trees	6.2
4	Deciduous Needleleaf Trees	3.0
5	Deciduous Broadleaf Trees	5.9
6	Evergreen Broadleaf Trees	11.1
18	Mixed Forest/woodland	3.3
19	Interrupted Forest	26.5
–	Remaining land points without high vegetation	43.6

high vegetation are obtained by combining the fractions from all the low and high vegetation types of Table 11.1. The index of the dominant low and high vegetation types are also coded as climatological fields for use by the land surface scheme. The latter two fields can not be interpolated by standard procedures to another resolution. The resulting fields are shown in Figs 11.9, 11.10, 11.11 and 11.12. Table 11.2 and Table 11.3 contain statistical information on the number of points in each vegetation class.

11.8 ROUGHNESS LENGTH

With the introduction of Cy31r1, the land roughness lengths are not from climatology any more and there is no orographic enhancement. Instead, the roughness lengths for momentum and heat are set by the model on the basis of correspondence Table 11.4 (Mahfouf *et al.*, 1995). The wet skin tile obtains values that are weighted between low and high vegetation according to their fractional cover. The exposed snow tile is set to table entry 12 (ice caps and glaciers), the snow under high vegetation tile has the roughness length of the high vegetation and the bare soil tile is set to the roughness length of table entry 8 (desert). The model uses the roughness lengths for the individual tiles and aggregates the fluxes. For postprocessing also an aggregated roughness length field is computed by tile averaging the neutral transfer coefficients and backing out the aggregated roughness lengths z_{oma} and z_{oha}.

$$\frac{1}{(ln10/z_{oma})^2} = \Sigma_i \frac{Fr_i}{(ln10/z_{omi})^2} \qquad \frac{1}{(ln10/z_{oha})^2} = \Sigma_i \frac{Fr_i}{(ln10/z_{ohi})^2} \tag{11.10}$$

The result with the T799 model is shown in Figs 11.13 and 11.14 for 1 August 2008.

Table 11.4 *Roughness lengths for momentum and heat associated with high and low vegetation types.*

Index	Vegetation type	H/L veg	z_{0m}	z_{0h}
1	Crops, mixed farming	L	0.150	0.015
2	Short grass	L	0.020	0.002
3	Evergreen needleleaf trees	H	2.000	2.000
4	Deciduous needleleaf trees	H	2.000	2.000
5	Deciduous broadleaf trees	H	2.000	2.000
6	Evergreen broadleaf trees	H	2.000	2.000
7	Tall grass	L	0.100	0.010
8	Desert	–	0.013	$1.3\ 10^{-3}$
9	Tundra	L	0.050	0.005
10	Irrigated crops	L	0.150	0.015
11	Semidesert	L	0.050	0.005
12	Ice caps and glaciers	–	$1.3\ 10^{-3}$	$1.3\ 10^{-4}$
13	Bogs and marshes	L	0.050	0.005
14	Inland water	–	–	–
15	Ocean	–	–	–
16	Evergreen shrubs	L	0.100	0.010
17	Deciduous shrubs	L	0.100	0.010
18	Mixed forest/woodland	H	2.000	2.000
19	Interrupted forest	H	0.500	0.050
20	Water and land mixtures	L	–	–

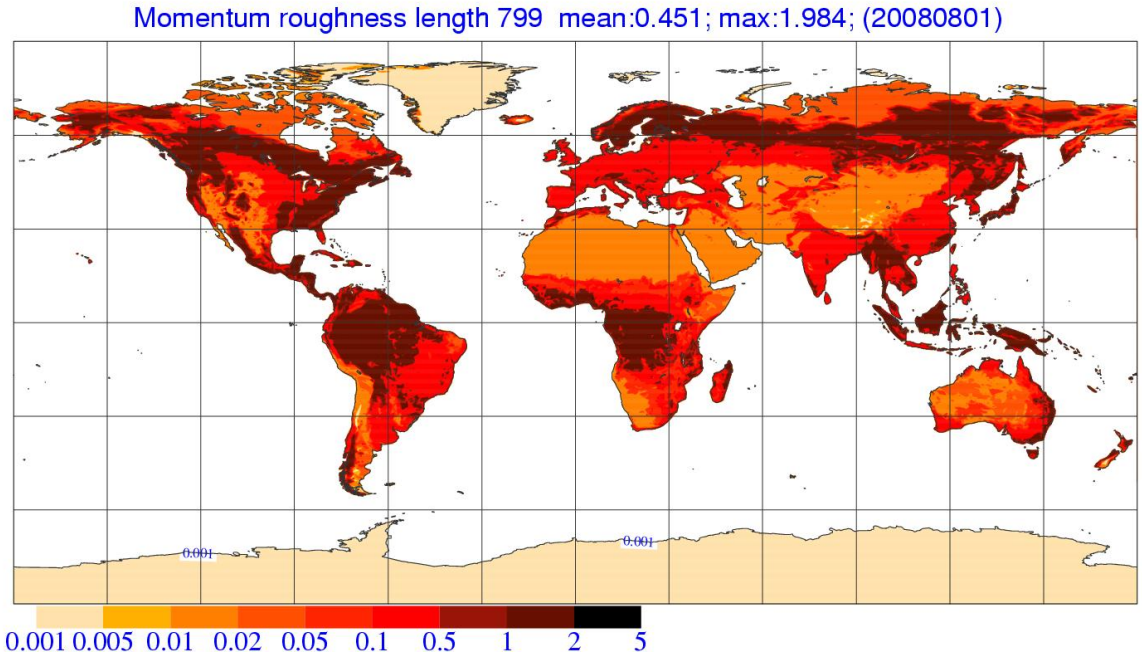

Figure 11.13 *Roughness length for momentum as produced by the T799 model for 1 August 2008, using the dominant vegetation type, snow cover and correspondence Table 11.4.*

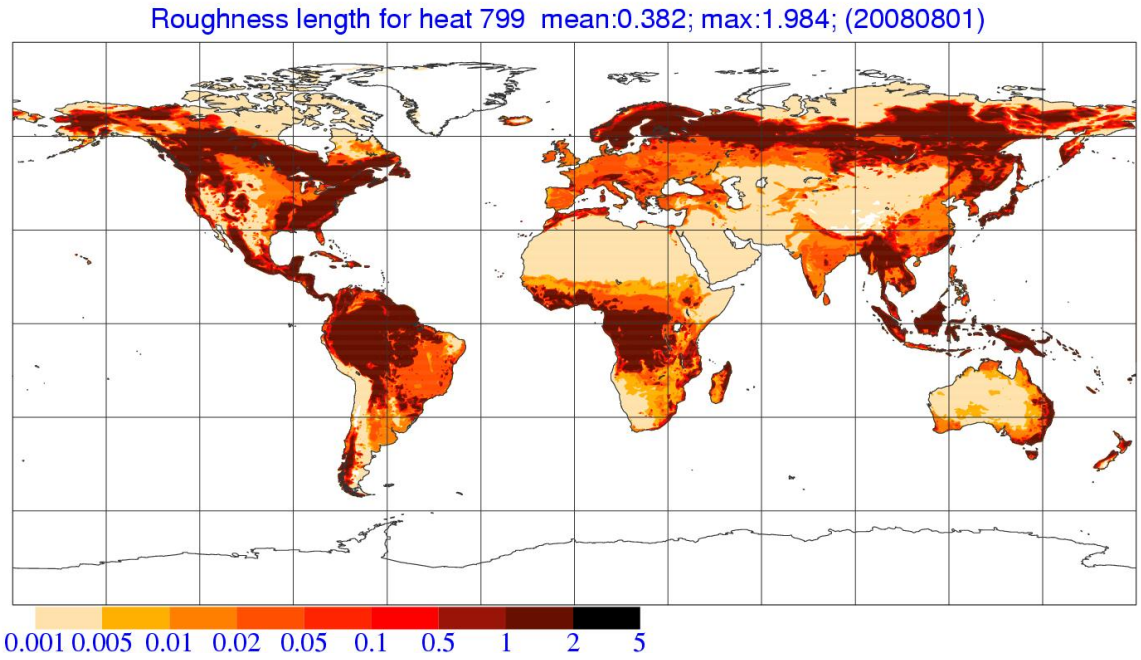

Figure 11.14 *Roughness length for heat as produced by the T799 model for 1 August 2008, using the dominant vegetation type, snow cover and correspondence Table 11.4.*

11.9 ALBEDO

Within the short-wave radiation scheme, the reflection at the surface is handled considering direct and diffuse radiation. Over land, the surface albedo is derived from monthly mean climatologies of its snow-free UV-visible (0.2 - 0.7 μm) and near-infrared (0.7 - 5.0 μm) direct and diffuse components built from 16-day MODIS albedo over the year 2000-2003 (Schaaf *et al.*, 2002).

The fields for July are shown in Figs 11.15, 11.16, 11.17 and 11.18. To obtain a smooth evolution in time, the model does a linear interpolation between successive months, assuming that the monthly field applies to the 15th of the month. The model adapts the background albedo over water, ice and snow as documented in the chapter on radiation.

11.10 AEROSOLS

Five types of tropospheric aerosols are considered in the model. The geographical distributions of sea-salt, dust, organic, black carbon, sulphate aerosols have been derived from the monthly climatology of Tegen *et al.* (1997). Fig. 11.19 to Fig. 11.23 give for each of the five types the distribution for January, April, July and October. They are distributed vertically according to the profiles in Fig. 11.24. Well-mixed (vertically and horizontally) tropospheric background aerosols with an optical thickness of 0.03 and stratospheric background aerosols with an optical thickness of 0.045 are added to the previous amounts with a rate of change of optical thickness with pressure of 0.037 and 0.233 /atm respectively. The transition from troposphere to stratosphere is obtained by multiplication of the background values with $1 - L_{\text{stratos}}$ and L_{stratos} respectively (see Fig. 11.24).

11.11 OZONE

The ozone climatology that is operational since August 1997, distributes the ozone mixing ratio as a function of pressure, latitude and month following Fortuin and Langematz (1994). Zonal mean averages are shown in Fig. 11.25.

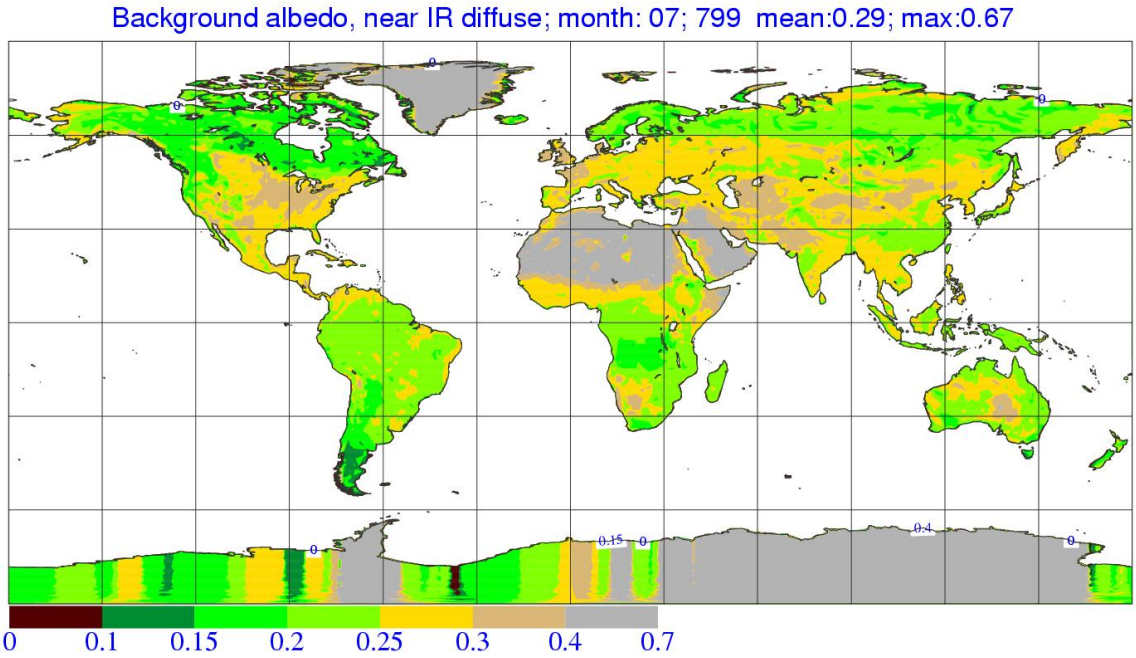

Figure 11.15 *Climatological background albedo for July (near infrared, diffuse).*

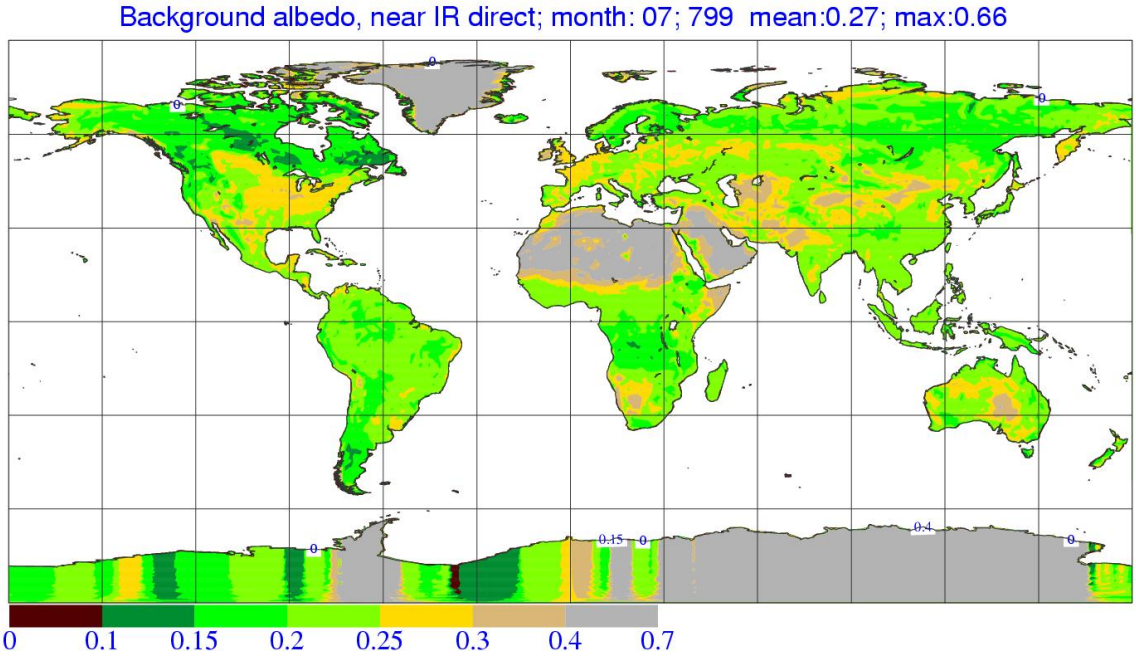

Figure 11.16 *Climatological background albedo for July (near infrared, direct).*

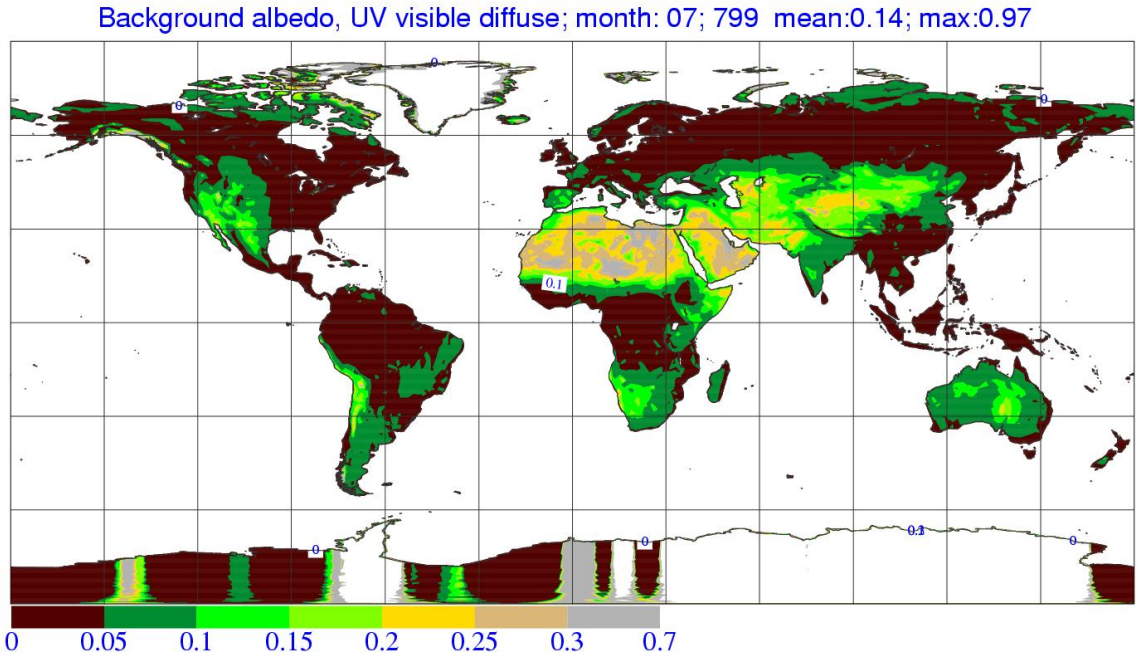

Figure 11.17 *Climatological background albedo for July (UV visible, diffuse).*

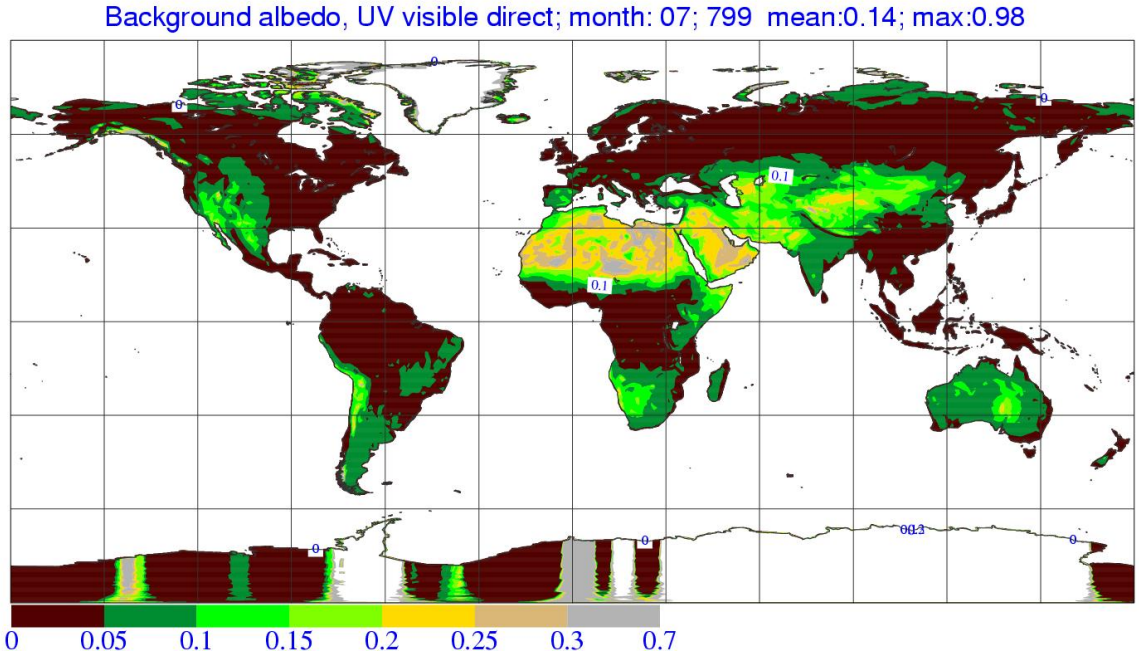

Figure 11.18 *Climatological background albedo for July (UV visible, direct).*

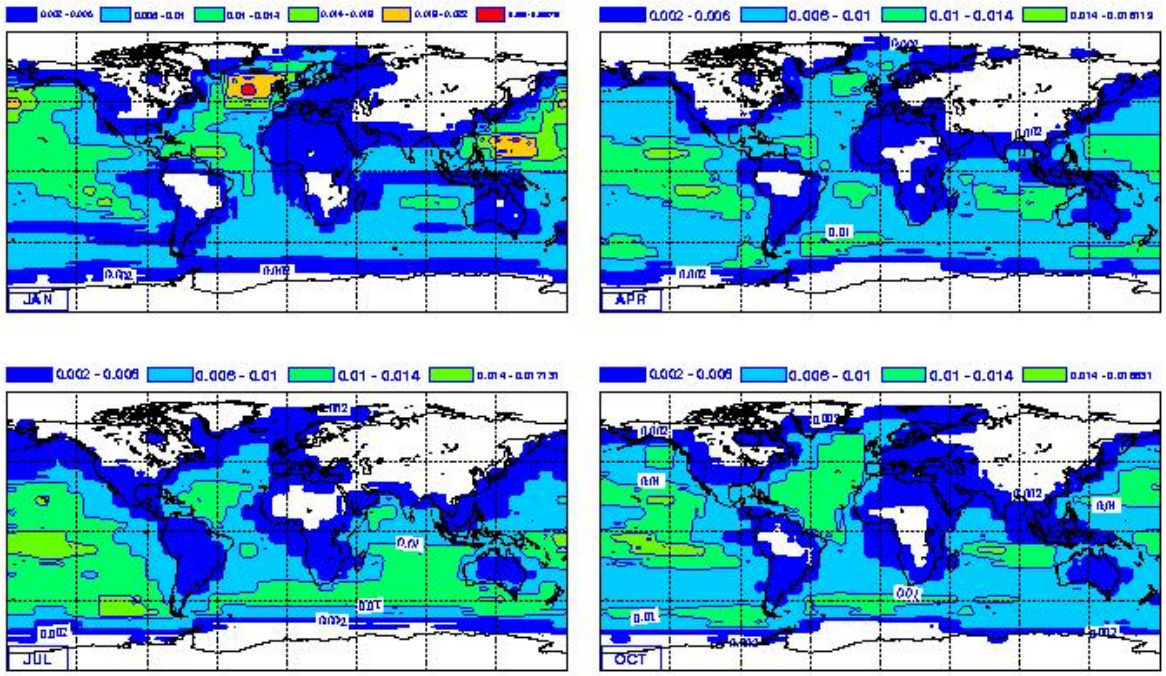

Figure 11.19 *Climatological distribution of sea salt aerosols for Jan, Apr, Jul, and Dec according to Tegen* et al. *(1997).*

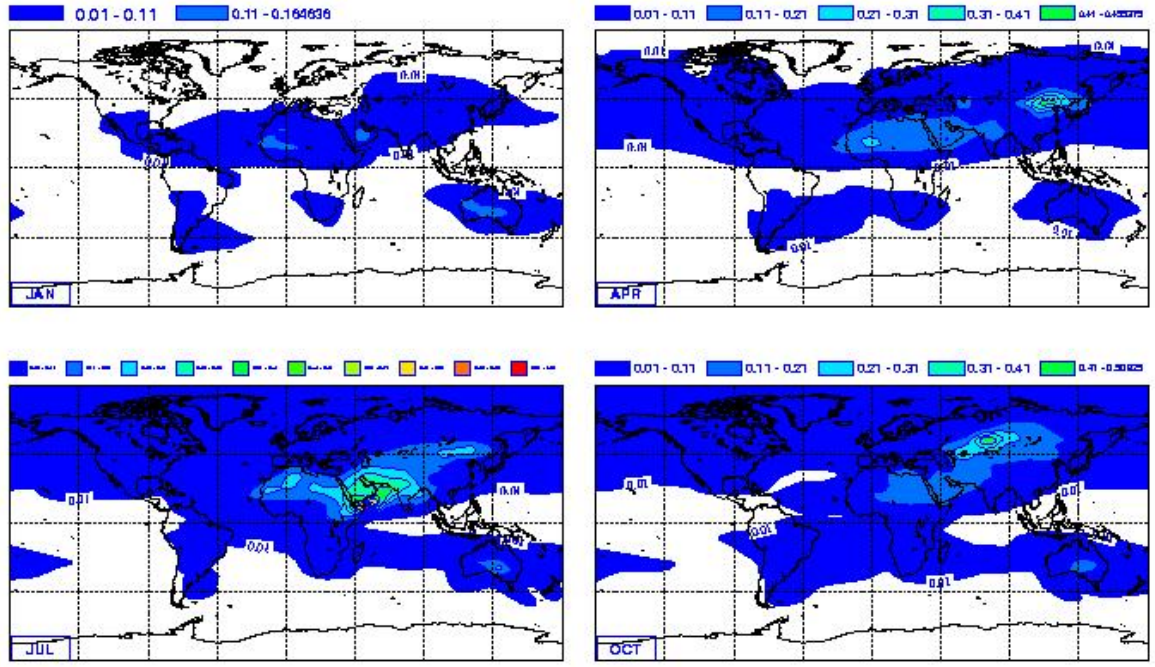

Figure 11.20 *Climatological distribution of dust aerosols for Jan, Apr, Jul, and Dec according to Tegen* et al. *(1997).*

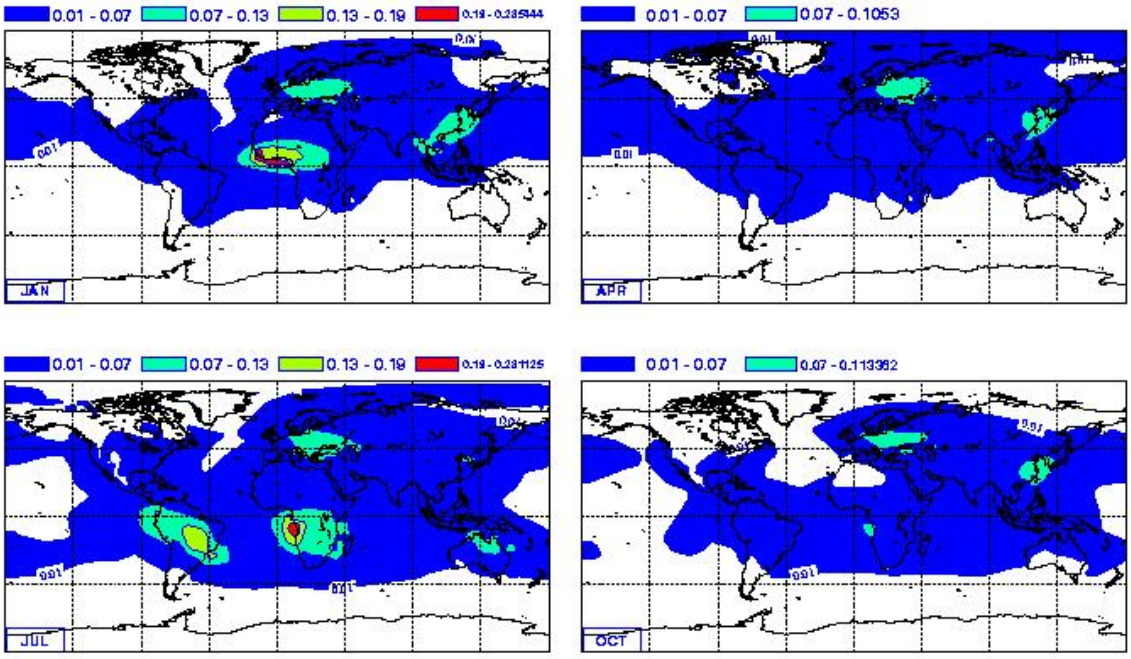

Figure 11.21 *Climatological distribution of organic aerosols for Jan, Apr, Jul, and Dec according to Tegen* et al. *(1997).*

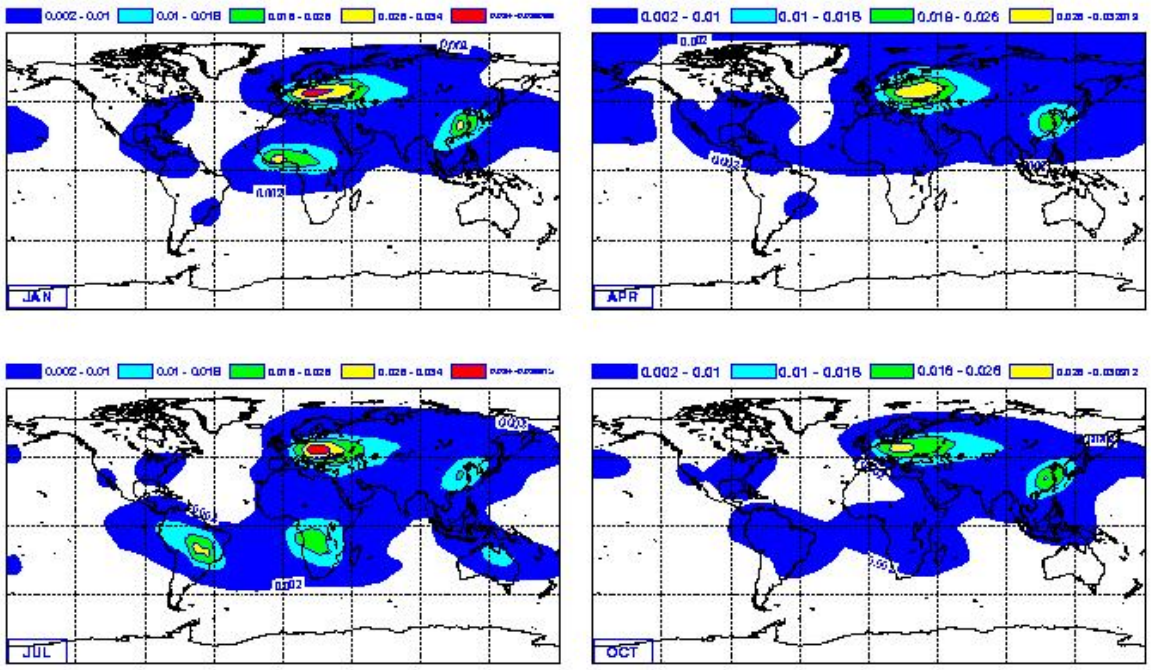

Figure 11.22 *Climatological distribution of black carbon aerosols for Jan, Apr, Jul, and Dec according to Tegen* et al. *(1997).*

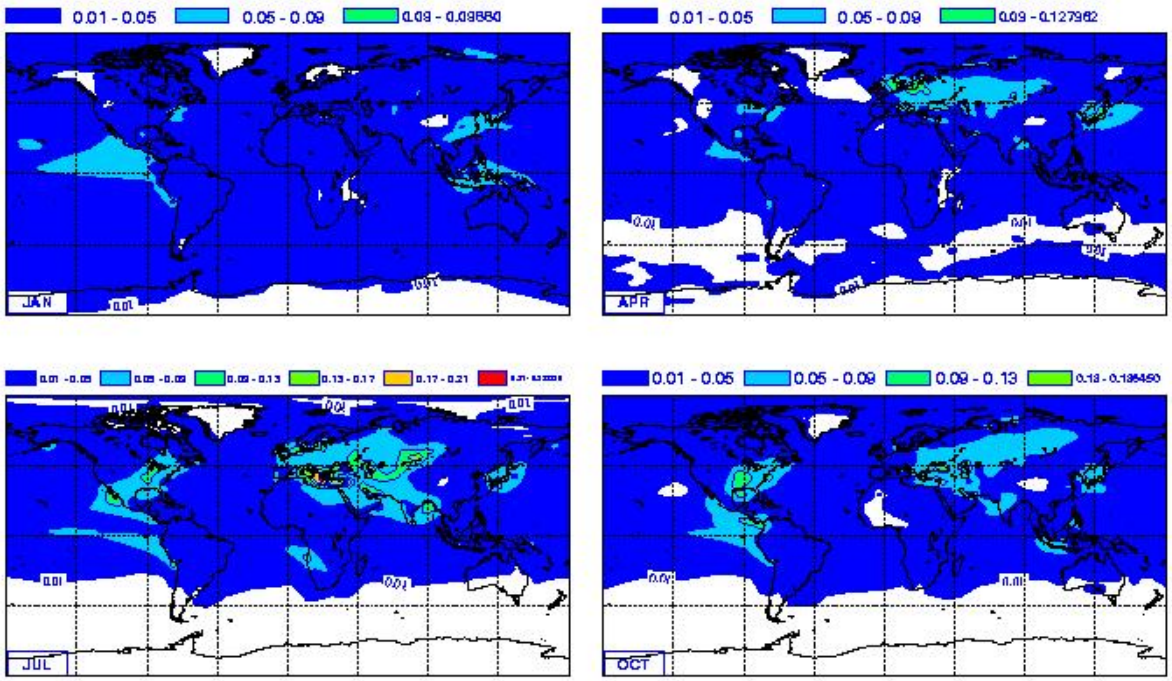

Figure 11.23 *Climatological distribution of sulphate aerosols for Jan, Apr, Jul, and Dec according to Tegen* et al. *(1997).*

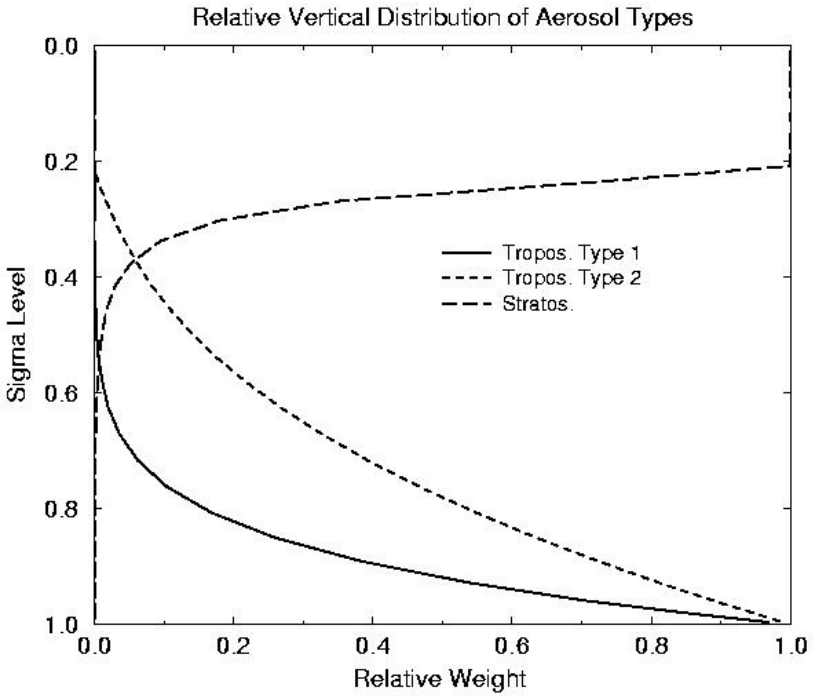

Figure 11.24 *(e) Type 1 (full line) profiles apply to maritime, continental and urban type aerosols; type 2 (short dashed line) applies to desert type; the third curve (long dashed line) represents* L_{stratos} *and is used to determine the transition from tropospheric to stratospheric background aerosols.*

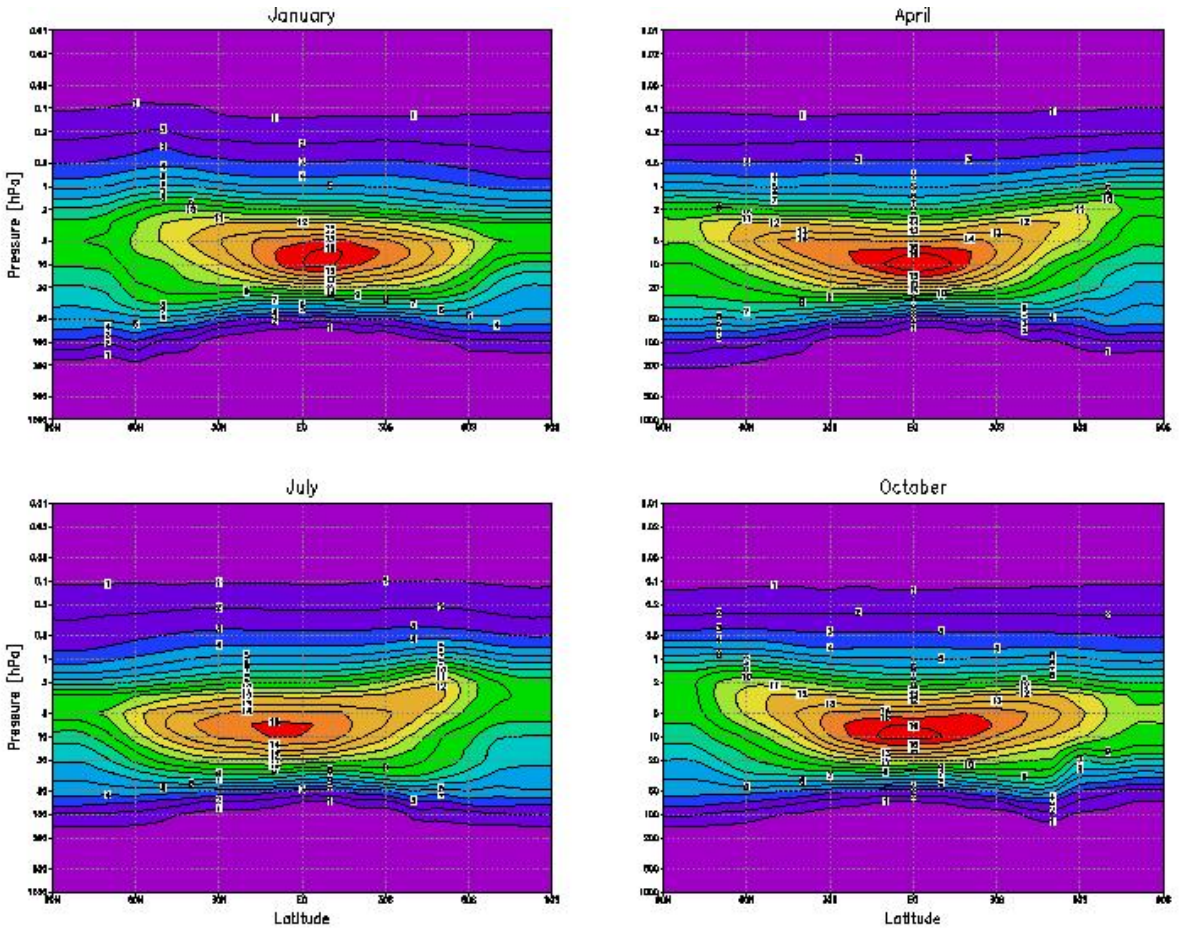

Figure 11.25 *Ozone climatology prescribed in the 91-level model as a zonal mean according to the climatology by Fortuin and Langematz (1994). This climatology is operational in the ECMWF model since August 1997. The contour interval is 1 Pa.*

11.12 TRACE GASES

A new description of the radiatively active trace gases has been introduced in the IFS with Cy35r3 on 8 September 2009. It replaces the previous globally averaged values for CO_2, CH_4, N_2O, $CFCl_3$, CF_2Cl_2 (with possibility of defining their history since 1850) by bi-dimensional (latitude/height) climatologies derived from either the MOBIDIC model or for CO_2, CH_4 and O_3 from the GEMS reanalysis effort. The effect of $CHFCl_2$ and CCl_4 have also been added using their globally-defined concentrations. A discussion of the impact of these new climatologies and of further model developments (dissipation of non-orographic gravity-waves) can be found in Bechtold *et al.* (2009).

11.13 SOIL TYPE

Soil types are derived from the FAO/UNESCO Digital Soil Map of the World, DSMW (FAO, 2003), which exists at a resolution of 5'x5' (about 10 km). FAO DSMW provides the information on two levels of soil depth namely 0–30 cm and 30–100 cm. Since the root zone is most important for the water holding, the 30–100 cm layer is selected for H-TESSEL. To interpolate to model target resolution, the dominant soil type is selected. This procedure has the advantage of preserving hydraulic properties when moving across various model resolutions (Balsamo *et al.*, 2008). The climate field used by the model has an index from 1 to 7 corresponding to the soil textures (see Fig. 11.26): 'coarse' (1),'medium' (2), 'medium fine' (3), 'fine' (4), 'very fine' (5), 'organic' (6), and 'tropical organic' (7).

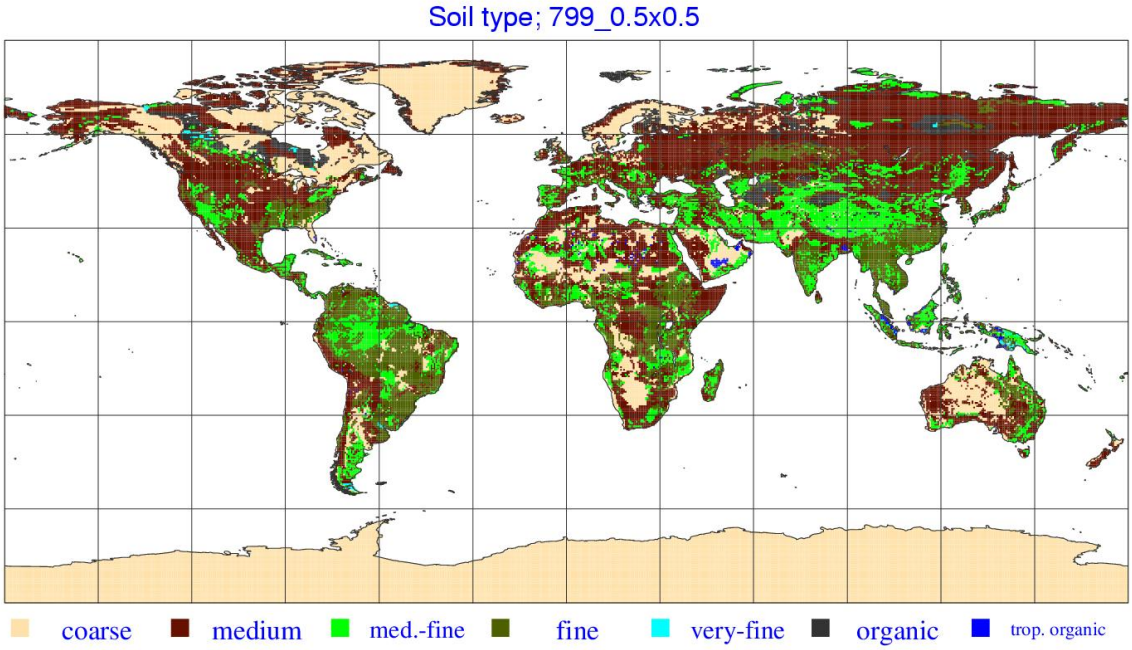

Figure 11.26 *Soil type classes as used in H-TESSEL.*

References

Abramopoulos, F., Rosenzweig, C. and Choudury, B. (1988). Improved ground hydrology calculations for global climate models (GCMs): Soil water movement and evapotranspiration. *J. Climate*, **1**, 921–941.

Alduchov, O. A. and Eskridge, R. E. (1996). Improved Magnus form approximation of saturation vapor pressure. *J. Appl. Meteorol.*, **35**, 601–609.

Anderson, E. A. (1976). A point energy and mass balance model of a snow cover. *NOAA Tech. Rep.*, **19**, 150pp.

Arakawa, A. and Schubert, W. H. (1974). Interaction of a cumulus cloud ensemble with the large-scale environment. Part I. *J. Atmos. Sci.*, **31**, 674–701.

Baines, P. G. and Palmer, T. N. (1990). Rationale for a new physically based parametrization of subgrid-scale orographic effects. *ECMWF Tech. Memo. No. 1699.*

Baker, D. G., Ruschy, D. L. and Wall, D. B. (1990). The albedo decay of prarie snows. *J. Appl. Meteorol.*, **29**, 179–187.

Balsamo, G., Viterbo, P., Beljaars, A., van den Hurk, B., Hirschi, M., Betts, A. K. and Scipal, K. (2008). A revised hydrology for the ecmwf model: Verification from field site to terrestrial water storage and impact in the integrated forecast system. *ECMWF Tech. Memo. No. 563.*

Barker, H., Pincus, R. and Morcrette, J.-J. (2003). The monte-carlo independent column approximation: Application within large-scale models. In *GCSS-ARM Workshop on the Representation of Cloud Systems in Large-Scale Models*, available at http://www.met.utah.edu/skrueger/gcss-2002/Extended-Abstracts.pdf.

Batchelor, G. K. (1967). *An Introduction to Fluid Dynamics.* Cambridge University Press, 615 pp.

Bechtold, P. and Bidlot, J.-R. (2009). Convective gusts. *ECMWF Newsletter No. 119*, pp. 15–18.

Bechtold, P., Chaboureau, J.-P., Beljaars, A., Betts, A. K., Köhler, M., Miller, M. and Redelsperger, J.-L. (2004). The simulation of the diurnal cycle of convective precipitation over land in a global model. *Q. J. R. Meteorol. Soc.*, **130**, 3119–3137.

Bechtold, P., Orr, A., Morcrette, J.-J., Engelen, R., Flemming, J. and Janiskova, M. (2009). Improvements in the stratosphere and mesosphere of the IFS. *ECMWF Newsletter No. 120*, pp. 22–31.

Beljaars, A. C. M. (1987). The influence of sampling and filtering on measured wind gusts. *J. Atmos. Oceanic Technol.*, **4**, 613–626.

Beljaars, A. C. M. (1991). Numerical schemes for parametrization. In *Proc. of ECMWF Seminar on Numerical Methods in Atmospheric Models*, Vol. 2, pp. 1–42, Reading, 9–13 September 1991.

Beljaars, A. C. M. (1994). The parametrization of surface fluxes in large-scale models under free convection. *Q. J. R. Meteorol. Soc.*, **121**, 255–270.

Beljaars, A. C. M. (1995). The impact of some aspects of the boundary layer scheme in the ECMWF model. In *Proc. of ECMWF Seminar on Parametrization of Sub-grid Scale Physical Processes*, pp. 125–161, Reading, 5–9 September 1994.

Beljaars, A. C. M. (1997). Air-sea interaction in the ECMWF model. In *Proc. of ECMWF Seminar on Atmosphere Surface Interaction*, pp. 33–52, Reading, 8–12 September 1997.

Beljaars, A. C. M., Bechtold, P., Köhler, M., Morcrette, J.-J., Tompkins, A., Viterbo, P. and Wedi, N. (2004a). The numerics of physical parametrization. In *Proc. of ECMWF Seminar on Recent Developments in Numerical Methods for Atmosphere and Ocean Modelling*, pp. 113–134, Reading, 6–10 September 2004.

Beljaars, A. C. M., Brown, A. R. and Wood, N. (2004b). A new parametrization of turbulent orographic form drag. *Q. J. R. Meteorol. Soc.*, **130**, 1327–1347.

Beljaars, A. C. M. and Viterbo, P. (1999). The role of the boundary layer in a numerical weather prediction model. In A. A. M. Holtslag and P. G. Duynkerke (Eds), *Clear and Cloudy Boundary Layers*, North Holland Publishers.

Bennets, D. A. and Hoskins, B. J. (1979). Conditional symmetric instability—a possible explanation for frontal rainbands. *Q. J. R. Meteorol. Soc.*, **105**, 945–962.

Bennets, D. A. and Sharp, J. C. (1982). The relevance of conditional symmetric instability to the prediction of meso-scale frontal rainbands. *Q. J. R. Meteorol. Soc.*, **108**, 595–602.

Best, M. J., Beljaars, A. C. M., Polcher, J. and Viterbo, P. (2004). A proposed structure for coupling tiled surfaces with the planetary boundary layer. *J. Hydr. Meteorol.*, **5**, 1271–1278.

Betts, A. K. (1973). Non-precipitating cumulus convection and its parameterization. *Q. J. R. Meteorol. Soc.*, **99**, 178–196.

Betts, A. K. and Ball, J. H. (1997). Albedo over the boreal forest. *J. Geophys. Res.*, **1028**, 28901–28909.

Betts, A. K., Viterbo, P. and Wood, E. (1998). Surface energy and water balance for the Arkansas–Red River basin from the ECMWF reanalysis. *J. Climate*, **11**, 19293–19306.

Bithell, M., Gray, L. J., Harries, J. E., Rusell III, J. M. and Tuck, A. F. (1994). Synoptic interpretation of measurements from HALOE. *J. Atmos. Sci.*, **51**, 2942–2956.

Blackadar (1962). The vertical distribution of wind and turbulent exchange in a neutral atmosphere. *J. Appl. Meteorol*, **30**, 327–341.

Bonan, G. B. (1994). Comparison of two land surface process models using prescribed forcings. *J. Geophys. Res.*, **99**, 25803–25818.

Boone, A. and Etchevers, P. (2001). An intercomparison of three snow schemes of varying complexity coupled to the same land surface model: Local-scale evaluation at an alpine site. *J. Hydrometeorol.*, **2**, 374–394.

Boone, A., Habets, F., Noilhan, J., Clark, D., Dirmeyer, P., Fox, S., Gusev, Y., Haddeland, I., Koster, R., Lohmann, D., Mahanama, S., Mitchell, K., Nasonova, O., Niu, G.-Y., Pitman, A., Polcher, J., Shmakin, A. B., Tanaka, K., van den Hurk, B., Vrant, S., Verseghy, D., Viterbo, P. and Yang., Z.-L. (2004). The Rhône-aggregation land surface scheme intercomparison project: An overview. *J. Climate*, **17(1)**, 187–208.

Bosveld, F. C., Holtslag, A. A. M. and van den Hurk, B. J. J. M. (1999). Interpretation of crown radiation temperatures of a dense Douglas fir forest with similaty theory. *Boundary-Layer Meteorol.*, **92**, 429–451.

Brankovic, C. and Van Maanen, J. (1985). The ECMWF climate system. *ECMWF Tech. Memo. No. 109.*

Brasseur, G. and Solomon, S. (1984). *Aeronomy of the Middle Atmosphere.* D. Reidel Publishing Co.

Browning, K. A., Hardman, M. E., Harrold, T. W. and Pardoe, C. W. (1973). The structure of rainbands within a mid-latitude depression. *Q. J. R. Meteorol. Soc.*, **99**, 215–231.

Brun, E., E., M., V., S., C., G. and C., C. (1989). An energy and mass model of snow cover suitable for operational avalanche forecasting. *J. Glaciol.*, **35**, 333–342.

Brun, E., P., D., M., S. and G., B. (1992). A numerical-model to simulate snow-cover stratigraphy for operational avalanche forecasting. *J. Glaciol.*, **38**, 13–22.

Brutsaert, W. (1982). *Evaporation in the Atmosphere*. D. Reidel.

Buck, A. L. (1981). New equations for computing vapor pressure and enhancement factor. *J. Appl. Meteorol.*, **20**, 1527–1532.

Cahalan, R. F., Ridgway, W., Wiscombe, W. J. and Bell, T. L. (1994). The albedo offractal stratocumulus clouds. *J. Atmos. Sci.*, **51**, 2434–2455.

Cariolle, D. and Déqué, M. (1986). Southern hemisphere medium-scale waves and total ozone disturbances in a spectral general circulation model. *J. Geophys. Res.*, **91D**, 10825–10846.

Cariolle, D. and Teyssèdre, H. (2007). A revised linear ozone photochemistry parameterization for use in transport and general circulation models: multi-annual simulations. *Atmos. Chem. and Phys. Disc.*, **7**, 1655–1697.

Cheinet, S. (2003). A multiple mass-flux parameterization for the surface generated convection. Part 1: Dry plumes. *J. Atmos. Sci.*, **60**, 2313–2327.

Cheinet, S. (2004). A multiple mass-flux parameterization for the surface generate d convection. part 2: Cloudy cores. *J. Atmos. Sci.*, **61**, 1093–1113.

Cheng, L., Yip, T.-C. and Cho, H.-R. (1980). Determination of mean cumulus cloud vorticity from GATE A/B-scale potential vorticity budget. *J. Atmos. Sci.*, **37**, 797–811.

Clapp, R. B. and Hornberger, G. M. (1978). Empirical equations for some soil hydraulic properties. *Water Resources Res.*, **14**, 601–604.

Clough, S. A. and Iacono, M. I. (1995). Line-by-line calculation of atmospheric fluxes and cooling rates, 2. Application to carbon dioxide, ozone, methane, nitrous oxide and the halocarbons. *J. Geophys. Res.*, **100D**, 16519–16536.

Clough, S. A., Iacono, M. J. and Moncet, J.-L. (1992). Line-by-line calculations of atmospheric fluxes and cooling rates: Application to water vapor. *J. Geophys. Res.*, **97D**, 15761–15786.

Clough, S. A., Kneizys, F. X. and Davies, R. W. (1989). Line shape and the water vapor continuum. *Atmos. Res.*, **23**, 229–241.

Clough, S. A., Shephard, M., Mlawer, E., Delamere, J., Iacono, M., Cady-Pereira, K., Boukabara, S. and Brown, P. (2005). Atmospheric radiative transfer modeling: A summary of the aer codes. *J. Quant. Spectros. Radiat. Transfer*, **91**, 233–244.

Coakley Jr., J. A. and Chylek, P. (1975). The two-stream approximation in radiation transfer: Including the angle of the incident radiation. *J. Atmos. Sci.*, **32**, 409–418.

Cosby, B. J., Hornberger, G. M., Clapp, R. B. and Ginn, T. (1984). A statistical exploration of the relationships of soil moisture characteristics to the physical properties of soils. *Water Resources Res.*, **20**, 682–690.

De Vries, D. A. (1975). Heat transfer in soils. In D. A. de Vries and N. H. Afgan (Eds), *Heat and Mass Transfer in the Biosphere. Part I: Transfer Processes in the Plant Environment*, pp. 4–28, Wiley.

Deardorff, J. W. (1974). Three dimensional numerical study of a heated planetary boundary layer. *Bound.-Layer Meteorol.*, **7**, 81–106.

Deardorff, J. W. (1978). Efficient prediction of ground surface temperature and moisture, with inclusion of a layer of vegetation. *J. Geophys. Res.*, **83C**, 1889–1903.

Deschamps, P.-Y., Herman, M. and Tanre, D. (1983). Modelisation du rayonnement solaire reflechi par l'atmosphere et la terre, entre 0.35 et 4 microns. *Rapport ESA 4393/80/F/DC(SC)*.

Dickinson, R., Henderson-Sellers, A. and Kennedy, P. (1993). Biosphere-atmosphere transfer scheme (BATS) version 1e as coupled to the NCAR community climate model. *Technical Report NCAR/TN-387 + STR*, NCAR Boulder, Colorado.

Dolman, A. J. and Gregory, D. (1992). The parameterization of rainfall interception in GCMs. *Q. J. R. Meteorol. Soc.*, **118**, 445–467.

Dorman, J. L. and Sellers, P. J. (1989). A global climatology of albedo, roughness length and stomatal resistance for atmospheric general circluation models as represented by the simple biosphere model (SB). *J. Appl. Meterol.*, **28**, 833–855.

Douville, H., Royer, J.-F. and Mahfouf, J.-F. (1995). A new snow parameterization for the Météo-France climate model. Part I: Validation in stand-alone experiments. *Climate Dyn.*, **12**, 21–35.

Dubuisson, P., Buriez, J.-C. and Fouquart, Y. (1996). High spectral resolution solar radiative transfer in absorbing and scattering media: Application to the satellite simulation. *J. Quant. Spectrosc. Radiat. Transfer*, **55**, 103–126.

Dümenil, L. and Todini, E. (1992). A rainfall-runoff scheme for use in the hamburg climate model. In *Advances in theoretical hydrology, A tribute to James Dooge. P. O'Kane*, European Geophysical Society Series on Hydrological Sciences 1, Elsevier, Amsterdam.

Dutra, E., Balsamo, G., Viterbo, P., Miranda, P., Beljaars, A., Schr, C. and Elder, K. (2009). New snow scheme in htessel: description and offline validation. *ECMWF Technical Memorandum*, **607**.

Dutra, E., Balsamo, G., Viterbo, P., Miranda, P., Beljaars, A., Schr, C. and Elder, K. (2010). An improved snow scheme for the ecmwf land surface model: Description and offline validation. *J. Hydrometeorol.*, **11**, 7499–7506.

Dyer, A. J. (1974). A review of flux-profile relationships. *Boundary-Layer Meteorol.*, **7**, 363–372.

Ebert, E. E. and Curry, J. A. (1992). A parametrization of ice cloud optical properties for climate models. *J. Geophys. Res.*, **97D**, 3831–3836.

Ebert, E. E. and Curry, J. A. (1993). An intermediate one-dimensional thermodynamic sea ice model for investigating ice-atmosphere interactions. *J. Geophys. Res.*, **98C**, 10085–10109.

Ekholm, S. (1996). A full coverage high-resolution topographic model of Greenland computed from a variety of digital elevation data. *J. Geophys. Res.*, **101 (B10)**, 21961–21972.

Elsasser, W. M. (1942). Heat transfer by infrared radiation in the atmosphere. *Harvard Meteorological Studies No. 6*, p. 107.

Emanuel, K. A. (1982). Inertial instability and mesoscale convective systems. Part II: Symmetric CISK in a baroclinic flow. *J. Atmos. Sci.*, **39**, 1080–1097.

Ern, M. P., Preusse, P. and Warner, C. D. (2004). Absolute values of gravity wave momentum flux derived from satellite data. *J. Geophys. Res.*, **109**, D20103.

Etling, D. (1989). On atmsopheric vortex streets in the wake of large islands. *Meteorol. Atmos. Phys.*, **41**, 157–164.

Fairall, C. W., Bradley, E. F., Godfrey, J. S., Wick, G. A. and Edson, J. B. (1996). Cool-skin and warm-layer effects on sea surface temperature. *J. Geophys. Res.*, **101**, 1295–1308.

FAO (2003). Digital soil map of the world (DSMW). *Technical report*, Food and Agriculture Organization of the United Nations, re-issued version.

Farouki, O. T. (1986). Thermal properties of soils. In W. R. van Wijk (Ed.), *Physics of Plant Environments*, North-Holland Publishing, Amsterdam.

Fels, S. B. (1979). Simple strategies for inclusion of Voigt effects in infrared cooling rate calculations. *Appl. Optics*, **18**, 2634–2637.

Flato, G. M. and Hibler III, W. D. (1992). Modeling the ice pack as a caitating fluid. *J. Phys. Oceanog.*, **22**, 626–651.

Fortuin, J. P. F. and Langematz, U. (1994). An update on the global ozone climatology and on concurrent ozone and temperature trends. Proceedings SPIE. *Atmos. Sensing and Modeling*, **2311**, 207–216.

Foster, D. S. (1958). Thunderstorm gusts compared with computed downdraught speeds. *Mon. Wea. Rev.*, **86**, 91–94.

Fouquart, Y. (1974). Utilisation des approximants de pade pour l'etude des largeurs equivalentes de raies formees en atmosphere diffusante. *J. Quant. Spectrosc. Radiat. Transfer*, **14**, 497–508.

Fouquart, Y. (1987). Radiative transfer in climate modeling. In M. E. Schlesinger (Ed.), *NATO Advanced Study Institute on Physically-Based Modeling and Simulation of Climate and Climate Changes*, pp. 223–283, Erice, Sicily, 11–23 May 1986.

Fouquart, Y. and Bonnel, B. (1980). Computations of solar heating of the earth's atmosphere: A new parameterization. *Beitr. Phys. Atmos.*, **53**, 35–62.

Fritsch, J. M. and Chappell, C. G. (1980). Numerical prediction of convectively driven mesoscale pressure systems. Part I: Convective parametrization. *J. Atmos. Sci.*, **37**, 1722–1733.

Fritts, D. C. and Nastrom, D. D. (1980). Sources of mesoscale variability of gravity waves. part ii: frontal, convective, and jet stream excitation. *J. Atmos. Sci.*, **49**, 111–127.

Fritts, D. C. and Nastrom, D. D. (1993). Spectral estimates of gravity wave energy and momentum fluxes. part i: Energy dissipation, acceleration, and constraints. *J. Atmos. Sci.*, **50**, 3685–3694.

Fu, Q. (1996). An accurate parameterization of the solar radiative properties of cirrus clouds. *J. Climate*, **9**, 2058–2082.

Fu, Q. and Liou, K.-N. (1992). On the correlated k-distribution method for radiative transfer in non-homogeneous atmospheres. *J. Atmos. Sci.*, **49**, 2139–2156.

Fu, Q., Yang, P. and Sun, W. B. (1998). An accurate parametrization of the infrared radiative properties of cyrrus clouds of climate models. *J. Climate*, **11**, 2223–2237.

Geleyn, J.-F. and Hollingsworth, A. (1979). An economical analytical method for the computation of the interaction between scattering and line absorption of radiation. *Beitr. Phys. Atmos.*, **52**, 1–16.

Gesch, D. B. and Larson, K. S. (1998). Techniques for development of global 1-kilometer digital elevation models. In *Proc. Pecora Thirteenth Symposium*, Sioux Falls, South Dakota, August 20–22, 1996 (CD-ROM), Am. Soc. Photogrammetry Remote Sens., Bethesda, Md.

Giard, D. and Bazile, E. (2000). Implentation of a new assimilation scheme for soil and surface variables in a global NWP model. *Mon. Wea. Rev.*, **128**, 997–1015.

Gierens, K., Kohlhepp, R., Spichtinger, P. and Schrödter-Homscheidt, M. (2004). Ice supersaturation as seen from tovs. *Atmos. Chem. Phys.*, **4**, 539–547.

Gierens, K., Schumann, U., Helten, M., Smit, H. and Marenco, A. (1999). A distribution law for relative humidity in the upper troposphere and lower stratosphere derived from three years of mozaic measurements. *Ann. Geophysicae*, **17**, 1218–1226.

Gierens, K., Schumann, U., Helten, M., Smit, H. and Wang, P. H. (2000). Ice-supersaturated regions and subvisible cirrus in the northern midlatitude upper troposphere. *J. Geophys. Res.*, **105**, 22743–22753.

Giorgetta, M. A. and Morcrette, J.-J. (1995). Voigt line approximation in the ECMWF radiation scheme. *Mon. Wea. Rev.*, **123**, 3381–3383.

Godfrey, J. S. and Beljaars, A. C. M. (1991). On the turbulent fluxes of buoyancy, heat and moisture at the air-sea interface at low wind speed. *J. Geophys. Res.*, **96**, 22043–22048.

Gregory, D. (1997). Parametrization of convective momentum transports in the ECMWF model: evaluation using cloud resolving models and impact upon model climate. In *Proc. ECMWF Workshop on New Insights and Approaches to Convective Parametrization*, pp. 208–227, Reading, 4–7 November 1996.

Gregory, D., Kershaw, R. and Inness, P. M. (1997). Parametrization of momentum transports by convection. II: Tests in single-column and general circulation models. *Q. J. R. Meteorol. Soc.*, **123**, 1153–1183.

Gurevitch, M. I. (1965). *Theory of Jets in Ideal Fluids*. Academic Press.

Haltiner, G. J. and Williams, R. T. (1980). *Numerical Prediction and Dynamic Meteorology*. John Wiley and Sons, 447 pp.

HAWKS (2000). The Hitran Atmospheric WorKStation. URL http://www.hitran.com.

Herzegh, P. H. and Hobbs, P. V. (1980). The mesoscale and microscale structure and organization of clouds and precipitation in mid-latitude cyclones. Part II: Warm frontal clouds. *J. Atmos. Sci.*, **37**, 597–611.

Hess, P., Koepke, P. and Schult, I. (1998). Optical properties of aerosols and clouds: The software package OPAC. *Bull. Am. Meteorol. Soc.*, **79**, 831–844.

Heymsfield, A. J. and Iaquinta, J. (2000). Cirrus crystal terminal velocities. *J. Atmos. Sci.*, **57**, 916–938.

Heymsfield, A. J., Miloshevich, L. M., Twohy, C., G. Sachse, G. and Oltmans, S. (1998). Upper-tropospheric relative humidity observations and implications for cirrus ice nucleation. *Geophys. Res. Lett.*, **25**, 1343–1346.

Hillel, D. (1982). *Introduction to Soil Physics*. Academic Press.

Hogan, R. J. and Illingworth, A. J. (2000). Deriving cloud overlap statistics from radar. *Q. J. R. Meteorol. Soc.*, **126A**, 2903–2909.

Hogan, R. J. and Illingworth, A. J. (2003). Parameterizing ice cloud inhomogeneity and the overlap of inhomogeneities using cloud radar data. *J. Atmos. Sci.*, **60**, 756–767.

Hogström, U. (1988). Non-dimensional wind and temperature profiles in the atmospheric surface layer: A re-evaluation. *Boundary-Layer Meteorol.*, **42**, 55–78.

Holtslag, A. A. M. (1998). Modelling of atmospheric boundary layers. In A. A. M. Holtslag and P. G. Duynkerke (Eds), *Clear and Cloudy Boundary Layers*, pp. 85–110, Royal Netherlands Academy of Arts and Sciences.

Holtslag, A. A. M. and Bruin, H. A. R. D. (1988). Applied modelling of the night-time surface energy balance over land. *J. Appl. Meteorol.*, **27**, 689–704.

Holtslag, A. A. M. and Moeng, C.-H. (1991). Eddy diffusivity and countergradient transport in the convect ive atmospheric boundary layer. *J. Atmos. Sci.*, **48**, 1690–1698.

Houze, R. A., Locatelli, J. D. and Hobbs, P. V. (1976). Dynamics and cloud microphysics of the rainbands in an occluded frontal system. *J. Atmos. Sci.*, **35**, 1921–1936.

Iacono, M., Delamere, J., Mlawer, E., Shephard, M., Clough, S. and Collins, W. (2008). Radiative forcing by long-lived greenhouse gases: Calculations with the aer radiative transfer models. *J. Geophys. Res.*, **113D**, 13103.

Jacquemin, B. and Noilhan, J. (1990). Sensitivity study and validation of a land-surface parameterization using the HAPEX-MOBILHY data set. *Boundary-Layer Meteorol.*, **52**, 93–134.

Jakob, C. and Klein, S. A. (2000). A parametrization of the effects of cloud and precipitation overlap for use in general circulation models. *Q. J. R. Meteorol. Soc.*, **126**, 2525–2544.

Jakob, C. and Siebesma, A. P. (2003). A new subcloud model for mass flux convection schemes. influence on triggering, updraught properties and model climate. *Mon. Wea. Rev.*, **131**, 2765–2778.

Janssen, P. A. E. M., Beljaars, A. C. M., Simmons, A. and Viterbo, P. (1992). The determination of the surface stress in an atmospheric model. *Mon. Wea. Rev.*, **120**, 2977–2985.

Jarvis, P. J. (1976). The interpretation of the variations in leaf-water potential and stomatal conductance found in canopies in the field. *Phil. Trans. R. Soc. London*, **B723**, 385–610.

Johansen, O. (1975). *Thermal conductivity of soils*. Ph.D. thesis, Trondheim, Norway.

Johnson, R. H. (1976). The role of convective-scale precipitation downdrafts in cumulus and synoptic scale interactions. *J. Atmos. Sci.*, **33**, 1890–1910.

Johnson, R. H. (1980). Diagnosis of convective and mesoscale motions during Phase III of GATE. *J. Atmos. Sci.*, **37**, 733–753.

Jones, R. L., Pyle, J. A., Harries, J. E., Zavody, A. M., Russell III, J. M. and Gille, J. C. (1986). The water vapour budget of the stratosphere studied using LIMS and SAMS satellite data. *Q. J. R. Meteorol. Soc.*, **112**, 1127–1143.

Joseph, J. H., Wiscombe, W. J. and Weinman, J. A. (1976). The Delta-Eddington approximation for radiative flux transfer. *J. Atmos. Sci.*, **33**, 2452–2459.

Kärcher, B. and Lohmann, U. (2002). A parameterization of cirrus cloud formation: Homogeneous freezing of supercooled aerosols. *Geophys. Res.*, **107**, doi:10.1029/2001JD000470.

Kessler, E. (1969). *On the distribution and continuity of water substance in atmopsheric circulation*, *Meteorological Monographs*, Vol. 10. Am. Meteorol. Soc., Boston, MA.

Khvorostyanov, V. and Sassen, K. (1998). Cirrus cloud simulation using explicit microphysics and radiation. part ii: Microphysics, vapor and ice mass budgets, and optical and radiative properties. *J. Atmos. Sci.*, **55**, 1822–1845.

Kirchoff, G. (1876). *Vorlesungen über Mathematische Physik*. Leipzig.

Klein, S. A. and Hartmann, D. L. (1993). The seasonal cycle of low stratiform cloud. *J. Climate*, **6**, 1587–1606.

Köhler, M. (2005). Improved prediction of boundary layer clouds. *ECMWF Newsletter No. 104*, pp. 18–22.

Koster, R. D. and Suarez, M. J. (1992). A comparative analysis of two land surface heterogeneity representations. *J. Climate*, **5**, 1379–1390.

Kuo, H. L. and Raymond, W. H. (1980). A quasi-one-dimensional cumulus cloud model and parametrization of cumulus heating and mixing effects. *Mon. Wea. Rev.*, **108**, 991–1009.

Lacis, A. A. and Oinas, V. (1991). A description of the correlated k distribution method for modeling nongray gaseous absorption, thermal emission, and multiple scattering in vertically inhomogeneous atmospheres. *J. Geophys. Res.*, **96D**, 9027–9063.

Landweber, L. (1961). *Motion of Immersed and Floating Bodies. Handbook of Fluid Dynamics*. McGraw-Hill, 1st edition.

Le Mone, M. A. and Pennell, W. T. (1976). The relationship of trade wind cumulus distribution to subcloud layer fluxes and structure. *Mon. Wea. Rev.*, **104**, 524–539.

Le Texier, L., Solomon, S. and Garcia, R. R. (1988). The role of molecular hydrogen and methane oxidation in the water vapour budget of the stratosphere. *Q. J. R. Meteorol. Soc.*, **114**, 281–295.

Lin, Y. L., Farley, R. D. and Orville, H. D. (1983). Bulk parameterization of the snow field in a cloud model. *J. Climate Appl. Meteorol.*, **22**, 1065–1092.

Lindzen, R. S. (1981). Some remarks on cumulus parametrization. *Rep. on NASA-GISS Workshop: Clouds in Climate: Modelling and Satellite Observational Studies*, pp. 42–51.

Liu, J. Y. and Orville, H. D. (1969). Numerical modeling of precipitation and cloud shadow effects on mountain-induced cumuli. *J. Atmos. Sci.*, **26**, 1283–1298.

Liu, Q. and Schmetz, J. (1988). On the problem of an analytical solution to the diffusivity factor. *Beitr. Phys. Atmos.*, **61**, 23–29.

Lock, A. P. (1998). The parameterization of entrainment in cloudy boundary layers. *Q. J. R. Meteorol. Soc.*, **124**, 2729–2753.

Lock, A. P., Brown, A. R., Bush, M. R., Martin, G. M. and Smith, R. N. B. (2000). A new boundary layer mixing scheme. Part I: Scheme description and single-column model tests. *Mon. Wea. Rev.*, **128**, 3187–3199.

London, J., Bojkov, R. D., Oltmans, S. and Kelley, J. I. (1976). Atlas of the global distribution of total ozone, July 1957–June 1967. *NCAR Technical Note 113+STR*.

Los, S. O., Collatz, G. J., Sellers, P. J., Malmström, C. M., Pollack, N. H., deFries, R. S., Bounoua, L., Parris, M. T., Tucker, C. J. and Dazlich, D. A. (2000). A global 9-year biophysical land surface dataset from NOAA AVHRR data. *J. Hydrometeorol.*, **1**, 183–199.

Lott, F. and Miller, M. J. (1997). A new subgrid-scale orographic drag parametrization: Its formulation and testing. *Q. J. R. Meteorol. Soc.*, **123**, 101–127.

Louis, J. F., Tiedtke, M. and Geleyn, J.-F. (1982). A short history of the operational PBL parametrization at ECMWF. In *Proc. ECMWF Workshop on Boundary Layer Parametrization*, pp. 59–80, Reading, 25–27 November 1981.

Loveland, T. R., Reed, B. C., Brown, J. F., Ohlen, D. O., Zhu, Z., Youing, L. and Merchant, J. W. (2000). Development of a global land cover characteristics database and IGB6 DISCover from the 1km AVHRR data. *Int. J. Remote Sensing*, **21**, 1303–1330.

Lundin, L.-C. (1989). Water and heat fluxes in frozen soils: Basic theory and operational modelling. In *Summary of Dissertations from the Faculty of Science*, Vol. 186, Uppsala University.

Lynch-Stieglitz, M. (1994). The development and validation of a simple snow model for the giss gcm. *J. Climate*, **7**, 1842–1855.

Mace, G. G. and Benson-Troth, S. (2002). Cloud-layer overlap characteristics derived from long-term cloud radar data. *J. Climate*, **15**, 2505–2515.

Mahfouf, J. F. and Jacquemin, B. (1989). A study of rainfall interception using a land surface paramterization for mesoscale meteorological models. *J. Appl. Meteorol.*, **28**, 1282–1302.

Mahfouf, J. F., Manzi, A., Noilhan, J., Giordani, H. and Dequé, M. (1995). The land surface scheme ISBA within the météo-france climate model ARPEGE. *J. Climate*, **8**, 2039–2057.

Mahfouf, J. F. and Noilhan, J. (1991). Comparative study of various formulations from bare soil using in situ data. *J. Appl. Meteorol.*, **30**, 1345–1365.

Mahrt, L. and Pan, H.-L. (1984). A two-layer model of soil hydrology. *Boundary-Layer Meteorol.*, **29**, 1–20.

Manzi, A. O. and Planton, S. (1994). Implementation of the ISBA parameterization scheme for land surface processes in a GCM: An annual-cycle experiment. *J. Hydrol.*, **155**, 355–389.

Martin, G. M., Johnson, D. W. and Spice, A. (1994). The measurement and parameterization of effective radius of droplets in warm stratocumulus. *J. Atmos. Sci.*, **51**, 1823–1842.

Mason, B. J. (1971). *The Physics of Clouds*. Clarendon Press.

McLandress, C. and Scinocca, J. F. (2005). The gcm response to current parameterizations of nonorographic garvity wave drag. *J. Atmos. Sci.*, **62**, 2394–2413.

Miles, J. W. and Huppert, H. E. (1969). Lee waves in a stratified flow. Part 4: Perturbation approximations. *J. Fluid Mech.*, **35**, 495–525.

Miller, M., Beljaars, A. C. M. and Palmer, T. N. (1992). The sensitivity of the ECMWF model to the parametrization of evaporation from the tropical oceans. *J. Climate*, **5**, 418–434.

Miller, M. J., Palmer, T. N. and Swinbank, R. (1989). Parametrization and influence of subgrid-scale orography in general circulation and numerical weather prediction models. *Meteorol. Atmos. Phys.*, **40**, 84–109.

Milly, P. C. D. (1982). Moisture and heat transport of hyseretic, inhomogeneous porous media: A matric head-based formulation and a numerical model. *Water Resources Res.*, **18**, 489–498.

Mlawer, E. J. and Clough, S. (1997). Shortwave and longwave enhancements in the rapid radiative transfer model. In *Proc. 7th Atmospheric Radiation Measurement (ARM) Science Team Meeting, U.S. Department of Energy, CONF-9603149.*, available from http://www.arm.gov/publications/proceedings/conf07/title.stm/mlaw-97.pdf.

Mlawer, E. J., Taubman, S. J., Brown, P. D., Iacono, M. J. and Clough, S. A. (1997). Radiative transfer for inhomogeneous atmospheres: RRTM, a validated correlated-k model for the longwave. *J. Geophys. Res.*, **102D**, 16663–16682.

Moody, E., M.D., K., C.B., S., D.K., H. and S., P. (2007). Northern hemisphere five-year average (2000-2004) spectral albedos of surfaces in the presence of snow: Statistics computed from terra modis land products. *Remote Sen. Environ.*, **111**, 337–345.

Morcrette, J.-J. (1991). Radiation and cloud radiative properties in the ECMWF operational weather forecast model. *J. Geophys. Res.*, **96D**, 9121–9132.

Morcrette, J.-J., Barker, H., Cole, J., Iacono, M. and Pincus, R. (2008a). Impact of a new radiation package, mcrad, in the ecmwf integrated forecasting system. *Mon. Wea. Rev.*, **136**, 4773–4798.

Morcrette, J.-J. and Fouquart, Y. (1985). On systematic errors in parametrized calculations of longwave radiation transfer. *Q. J. R. Meteorol. Soc.*, **111**, 691–708.

Morcrette, J.-J. and Fouquart, Y. (1986). The overlapping of cloud layers in shortwave radiation parameterizations. *J. Atmos. Sci.*, **43**, 321–328.

Morcrette, J.-J., Mlawer, E., Iacono, M. and Clough, S. (2001). Impact of the radiation transfer scheme rrtm in the ecmwf forecasting system. *ECMWF Newsletter No. 91*, pp. 2–9.

Morcrette, J.-J., Mozdzynski, G. and Leutbecher, M. (2008b). A reduced radiation grid for the ecmwf integrated forecasting system. *Mon. Wea. Rev.*, **136**, 4760–4772.

Morcrette, J.-J., Smith, L. and Fouquart, Y. (1986). Pressure and temperature dependence of the absorption in longwave radiation parametrizations. *Beitr. Phys. Atmos.*, **59**, 455–469.

Nieuwstadt, F. T. M. (1984). The turbulent structure of the stable, nocturnal boundary layer. *J. Atmos. Sci.*, **41**, 2202– 2216.

Nitta, T. (1975). Observational determination of cloud mass flux distributions. *J. Atmos. Sci.*, **32**, 73–91.

Nordeng, T.-E. (1994). Extended versions of the convection parametrization scheme at ECMWF and their impact upon the mean climate and transient activity of the model in the tropics. *ECMWF Tech. Memo. No. 206.*

Oreopoulos, L. and Barker, H. (1999). Accounting for subgrid-scale cloud variability in a multi-layer 1d solar radiative transfer algorithm. *Q. J. R. Meteorol. Soc.*, **125**, 301–330.

Orr, A., Bechtold, P., Scinocca, J. F., Ern, M. and Janiskova, M. (2010). Improved middle atnosphere climate and forecasts in the ECMWF model through a non-orographic gravity wave drag parametrization. *J. Climate*.

Ou, S. C. and Liou, K.-N. (1995). Ice microphysics and climatic temperature feedback. *Atmos. Res.*, **35**, 127–138.

Paltridge, G. W. and Platt, C. M. R. (1976). *Radiative Processes in Meteorology and Climatology*. Elsevier, New York, 318 pp.

Panofsky, H. A., Tennekes, H., Lenschow, D. H. and Wyngaard, J. C. (1977). The characteristics of turbulent velocity components in the surface layer under convective conditions. *Boundary-Layer Meteorol.*, **11**, 355–361.

Patterson, K. A. (1990). *Global Distribution of Total and Total-available Soil Water-holding Capacities*. Master's thesis, Department of Geography, University of Delaware.

Paulson, C. A. (1970). The mathematical representation of wind speed and temperature profiles in the unstable atmospheric surface layer. *J. Appl. Meteorol.*, **9**, 857–861.

Penner, E. (1970). Thermal conductivity of frozen soils. *Canadian J. Earth Sci.*, **7**, 982–987.

Peters-Lidard, C. D., Blackburn, E., Liang, X. and Wood, E. F. (1998). The effect of soil conductivity parametrization on surface energy fluxes and temperature. *J. Atmos. Sci.*, **55(7)**, 1209–1224.

Philip, J. R. (1957). Evaporation and moisture and heat fields in the soil. *J. Meteorol.*, **14**, 354–366.

Phillips, S. P. (1984). Analytical surface pressure and drag for linear hydrostatic flow over three-dimensional elliptical mountains. *J. Atmos. Sci.*, **41**, 1073–1084.

Pincus, R., Barker, H. and Morcrette, J.-J. (2003). A fast, flexible, approximate technique for computing radiative transfer in inhomogeneous clouds. *J. Geophys. Res.*, **108D**, 4376.

Pincus, R. and Klein, S. A. (2000). Unresolved spatial variability and microphysical process rates in large-scale models. *J. Geophy. Res.*, **105**, 27059–27065.

Pitman, A. J., Yang, Z.-L., Cogley, J. G. and Henderson-Sellers, A. (1991). Description of bare essentials of surface transfer for the Bureau of Meteorology Research Centre AGCM. *Meteorological Research Report 32*.

Press, W. H., Teukolsky, S. A., Vetterling, W. T. and Flannery, B. P. (1992). *Numerical Recipes in Fortran*. Cambridge University Press.

Räisänen, P. and Barker, H. W. (2004). Evaluation and optimization of sampling errors for the monte carlo independent column approximation. *Q. J. R. Meteorol. Soc.*, **130**, 2069–2086.

Räisänen, P., Barker, H. W., Khairoutdinov, M. F., Li, J. and Randall, D. A. (2004). Stochastic generation of subgrid-scale cloudy columns for large-scale models. *Q. J. R. Meteorol. Soc.*, **130**, 2047–2067.

Randel, W. J., Wu, F., Russell III, J. M., Roche, A. and Waters, J. W. (1998). Seasonal cycles and QBO variations in straospheric CH_4 and H_2O observed in UARS HALOE data. *J. Atmos. Sci.*, **55**, 163–185.

Richards, L. A. (1931). Capillary conduction of liquids through porous mediums. *Physics*, **1**, 318–333.

Ridder, K. D. (2001). Rainwater storage on plant canopies. *J. Geophys. Res.*, **106**(D14), 14819–14826.

Rodgers, C. D. (1967). The radiative heat budget of the troposphere and lower stratosphere. *Report A2*, Planetary Circulation Project, Dept. of Meteorology, M.I.T., Cambridge, Mass.

Rodgers, C. D. and Walshaw, C. D. (1966). The computation of the infrared cooling rate in planetary atmospheres. *Q. J. R. Meteorol. Soc.*, **92**, 67–92.

Rothman, L. S., Gamache, R. R., Goldman, A., Brown, L. R., Toth, R. A., Pickett, H. M., Poynter, R. L., Flaud, J.-M., Camy-Peyret, C., Barbe, A., usson, N., Rinsland, C. P. and Smith, M. A. H. (1986). The HITRAN database, 1986 edition. *Appl. Optics*, **26**, 4058–409.

Rothman, L. S., Gamache, R. R., Tipping, R. H., Rinsland, C. P. *et al.* (1992). The HITRAN database: Editions of 1991 and 1992. *J. Quant. Spectros. Radiat. Transfer*, **48**, 469–507.

Rotstayn, L. D. (2000). On the "tuning" of autoconversion parameterizations in climate models. *J. Geophy. Res.*, **105**, 15495–15507.

Rouse, W. R. (1984). Microclimate of the Arctic tree line. 2: Soil microclimate of tundra and forest. *Water Resources Res.*, **20**, 67–73.

Rutter, A. J., Kershaw, K. A., Robins, P. C. and Morton, A. J. (1972). A predictive model of rainfall interception in forests. Part I: Derivation of the model from observations in a plantation of Corsican pine. *Agric. Meteorol.*, **9**, 367–384.

Rutter, A. J., Morton, A. J. and Robins, P. C. (1975). A predictive model of rainfall interception in forests. Part II: Generalization of the model and comparison with observations in some coniferous and hardwood stands. *J. Appl. Ecol.*, **12**, 367–380.

Sardeshmukh, P. and Hoskins, B. (1984). Spatial smoothing on the sphere. *Mon. Wea. Rev.*, **112**, 2524–2529.

Savijarvi, H. and Räisänen, P. (1997). Long-wave optical properties of water clouds and rain. *Tellus*, **50A**, 1–11.

Schaaf, C., Gao, F., Strahler, A., Lucht, W., Li, X., Tsang, T., Strugnell, N., Zhang, X., Jin, Y., Muller, J.-P., Lewis, P., Barnsley, M., Hobson, P., Disney, M., Roberts, G., Dunderdale, M., Doll, C., d'Entremont, R., Hu, B., Liang, S., Privette, J. and Roy, D. (2002). First operational brdf, albedo nadir reflectance products from modis. *Remote Sensing Environm.*, **83**, 135–148.

Scinocca, J. F. (2003). An accurate spectral nonorographic gravity wave drag parameterization for general circulation models. *J. Atmos. Sci.*, **60**, 667–682.

Sellers, P. J., Los, S. O., Tucker, C. J., Justice, C. O., Dazlich, D. A., Collatz, G. J. and Randall, D. A. (1996). A revised land surface parameterization (SiB2) fro GCMs. Part II: The generation of global fields of terrestrial biophysical parameters from satellite data. *J. Climate*, **9**, 706–737.

Shao, Y. and Irannejad, P. (1999). On the choice of soil hydraulic models in land-surface schemes. *Boundary-Layer Meteorol.*, **90**, 83–115.

Shettle, E. P. and Weinman, J. A. (1970). The transfer of solar irradiance through inhomogeneous turbid atmospheres evaluated by Eddington's approximation. *J. Atmos. Sci.*, **27**, 1048–1055.

Siebesma, P. (1998). Shallow cumulus convection. In E. J. P. et al. (Ed.), *Buoyant Convection in Geophysical Flows*, pp. 441–486, Kluwer Academic.

Siebesma, P. and Cuijpers, J. W. M. (1995). Evaluation of parametric assumptions for shallow cumulus convection. *J. Atmos. Sci.*, **52**, 650–666.

Siebesma, P. and Teixeira, J. (2000). An advection-diffusion scheme for the convective boundary layer: description and 1D-results. In *Proc. 14th Symposium on Boundary Layers and Turbulence*, Amer. Meteor. Soc.

Simmons, A. J., Untch, A., Jacob, C., Kallberg, P. and Under, P. (1999). Stratospheric water vapour and tropical tropopause temperatures in ECMWF analyses and muli-year simularions. *Q. J. R. Meteorol. Soc.*, **125**, 353–386.

Simpson, J. (1971). On cumulus entrainment and one-dimensional models. *J. Atmos. Sci.*, **28**, 449–455.

Simpson, J. and Wiggert, V. (1969). Models of precipitating cumulus towers. *Mon. Wea. Rev.*, **97**, 471–489.

Slingo, A. (1989). A GCM parameterization for the shortwave radiative properties of water clouds. *J. Atmos. Sci.*, **46**, 1419–1427.

Smith, E. A. and Shi, L. (1992). Surface forcing of the infrared cooling profile over the Tibetan plateau. Part I: Influence of relative longwave radiative heating at high altitude. *J. Atmos. Sci.*, **49**, 805–822.

Spichtinger, P., Gierens, K. and Read, W. (2003). The global distribution of ice-supersaturated regions as seen by the microwave limb sounder. *Q. J. R. Meteorol. Soc.*, **129**, 3391–3410.

Sundqvist, H. (1978). A parameterization scheme for non-convective condensation including prediction of cloud water content. *Q. J. R. Meteorol. Soc.*, **104**, 677–690.

Sverdrup, H. U., Johnson, M. W. and Fleming, R. H. (1942). *The Oceans: Their Physics, Chemistry and General Biology.* Prentice Hall, 1087 pp.

Tanre, D., Geleyn, J.-F. and Slingo, J. M. (1984). First results of the introduction of an advanced aerosol-radiation interaction in the ECMWF low resolution global model. In H. E. Gerber and A. Deepak (Eds), *Aerosols and Their Climatic Effects*, pp. 133–177, A. Deepak Publ., Hampton, Va.

Taylor, J. P., Edwards, J. M., Glew, M. D., Hignett, P. and Slingo, A. (1996). Studies with a flexible new radiation code. II: Comparisons with aircraft short-wave observations. *Q. J. R. Meteorol. Soc.*, **122**, 839–862.

Tegen, I., Hoorig, P., Chin, M., Fung, I., Jacob, D. and Penner, J. (1997). Contribution of different aerosol species to the global aerosol extinction optical thickness: Estimates from model results. *J. Geophys. Res.*, **102**, 23895–23915.

Tiedtke, M. (1989). A comprehensive mass flux scheme for cumulus parameterization in large-scale models. *Mon. Wea. Rev.*, **117**, 1779–1800.

Tiedtke, M. (1993). Representation of clouds in large-scale models. *Mon. Wea. Rev.*, **121**, 3040–3061.

Tiedtke, M. (1996). An extension of of cloud-radiation parameterization in the ecmwf model: The representation of sub-grid scale variations of optical depth. *Mon. Wea. Rev.*, **124**, 745–750.

Tompkins, A. M. (2002). A prognostic parameterization for the subgrid-scale variability of water vapor and clouds in large-scale models and its use to diagnose cloud cover. *J. Atmos. Sci.*, **59**, 1917–1942.

Tompkins, A. M., Bechtold, P., Beljaars, A., Benedetti, A., Cheinet, S., Janisková, M., Köhler, M., Lopez, P. and Morcrette, J. (2004). Moist physical processes in the IFS: Progress and Plans. *Technical report*, European Centre for Medium-Range Weather Forecasts.

Tompkins, A. M., Gierens, K. and Rädel, G. (2007). Ice supersaturation in the ECMWF integrated forecast system. *Q. J. R. Meteorol. Soc.*, **133**, 53–63.

Troen, I. and Mahrt, L. (1986). A simple model of the atmospheric boundary layer; sensitivity to surface evaporation. *Boundary-Layer Meteorol.*, **37**, 129–148.

Van den Hurk, B. J. J. M. and Viterbo, P. (2003). The Torne-Kalix PILPS 2(e) experiment as a test bed for modifications to the ECMWF land surface scheme. *Global and Planetary Change*, **38**, 165–173.

Van den Hurk, B. J. J. M., Viterbo, P., Beljaars, A. C. M. and Betts, A. K. (2000). Offline validation of the ERA40 surface scheme. *ECMWF Tech. Memo. No. 295.*

van Genuchten, M. (1980). A closed form equation for predicting the hydraulic conductivity of unsaturated soils. *Soil Science Society of America Journal*, **44**, 892–898.

Verseghy, D. L. (1991). Class-A Canadian land surface scheme for GCMs. I: Soil model. *Int. J. Climatol.*, **11**, 111–133.

Viterbo, P. and Beljaars, A. C. M. (1995). An improved land surface parametrization scheme in the ECMWF model and its validation. *ECMWF Tech. Report No. 75*, Research Department, ECMWF.

Viterbo, P., Beljaars, A. C. M., Mahouf, J.-F. and Teixeira, J. (1999). The representation of soil moisture freezing and its impact on the stable boundary layer. *Q. J. R. Meteorol. Soc.*, **125**, 2401–2426.

Viterbo, P. and Betts, A. K. (1999). Impact on ECMWF forecasts of changes to the albedo of the boreal forests in the presence of snow. *J. Geophys. Res.*, **104**, 27803–27810.

Wallace, J. M., Tibaldi, S. and Simmons, A. (1983). Reduction of systematic forecast errors in the ECMWF model through the introduction of an envelope orography. *Q. J. R. Meteorol. Soc.*, **109**, 683–717.

Warner, C. D. and McIntyre, M. E. (1996). An ultra-simple spectral parametrization for non-orographic gravity waves. *J. Atmos. Sci.*, **58**, 1837–1857.

Warrilow, D. L., Sangster, A. B. and Slingo, A. (1986). Modelling of land-surface processes and their influence on European climate. *UK Met Office Report, Met O 20, Tech Note 38.*

Washington, W. M. and Williamson, D. L. (1977). A description of the NCAR GCMs. In J. Chang (Ed.), *GCMs of the Atmosphere. Methods in Computational Physics*, Vol. 17, pp. 111–172, Academic Press.

Wexler, R. and Atlas, D. (1959). Precipitation generating cells. *J. Meteorol.*, **16**, 327–332.

Wilcox, R. W. and Belmont, A. D. (1977). Ozone concentration by latitude, altitude and month, near 80 W. *Report, Control Data Corporation, Contract No. DOT-FA77WA-3999.*

Williams, P. J. and Smith, M. W. (1989). *The Frozen Earth: Fundamentals of Geocryology.* Cambridge University Press, UK.

Wilson, D. and Ballard, S. (1999). A microphysical based precipitation scheme for the UK Meteorological Office numerical weather prediction model.

Wood, N., Brown, A. R. and Hewer, F. E. (2001). Parametrizing the effects of orography on the boundary layer, an alternative to effective roughness lengths. *Q. J. R. Meteorol. Soc.*, **127**, 759–778.

Wood, N. and Mason, P. J. (1993). The pressure force induced by neutral, turbulent flow over low hills. *Q. J. R. Meteorol. Soc.*, **119**, 1233–1267.

Zeng, X. and Beljaars, A. C. M. (2005). A prognostic scheme of sea surface skin temperature for modelling and data assimilation. *Geophys. Res. Lett.*, **32**, L14605.

Zeng, X., Dai, Y.-J., Dickinson, R. E. and Shaikh, M. (1998a). The role of root distribution for land climate simulation. *Geophys. Res. Lett.*, **25**, 4533–4536.

Zeng, X., Zhao, M. and Dickinson, R. E. (1998b). Intercom-parison of bulk aerodynamic algorithms for the computation of sea surface fluxes using the toga coare and tao data. *J. Climate*, **11**, 2628–2644.